UNIVERSITÀ DEGLI STUDI DI NAPOLI FEDERICO II

PH.D. THESIS

IN

INFORMATION AND COMMUNICATION TECHNOLOGY FOR HEALTH

TOMOGRAPHIC PHASE MICROSCOPY IN FLOW CYTOMETRY

DANIELE PIRONE

TUTOR: PROF. ANGELO LISENO

CO-TUTOR: PROF. AMEDEO CAPOZZOLI

CO-TUTOR: PROF. CLAUDIO CURCIO

CO-TUTOR: DR. PIETRO FERRARO

CO-TUTOR: DR. PASQUALE MEMMOLO

COORDINATOR: PROF. DANIELE RICCIO

XXXV CYCLE

SCUOLA POLITECNICA E DELLE SCIENZE DI BASE

DIPARTIMENTO DI INGEGNERIA ELETTRICA E DELLE TECNOLOGIE DELL'INFORMAZIONE

FRIDERICVS·DEI·GRA·IMPERATOR·ROMANORVM·SEMPER·AVGVST

To my Family

FRIDERICVS·DEI·GRA·IMPERATOR·ROMANORVM·SEMPER·AVGVST

TOMOGRAPHIC PHASE MICROSCOPY IN FLOW CYTOMETRY

Ph.D. Thesis presented
for the fulfillment of the Degree of Doctor of Philosophy
in Information and Communication Technology for Health

by

DANIELE PIRONE

October 2022

Approved as to style and content by

Prof. Angelo Liseno, Tutor

Prof. Amedeo Capozzoli, Co-Tutor

Prof. Claudio Curcio, Co-Tutor

Dr. Pietro Ferraro, Co-Tutor

Dr. Pasquale Memmolo, Co-Tutor

Università degli Studi di Napoli Federico II

Ph.D. Program in Information and Communication Technology for Health

XXXV Cycle - Coordinator: Prof. Daniele Riccio

https://icth.dieti.unina.it

Candidate's declaration

I hereby declare that this thesis submitted to obtain the academic degree of Philosophiæ Doctor (Ph.D.) in Information and Communication Technology for Health is my own unaided work, that I have not used other than the sources indicated, and that all direct and indirect sources are acknowledged as references.

Parts of this dissertation have been published in international journals and/or conference articles (see list of the author's publications at the end of the thesis).

Napoli, October 31, 2022

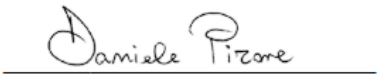

Daniele Pirone

Abstract

The future of early diagnosis and precision medicine will be based on the advanced single-cell analysis. To date, the gold-standard technique is Fluorescence Imaging Flow Cytometry (FIFC), which is able to quickly record 2D images of stained single cells while flowing through a measuring device. Thus, FIFC can satisfy the need for large informative datasets typical of Artificial Intelligence (AI), which has made possible a fast, automatic, and objective cell phenotyping. However, the staining process and the 2D qualitative information limit the FIFC clinical applications. Conversely, Tomographic Phase Microscopy (TPM) is a label-free optical microscopy technique that allows reconstructing the 3D spatial distribution of the refractive index (RI) at the single-cell level. The cellular RI is a key biophysical parameter proved to be an effective descriptor of cellular heterogeneity. In 2017, TPM has been proved working in Flow Cytometry (FC) mode. In TPM-FC, digital holograms of single cells are recorded in continuous flow while rotating in microfluidic environment. The TPM-FC tool is expected to create a breakthrough in the cell biology studies and in the clinical practice. Therefore, several computational strategies are developed in this Ph.D. Thesis for transferring the original proof of concept of TPM-FC into a concrete technology for the single-cell analysis. In particular, various issues to achieve the high-throughput property have been fixed and the lack of intracellular specificity, due to the label-free modality, has been filled for some organelles. Finally, the large datasets of single cells, collected through the TPM-FC system, have been used to train AI models for phenotyping cancer cells and recognizing drug resistance. In the near future, the attained results are expected to contribute in providing a solution to the challenging topic of the Liquid Biopsy (LB) technology, which aims to the early diagnosis of cancer and the development of personalized therapies by means of blood tests.

Keywords: Single-Cell Analysis, Digital Holography, Imaging Flow Cytometry, Tomographic Phase Microscopy, Artificial Intelligence, Liquid Biopsy.

Sintesi in Lingua Italiana

Il futuro della diagnosi precoce e della medicina di precisione si baserà sull'analisi avanzata a singola cellula. Ad oggi, la tecnica di riferimento è la citometria a flusso basata su imaging a fluorescenza (FIFC), capace di registrare rapidamente immagini 2D di singole cellule marcate mentre fluiscono attraverso un dispositivo di misurazione. FIFC può fornire grandi set di dati informativi all'intelligenza artificiale (AI), che ha reso possibile una fenotipizzazione cellulare veloce, automatica e oggettiva. Tuttavia, il processo di colorazione e le informazioni qualitative 2D limitano le sue applicazioni cliniche. Al contrario, la microscopia tomografica a contrasto di fase (TPM) è una tecnica di microscopia ottica senza coloranti che consente di ricostruire la distribuzione spaziale 3D dell'indice di rifrazione (RI) di singole cellule. L'RI cellulare è un parametro biofisico chiave in grado di descrivere l'eterogeneità cellulare. Il funzionamento della TPM in modalità citometrica a flusso (TPM-FC) è stato dimostrato nel 2017. Nella TPM-FC, gli ologrammi digitali di singole cellule vengono registrati mentre ruotano in un flusso microfluidico. La TPM-FC potrebbe creare una svolta negli studi di biologia cellulare e nella pratica clinica. Pertanto, in questa Tesi di Dottorato vengono sviluppate diverse strategie computazionali per trasformare l'originale proof of concept della TPM-FC in una tecnologia concreta. In particolare, sono stati risolti vari problemi per ottenere la proprietà di high-throughput e, per alcuni organelli, è stata colmata la mancanza di specificità intracellulare dovuta all'assenza di coloranti. Infine, sono stati addestrati modelli AI per la fenotipizzazione di cellule tumorali e il riconoscimento della resistenza ai farmaci. In futuro, i risultati raggiunti potrebbero contribuire a fornire una soluzione al difficile problema della biopsia liquida (LB), che mira alla diagnosi tumorale precoce e allo sviluppo di terapie personalizzate tramite analisi del sangue.

Parole chiave: Analisi a Singola Cellula, Olografia Digitale, Citometria a Flusso basata su Imaging, Microscopia Tomografica a Contrasto di Fase, Intelligenza Artificiale, Biopsia Liquida.

Contents

Acknowledgements

The research presented in this dissertation has been supported by the Institute of Applied Sciences and Intelligent Systems (ISASI) of the Italian National Research Council (CNR). The author's work has been carried out at the ISASI-CNR laboratory in Pozzuoli (Italy) in the framework of the PRIN 2017 (Progetti di Rilevante Interesse Nazionale) project MORFEO (MORphological biomarkers For Early diagnosis in Oncology), Prot. 2017N7R2CJ, under the scientific responsibility of Dr. Pietro Ferraro.

The author has spent three months of his Ph.D. research activity at the Optics Laboratory of Prof. Demetri Psaltis at the École Polytechnique Fédérale de Lausanne (EPFL) in Switzerland.

AVGVST FRIDERICVS ROMANORVM IMPERATOR SEMPER

List of Acronyms

3DZD	3D Zernike Descriptors
AI	Artificial Intelligence
AM	Amplitude Map
AUC	Area Under Curve
BPM	Beam Propagation Method
CAN	Context Aggregation Network
CCD	Charge Coupled Device
CIS	Contact Image Sensor
CMOS	Complementary Metal-Oxide-Semiconductor
CNR	Italian National Research Council
CSSI	Computational Segmentation based on Statistical Inference
CTC	Circulating Tumor Cell
DCNN	Deep Convolutional Neural Network
DH	Digital Holography
DHM	Digital Holography in Microscopy
DWT	Discrete Wavelet Transform
DL	Deep Learning
EC	Endometrial Cancer
EP	Edge-Preserving
ER	Endoplasmic Reticulum
FACS	Fluorescent Activated Cell Sorter
FBP	Filtered Back Projection

FC	Flow Cytometry
FIFC	Fluorescence Imaging Flow Cytometry
FM	Fluorescence Microscopy
FOV	Field Of View
FPM	Fourier Ptychographic Microscopy
FSC	Forward Scatter
FT	Fourier Transform
GFM	Graphene Family Material
GLCM	Gray-Level Co-occurrence Matrix
GLSZM	Grey-Level Size Zone Matrix
GMSD	Gradient Magnitude Similarity Deviation
GO	Graphene Oxide
GPU	Graphics Processing Unit
Hb	Hemoglobin
HIFC	Holographic Imaging Flow Cytometry
HOT	Holographic Optical Tweezers
IACS	Image-Activated Cell Sorter
IFC	Imaging Flow Cytometry
ISASI	Institute of Applied Sciences and Intelligent Systems
ISC	Illumination Scanning Configuration
KNN	K-Nearest Neighbor
LB	Liquid Biopsy
LD	Lipid Droplet
LDA	Linear Discriminant Analysis

LED	Light-Emitting Diode
LOC	Lab-On-Chip
LR	Logistic Regression
LT	Learning Tomography
MAE	Mean Absolute Error
ML	Machine Learning
MLP	Multilayer Perceptron
MO	Microscope Objective
MTT	Methyl Thiazolyl Tetrazolium
NA	Numerical Aperture
NAR	Nucleus Aspect Ratio
NCAR	Nucleus-Cell Area Ratio
NCVR	Nucleus-Cell Volume Ratio
NF-kB	Nuclear Factor kB
nGO	NanoGraphene Oxide
NGTDM	Neighborhood Grey-Tone Difference Matrix
NNC	Non-Negativity Constraint
NNCCD	Normalized Nucleus-Cell Centroid Distance
NP	NanoParticle
NRMSE	Normalized Root Mean Square Error
NSVR	Nucleus Surface-Volume Ratio
OCH	Organelle Convex Hull
ODT	Optical Diffraction Tomography
OPL	Optical Path Length

PBMC	Peripheral Blood Mono-Nuclear Cell
PBS	Polarizing Beam Splitter
PCA	Principal Component Analysis
PSF	Point Spread Function
QPI	Quantitative Phase Imaging
QPM	Quantitative Phase Map
RBC	Red Blood Cell
RI	Refractive Index
RMSE	Root Mean Square Error
ROC	Receiver Operating Characteristic
RSM	Random Subspace Method
RT	Radon Transform
SCC	Spatial Correlation Coefficient
SFS	Shape From Silhouette
SLM	Spatial Light Modulator
SRC	Sample Rotation Configuration
SSC	Side Scatter
SSIM	Structural Similarity Index
SVM	Support Vector Machine
TAM	Tomographic Amplitude Microscopy
TC	Tamura Coefficient
TDI	Time Delay and Integration
TNFα	Tumor Necrosis Factor α
TPM	Tomographic Phase Microscopy

TSI	Tamura Similarity Index
t-SNE	t-Distributed Stochastic Neighbor Embedding
TV	Total Variation
UIQI	Universal Image Quality Index
WBC	White Blood Cell
WMW	Wilcoxon-Mann-Whitney

AVGVST FRIDERICVS ROMANORVM IMPERATOR SEMPER

List of Figures

FRIDERICVS·DEI·GRA·IMPERATOR·ROMANORVM·SEMP·AVGVST

List of Tables

AVGVST FRIDERICVS IMPERATOR ROMANORVM SEMPER

Introduction

Cellular populations are often heterogeneous with respect to cell cycle phase, size, shape, and physiological state. Therefore, a deep inspection of intraspecies variability is essential for assaying diversity and searching for rare cells with specific features (e.g., tumor cells, stem cells, etc.), which instead could be most likely lost within average measurements. Therefore, the future of early diagnosis and precision medicine will be based on the accurate screening at single-cell level. The gold standard imaging technique to render a cell and its organelles visible on a selective basis is Fluorescence Microscopy (FM), which uses various stains or fluorescent tags.

For a long time, single-cell analysis has been based on the visual phenotyping, that is the characterization and quantification of distinctive cellular and sub-cellular traits in FM images by a human operator. However, visual cell phenotyping is limited by the operator's experience and prevents an advanced cellular inspection as complex phenomena could be hidden at the human eye. Therefore, a revolution in the cytometry framework has been introduced by AI. AI largely extends the variety of tasks that image analysis can accomplish, thus aiding the cell phenotyping by making it automatic and objective, that is, not dependent on specific skills of the operator.

The main limitation of AI is the need for large informative datasets, which often cannot be easily collected. In the context of single-cell analysis, a solution has been provided by Imaging Flow Cytometry (IFC). IFC is a sophisticated technique able to record bright-field, dark-field, and fluorescent images of single cells while flowing in suspension through a measuring device at high-throughput. From the collected images, multiple parameters can be extracted,

related to the whole cell and its intracellular organelles (e.g., size, shape, granularity, fluorescence intensity, and many others). Therefore, fitting between AI and IFC has demonstrated being fruitful as each of these two techniques takes advantage from the other's capabilities, thus pushing up the development and innovation of high-throughput cell biology applications, which are moving toward well-defined protocols for the final clinical approval in cancer biology, immunology, microbiology and stem cell biology.

Multimodal imaging based on the combination between bright-field microscopy and FM still remains the gold standard in IFC. However, although FM has allowed to achieve meaningful progress in cell biology, thus greatly advancing the scientific knowledge, some important drawbacks limit its application in biomedicine. While stains and tags offer high-contrast imaging with intracellular specificity, often they are incompatible with live cell analysis and may have confounding effects on the cells. Moreover, the knowledge about exogenous biochemical markers is requested to identify a certain cellular trait, that is cumbersome in the case of unknown and rare cell types in a highly heterogeneous population. Furthermore, large-scale FM assays can be sample preparation-dependent, costly, labor-intensive, and time-consuming, thus hindering their applications in biology and biomedicine. In addition, photobleaching can alter the quality of the imaging, above all in long experiments, the use of exogenous labelling agents may alter the normal physiology of cells (phototoxicity), thus reducing the reliability of FM information, and labelled cells cannot be re-injected into the human body. Finally, FM imaging is mainly qualitative, which means that only morphological parameters and fluorescence signals can be measured, while missing the quantitative characterization of the biophysical properties of a cell, able to reflect its current state (e.g., healthy or sick). Therefore, these limitations have prompted the development of label-free methods for live imaging in order to avoid chemical staining.

Among label-free methods, Digital Holography (DH) has settled as rapid, non-destructive, and minimally invasive imaging technique for the single-cell

analysis. The exogeneous staining is avoided in DH because, by exploiting the interferometric principles, the endogenous phase contrast of the cell is imaged by recording the fringe pattern produced after the interference between a reference wave and an object wave (passed through the sample). Then, a numerical holographic processing allows retrieving the quantitative phase map (QPM) of a single cell from the recorded digital hologram. The QPM is a 2D image in which the information about the 3D cell morphology is coupled to the information about the 3D spatial distribution of the cellular RI. The cellular RI is related to the biophysical properties of the cell (e.g., dry mass), and has been exploited for studying a multitude of cellular processes, such as cell-cycle progression, cell differentiation, and malignant transformation, thus proving to be an effective descriptor of the cellular heterogeneity. For these reasons, Quantitative Phase Imaging (QPI) has emerged as a very useful tool in label-free microscopy, being complementary to FM but without the staining-related drawbacks, and many significant results have been achieved in the label-free single-cell analysis. Even though QPI can be obtained by means of different imaging techniques, DH is the most common one mainly because of its refocusing capability, meaning that the focus plane of the cell can be numerically retrieved after the experiment. Thus, the DH refocusing property has been exploited for realizing label-free holographic IFC (HIFC). Besides the lack of exogeneous staining and the related advantages, HIFC is emerging over the conventional FIFC thanks to the wealth of biophysical information that can be measured in high-throughput from the QPM of a single cell, thus addressing much better the AI need for information-rich quantitative measurements. Hence, the combination between HIFC and AI is boosting the detection and analysis of cellular heterogeneity with respect to conventional FIFC.

Since the mid-1990s, QPI has been successfully used for many cellular studies. However, in case of complex 3D structures, QPI can lead to inaccurate interpretations since, as a first approximation, a QPM can be considered as the integral of the cellular RI along the optical axis. To fully exploit the great potential of QPI, TPM has been proposed for the first time in 2006. TPM is a

label-free optical microscopy technique that allows reconstructing the 3D RI spatial distribution of single cells. Therefore, TPM gives access to the highest informative content at the single-cell level, that is the full reconstruction of the cellular volume and its RI content in 3D. At this aim, in analogy to Computed Tomography (CT), multiple QPMs are recorded at several viewing angles around the sample in order to decouple the two quantities encoded inside a single QPM. Starting from 2006, TPM has undergone a fast development. In particular, the actual state-of-the-art TPM systems work in static environment. They are based on the illumination of the fixed sample while changing the beam direction or on the illumination of the sample along a fixed beam direction while rotating because of mechanical/optical forces. In the first case, the tomographic reconstruction is not isotropic, while, in the second case, the tomogram is isotropic, but the sample can be biologically altered by the external forces needed to rotate it and the complex recording system prevents the tomographic recording of large number of cells.

To overcome these drawbacks, the first proof of concept of TPM in FC mode has been demonstrated in 2017 at the Institute of Applied Sciences and Intelligent Systems (ISASI) of the Italian National Research Council (CNR). In TPM-FC, digital holograms of single cells are recorded along a fixed beam direction while flowing along a microfluidic channel and rotating because of the hydrodynamic forces of the laminar flow generated by a microfluidic pump. In the TPM-FC recording system, cells experience a full rotation during DH recording, thus the reconstruction is isotropic and no external alteration is introduced on the cell. Moreover, cells are recorded in suspension in a buffer medium and not in adhesion, thus they are not spread at rest on a surface and, as a consequence, the 3D RI tomograms reveal their actual shape and inner organization, i.e. the volumetric distribution of intracellular organelles.

Regarding this latter aspect, label-free techniques like QPI and TPM suffer a main drawback with respect to FM, that is the lack of intracellular specificity. In fact, in FM, the employment of organelle-specific exogeneous markers allows distinguishing the intracellular components among them, thus

providing a subcellular analysis at single-cell level. Instead, the endogenous phase-contrast in QPI, and then the resulting RI-contrast in TPM, often are not enough to guarantee the recognition of a certain organelle. For this reason, even though TPM provides the 3D spatial distribution of the RIs inside the cellular volume, only an overall intracellular analysis can be performed without organelle specificity. Recently, AI-based strategies have been proposed to fill the specificity gap between FM and label-free QPI and conventional static TPM. Unfortunately, these AI approaches cannot be replicated in TPM-FC, as the creation of a dataset of flowing suspended cells with a voxel-level registration between 3D RI and 3D fluorescence tomograms is not obtainable, thus the AI model cannot learn from examples of co-registered data pairs. At the same time, AI has started to be used to solve classification problems of single cells reconstructed by means of conventional static TPM, taking great advantage of the high-content quantitative information contained inside a cellular 3D RI tomogram. However, the small tomographic dataset that can be created in static condition represents a limitation for the huge potential that the combination between AI and TPM could offer to the single-cell analysis. Of course, a solution is expected to be provided when the potential high-throughput property of TPM-FC will be fully exploited and the intracellular specificity will be accessed inside TPM-FC tomograms.

This Ph.D. Thesis, carried out at ISASI-CNR, aims to develop computational strategies for transferring the original proof of concept of TPM-FC into a concrete technology for the single-cell analysis to be exploited for clinical applications. The TPM-FC tool is expected to create a breakthrough for the cell biology studies and for the clinical practice, because, unlike the gold-standard FIFC, single-cell analysis can be performed in quantitative way, in 3D, and without the employment of exogenous labels, but providing at the same time the high-throughput property requested by AI models. In particular, among the others, the most promising application of TPM-FC in biomedicine is LB. It is a test done on a sample of blood to search for circulating tumour cells

(CTCs). Unlike conventional tissue biopsy, LB is cheaper, minimally invasive, and aims to the early diagnosis of tumours and the development of personalized therapies. TPM-FC, combined to AI, is the ideal candidate for realizing the LB paradigm, as it gives a powerful tool for searching rare cells into the bloodstream thanks to the FC mode and the possibility of extracting the most reliable fingerprint at the single-cell level, that can be used as cancer biomarker. Finally, thanks to the DH underlying principle, such a LB tool based on TPM-FC has great chances to be miniaturized into lab-on-chip (LOC) devices for rapid, cheap, and easily accessible point-of-care biomedical applications.

This Ph.D. Thesis is structured as follows.

In Chapter 1, a general overview about the DH theory and the QPI applications in biomedicine is introduced. The conventional TPM technology working in static conditions is described. In particular, the state-of-the-art TPM setups are introduced, along with their advantages and drawbacks, and the tomographic algorithms commonly implemented for reconstructing the 3D RI tomograms from the recorded QPMs are discussed. Then, the latest TPM applications developed in the biomedical field are presented. Finally, a first result of this Thesis is described, regarding the implementation of an alternative static TPM system for the non-destructive tomographic reconstruction directly at the nuclear level within plant cells based on the dehydration process.

In Chapter 2, after an overview of the IFC tool and its applications in both fluorescence and label-free modality, the main topic of this Ph.D. Thesis is introduced, that is TPM-FC. From this point of the Thesis onwards, the main results obtained during the Ph.D. research activity are presented. In particular, the latest implementation of the opto-fluidic recording system developed at the aim of optimizing the TPM-FC performance is described. To replicate the high-throughput property of a conventional IFC system, an automatic reconstruction pipeline is proposed, including the QPMs retrieval of a cell flowing and rotating along a microfluidic channel and the estimation of its

unknown viewing/rolling angles, in order to reconstruct the cell's 3D RI tomogram. Finally, an assessment is performed on the hydrodynamic mutual interactions that could arise among cells and perturb their tomographic reconstructions when high-throughput conditions are met, thus setting an upper bound about the achievable throughput.

In Chapter 3, after fixing the TPM-FC system and the numerical processing pipeline, some applications are explored for the single-cell analysis, based on the combination between TPM-FC data and AI models. AI is firstly exploited for greatly speeding up the heavy and time-consuming numerical holographic processing requested by TPM-FC, thus representing a further step toward the recording of large tomographic datasets in short times. Then, AI models are employed to solve classification problems based on the datasets collected by means of a TPM-FC system. In particular, from the diagnostic point of view, cancer cells are identified within a background of healthy blood cells, and then phenotyping of cancer cells is performed, also exploiting the principles of fractal geometry. Instead, from the therapeutical point of view, the possibility of recognizing the drug resistance is proved, useful for establishing precision medicine. At this aim, three possibilities are explored, i.e. the classification of the raw holographic data, classification of the phase signature, and classification of the 3D RI distribution.

In Chapter 4, the main TPM-FC issue related to the lack of intracellular specificity is addressed by means of computational methods avoiding AI, thus filling the specificity gap with FIFC. In particular, the nucleus is segmented from the 3D RI tomogram of the whole cell through a statistical approach aiming at identifying statistical similarities between groups of RI cellular voxels. The same approach is demonstrated working also for the nucleolus by means of a numerical cell phantom. A RI threshold-based segmentation is employed for the counting, localization, and analysis of lipid droplets (LDs) inside the TPM-FC tomograms. The latter approach has also been exploited as analytical tool for inspecting the possibility of detecting LDs inside 2D QPMs recorded in FC mode by studying the way their presence changes the

focalization property of the whole cell, modelled as a biolens. After considering endogenous organelles, a variant of TPM-FC is described at the aim of visualizing in 3D the internalization of nanographene oxide inside live suspended cells, useful for example for drug delivery applications. Finally, a method for the quasi-lossless compression of the 3D RI tomograms based on the 3D Zernike polynomials is proposed. In fact, unlike conventional FIFC in which 2D images must be saved, the storage of 3D tomograms recorded in high-throughput modality represents a practical problem to be solved for the clinical implementation of TPM-FC. Thanks to the proposed method, reducing the size of the recorded tomograms without losing their intracellular RI content and then the reliability of the achievable biomarkers is possible.

This Ph.D. Thesis ends with the conclusions in Chapter 5, reporting an overview about LB, in which its main challenges are discussed along with the perspectives opened by the new TPM-FC paradigm and the multiple topics herein addressed.

CHAPTER

1 Tomographic Phase Microscopy

Imaging of biological cells and tissues is critical for biological research and medical diagnosis. Therefore, microscopy has become the most used tool in medicine and biology. However, despite significant breakthroughs, optical imaging of biological samples remains an active research field, with the aim of further improving its performances and applications in biomedicine. Since the mid-1990s, the role of FM as gold standard technique in the optical microscopy field has been questioned by label-free QPI [1]. In a QPM, the information about the physical thickness of the sample and its RI are coupled together in the same 2D integral image. To record a QPM, exogenous staining is avoided because the endogenous phase contrast of the cell is imaged, usually by exploiting the interference principles of DH systems [2] [3]. Furthermore, in order to gain the whole 3D cell information, the first tomographic version of QPI has been implemented in 2006, termed TPM [4]. TPM is a label-free optical microscopy technique that allows decoupling the two quantities encoded in the 2D QPM, thus reconstructing the 3D spatial distribution of RIs at the single-cell level. Hence, TPM provides a label-free quantitative full characterization of the cell. Indeed, cell RI is correlated with other cell biophysical properties (mechanical, electrical, and optical), and not only represents the intracellular mass and concentration of a cell, but also provides important insights for various biological models [5]. Therefore, starting from the first attempt in 2006, TPM has captured enormous attention in the optics world due to its promising biomedical applications, and a fast and considerable development has occurred for both the hardware and software

components, i.e. the optical setup and the reconstruction algorithm, respectively.

In this Chapter, the general concepts about DH and QPI are introduced, along with an overview of their implications in the biomedical field. The conventional TPM optical systems and the common tomographic reconstruction algorithms are then described. A discussion follows about the TPM applications in biomedicine developed in recent years. Finally, an alternative TPM strategy herein developed for reconstructing the 3D RI tomogram directly at the intracellular level inside plant cells is presented [6].

1.1 Quantitative Phase Imaging by Digital Holography

Contrast defines how clearly a subject of interest is distinguished from the background. For a biological specimen, the thickness and RI inhomogeneity determine how much light scattering it produces. As in the visible spectrum most cells and tissues do not absorb significantly, contrast of a biological specimen is mainly determined by its light scattering. The scattered light generated by single cells and thin tissue slices is orders of magnitude weaker than the incident light. This class of specimens is referred to as *phase objects*, as they affect significantly only the phase of the incident field [1]. The gold standard imaging technique to render such structures visible is FM, which consists in converting them into *amplitude objects* using various stains or fluorescent tags [7]. However, while stains and tags offer high-contrast imaging with molecular specificity, FM is often qualitative and sample preparation-dependent, while photobleaching and phototoxicity limit fluorescent imaging of live cells. Furthermore, the use of exogenous labelling agents, such as fluorescent proteins or dyes, may alter the normal physiology of cells and, furthermore, labelled cells cannot be re-injected into the human

body [1]. Instead, QPI is emerging as a powerful label-free approach for cells and tissues, since it makes possible a nanoscale sensitivity to morphology and dynamics, 2D, 3D and 4D non-destructive imaging of completely transparent structures, and quantitative imaging based on intrinsic contrast. QPI is complementary to FM but avoids the phototoxicity and photobleaching limitations. A QPM contains the optical path length (OPL) delays introduced by the sample, i.e.

$$\begin{cases} QPM(x,y) = \frac{2\pi}{\lambda} OPL(x,y) \\ OPL(x,y) = \int_z \left[n(x,y,z) - n_{\mathrm{m}} \right] dz \end{cases}, \tag{1.1}$$

where λ is the wavelength, z is the optical axis, $n(x,y,z)$ is the 3D spatial distribution of the cell RI, and n_{m} is the RI of the surrounding medium (supposed homogeneous). Therefore, QPI provides a quantitative measurement of both the cell morphology and biophysical properties related to its RIs [1]. In particular, among several strategies [1] [3], Digital Holography in Microscopy (DHM) is the most common way to record a QPM.

1.1.1 Digital Holography in Microscopy

The term holography comes from the Greek words *holos*, which means *whole*, and *graphein*, which means *to write*. It is indeed an imaging method to record and reconstruct the whole information contained within an optical wavefront (i.e., amplitude and phase), instead of the sole intensity, as occurs with a conventional photograph. Holography was invented by Dennis Gabor in 1948 at the aim of correcting spherical aberrations, thus improving the images of electron microscopy [8]. However, due to the poor quality of the reconstructed images, the interest around holography declined until the 1960s, when the development of lasers made available a powerful source of coherent light. Therefore, in 1971 Gabor received the Nobel Prize in physics for his invention.

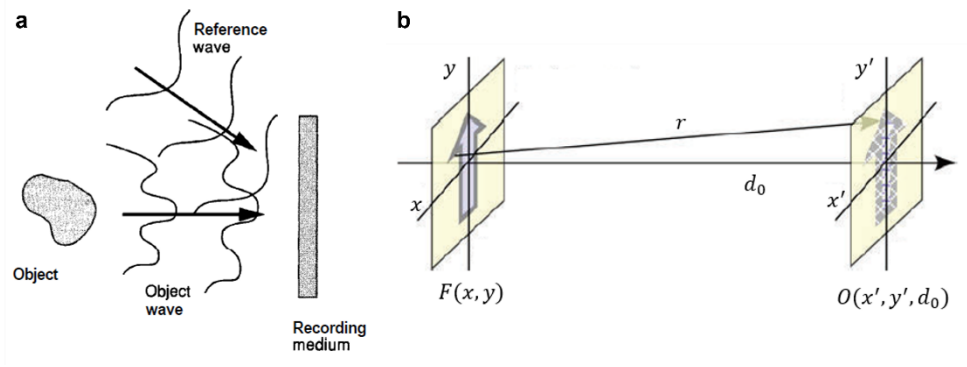

Figure 1.1 Hologram recording.
(a) The interference pattern produced by the reference wave and the object wave is recorded. **(b)** Geometry of diffraction. $\{x, y\}$ is the object plane. $\{x', y'\}$ is the hologram plane. (Figure a reproduced from Ref. [8]; Figure b reproduced from Ref. [2])

Although the holographic principle could be applied to the electromagnetic waves in all regions of the spectrum, in the follow the focus will be restricted to the field of optics.

The holographic process is made of two successive steps, i.e. a recording step and a reconstruction step of both the amplitude and phase components of an optical wavefront coming from a coherently illuminated object [2]. As the recording media respond only to light intensity, the phase information must be converted into an intensity variation. At this purpose, interferometry can be exploited. A reference wavefront, with known amplitude and phase, is added to the unknown object wavefront, as shown in Figure 1.1(a).

Holography became a working tool to record and reconstruct whole wavefields both in amplitude and phase and, thanks to this unique feature, it found application in numerous fields, like the optical metrology. In fact, this technique allows the measurement of the changes of the phase of the wavefield and thus the changes of any physical quantity that affects the phase. An important step forward occurred when the development of computer technology and solid state image sensors made it possible digital recording on

charge coupled device (CCD) and numerical holographic reconstruction, thus giving origin to DH. In the following, the DH process is described in the framework of digital Fresnel holography [9].

Phenomena involved in DH are linear processes. Therefore, it seems reasonable to associate object and image by means of a convolutional relation. The reconstructed field can be written in the form of a convolution product between the real object and the impulse response of the full DH process. Considering a reference system of coordinates $\{x, y\}$ attached to the principal surface of a real object, and a z-axis perpendicular to this surface, that corresponds to the propagation direction of the diffracted light beam, it results

$$F_R(x,y) = F(x,y) \otimes T(x,y), \tag{1.2}$$

where $F_R(x,y)$ is the reconstructed field, $F(x,y)$ is the real object, and $T(x,y)$ is the full process related to the image formation. The object surface illuminated by a coherent beam produces the following object wavefront

$$F(x,y) = F_0(x,y)\exp[j\Phi_0(x,y)], \tag{1.3}$$

where $\Phi_0(x,y)$ is related to the roughness of the object surface and can be modeled as uniformly distributed, i.e. $\Phi_0(x,y) \sim U(-\pi,\pi)$. It is possible that the object is not perfectly centered in the origin of the reference system. However, without loss of generality, the case $x_0 = y_0 = 0$ is considered.

The object wavefront propagates through at distance d_0, in which the reference set of coordinates is chosen to be $\{x', y'\}$, as reported in Figure 1.1(b). The diffracted field produced by the object is given by the Fresnel–Kirchhoff diffraction formula [3]

(1.4)

$$O(x',y',d_0) = -\frac{j}{\lambda d_0} \times \times \iint_{R^2} F(x,y)\exp\left[j\frac{2\pi}{\lambda}\sqrt{(x-x')^2+(y-y')^2+{d_0}^2}\right]dxdy'$$

where λ is the wavelength. The distance d_0 is called recording distance. The Eq. (1.4) can be written as a convolution integral

$$O(x', y', d_0) = F(x, y) \otimes S_H(x', y', d_0), \tag{1.5}$$

where the Point Spread Function (PSF)

$$S_H(x', y', d_0) = -\frac{j}{\lambda d_0} \exp\left[j \frac{2\pi}{\lambda} \sqrt{x'^2 + y'^2 + {d_0}^2} \right] \tag{1.6}$$

is the Huygens spherical wavelet [3].

For paraxial approximation, valid for

$${d_0}^3 \gg \frac{\pi}{4\lambda} [(x - x')^2 + (y - y')^2]^2_{max}, \tag{1.7}$$

the Fresnel PSF is obtained from the Eq. (1.6) as

$$S_F(x', y', d_0) = -\frac{j}{\lambda d_0} \exp\left[j \frac{2\pi}{\lambda} d_0 + \frac{j\pi}{\lambda d_0} \left(x'^2 + y'^2 \right) \right]. \tag{1.8}$$

Hence, the diffracted field produced by the object is given by the Fresnel approximation

$$\begin{aligned} O(x', y', d_0) = \; & \frac{j \exp\left[j \frac{2\pi d_0}{\lambda} \right]}{\lambda d_0} \times \\ & \times \iint_{R^2} F(x, y) \exp\left\{ j \frac{\pi}{\lambda d_0} [(x - x')^2 + (y - y')^2] \right\} dx dy \end{aligned}. \tag{1.9}$$

With a simple mathematical manipulation, the Eq. (1.9) can be rewritten in terms of Fourier Transform (FT)

$$O(x', y', d_0) = Z(x', y', d_0) \mathcal{FT}\{F(x, y) W(x, y, d_0)\}, \tag{1.10}$$

where

$$\begin{cases} Z(x', y', d_0) = \frac{j}{\lambda d_0} \exp\left\{ \frac{2\pi}{\lambda} \left[d_0 + \frac{x'^2 + y'^2}{2 d_0} \right] \right\} \\ W(x, y, d_0) = \exp\left\{ j \frac{\pi}{\lambda d_0} (x^2 + y^2) \right\} \end{cases}. \tag{1.11}$$

As shown in Eq. (1.10), each optical field consists of an amplitude distribution as well as a phase distribution, but all detectors register the sole intensity,

while the phase is lost in the registration process. Instead, if two waves of the same frequency interfere, the resulting intensity distribution is temporally stable and depends on the phase difference. This is used in DH where the phase information is coded by interference into a recordable intensity. The diffracted field produced in Eq. (1.10) interferes with a reference wave having spatial coordinates $\{u_R, v_R\}$ on the plane $\{x', y'\}$, i.e.

$$R(x', y') = a_R \exp[j2\pi(u_R x' + v_R y') + j\Omega(x', y')], \tag{1.12}$$

where the term $\Omega(x', y')$ corresponds to aberrations of the reference wavefront. Finally, in the interference plane, the hologram H is written as

$$\begin{aligned} H(x', y', d_0) = \; & |O(x', y', d_0)|^2 + |R(x', y')|^2 + \\ & + R^*(x', y')O(x', y', d_0) + R(x', y')O^*(x', y', d_0) \end{aligned} \tag{1.13}$$

In Eq. (1.13) there are three terms, also called diffraction order terms. The zero order term, indicated by $Q(x', y', d_0)$, is given by

$$Q(x', y', d_0) = |O(x', y', d_0)|^2 + |R(x', y')|^2. \tag{1.14}$$

The other two orders, noted by $H^{+1}(x', y', d_0)$ and $H^{-1}(x', y', d_0)$, are called $+1$ order (or real order) and -1 order (or conjugate/virtual order), respectively, i.e.

$$\begin{aligned} H^{+1}(x', y', d_0) \; & = R^*(x', y')O(x', y', d_0) = \\ & = a_R |O(x', y', d_0)| \exp\{j\arg[O(x', y', d_0)]\} \times, \\ & \quad \times \exp\{-j2\pi(u_R x' + v_R y') - j\Omega(x', y')\} \end{aligned} \tag{1.15}$$

and it is simple to note that $H^{-1}(x', y', d_0) = \{H^{+1}(x', y', d_0)\}^*$.

Finally, the Eq. (1.13) can be rewritten as

$$H(x', y', d_0) = Q(x', y', d_0) + H^{+1}(x', y', d_0) + H^{-1}(x', y', d_0). \tag{1.16}$$

An alternative approach to describe diffraction is by analysis of the Angular Spectrum [3]. The Angular Spectrum is defined as the FT of the real object $F(x, y)$ in the object plane $\{x, y\}$, i.e.

$$A_0(k_x,k_y) = \mathcal{FT}\{F(x,y)\} = \frac{1}{2\pi}\iint_{R^2} F(x,y)\exp\left[-j\left(k_x x + k_y y\right)\right]dxdy \tag{1.17}$$

Then, the input field $F(x,y)$ is the inverse FT

$$F(x,y) = \mathcal{FT}^{-1}\{A_0(k_x,k_y)\} = \frac{1}{2\pi}\iint_{R^2} A_0(k_x,k_y)\exp\left[j\left(k_x x + k_y y\right)\right]dk_x dk_y \tag{1.18}$$

The exponential phase factor is the $\{x,y\}$ projection of a plane wave with a wave vector $\vec{k} = (k_x,k_y,k_z)$, where $k_z = \sqrt{k^2 - {k_x}^2 - {k_y}^2}$. After propagation over a distance d_0, the plane wave acquires an additional phase factor $\exp(jk_z d_0)$, so that the diffracted field produced by the object is given by

(1.19)

$$\begin{aligned} O(x',y',d_0) &= \frac{1}{2\pi}\iint_{R^2} A_0(k_x,k_y)\exp\left[j\left(k_x x' + k_y y' + \sqrt{k^2 - {k_x}^2 - {k_y}^2}\,d_0\right)\right]\times \\ &\times circ\left(\frac{\sqrt{{k_x}^2+{k_y}^2}}{k}\right)dk_x dk_y = \\ &= \mathcal{FT}^{-1}\left\{A_0(k_x,k_y)exp\left[j\sqrt{k^2 - {k_x}^2 - {k_y}^2}\,d_0\right]circ\left(\frac{\sqrt{{k_x}^2+{k_y}^2}}{k}\right)\right\}_{[x',y']} \end{aligned}$$

The circle function *circ*, whose value is 1 where the argument is less than 1 and 0 otherwise, is necessary to restrict k_z to be real. Ordinarily, $k^2 \geq {k_x}^2 + {k_y}^2$, and the circle function can be dropped. The Eq. (1.19) can be also expressed as a convolution, i.e.

$$O(x',y',d_0) = F(x,y) \otimes S_A(x',y',d_0), \tag{1.20}$$

where

$$S_A(x',y',d_0) = \frac{1}{2\pi}\mathcal{FT}^{-1}\left\{exp\left[j\sqrt{k^2 - {k_x}^2 - {k_y}^2}\,d_0\right]\right\}_{[x',y']}. \tag{1.21}$$

Note that the Fresnel PSF in Eq. (1.8) can be expressed as

$$S_F(x', y', d_0) = \frac{1}{2\pi}\mathcal{FT}^{-1}\left\{exp\left[jkd_0 - \frac{j\lambda d_0}{4\pi}\left({k_x}^2 + {k_y}^2\right)\right]\right\}_{[x',y']}. \tag{1.22}$$

Under paraxial approximation, the Fresnel transform and Angular Spectrum methods are equivalent, otherwise the second one or the Fresnel-Kirchhoff diffraction formula must be used.

1.1.2 Recording Systems

A basic DHM setup consists of an illumination source, an interferometer, a digitizing camera, and a computer [3]. Most often, a laser is used for illumination with the necessary coherence to produce interference, even if there are also low-coherence techniques for the purpose of reducing speckle noise. In the in-line DHM scheme, the object and reference waves propagate along the same direction, while in the off-axis configuration, the reference wave has an appreciable angle in respect to the object wave [8]. Even if the in-line system is simpler to build, it is limited by the poor quality of the reconstructed image because of the superimposition of the virtual image and the scattered light from the directly transmitted beam (i.e., the so-called twin-image problem). Instead, in the off-axis setup, the two images are well separated without overlapping [10]. Two main types of interferometers are commonly employed, i.e. the Michelson interferometer for reflective objects and the Mach-Zehnder interferometer for transmissive objects. In both designs, the object is illuminated with a plane wave, and the reference arrives at the sensor plane with the same wavefront curvature as the object wave, except for an offset in the angle of incidence for off-axis holography [3]. The Mach-Zehnder types require more components but offer more flexibility in alignment, especially when microscopic imaging optics are used. A CCD or a complementary metal-oxide-semiconductor (CMOS) camera can be used to capture and digitize a holographic interference pattern. The pixel size of these devices is several microns with pixel counts up to tens of millions. Of course,

the higher the pixel number, the larger the amount of data to store and the lower the maximum camera frame rate. These parameters, coupled to the properties of the microscope objective (MO), define the perimeter of possible DHM applications, but one would expect them to continue to improve in the coming years. The captured hologram pattern is digitized by the camera and input to the computer as a 2D array of integers with 8-bit or higher grayscale resolution. The main task of the computer is to carry out the DH processing to extract a QPM from the recorded digital hologram [3].

1.1.3 Numerical Processing

In order to describe the main numerical operations in DHM [3], the example in Figure 1.2 is used, reporting the imaging of several cells on a Petri dish. The corresponding digital hologram is shown in Figure 1.2(a). In the red inset, the interference fringe pattern is overlapped to a zoomed-in cell. The common DHM numerical processing implemented to extract the QPM from the recorded digital hologram is made of apodization, suppression of DC and twin image terms, refocusing, aberration compensation, and phase unwrapping.

Apodization

The sharp boundaries of the hologram aperture can cause spurious fringing in the reconstructed images, especially in the case of phase images. This effect can be numerically reduced by apodization of the boundary of the hologram with a smoothly attenuating function [11]. In fact, apodization is a method for obtaining a better concentration of energy in the center of the images by reducing the losses due to diffractions. An example of apodization is displayed in Figure 1.2(b).

Suppression of DC and Twin Image Terms

The DC term, which includes reference and object field intensities, can be reduced by subtracting the average value from the hologram array. Since the

object as well as the reference fields have spatial variations, the DC component has a finite amount of spectral spread around the zero frequency. Therefore, in a DH off-axis configuration, a high-pass filtering in the Fourier spectrum can be applied to suppress the DC term and also to select one of the twin first order terms as well as eliminate spurious spectral components due to parasitic reflections and interference, thus improving the quality of the reconstructed image [12]. In fact, as shown in Figure 1.2(c), the three diffraction orders are separated in the Fourier spectrum thanks to the off-axis mode. The inverse FT of the filtered hologram corresponds to the demodulated hologram. An example of demodulated hologram is displayed in Figure 1.2(d).

Refocusing

In classical imaging systems, it is difficult or impossible to recover the focused image from a defocused one. With DHM, the image can be calculated at any distance from the hologram, since a hologram contains information of the full 3D space of the specimen. To determine if an image is in focus, a sharpness metric can be used [13], thus making automatic the numerical refocusing (also named autofocusing), as discussed in more detail in Section 2.4.2. An example of amplitude component of the reconstructed in-focus wavefield is displayed in Figure 1.2(e).

Aberration Compensation

Because of the direct numerical access to the phase profile of the wavefront, with DH it is possible to manipulate the phase profiles with flexibility and versatility unmatched by any other imaging method, thus simplifying the compensation of aberrations. Among several methods [3] [14], the phase aberration compensation step can be achieved with fitting-based processing [15] or by acquiring a reference hologram (i.e. without the sample in the imaged field of view (FOV)) to be subtracted to the aberrated phase image [16]. An example of amplitude component of the reconstructed in-focus

wavefield with phase aberrations is displayed in Figure 1.2(f), while the corresponding one after the aberration compensation in displayed in Figure 1.2(g).

Phase Unwrapping

Phase images generated by DH, as well as most other phase imaging techniques, suffer from modulo 2π ambiguities. An object whose optical thickness variation exceeds the wavelength produces wrapped phase images, with discontinuities at every 2π of the phase profile. Numerous phase unwrapping algorithms have been developed based on different strategies to find the phase discontinuities and to make judgments on how to stitch the discontinuous regions. For example, the PEARLS algorithm is divided into two steps [17], i.e. a local adaptive denoising scheme based on local polynomial approximations is firstly applied to the wrapped noisy phase, and then the denoised wrapped phase is subjected to a robust unwrapping algorithm, namely the PUMA algorithm [18], which is based on the exact minimization of an energy functional in the case of convex problems and on the approximate minimization in the case of non-convex problems. In Figure 1.2(g), three phase jumps are evident, which have been corrected through the PEARLS algorithm in Figure 1.2(h).

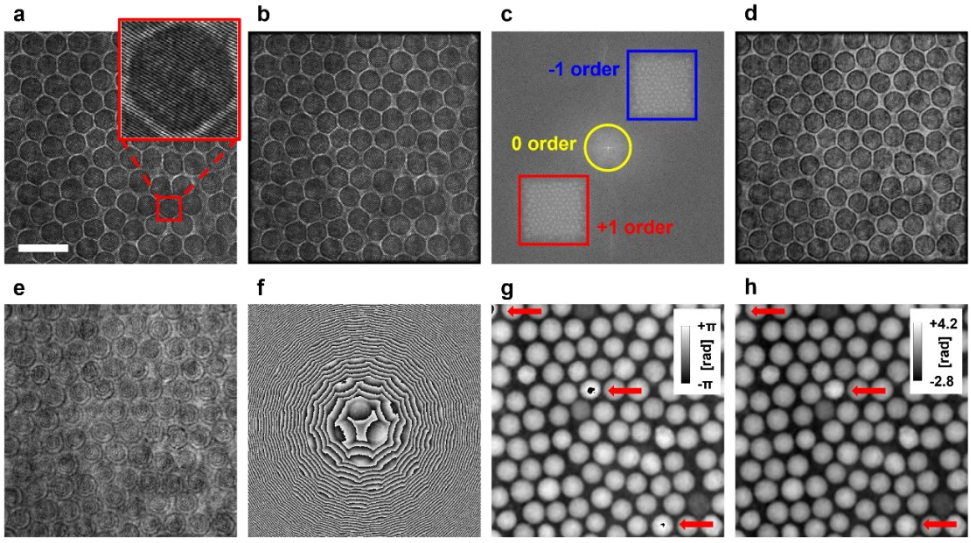

Figure 1.2 Holographic processing to compute the QPM of several cells on a Petri dish by DHM in off-axis configuration.
(a) Recorded digital hologram (1024×1024) with the interference fringe pattern highlighted in the inset. The scale bar is 20 μm. **(b)** Apodized digital hologram. **(c)** Amplitude of the FT of the apodized digital hologram. The three diffraction orders are highlighted in red (real order), yellow (zero order), and blue (virtual order). **(d)** Amplitude of the hologram demodulated by filtering the red square in the Fourier spectrum in (c). **(e)** Amplitude of the reconstructed in-focus wavefield. **(f)** Phase of the reconstructed in-focus wavefield, with overlapped residual aberrations. **(g)** Phase of the reconstructed in-focus wavefield after aberration compensation, with phase jumps highlighted by the red arrows (wrapped phase). **(h)** QPM of several cells on a Petri dish after phase unwrapping.

1.1.4 Applications in Biomedicine

DHM is a very effective process for achieving high-precision QPI in microscopy. As reported in Eq. (1.1), the QPM is a quantitative representation of the object profile with nanometer precision [19]. In Figure 1.3, some examples of QPMs by DHM are shown in pseudo-3D, in the sense that the apparent height profile is the profile of optical thickness that includes both physical thickness and RI variation, i.e. the OPL in Eq. (1.1) [3]. In Figure 1.3(a), a group of three bars on a resolution target is reported. The thickness of the

chromium film is measured to be about 50 nm, consistent with the manufacturer's estimate. In Figure 1.3(b,c), several intracellular components such as the nuclear membrane and chromosomes can be discerned in fixed SKOV-3 ovarian cancer cells. In Figure 1.3(d), several red blood cells (RBCs) are displayed, while in Figure 1.3(e) one can notice a fold of the cheek epithelial cell, as well as its nucleus and mitochondria. Finally, Figure 1.3(f) is an image of a small quartz crystal in common sand.

One of the first demonstrations of QPI is based on the utility of optical phase for sensing cell structure and dynamics at the nanoscale. Due to this sensitivity of QPI for probing cell membrane dynamics, it has been applied to the study of RBCs [20]. As RBCs have distinct biconcave morphology without subcellular organelles, 2D QPI techniques are well suited to investigate their biophysical and pathophysiological properties.

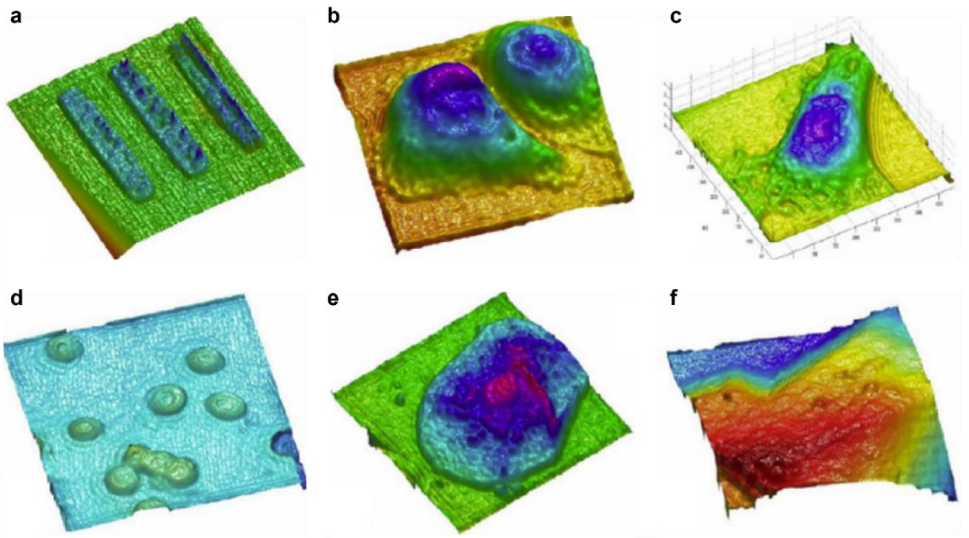

Figure 1.3 Examples of QPI by DHM.
(a) Resolution target (25×25 μm², 452×452 pixels²). **(b,c)** SKOV-3 ovarian cancer cells (60×60 μm², 404×404 pixels²). **(d)** RBCs (50×50 μm², 404×404 pixels²). **(e)** Cheek epithelial cell (60×60 μm², 404×404 pixels²). **(f)** Quartz crystal of sand (60×60 μm², 404×404 pixels²). (Figure reproduced from Ref. [3])

For example, QPMs of RBCs have been characterized by studying their behavior as adaptive optofluidic microlenses [21] [22]. The sensitivity to nanoscale changes in thickness was employed to study live neurons during electrical activity, in which neuronal network activity was monitored optically by the phase signal [23]. Moreover, differences between RBCs of diabetic patients and healthy patients have been detected in the QPMs [24].

One of the most impactful applications of QPI to date is measuring single-cell volume and mass, non-destructively, over arbitrary periods of time in both adherent and flowing cell populations. The unique ability of QPI to weigh cells by simply imaging them stems from the fact that the RI is linearly proportional to cell density. Since the cell QPM is measured with respect to just culture medium, QPI yields the dry mass density map of the cellular structure, that is, the density of the non-aqueous content of the cell, which is mainly proteins and lipids. Therefore, the dry mass surface density σ of the cellular matter can be obtained from the measured QPM as [1]

$$\sigma(x,y) = \frac{\lambda}{2\pi\alpha} QPM(x,y), \tag{1.23}$$

where α is called refractive increment. Several studies confirm that it is a very reasonable assumption to use a constant value of $\alpha = 0.19$ ml g^{-1} [1]. Thus, σ can be used to quantify cell growth non-invasively, using optical images alone. For example, combining QPI with a fluorescent marker, the phases of the cell cycle and the cell growth in each phase have been measured for the first time [25].

The morphologies of live cells are significantly altered by disease states such as viral infection and cancer, and the optical characterization of these alterations using QPI has several advantages over conventional imaging approaches [20] [26]. Because QPI does not require fixation or sample preparation procedures or exogenous labelling agents, subtle changes in live cells can be monitored for an extended period of time. By measuring cell thickness using QPI, phenotyping of cancer cells was demonstrated [27]. Quantitative and label-free imaging capability makes QPI an effective method

for blood screening. For example, the measured OPL information can be translated into hemoglobin (Hb) concentration for detecting sick RBCs [28] and anemias [29] [30]. By means of QPI, infections have been detected [31], cytotoxicity effects have been observed [32] [33], cell division [34] and cancer cell migration [35] have been studied, cell death has been revealed [36], and cell cycle has been monitored [37]. Also, it has been shown that QPI provides label-free sperm analysis, which can be potentially used in in-vitro fertilization [38], as well inspection of virus and bacterial infection [39].

Finally, it is important to mention the latest frontier of QPI, i.e. the Fourier Ptychographic Microscopy (FPM). A common characteristic of QPI is the need to engineer the optical system in order to ensure a convenient trade-off between spatial resolution and FOV. This is particularly important in the case the specimen is a tissue, since imaging a large area without sacrificing resolution of the tiniest details is pivotal to investigate the non-local effects of drugs and specific treatments, to study the interplay between different sample elements, and to allow robust classification of phenotypes. FPM exploits a synthetic aperture principle to achieve gigapixel QPI, i.e., the complex amplitude of the sample is retrieved with a large space-bandwidth product [40] [41]. In FPM, the specimen is probed by multiple angles using low coherence light sources to achieve large FOV imaging with computational super-resolution, thus exceeding the limits imposed by the optical system. Typically, Light Emitting Diodes (LEDs) arranged in a planar matrix [40] or a domed array configuration [42] are used to collect multiple images of the specimen, each one carrying a different content of its spatial frequencies, which are devoted to be stitched in the Fourier domain. Numerical methods have been proposed to correct effects of misalignments in the FPM recording system [43], also based on the employment of deep learning (DL) [44]. Recently, FPM has been exploited for the multi-scale monitoring of cell layers onto micropatterned substrates [45] and for measurements of the heavy metal pollution in marine environment [46].

1.2 State-of-the-Art TPM Techniques

The decoupling of the RI information from the physical thickness one encoded in the 2D QPM is possible by recording several QPMs at multiple viewing angles around the sample. To scan the incident angle with respect to the sample, two conventional TPM approaches have been developed [1] [47] [48]. In the illumination scanning configuration (ISC), sketched in Figure 1.4(a), the illumination beam is rotated with respect to the fixed sample [49] [50]. In the sample rotation configuration (SRC), sketched in Figure 1.4(b), the sample is rotated with respect to the fixed illumination by means of mechanical [4] [51] or optical [52] forces.

The main advantage of TPM-ISC is the lack of a direct interaction with the sample. The technique may be regarded as synthetic aperture approach, since the illumination direction is altered and the detector is kept stationary. With each hologram, a different frequency content is recorded and, as a result, the resolution in the sample plane is increased. The systems may be grouped based on the key component used to produce the beam rotation, i.e. a galvanometric mirror [49] [53], a spatial light modulator (SLM) [54] or a digital micromirror device [55].

Instead, the TPM-SRC approach is achieved by keeping the illumination beam stationary without any tilt angles, because the angular scanning is attained by rotating the sample under observation. This approach has high potential to deliver an isotropic frequency coverage when the sample rotates in full-angle directions, which results in high-quality tomographic image reconstruction. There are several methods demonstrated to rotate the sample. In general, the sample is loaded into a micropipette [4] or cuvette with a motorized rotating stage [56]. These types of capillary-supported rotation approaches suffer from the aberrations due to the perturbations created by tumbling of whole sample medium during the rotation [51]. Additionally, there is also a RI mismatch between the cell culture medium and the surrounding medium.

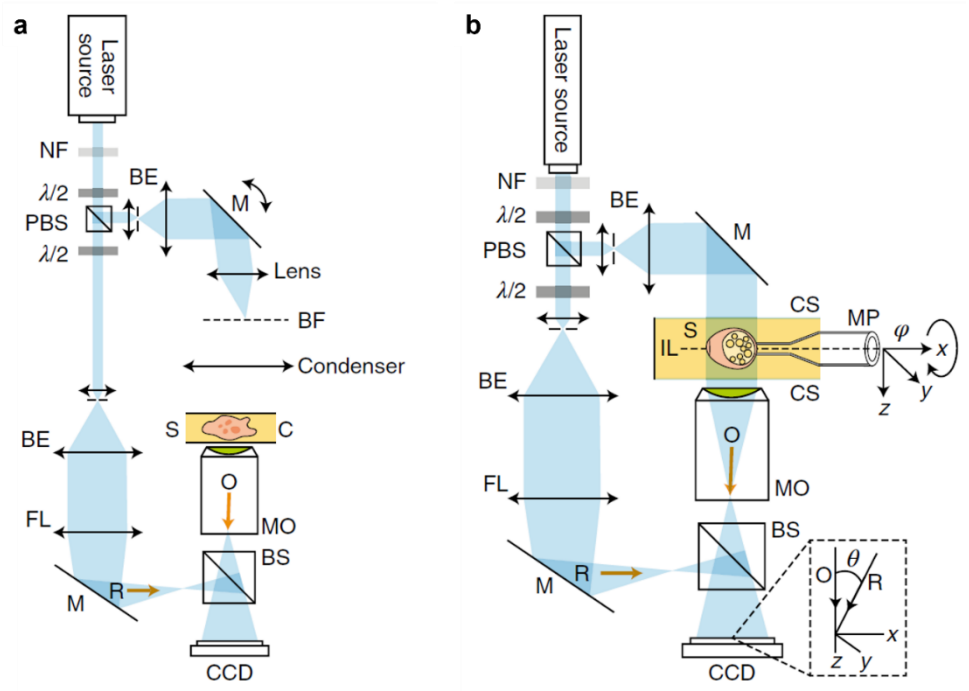

Figure 1.4 Conventional approaches for TPM.
(a) TPM-ISC: the illumination is fixed, while the sample is rotated. **(b)** TPM-SRC: the illumination angle is varied via a rotating mirror. NF, neutral filter; λ/2, half-wave plate; PBS, polarizing beam splitter; BE, beam expander; M, mirror; FL, focusing lens; S, sample; MP, micropipette; CS and C, coverslip; BF, back focal plane; MO, microscope objective; CCD, charge-coupled device camera; R, reference beam; O, object beam. (Figure reproduced from Ref. [1])

It is highly difficult to match the RI of the cell culture medium and the capillary, which results in stronger fraction from the inner boundary of the surface. However, this problem has been addressed with a computational data processing algorithm, and a compensation approach was demonstrated and verified with both numerical simulation and experimental data [57]. Furthermore, these approaches are limited in handling the sample due to the limitations imposed by the mechanical components used [58]. The limited single direction sample rotation (either in the x-z or y-z directions) observation results in missing spatial frequencies. Instead, holographic optical

tweezers (HOT) are a potential approach to manipulate the free-floating biological sample in all directions [52]. The HOT uses an SLM to generate a controlled twin trap beam for the trapping and rotation with an angular scanning range of 180°, which allowed a non-invasive tomographic imaging of suspended live cells. Later, the HOT-based TPM-SRC system extended the angular scanning range to 360° to achieve a full-angle sample rotation, resulting in the isotropic frequency coverage [59]. This experimental architecture allows manipulation of the single live cell in a more convenient way in all directions without any mechanical components.

In summary, the TPM-SRC allows for an isotropic reconstruction but the sample can be perturbed by the external mechanical/optical forces needed to rotate it. Moreover, the complex rotation system prevents a high-throughput recording.

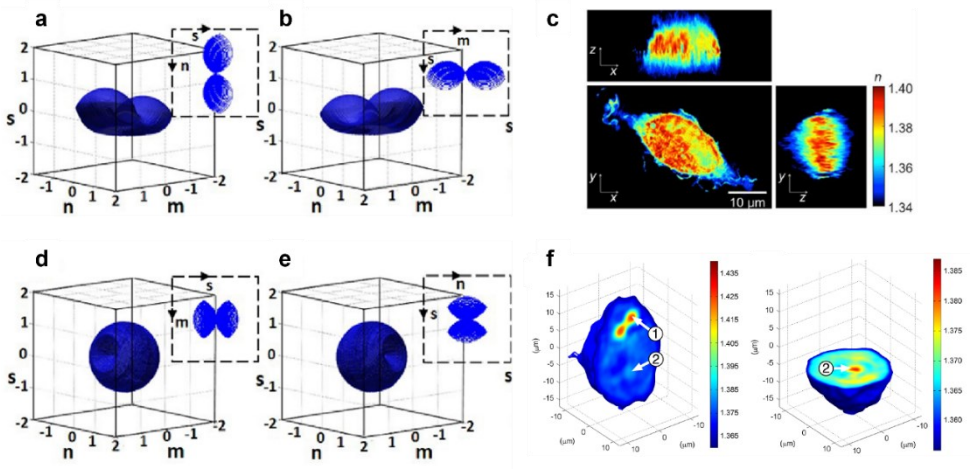

Figure 1.5 Difference between the TPM-ISC (a-c) and TPM-SRC (d-f) tomographic reconstructions.
(a,b) Transfer function of the TPM-ISC system. **(c)** Central slices of a hepatocyte reconstructed by TPM-ISC. The 3D tomogram is non-isotropic due to the missing cone problem. **(d,e)** Transfer function of the TPM-SRC system. **(f)** Central slices of a HT-1080 cell with incorporated SiO_2 microspheres reconstructed by TPM-SRC. Label 1 are the microspheres. Label 2 is the nucleolus. The 3D tomogram is isotropic. (Figure a,b,d,e reproduced from Ref. [48]; Figure c reproduced from Ref. [60]; Figure f reproduced from Ref. [51])

Instead, the recording step in TPM-ISC is much simpler and external biological alterations of the cell are avoided, but the 3D reconstruction is non-isotropic as the illumination angle is typically limited to the ±70° range. The latter is the so-called missing cone problem along the optical *z*-axis, which leads to limited frequency coverage in the axial direction. The limited angle of acceptance of the imaging system is determined by the numerical aperture (NA) of an objective lens. In fact, even with a high-NA objective lens, only fraction of diffracted light from a sample can be utilized for the tomographic reconstruction [61]. The missing cone problem can be better understood by considering the transfer functions of both the TPM-ISC and TPM-SRC systems. The transfer functions are evaluated using the Fourier diffraction theorem [62], which states that each scattered field carries information about the sample spatial frequencies that lie on a spherical Ewald cap in the 3D object spectrum [63]. The missing cone problem of the TPM-ISC system is evident in the transfer function in Figure 1.5(a,b), in which only a small percentage of the 3D Fourier frequencies are filled compared to the TPM-SRC transfer function in Figure 1.5(d,e), that is instead almost a full sphere [48]. As a consequence, the missing cone problem results in the underestimated RI values in reconstructed tomograms and in the elongation of the TPM-ISC reconstructed shape of a sample along the optical *z*-axis, as displayed in Figure 1.5(c), while this phenomenon is skipped in the TPM-SRC isotropic reconstruction of Figure 1.5(f).

1.3 Reconstruction Algorithms

In the early TPM works [4] [49], the 3D reconstruction physical model was based on a filtered back projection (FBP) method, similar to the algorithm used in x-ray CT [64]. It assumed phase measurement to be an integration of RI along the projection angle, as reported in Eq. (1.1), which ignored the

significance of the optical diffraction effect, thus limiting the earlier TPM systems for small sample RI variations over the wavelength scale. In cell imaging experiments, this inaccurate tomography model can significantly affect the 3D reconstruction resolution, especially for cells that are much thicker than the depth of field of the imaging systems [65]. In the 1960s, Wolf proposed the idea of using DH for 3D object reconstruction by developing a diffraction-based tomography model, known as optical diffraction tomography (ODT) [62]. However, this concept was not implemented to TPM for 3D imaging of cells until 2009 [65]. Since then, there have been numerous developments in ODT [60] [66]. Although hardware improvements have occurred during last decade, there still are physical limitations that affect the performance of ODT [47]. Most recently, advanced image processing tools, including total variation (TV) regularization [67] [68] and 3D deconvolution algorithms [69], have been applied to ODT to overcome the hardware and physical limits. For example, regularized ODT models that use sample priori information, such as non-negativity and piecewise smoothness, have been implemented to alleviate the missing cone issue in TPM-ISC [61] [66]. In 2015, a new physical model, based on the beam propagation method (BPM) to treat light diffraction, was demonstrated for 3D RI reconstruction in TPM [68] [70]. This work has pioneered the integration of machine learning (ML) concept in TPM framework [71].

1.3.1 Physical Models for RI Reconstruction

By treating a 3D object as a black box and performing multiple intensity or field measurements along different directions, one is expected to be able to retrieve the 3D RI structure of the object by solving an inverse scattering problem [47].

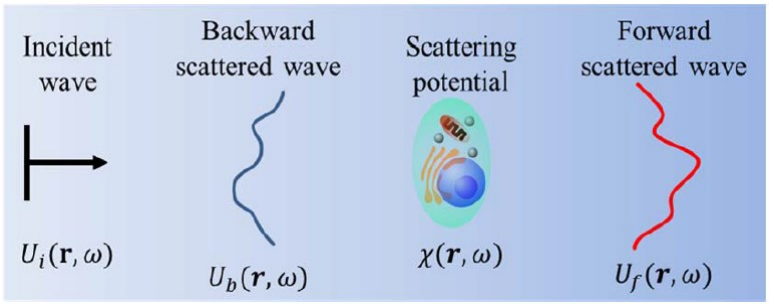

Figure 1.6 Illustration of the scattering process.
An object with a certain scattering potential produces a forward and a backward scattered wave when illuminated by an incident wave. (Figure reproduced from Ref. [47])

As sketched in Figure 1.6, the physical structure of an object is described by the object scattering potential function

$$\chi(x,y,z) = \beta_0^2[n^2(x,y,z) - n_m^2], \tag{1.24}$$

where $\beta_0 = 2\pi/\lambda_0$ is the propagation constant in free space, λ_0 is the illumination wavelength in free space, $n(x,y,z)$ is the RI distribution of the object (i.e., the unknown quantity), and n_m is the RI of the surrounding medium. With a plane wave incident on the object, scattered fields are generated in both forward and backward directions. The scattered field, U_s, is described by the following inhomogeneous wave equation [62]

$$\nabla^2 U_s(\boldsymbol{r}) + \beta^2 U_s(\boldsymbol{r}) = -\chi(\boldsymbol{r})U(\boldsymbol{r}), \tag{1.25}$$

where $\beta = n_m\beta_0$ is the propagation constant in the medium and $U(\boldsymbol{r})$ is the total field, that has contributions from the incident field plane wave, $U_i(\boldsymbol{r})$, and the scattered field, $U_s(\boldsymbol{r})$, i.e.

$$U(\boldsymbol{r}) = U_i(\boldsymbol{r}) + U_s(\boldsymbol{r}). \tag{1.26}$$

Two approximations can be used to solve the scattered field in Eq. (1.25). The first approximation, also called the first Born approximation, which assumes that $U_s(\boldsymbol{r}) \ll U_i(\boldsymbol{r})$, results in

(1.27) $$U(\boldsymbol{r}) \approx U_i(\boldsymbol{r}) = e^{i\boldsymbol{k_i}\cdot\boldsymbol{r}},$$

where $\boldsymbol{k_i} = \beta\widehat{\boldsymbol{k}}_{\boldsymbol{i}} = \left(k_{xi}, k_{yi}, k_{zi}\right)$ is the incident wave vector and $\widehat{\boldsymbol{k}}_{\boldsymbol{i}}$ is the direction unit vector with $\widehat{\boldsymbol{k}}_{\boldsymbol{i}} = \left(\hat{k}_{xi}, \hat{k}_{yi}, \hat{k}_{zi}\right)$. In the medium, where the incident field emerges, the dispersion relation establishes that

(1.28) $$k_{xi}^2 + k_{yi}^2 + k_{zi}^2 = \beta^2 = n_m^2\beta_0^2.$$

Through a Green's function approach [62], the scattered field is solved in the transverse Fourier space for a particular focal plane z ($z = 0$ is the imaging plane) as

(1.29) $$U_s\left(k_x, k_y; z\right) = \frac{e^{\pm iqz}}{q}\chi\left(k_x - k_{xi}, k_y - k_{yi}, \pm q - k_{zi}\right),$$

where $+q$ represents the forward scattered field and $-q$ represents the backward scattered field, k_x and k_y represent the scattered field transverse spatial frequencies, and $q = \sqrt{\beta^2 - k_x^2 - k_y^2}$ is the axial spatial frequency projection of the scattered field. For simplicity in the formulation, the variables of a function have been used to indicate the exact transformation domain [47]. The Eq. (1.29) reveals the relationship between the scattered field and scattering potential in a FT relation, which can also be written in the integral form of the Lipmann-Schwinger equation. The inverse scattering solution to the object function is therefore given by [62]

(1.30) $$\chi(U, V, Z) = \frac{q}{e^{\pm iqz}}U_s\left(k_x, k_y; z\right),$$

where $U = k_x - k_{xi}$, $V = k_y - k_{yi}$, and $Z = \pm q - k_{zi}$. The measurement is usually performed at the imaging plane, and thus

(1.31) $$\chi(U, V, Z) = qU_s\left(k_x, k_y; z = 0\right) = q\mathcal{FT}\{U_s(x, y; z = 0)\}.$$

According to this equation, each measurement of $U_s(x, y; z = 0)$ can be mapped to a particular spherical surface on the Ewald sphere in the (U, V, Z) space. As illustrated in Figure 1.5(a,b,d,e), through changing the illumination angle on the sample, i.e., changing the pair k_{xi} and k_{yi}, and mapping the

corresponding scattered field into the Ewald sphere, the 3D spatial frequency region for $\chi(U,V,Z)$ can be recovered. After a complete mapping, with a 3D inverse FT of $\chi(U,V,Z)$, the 3D object function in real space can be obtained, which will allow to obtain the 3D RI tomogram. However, as shown in Figure 1.5(a,b), in the common TPM-ISC systems working in transmission mode, the central low U-V frequencies in the 3D Fourier space cannot be recovered, which is called the missing cone problem. Reflection-mode measurements can fill the missing cone region by mapping also the back scattered fields into the Ewald sphere [47]. However, building an angle scanning reflection-mode TPM experimental system for biological imaging is very difficult, mainly because the back scattered fields from the cellular structures are very weak due to the small RI contrast of about 0.03 [47]. In fact, the detector will be mostly saturated by the background reflection from the sample holders such as cover glasses.

The first Born approximation is valid when the total phase delay of the field is small and there is substantially low optical absorption, which means that it works well for thin objects with weak RI contrasts to the media. For relatively thick objects, the Rytov approximation is more appropriate, as it assumes that the total field has a complex phase function $\phi_s(\boldsymbol{r})$ related to the scattered field, i.e. [72]

$$U(\boldsymbol{r}) = e^{\phi_i(\boldsymbol{r})+\phi_s(\boldsymbol{r})} = U_i(\boldsymbol{r})e^{\phi_s(\boldsymbol{r})}. \tag{1.32}$$

Under the Rytov approximation, the reconstruction still follows Eq. (1.30), except that the scattered field U_s is replaced with

$$U_s(\boldsymbol{r}) = U_i(\boldsymbol{r}) \ln\left(\frac{U(\boldsymbol{r})}{U_i(\boldsymbol{r})}\right), \tag{1.33}$$

and $U(\boldsymbol{r})$ can be measured from a QPI system. The Rytov approximation is known to be more appropriate than the Born approximation for many biological applications [65]. However, also the Rytov approximation is valid when the gradient of the RI is small, which means the objects need to be smooth in RI distribution. This is mostly true for imaging single cells. Instead,

when a sample is thicker and more complex, the Rytov approximation is no longer valid [73].

In summary, the RI distribution can be reconstructed through the Fourier diffraction theorem [74], which relates the complex scattering potential of an object with the complex amplitude of an object's projections. This relation is linear through application of first-order Born or Rytov approximation, assuming that only first-order scattering is taking place when the incident field propagates through the investigated sample.

1.3.2 Filtered Back Projection Algorithm

In the TPM-ISC system, the use of an advanced reconstruction algorithm is needed to solve the missing cone problem due to the employed hardware, thus moving toward an isotropic tomogram. Instead, in the TPM-SRC case, the software complexity can be relaxed thanks to the hardware properties that allow filling in a more complete way the 3D Fourier space, thus avoiding the issue of non-isotropic reconstruction. In this framework, the FBP algorithm is commonly employed due to its much lower computational burden, thus resulting in a time- and resource-saving tomographic algorithm. In fact, the FBP algorithm is based on the straight-ray approximation of the light propagation and, unlike the ODT, it neglects the scattering effect inside the cell. The measured field is indeed regarded as the integral of a sample's quantity along the optical axis, e.g. the absorption coefficient in the x-ray CT [64]. In the TPM case, the FBP approximates the QPM as a line integral of the RI along the propagation direction, as reported in Eq. (1.1).

Let consider a source-detector system rotating around a fixed sample, as sketched in Figure 1.7(a), assumed here as a RBC. Without losing generality, this situation is equivalent to the rotation of the sample while keeping fixed the source-detector system. Let $f(x, y)$ be the 2D image to be reconstructed, i.e. the 2D central slice of the 3D RI distribution of the RBC, as displayed in Figure 1.7(b). In Figure 1.7(b), the reference system $\{x, y\}$ of the image $f(x, y)$

is marked in green, while the cyan $\{t, s\}$ is a new reference system rotated counterclockwise with respect to $\{x, y\}$ by an angle θ, i.e.

$$\begin{cases} t = xcos\theta + ysin\theta \\ s = -xsin\theta + ycos\theta \end{cases}. \tag{1.34}$$

Hence, θ is the rotation angle of the source-detector system with respect to the fixed sample, which is illuminated along the s axis. For a fixed angle θ, the sample's projection can be defined as the line integral

$$P_\theta(t) = \int_s f(x,y)ds = \iint f(x,y)\delta\,(xcos\theta + ysin\theta - t)dxdy. \tag{1.35}$$

An example of two projections along the directions $\theta = 0°$ and $\theta = 90°$ is shown in Figure 1.7(c). However, from a single 1D integral information, the 2D image $f(x, y)$ cannot be reconstructed. Therefore, the source-detector system must rotate around the sample. In particular, by collecting the several projections $P_\theta(t)$ by varying the angle θ, the Radon transform (RT) $R(\theta, t)$ of the function $f(x, y)$ can be obtained. In Figure 1.7(d), a common visualization of the RT $R(\theta, t)$, called sinogram, is reported, which consists in arranging the different projections $P_\theta(t)$ inside the columns of a 2D array. The Fourier slice theorem states that the FT $S_\theta(w)$ of a projection $P_\theta(t)$ is a line of the sample's Fourier spectrum $F(U, V)$ oriented at the angle θ, i.e.

$$S_\theta(w) = \mathcal{FT}\{P_\theta(t)\} = F(U,V) = F(wcos\theta, wsin\theta). \tag{1.36}$$

In theory, according to the Fourier slice theorem, the sample $f(x, y)$ could be reconstructed by an inverse FT of the 2D spectrum filled by the $S_\theta(w)$ lines at multiple θ. However, the Fourier slice theorem fills the Fourier spectrum in a polar grid, while the image $f(x, y)$ is defined in a cartesian grid. Even if a non-uniform inverse FT could be exploited to map a polar spectrum into a cartesian function [75], the common way to invert the RT is the FBP algorithm [64], which can be defined as

$$\hat{f}(x,y) = \int_0^\pi \mathcal{FT}^{-1}\{|w|S_\theta(w)\}d\theta = \int_0^\pi Q_\theta(t)d\theta, \tag{1.37}$$

with $t = xcos\theta + ysin\theta$.

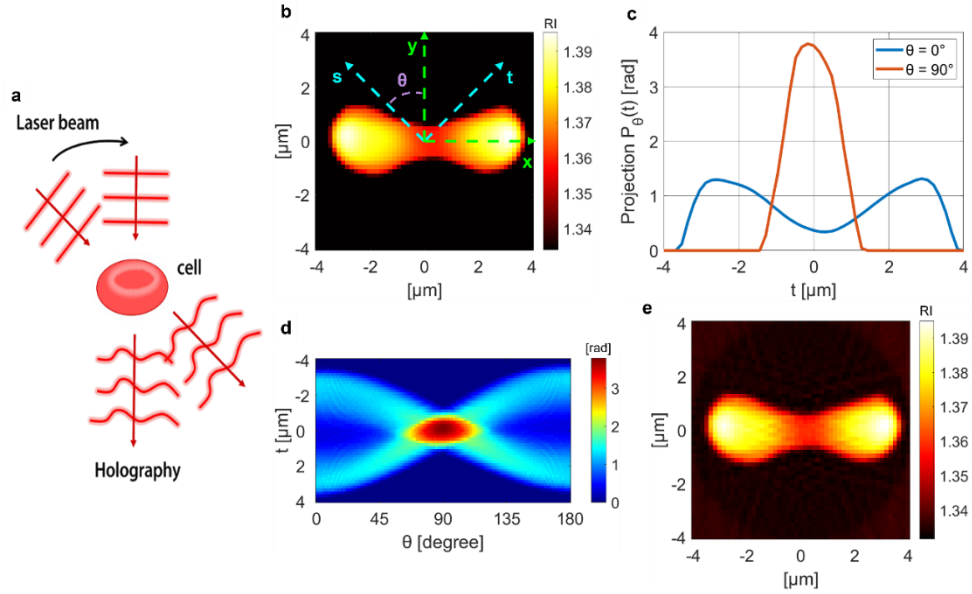

Figure 1.7 Illustration of the FBP algorithm.
(a) Sketch of the data collection. **(b)** Central slice $f(x,y)$ of a RBC, along with (green) its reference system $\{x,y\}$ and (cyan) a new one $\{t,s\}$ rotated by an angle θ. **(c)** Two projections $P_\theta(t)$ at $\theta = 0°$ and $\theta = 90°$ computed from the image $f(x,y)$ in (b). **(d)** Sinogram $R(\theta,t)$ of the image $f(x,y)$ in (b). **(e)** FBP reconstruction $\hat{f}(x,y)$ of the central slice $f(x,y)$ in (b). (Figure a reproduced from Ref. [60])

In summary, the FBP algorithm is made of four successive steps, i.e.

1. collection and FT of the projections $P_\theta(t)$ at multiple beam directions θ in order to obtain the corresponding transformed projections $S_\theta(w)$;
2. high-pass filtering of the transformed projections $S_\theta(w)$ by multiplying them by the $|w|$ term;
3. inverse FT of the filtered spectrum $|w|S_\theta(w)$ in order to obtain the filtered projections $Q_\theta(t)$ at multiple θ;
4. summing up of the filtered projections $Q_\theta(t)$ back projected along the lines $t = xcos\theta + ysin\theta$.

The reconstructed slice is illustrated in Figure 1.7(e), in which some artefacts due to the filtering step can be noticed. When used in TPM to reconstruct the 3D RI distribution of a biological specimen, the 2D FBP algorithm is implemented slice-by-slice by extracting each sinogram from the QPMs recorded at multiple viewing angles [49].

1.3.3 Regularized TPM

As discussed in Section 1.2, the missing cone problem in TPM-ISC systems can cause the elongation of an object along the z-axis (i.e., the optical axis), thus reducing axial resolution. Importantly, this issue results in underestimation of RI values [61]. It has been proposed that, by combining angle scanning and sample rotation techniques, one can fill the whole Ewald sphere to achieve isotropic resolution in TPM. However, this latter solution requires a complex management of the system. Over the past decades, there has been intensive research work on relieving the missing cone problem and improving the accuracy of reconstructed tomograms mainly in the areas of CT, electron microscope, and magnetic resonance imaging. In the last years, some of the ideas have been innovatively introduced into TPM to significantly enhance the quality of reconstructed RI maps [49] [61] [66] [67] [68] [70] [76]. Basically, all these methods are based on constructing a cost function comprising one quadratic ℓ_2 norm error term and one regularization term, which is expressed as

$$J(f) = \|Af - g\|_{\ell_2}^2 + \alpha R(f), \tag{1.38}$$

where f is the unknown variable to be solved, A is the forward operator characterized by the reconstruction model, Af represents the computed field, g is the measured field, α is the regularization coefficient, and $R(f)$ is the regularization term. Specifically, for TPM-ISC, the error term in the cost function in Eq. (1.38) can be further expressed as

$$\|Af - g\|_{\ell_2}^2 = \sum_m \left\|A^{(m)}f - g^{(m)}\right\|_{\ell_2}^2, \tag{1.39}$$

where m denotes different illumination angles, f corresponds to the scattering potential to be reconstructed (note that earlier it was χ), $A^{(m)}f$ can be interpreted as the m-th diffraction projection of f onto the sample plane $z = 0$, which provides a 2D scattering field of a 3D object with respect to the m-th incident beam illumination direction unit vector $\widehat{\boldsymbol{k}_{\boldsymbol{i}}}^{(m)} = \left(\hat{k}_{xi}{}^{(m)}, \hat{k}_{yi}{}^{(m)}, \hat{k}_{zi}{}^{(m)}\right)$, and $g^{(m)}$ is the m-th measured scattered field.

According to the ODT theorem [76], the forward operator can be further specified as a 2D FT relation

$$A^{(m)}f = \iint \frac{1}{q^{(m)}} f(U,V,W) e^{i(Ux+Vy)} dU dV, \tag{1.40}$$

where f is the scattering potential function in the 3D Fourier space (U,V,W), as indicated by its variables $U = k_x - \hat{k}_{xi}{}^{(m)}$, $V = k_y - \hat{k}_{yi}{}^{(m)}$, and

$$\begin{aligned} W &= q^{(m)} - \hat{k}_{zi}{}^{(m)} = \\ &= \sqrt{\beta^2 - \left(U + \hat{k}_{xi}{}^{(m)}\right)^2 - \left(V + \hat{k}_{yi}{}^{(m)}\right)^2} - \hat{k}_{zi}{}^{(m)}. \end{aligned} \tag{1.41}$$

The error term in Eq. (1.38) measures the difference between the computed field and experimentally measured field, and the regularization term imposes certain constraints on the reconstructed image by using prior knowledge of target samples. Then, an iterative algorithm is utilized to minimize this cost function until a convergence is reached. The first used prior information is the non-negativity constraint (NNC), which is grounded in the truth that the difference between the RIs of samples and the surrounding medium should always be non-negative. It has been demonstrated that the missing cone issue is significantly reduced compared with when no regularization is imposed [49]. NNC is easy to implement and can always be combined with other methods [76]. Later on, the TV regularization method, which measures the total image gradient and possesses stronger constraining effects, has been implemented to TPM [61] [67] [70]. The TV regularizer has two common variants [77]. One is isotropic TV, i.e.

$$R_{iTV}(f) \equiv \sum_n \|[\nabla f]_n\|_{\ell_2} = \sum_n \sqrt{([\nabla_x f]_n)^2 + \left([\nabla_y f]_n\right)^2 + ([\nabla_z f]_n)^2}. \tag{1.42}$$

where n is the pixel index. The isotropic TV has the capability of denoising, deblurring, and invasively yielding sharp edges. It works best for piece-wise smooth images that consist of piece-smooth regions separated by sharp edges. In this case, this functional can smooth out noise while well preserving the boundaries [78]. On the other hand, this isotropic TV regularizer can be interpreted as an ℓ_1 penalty on the magnitudes of the image gradient, which bears the sparsity promoting effects on the gradient components of images. Thanks to this sparsity property, the isotropic TV regularizer has been demonstrated enhancing the accuracy of the solution to ill-posed inverse problems that affected by high under-sampling conditions [68]. Benefitted from the edge-preserving (EP) characteristic of the isotropic TV regularizer, the so-called EP regularization was proposed by further adding a function to the ℓ_2 norm of the image gradient. Therefore, this regularizer can be formularized as [78]

$$R_{EP}(f) \equiv \phi\left(\sum_n \|[\nabla f]_n\|_{\ell_2}\right), \tag{1.43}$$

where ϕ is determined by prior knowledge about sample edges that need to satisfy certain defined conditions. For example, $\phi(t) = T^2 ln(1 + t/T)$ is one of the choices, where the parameter T can be tuned depending on how sharp the edges need to be kept. Therefore, in the case when sharp edges of samples are highly desired, this functional $\phi(t)$ can be implemented. In Figure 1.8(a-d), a comparison of different regularization methods, including respectively no regularization, NNC, EP regularization, and TV regularization, is reported for 3D RI reconstruction of a hepatocyte cell [47]. As can be seen in Figure 1.8(d), the isotropic TV regularizer can significantly smooth out the noise, while making the edges of the cell's inner structures sharp and clear. Furthermore, the RI values are no longer underestimated compared with the case using no regularization, as shown in Figure 1.8(a). By sacrificing some noise removal

capability, EP regularization can further sharpen the edges, as shown in Figure 1.8(c).

In the other TV regularizer, i.e. the anisotropic TV, the cost function is very similar to that of the isotropic TV, but the regularizer form is replaced with

$$R_{aTV}(f) \equiv \sum_n \|[\nabla f]_n\|_{\ell_1} = \sum_n |[\nabla_x f]_n| + \left|[\nabla_y f]_n\right| + |[\nabla_z f]_n|. \tag{1.44}$$

This anisotropic TV regularizer can be interpreted as an ℓ_1 penalty directly on the image gradient. It is a very strong regularizer, which offers improvements on reconstruction quality to a great extent compared with the isotropic counterpart [79]. However, unlike isotropic TV, the anisotropic TV is not rotationally invariant, which causes geometric distortions by favoring edge orientations that are aligned with coordinate axes [80]. Therefore, its usage is limited when biological samples have complex inner structures.

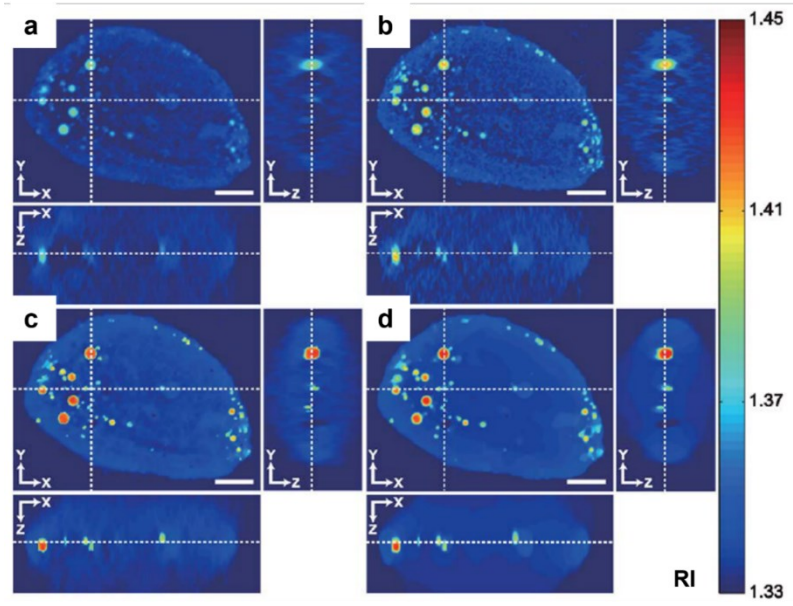

Figure 1.8 Comparison of the 3D RI distribution of a hepatocyte cell reconstructed by different methods in a TPM-ISC system.
(a) Direct Fourier mapping without regularization. **(b)** NNC regularization. **(c)** EP regularization. **(d)** Isotropic TV regularization. The scale bar is 5 μm. (Figure reproduced from Ref. [47])

1.3.4 Machine Learning-Based Reconstruction

During the last decade, a significant shift has been visible within the research groups working in the field of TPM toward development of reconstruction procedures that are utilizing ML [47] [81]. One example includes a sparse dictionary learning algorithm which specifically addresses the missing-cone artifacts in TPM-ISC [82]. In this approach, first a TV-regularized reconstruction is calculated with traditional algorithms. From the obtained result, features from lateral planes are extracted to form a dictionary which is then used in the final reconstruction to correct features in the lateral and axial directions, thus minimizing the missing-cone artifacts. Another method, called deep prior diffraction tomography, uses a deep convolutional neural network (DCNN) without training [83]. DeepRegularizer is a more traditional approach, in which pairs of reconstructions have been generated, one with a quick low-resolution algorithm and another with a high-resolution procedure that utilizes TV regularization [84]. These pairs have been then used to train a DCNN, which later was applied to rapidly transform low-resolution reconstructions into high-quality ones. Furthermore, a DCNN has been trained to reconstruct the 3D RI distribution from 2D phase measurements by using a numerical cell phantom, and it has been demonstrated working on experimental RBCs [85].

1.3.5 Learning Tomography

In the Born or Rytov approximation-based tomographic reconstruction models described in Section 1.3.1, weak light scattering or single scattering in the unknown objects must be assumed. A BPM-based tomographic reconstruction model allows considering multiple scattering events by dividing the object into multiple layers and subsequently forming an artificial neural network geometry to model the RI distribution [68] [70], as sketched in Figure 1.9(a). For this reason, this technique has been called Learning Tomography (LT) [73] [86]. Therefore, the BPM reconstruction model applies

to thicker or highly inhomogeneous biological objects and uses complex field measurements from a typical TPM-ISC system. In the BPM model, an inhomogeneous sample is virtually divided into thin slices along the propagation direction z. Light propagation is modeled as phase modulation based on the paraxial wave equation. After each layer, the optical field is described as [68]

$$U(\boldsymbol{r}) = a(\boldsymbol{r})e^{i\beta_0 n_m z}, \tag{1.45}$$

where $a(\boldsymbol{r})$ is a complex envelope function that models light diffraction in each sample layer. The sample RI distribution $n(\boldsymbol{r})$ is decomposed into a constant medium n_m and a perturbation $\delta n(\boldsymbol{r})$ due to inhomogeneity. Therefore, the propagation constant in the sample, $\beta_s(\boldsymbol{r})$, is written as

$$\beta_s(\boldsymbol{r}) = \beta_0 n(\boldsymbol{r}) = \beta_0\big(n_m + \delta n(\boldsymbol{r})\big). \tag{1.46}$$

The complex envelope $a(\boldsymbol{r})$ evolves along the optical axis as [68]

$$\begin{aligned} a(x, y, z + \delta z) \quad &= e^{i\beta_0 \delta n(\boldsymbol{r})\delta z} \times \\ &\times \mathcal{FT}^{-1}\left\{ \mathcal{FT}\{a(x, y, z)\} e^{-i\left(\frac{k_x^2 + k_y^2}{\beta_0 n_m + \sqrt{\beta_0^2 n_m^2 - k_x^2 - k_y^2}}\right)} \right\}, \end{aligned} \tag{1.47}$$

where δz is the step size or sample slice size along z direction. The right-hand side of this equation can be decomposed into two parts. The first term $e^{i\beta_0 \delta n(\boldsymbol{r})\delta z}$ takes refraction into account, whereas the other term deals with the diffraction. By repeatedly using this equation step-by-step, it can be known how the complex field evolves after propagating over an arbitrary distance along the optical axis. In other words, once given the initial condition, the optical field distribution can be obtained anywhere in space (note that reflected light has not been considered in the current BPM model). Therefore, in LT, the plane wave for each illumination direction is propagated through the estimate of the reconstruction with the BPM model. Then, the resultant field is compared with the measured field.

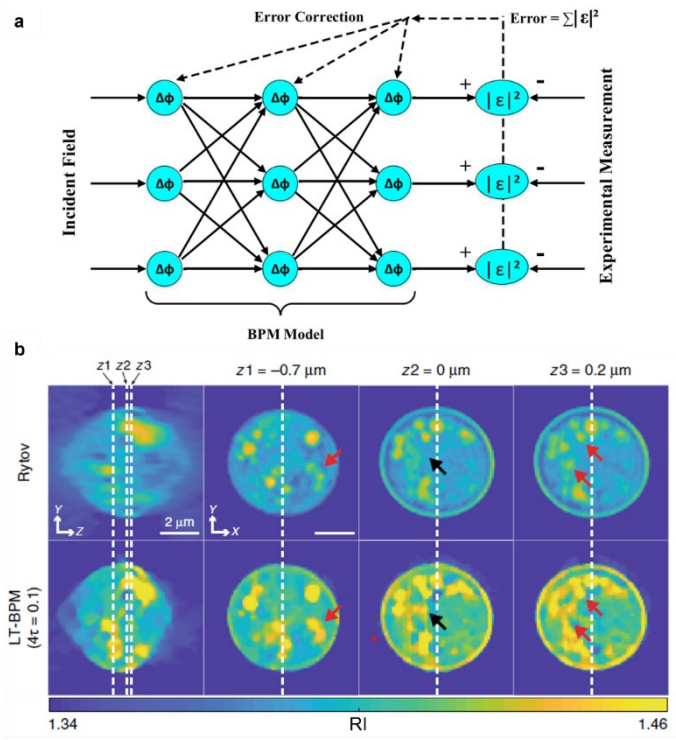

Figure 1.9 LT based on BPM.

(a) Schematic diagram of object reconstruction by learning the 3D RI distribution that minimizes the error ε, defined as the mean squared difference between the experimental measurement and the prediction of a computational model based on the BPM. **(b)** Reconstruction results of a yeast cell by using Rytov (first row) and LT (second row). (Figure a reproduced from Ref. [70]; Figure b reproduced from Ref. [73])

The difference between the fields is treated as a cost function, which is minimized with an optimization procedure. As a result, the reconstruction is corrected in each iteration. By applying constraints in each iteration, such as non-negativity or smoothness of the result, this approach allows minimization of the missing-cone artifacts [68] [70]. Compared with the ODT reconstruction model, BPM no longer uses the scattering potential to represent the RI in a quadratic function. Instead, it directly seeks an equation to link RI and the measured electromagnetic field, which makes the BPM model non-linear.

Therefore, compared with its linear counterpart, this non-linear physical model can be more accurate when the scattering effects are strong, as displayed in Figure 1.9(b) [73].

1.4 Biological Insight and Applications

TPM is able to non-invasively retrieve the 3D RI distributions of biological samples, providing rich information about subcellular structures without any exogenous contrast agents. Based on the RI maps, both morphological and biochemical information can be further extracted to achieve comprehensive label-free visualization and quantification of living cells, which opens a new avenue to the investigation of their functionalities and mechanisms at the individual level [47].

Thanks to the 3D imaging capability, 3D geometric parameters can be easily obtained by TPM, making it a powerful tool to deeply explore the cells in the morphological world. For example, surface-to-volume ratio is a typical parameter, which is known to have an influence on the uptake of light, digestion of nutrients, and release of waste of a cell. RBC is one of most popular candidates due to its special biconcave shape and simple inner structures. Based on the TPM technique, it has been found out that the volume and surface area of the cord RBCs of newborn infants are much larger than those of the RBCs of non-pregnant women and flatter than those of adults [87]. Moreover, the 3D RI mapping of living cells can implicate some pathological states that accompany human diseases. RI distribution has been intensively explored for visualizing the morphological alterations of RBCs caused by parasitic protozoa, such as P. falciparum [88] and B. microti [89]. The cytoplasm of RBCs is mainly composed of Hb, which is the iron-containing oxygen-transport metalloprotein. The properties of Hb are sensitive to subtle alterations of pathological states of RBCs resulting from infectious diseases and genetic

disorders, e.g., malaria and sickle cell diseases. To quantify Hb, mean corpuscular Hb concentration and mean corpuscular Hb content are being used for medical diagnosis on a daily basis in medical laboratories, and they can be measured with TPM [90].

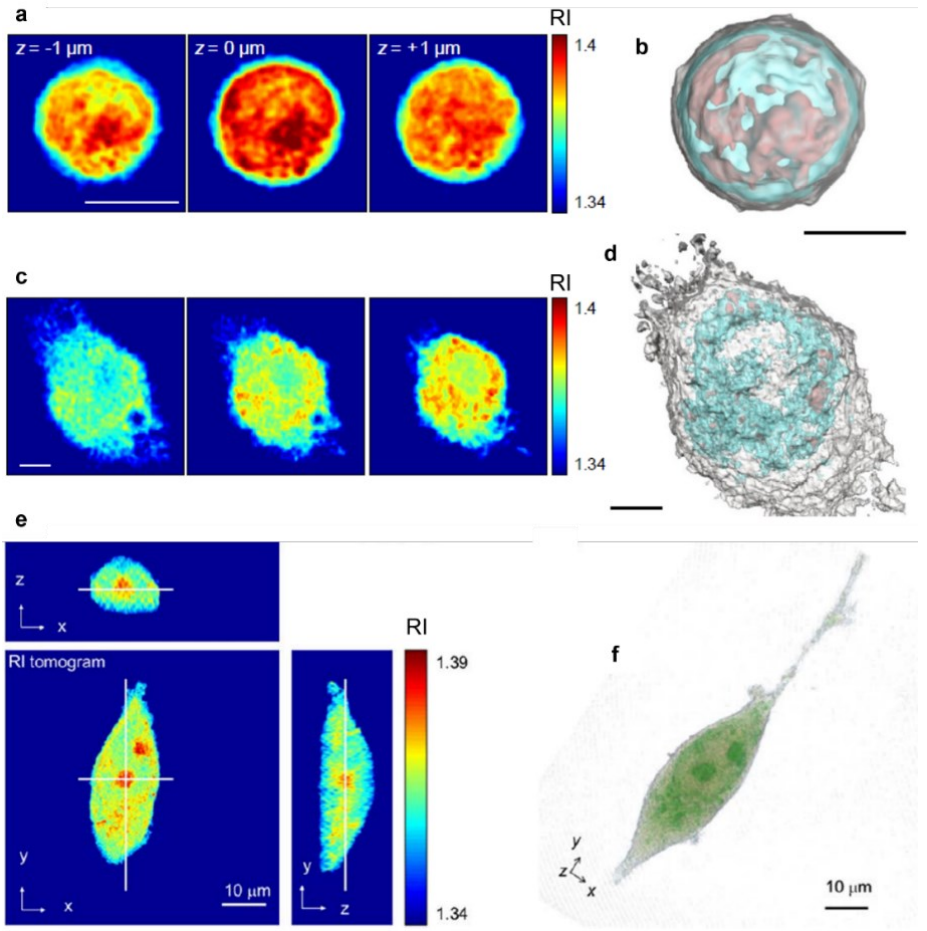

Figure 1.10 Examples of 3D RI tomograms by TPM.
(a,b) Cross-sectional slices of the RI distribution of a lymphocyte and corresponding isolevels representation, respectively. The scale bar is 4 µm. **(c,d)** Cross-sectional slices of the RI distribution of a macrophage and corresponding isolevels representation, respectively. The scale bar is 3 µm. **(e,f)** Cross-sectional slices of the RI distribution of an SHSY5Y neuroblastoma cell and corresponding isolevels representation, respectively. (Figure a-d reproduced from Ref. [91]; Figure e,f reproduced from Ref. [92])

Besides RBCs, TPM has also been widely utilized to study the morphological features of other types of eukaryotic cells, such as white blood cells (WBCs) (Figure 1.10(a-d)) [91], neuron cells (Figure 1.10(e,f)) [92], hepatocytes [60], phytoplanktons [51], and cancer cells [60]. TPM time-lapses have confirmed the appearance of membrane blebs, cytoskeleton disruption, neurite shortening, cell shrinkage, and rounding inside neurons treated with a substance known to cause Parkinson's disease [92]. Quantitative monitoring capabilities of TPM were also used to quantify differences in single live platelet in its morphology, cell volume, as well as changes in biophysical parameters [93]. Most recently, multimodal approaches combining TPM and FM techniques have been used in the correlative study of cell pathophysiology [94].

Besides being able to unfold biophysical features, RI maps of living cells can also carry biochemical information about cells. This is due to the linear relation between the RI value of a biological sample, $n(x,y,z)$, and the dry mass concentration (or called dry mass density) of organic molecules $\sigma(x,y,z)$, i.e.

$$\sigma(x,y,z) = \frac{n(x,y,z)-n_m}{\alpha}, \tag{1.48}$$

where α is the refractive increment [1] and n_m is the RI of the surrounding medium. Therefore, the dry mass quantifies the total mass of all the non-aqueous contents of a cell. To make reliable the use of the 3D RI map from TPM, the volume integral of the dry mass density can give the total cell dry mass, which is inaccessible through a 2D QPI modality. Applying dry mass and dry mass density determined by TPM measurements as a biomarker enables measurement and monitoring of cell processes such as mitosis or cell death, either as apoptosis or necrosis. It has been demonstrated that compaction and decompaction of chromosomes induced by osmotic change were characterized by linked changes in chromosome RI, volume, and the motilities of fluorescent proteins [95]. Variations in induced apoptosis have been presented, like responses of normal muscle cells and rhabdomyosarcoma cells

to calcium electroporation, which previously has been reported as an effective method of rhabdomyosarcoma cells reduction [96].

Cell size, balanced by cell growth and division, is an important phenotypic characteristic of any type of cell. Although the process of how it is regulated has fascinated generations of biologists, details have remained largely obscure, mainly because accurate measurements at the single-cell level were difficult to carry out [97]. With high image contrast, TPM can accurately retrieve cell volume and dry mass parameters simultaneously, even at the nanoscale level [98], without any exogenous labeling agent. Dry mass density can be then calculated. All these features make TPM a perfect tool for quantifying cell size in the study of cell growth, proliferation, apoptosis, etc. By quantitatively monitoring the dry mass of lymphoblasts and epithelial cells during cell division, it has been found out that both cell types maintain a linear relation between average growth rate and cell mass over the majority of size range [99]. Utilizing TPM to take time-lapse measurements of cell volume, dry mass, and dry mass density of mouse chondrocytes simultaneously, three distinct phases of hypertrophic cell enlargement have been discovered [100]. This result is remarkable as it reveals the mechanism of cell size increase and the regulation of growth rate.

Finally, an important field of application of TPM systems is cancer biology. Recently, 3D RI tomograms of human alveolar epithelial A549 cells infected with H3N2 influenza have been reconstructed [101]. The 3D RI of healthy and cancerous epithelial cells (CA9-22 and BCC cell lines) were measured and analyzed [102], live HT29 cells were investigated to image a human colon adenocarcinoma cell line [65], the mass of chromosomes in intact living cells was quantified and two human colon cancer lines HT-29 and T84 cells were differentiated [66]. Angle- and wavelength-dependent light scattering distributions provide information about the morphological changes accompanying early-stage malignancy of cancers, thus making light scattering a valuable tool for cancer diagnosis over the past decade. For instance, a light scattering analysis based on TPM showed that the total light scattering cross

section and backscattering cross section of cancerous cell lines (CA9-22, BCC) were both significantly higher than those of normal cell lines (HaCaT, SG) [102].

1.5 Intracellular TPM for Plant Cells

As will be discussed in detail in Chapter 4, due to the absence of exogeneous markers, QPI and TPM suffer the lack of intracellular specificity, which is instead the main strength in FM. This means that the phase or RI values can hardly be assigned to specific organelles inside the reconstructed cell. The main reason is the lack of a suitable phase contrast in the recorded QPMs. However, to cope this issue in the case of plant cells, herein an alternative strategy for realizing intracellular TPM has been proposed [6]. In particular, the dehydration process has been induced in non-invasive way in epidermal onion cells in order to enhance the phase contrast and promote the nuclear rotation, at the aim of reconstructing the 3D RI tomogram directly at the nuclear level and then segmenting the nucleolus by means of a RI threshold. In fact, the dehydration provokes the progressive loss of intracellular water content inducing rotation of the cell nucleus over a wide range of angles, thus permitting the accomplishment of 3D imaging by TPM without any mechanical or electro-optical laser beam scanning device. The dehydration process has been studied through DHM time-lapse experiments, and an optimal time window has been determined to observe the sample before plasmolysis starts, when the induced process is reversible. Thus, TPM has been realized in nondestructive manner. In fact, plant cells contain the vacuole, i.e. a roundish tank surrounded by the tonoplast membrane. In a mature plant cell, the vacuole occupies between the 80 % and the 90 % of the internal cell volume and is responsible for turgor pressure. Turgor pressure gives solidity to the cell and is generally determined by the water content of the vacuole. By

controlling the environmental temperature and humidity, the cell turgor can be altered through the variation of its aqueous content. Upon the dehydration process starts, curved streamlines develop in the liquid inside the cell. At the same time, dehydration also leads to a rearrangement of the cytoskeletal structures and to a relaxation of the mechanical constraints that keep the nucleus fixed in its initial position [103] [104]. As a result, the nucleus begins to rotate. Here it has been demonstrated that, when specific conditions are met, it is possible to exploit this induced rotation to accomplish TPM of the nuclei. However, the rotations experienced by the nuclei occur spontaneously, thus they are unknowns in the tackled problem. For this reason, an ad hoc angle tracking algorithm has been developed to estimate them. In particular, an equivalent 3D ellipsoid representing the nucleus has been created, and its rotation has been simulated according to the variation of the nucleus area in the DHM time lapse, in order to fit the unknown rolling angles. The FPM algorithm has been implemented to reconstruct the 3D RI tomogram directly at the nuclear level and, thanks to the enhanced contrast, a RI threshold has been set to segment the inner nucleolus. Finally, both the nucleus and nucleolus have been quantitatively characterized in label-free manner by means of RI-based parameters, like the dry mass [6].

The results of the 3D tomographic pipeline for two analyzed nuclei are reported in Figure 1.11. In Figure 1.11(a,d), the rolling angles recovered by using the method described above are shown. The two leftmost images in Figure 1.11(b,e) show two central slices of the 3D reconstructed nucleus, cut along two orthogonal directions. The tomographic technique allows to obtain the 3D spatial distribution of RI. In the leftmost slice in Figure 1.11(b), it is clear the presence of a localized region at the highest RI values, which can be identified as the nucleolus. Therefore, the nucleus has been segmented into nucleoplasm and nucleolus by finding the corresponding interval of RI values. The third image in Figure 1.11(b,e) is an iso-levels representation of the nucleus, in which the nucleolus is highlighted in red. Finally, the histograms of the RI values of the nucleus and nucleolus are reported in Figure 1.11(c,f).

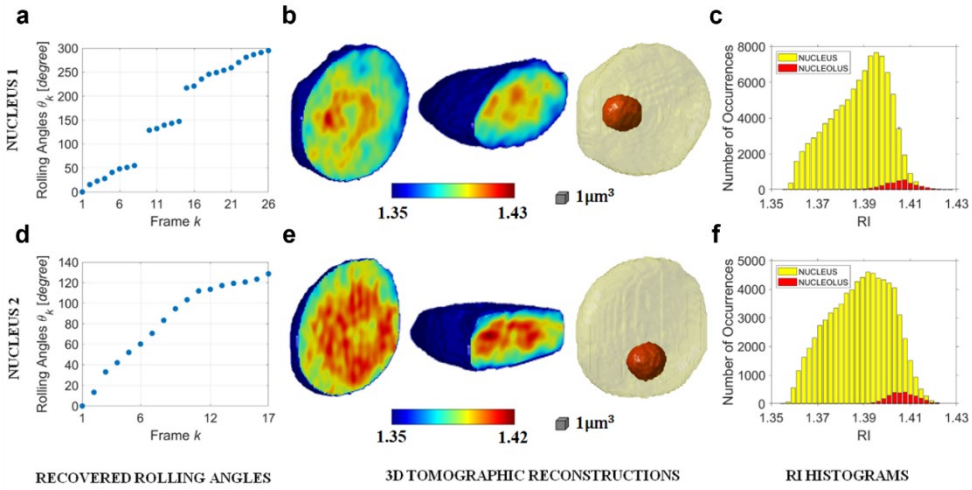

Figure 1.11 3D tomographic reconstructions of two plant cells' nuclei. **(a,d)** Rolling angles recovered by the minor axes' lengths of the elliptic binary masks used to segment QPMs. **(b,e)** Central slices taken from the 3D reconstructed tomograms along two different directions (first two images) and iso-levels representation with the nucleolus highlighted in red (third image). **(c,f)** Histograms of the RI distribution of the nucleus (yellow) and the nucleolus (red).

It is worth remarking that this simple strategy proposed here is fully reversible as wide angle rotations are observed before the plasmolysis event. Thereby, the dehydration process can be stopped before the cells experience irreversible damages. This means the sample could be brought back to its normal healthy state by reversing the dehydration process after the tomographic shooting. The presented results are a proof of concept of the possibility to exploit a natural biological process like dehydration in a functional way, i.e. as a tool that allows 3D tomographic imaging of nuclei in plant cells using a conventional setup, thus providing a possible strategy for recovering the missing intracellular specificity in label-free TPM. The approach demonstrated here could improve the investigation in plant biology by a non-destructively controlled procedure and by means of a conventional label-free holographic microscope able to furnish 3D quantitative analysis at sub-nuclear level.

FRIDERICVS·IMPERATOR·ROMANORVM·SEMPER·AVGVST

CHAPTER

2 Holo-Tomographic Imaging Flow Cytometry

Several types of high-throughput instrumentation for analyzing and quantifying different aspects of cell biology are available, such as for example plate readers, sequencing platforms, DNA, RNA and protein microarrays, Western blotting, and so on. However, many platforms allow only analysis at the cell population level. Instead, cellular populations are often heterogeneous with respect to cell cycle phase, size, volume, physiological state, and their individual development history. Therefore, an overall analysis that only provides average measurements risks discarding the intra-cellular variability, which is instead essential for assaying diversity and searching for rare cells with specific features (e.g., tumor cell, stem cells, etc.). FC is a sophisticated technology measuring multiple physical characteristics of a single cell simultaneously (e.g., size and granularity) as the cell flows in suspension through a measuring device. Its working depends on the light scattering features of the cells under investigation, which may be derived from dyes or monoclonal antibodies targeting either extracellular molecules located on the surface or intracellular molecules inside the cell. This approach makes FC a powerful tool for detailed analysis of complex populations in a short period of time due to the high-throughput property related to the flow condition [105]. A remarkable enhancement of the FC potential has been represented by the development of IFC systems, in which each cell is associated to a bright-field image, a dark-field image, and several fluorescent images related to a specific marked intracellular component. As such, IFC has greatly extended the set of possible single-cell measurements despite the limitations of the fluorescence

imaging. The last frontier of IFC is the implementation of these systems in the label-free modality, thus yielding to the development of HIFC for the label-free QPI in FC environment. But, as discussed in Chapter 1, the most powerful evolution of QPI is TPM. The first attempts to realize TPM of cells flowing in a microfluidic channel date back to 2014 [106]. The TPM paradigm has been demonstrated effectively working in FC conditions at ISASI-CNR in 2017, thus realizing for the first time a TPM-FC system [107]. Therefore, TPM-FC combines two powerful techniques in order to provide the 3D, label-free, and quantitative characterization of single cells in high-throughput.

In this Chapter, an overview of the FC and IFC tools and the very recent achievements in HIFC are presented. After that, the TPM-FC technique is introduced. After describing the TPM-FC working principle, the automatization process of the reconstruction pipeline herein developed is described [108], which aims to move this technique towards the analysis of large number of cells. Finally, the possibility of reaching the TPM-FC high-throughput property is discussed by performing fluid dynamic numerical simulations to replicate in-flow experimental results [109].

2.1 Flow Cytometry

Historically, the first developed flow cytometer was a single-parameter instrument detecting only the cell size. Currently, highly sophisticated instruments have evolved with the capability of detecting 14 parameters simultaneously [110]. FC has the ability to measure the optical and fluorescence characteristics of a single cell or any other particle such as microorganisms, nuclei and chromosome preparations in a fluid stream when they pass through a light source [111]. Size, granularity and fluorescent features of the cells, derived from either antibodies or dyes, are also examples of parameters used to analyze and differentiate the cells. The underlying

principle of FC is related to light scattering and fluorescence emission, which occurs as light from the excitation source (commonly a laser beam) strikes the moving particle, as sketched in Figure 2.1(a). The data obtained could give valuable information about biochemical, biophysical and molecular aspects of particles. Light scattering is directly related to structural and morphological properties of the cell while fluorescence emission derived from a fluorescence probe is proportional to the amount of fluorescent probe bound to the cell or cellular component [111]. Two types of light scatter occur, named as forward scatter (FSC) and side scatter (SSC) [105], as illustrated in Figure 2.1(b). The factors affecting total light scatter include the membrane, nucleus, granularity of the cell, cell shape and surface topography. FSC light is a result of diffraction collected along the same axis as the laser beam. FSC is proportional to cell surface area or size and suitable for detecting particles greater than a given size, that makes it the most commonly used method for immunophenotyping. On the other hand, SSC light is a measurement of mostly refracted and reflected light, which is collected at approximately 90° to the laser beam. SSC is proportional to cell granularity or internal complexity. In order to differentiate the cell types in a heterogeneous population, correlated measurements of FSC and SSC can be used [112].

The main components of flow cytometers are basically fluidics, optics (excitation and collection), an electronic network (detectors) and a computer [105]. The fluidics is responsible for directing liquid containing particles to the focused light source. The excitation optic focuses the light source on the cells/particles while collection optics transmits the light scatter or fluorescent light of the particle to an electronic network. The electronic network detects the signal and converts it to a digital data that is proportional to light intensity, and the computer is also required to analyze data. FC data analysis consists in finding a gate, i.e. one or more regions in a 2D chart selected according to the measured parameters [105]. For example, in this way unwanted particles such as dead cells and debris can be eliminated. The most common application of gating strategy is to use FSC and SSC plots, as shown in the example in Figure

2.1(c), in which the different physical characteristics of some WBCs, i.e, granulocytes, monocytes and lymphocytes, allow them to be distinguished from other blood cells. Additionally, a gate is a numerical or graphical boundary that can be used to define the characteristics of particles for further analysis. For example, in a blood sample containing a mixed population of cells, the analysis can be restricted to the sole lymphocytes. A gate can be set on the FSC vs. SSC plot for the analysis of lymphocytes, and then the fluorescence properties of the sole lymphocytes can be performed, as reported in Figure 2.1(d). Furthermore, a quadrant marker can divide a 2D plot into four sections to discriminate populations as negative, single positive or double positive to certain labels, as displayed in Figure 2.1(e) about the identification of lymphocytes within the peripheral blood mono-nuclear cells (PBMCs). Scatter plots in Figure 2.1(c-e) are density plots, since they display two parameters as a frequency distribution by using the color to code the different frequencies of events.

The distinctive property of FC technology of collecting information about large datasets while keeping the single-cell level makes it an eligible tool for several biomedical applications [105]. For this reason, FC is now routinely used as a diagnostic technology for health disorders, especially hematologic diseases [113]. FC is used in various applications based on the detection of the membrane, cytoplasmic and nuclear antigens. Additionally, whole cells and cellular components such as organelles, nuclei, DNA, RNA, chromosomes, cytokines, hormones and protein content can also be investigated by FC. Analysis of cell proliferation and cell cycle, measurements of calcium flux and membrane potentials are the commonly used examples of methods developed for FC [105]. Cells undergoing apoptosis (i.e., programmed cell death) can be revealed by FC by rapidly collecting cell apoptotic properties. Immunophenotyping or phenotypic characterization of cells is the identification and quantification of a specific cell group in the mixed population using FC, e.g. immune cells of the blood, by detecting specific cell surface membrane proteins.

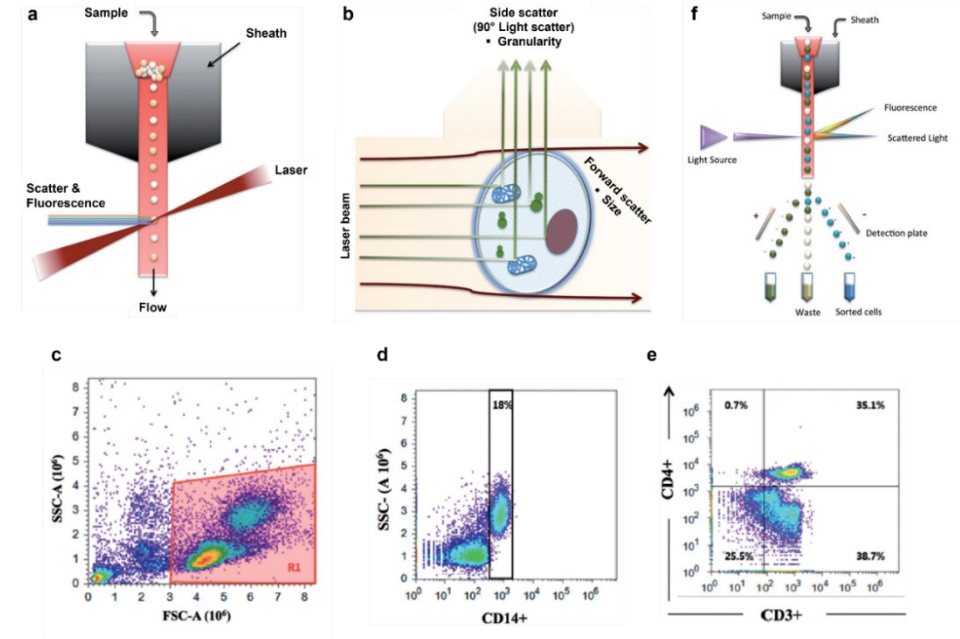

Figure 2.1 FC working principle and applications.

(a) In a FC system, the sample is illuminated by a laser while flowing along a channel, and the light scatter or fluorescent light is collected. **(b)** Light scattering in FC. FSC is proportional to cell size while SSC is proportional to cell granularity or internal complexity. **(c)** FC gating of granulocytes, monocytes, and lymphocytes with respect to the other blood cells. **(d)** FC rectangular gating of the lymphocytes within the PBMCs. **(e)** FC quadrant gating of the lymphocytes (upper-right quadrant) within the PBMCs. **(f)** Cell sorting based on the electrostatic deflection of charged droplets. (Figure reproduced from Ref. [105])

Moreover, a cell sorting module can be integrated to a FC system and exploit its collected information, as sketched in Figure 2.1(f). For example, Fluorescent Activated Cell Sorters (FACS) are flow cytometers that have the capacity to sort fluorescent-labeled cells from a mixed cell population [110]. Cell sorting is responsible for capturing and separation of the cells based on a single parameter or a combination of several parameters [105]. Once the cells of interest are collected, they can be used for further analysis such as

microscopic, biochemical and functional studies. A single parameter or combination of several parameters can be used for cell sorting.

In the field of FC, many advantages have been provided by the development of microfabricated flow cytometers that use microfluidics [105]. Microfluidics are defined as cutting-edge science and technology in which small amounts of fluids (10^{-9}–10^{-18} liters) can be processed and manipulated in channels with very small dimensions. Therefore, microfluidic flow cytometers can be used to analyze single cells in a small population, cellular differences in gene expression or response to a drug within a population of cells. These chip-based flow cytometers are cost- and size-effective and portable when compared to conventional benchtop instruments. Microfluidic flow cytometers have several advantages over conventional flow cytometers. For instance, a typical flow cytometer delivers a sample of interest at rates of 10–100 µl per minute, which is not practical to detect the cells such as CTCs and hematopoietic stem cells found in very small numbers in the total sample. Conventional flow cytometers require analysis of several milliliters of the sample to detect small numbers of cells. Instead, microfluidic flow cytometers have the ability to concentrate cells and particles at the center of a microfluidic channel for direct analysis. Therefore, a high-throughput screening is enabled, in which small volumes of hundreds of thousands of samples can be analyzed simultaneously.

2.2 Imaging Flow Cytometry

Due to its high-throughput and multiparametric analysis, by supporting detection of single cell properties at rates from hundreds to 10^5 cells per second, conventional FC is an irreplaceable cytologic instrumentation when a study of high-volume cell populations and subpopulations needs to be performed. However, although FC can identify and sort rare cell populations with high speed, dealing with rare cell detection using this approach is plagued

by the contamination of false-positive events due to autofluorescence, nonspecific immunostaining, and cell aggregates [114]. Meanwhile, due to the lack of spatial resolution in exchange for higher throughput, users have to make gating decisions blind to some of the most informative and relevant sample attributes contained in cell images. Imaging is indubitably indispensable for cell analysis because images effectively convey certain messages about cells, such as cell size, shape, morphology, and distribution or location of labeled biomolecules within cells. As cellular morphology analysis plays an important role in various biological studies and clinical diagnoses (e.g., cancer screening), conventional FC is much anticipated to incorporate imaging capabilities. In contrast to pure quantitative measurements provided by conventional FC, microscopy allows capturing cell images that contain a wealth of information about a cell. For example, while conventional FC measures FSC light to estimate the relative cell size, microscopy yields the exact cell size through its brightfield image. Recent advances in imaging technologies, electronics, and digital computing have enabled IFC [115] [116]. IFC combines the single-cell imaging capabilities of microscopy with the high-throughput capabilities of conventional FC. Therefore, it becomes an ideal approach to simultaneously fulfill both analysis of morphological characteristics and phenotypic characterization of single cells within an enormous and heterogeneous population. Also, as the interest in performing IFC systems grows, the necessity of combining this technique with cell sorting becomes evident [117]. The basic idea behind IFC is scaling up FC spatial resolution to analyze more properties of cells. IFC aims at the fluidic-based platforms that have optical imaging functionality at informative spatial resolution while retaining the main features of conventional FC. For this reason, recent advances in IFC are remarkably revolutionizing single-cell analysis [115].

The IFC developed by Millipore, e.g. Amnis ImageStream® and FlowSight®, relies on high-speed CCD cameras that use the time delay and integration (TDI) technique, which is originally designed to image objects moving along

one axis at low light levels [118]. The ImageStream® system is sketched in Figure 2.2(a). Using spectral decomposition elements, 12 images per cell can be acquired simultaneously by 2 CCD cameras. Because of the rich subcellular information acquired by Amnis ImageStream®, various analyses and ML algorithms can be applied to study cell phenotype and subgroup classification. As the translation of the cell is exactly synchronized with the vertical charge transfer of each pixel on the CCD, using the TDI reading out technique requires a closely controlled fluidic system to ensure cells are centered and flow at a constant speed without rotation. This strict requirement hinders the system to adopt a sorting mechanism, since any minor fluidic disturbance from downstream cell sorting can cause imaging instability. One limitation of the system speed is the inherent data downloading method of CCD. On the other side, obtaining enough sensitivity without any gain like electron multiplication also prevents the system to reach throughput higher than 1000 cells per second. Although the sensitivity can be improved by increasing the excitation laser power, it may lead to photobleaching or saturation of fluorescence.

For blood cells, bone marrow cells, and many cancer cells flowing in the blood vessels, IFC is the most promising approach to study their morphological changes [114] [119]. The multiple applications of IFC include analysis of nuclear-cytoplasmic translocation [120], quantification of apoptosis based on the changes in nuclear morphology [121], and quantitative analysis of internalized bacteria and protozoan parasites [122]. In recent years, IFC was also employed for the evaluation of asymmetric cell division [123], internalization of CypHer5E-conjugated antibodies and PKH-labeled exosomes [124], intercellular communication by exchange of cytoplasmic material [125], and analysis of cell interactions and immune synapse [126]. Recently, IFC, combined with cell sorting pre-enrichment, was successfully employed for the identification and characterization of a novel pluripotent population of very small embryonic-like stem cells (VSELs) in human and animal tissues [127].

As an example of single-cell analysis using camera-based IFC, a quantitative evaluation of nuclear factor kB (NF-kB) activation of mammalian cells based on a commercial IFC, i.e. Amnis ImageStream®, is discussed [128] [129]. NF-kB is a transcription factor that regulates cellular processes such as proliferation, apoptosis, and survival.

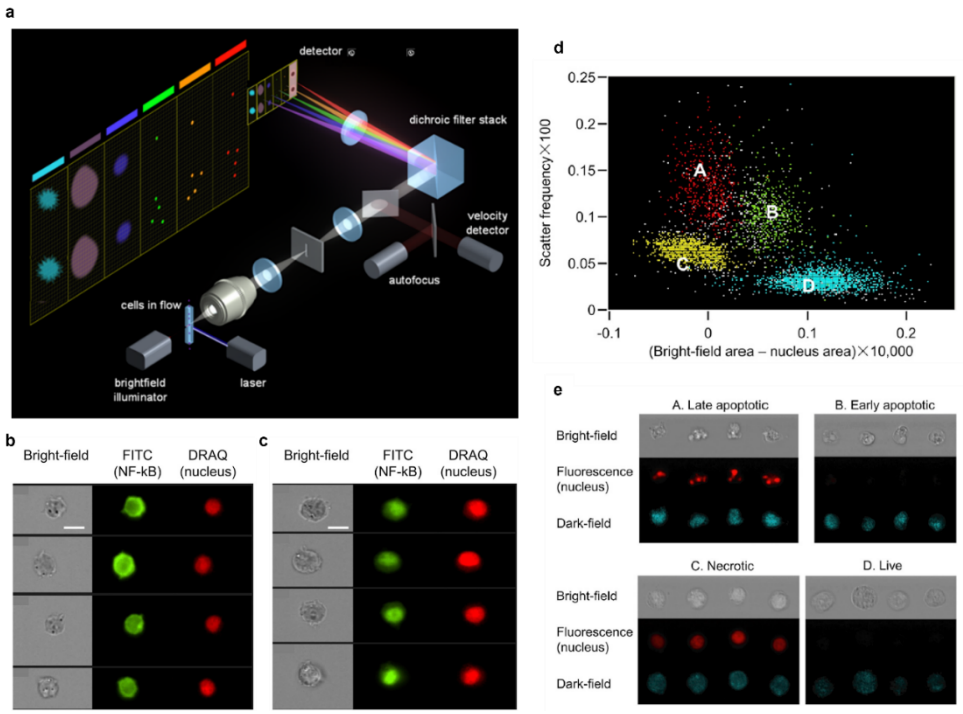

Figure 2.2 Amnis ImageStream®.

(a) Sketch of the otpo-fluidic recording system. **(b)** Unstimulated ML1 cells and **(c)** ML1 cells stimulated with 10 ng/mL TNFα. The gray, green, and red colors represent bright-field, FITC (specific to NF-kB), and DRAQ (specific to nuclei) images, respectively. The scale bars are 10 μm. **(d)** Scatterplot of Jurkat cells in four distinct states (blue, live; green, early stage of apoptosis; red, late stage of apoptosis; yellow, necrosis). **(e)** Examples of captured images of Jurkat cells in (d) (bright-field, dark-field, and fluorescence images). The fluorescence images are obtained by 7-aminoactinomycin D staining and represent nucleus morphology. (Figure a reproduced from Ref. [118]; Figure b-e reproduced from Ref. [128])

Since the p65 fragment of an active NF-kB complex is translocated to the nucleus, the activation level of NF-kB can be measured by the similarity of fluorescence images of NF-kB/p65 and the nucleus in a cell. Fluorescence images of unstimulated ML1 cells and ML1 cells stimulated with 10 ng/mL tumor necrosis factor α (TNFα) obtained by Amnis ImageStream® are shown in Figure 2.2(b,c), respectively. Whereas images of unstimulated ML1 cells show distinct differences between an NF-kB/p65 image and a nucleus image, images of stimulated ML1 cells show similarities between the two fluorescence images as a result of the activation of NF-kB. Note that these results cannot be obtained either by a conventional FC or by a bright-field IFC, hence demonstrating the strong utility of fluorescence IFC.

Another example of single-cell analysis where camera-based IFC plays a key role is the analysis of cell death [128] [130]. A scatterplot of four populations of Jurkat cells with distinct states (live, early stage of apoptosis, late stage of apoptosis, and necrosis) is displayed in Figure 2.2(d), while examples of three-color (bright-field, dark-field, and fluorescence of nuclei stained by 7-aminoactinomycin D) images obtained by Amnis ImageStream® are reported in Figure 2.2(e). The differences between the cell area (obtained by a bright-field image) and nucleus area (obtained by a nucleus fluorescence image), and the spatial scattering frequency (obtained by the dark-field image) are used as the horizontal and vertical axes in the scatter plot in Figure 2.2(d), respectively. The plot clearly discriminates the four states. On the other hand, standard FC cannot differentiate them under the same sample conditions because of the lack of morphological information, such as the cell area and nucleus area. This proof-of-concept demonstration indicates that camera-based IFC can be used for monitoring populations of modes of cell death in a large population of cells [128].

In commercial IFC instruments like Amnis ImageStream®, the high-throughput of 1000 events per second is counterbalanced by a poor resolution with respect to traditional microscopy (i.e., ~ 0.5 μm per pixel). Moreover, the maximal speed can only be achieved with a relatively high sample

concentration that is about 10^7 cells per milliliter. The acquisition timescale in IFC ranges in minutes, all the way from tenths of a minute to 100 minutes needed to push through tens of thousands of events from samples with a low cellular concentration. In this case, an issue could be represented by the lack of availability of nutrients and oxygen over long time periods, because samples presumably are run in phosphate-buffered saline. Focusing is a large contributor to the length of time required for analysis, because a large percentage of cells will be excluded from analysis due to focusing problems. Moreover, if fluorescence labeling with cell tracking and vital dyes is used, additional experiments are required to exclude phototoxicity as a reason for observed differences between the experimental and control cells [114].

Compared to the data format in conventional FC, including integral, peak and width of light intensity, cell images produced by IFC are much more complex. Since IFC can produce thousands of multi-spectral cell images per second, files generated by IFC can tremendously burden the digital image transportation and processing realized by the back-end data handling unit. A test of a few minutes can easily create a data file beyond tens of GB. For a possible solution, a compressive sensing theory-based method has recently been explored to build analog compression directly into the acquisition process so that the sampling can be significantly more efficient [131]. Computational requirements for IFC platforms are unprecedented. There are many software packages and tools for use in high-throughput image analysis, mainly for microscopy platforms, including CellProfiler and ImageJ, but in general, the pipelines of these tools are for offline image analysis [132]. In order to combine cell sorting with IFC to fully realize its tremendous potential, real-time image construction and analysis is required. Hence, the ability to produce, measure and analyse cell images, and sort cells in a real-time manner will be the next major milestone for IFC. Possible approaches to extract cell characteristics in real time include the use of field-programmable gate arrays (FPGA) or graphics processing units (GPUs) to implement various image processing and AI. Recently, thanks to AI, the FACS has been transferred into

the IFC world, thus implementing an Image-Activated Cell Sorter (IACS) [133] [134] [135].

Although the images have a high information content, containing rich morphological and spatial information (even in a single bright-field channel), data analyses often have low information content, that is, analyses are based on only very few selected features, which are often manually identified by the user by applying binary gates on cell populations of interest [136]. These approaches are highly subjective, thus operator bias always have to be considered, require significant user interaction, and only utilize a few morphological features instead of the hundreds that are inherently present in the data. Yet, even with these limitations, some IFC applications are already heading toward the clinic, such as the diagnostic assessment of acute leukemia [137], even if IFC is currently primarily used in research. These issues might be overcome with AI approaches. As well, there is a need for standardization of IFC, which should include standard operating procedures and standardized quality control of hardware performance. Although a common practice for conventional FC, this has not yet been implemented as such in IFC. Furthermore, cloud computing can overcome the computational infrastructure hurdles. These developments are key for practical IFC applications to reach the clinic, fueling the applicability of IFC as a diagnostic, prognostic, and therapeutic tool [136].

2.3 Label-Free Imaging Flow Cytometry

A major challenge in many modern biological laboratories is obtaining information-rich measurements of cells in high-throughput and at single-cell level. In conventional FC and IFC, the fluorescent stains are used to label cellular components or processes, revealing specific cell phenotypes in the population and quantifying the particular state of each cell. However, often

these stains are incompatible with live cell analysis and may have confounding effects on the cells. For example, the commonly used Hoechst 33342 stain, which binds to the minor groove of the double-stranded DNA, can induce single-strand DNA breaks [138], or DRAQ5, the nuclear stain that intercalates with the cell's DNA, can influence chromatin organization and lead to histone dissociation [139]. Also, several different markers are usually required to unambiguously identify all cell cycle phases [140]. Moreover, exogenous biochemical markers are not always effective, especially when there is poor prior knowledge of the markers of a yet-to-be identified population [141]. For instance, cell surface markers or other factors that are expressed by the unknown and rare cell types in a highly heterogeneous population (such as stem/progenitor cells and aberrant rare cancer stem cells) might not be known. Furthermore, large-scale biochemical cellular assays are costly, labor-intensive, and time-consuming, thus hindering their applications for routine disease diagnosis or screening. Finally, above all in long experiments, photobleaching could alter the overall imaging and photodamaging could change the cell physiology. Therefore, a label-free assay that avoids the stains required to characterize single-cells in high-throughput mode is particularly attractive [142]. Besides, state-of-the-art IFC does not provide quantitative images of cells from which biophysical cell properties can be extracted [143], such as RI, dry mass and biovolume, which are related to various cellular functions and features [5] [144] [145]. To obtain new scientific insights and to enrich the diagnostic toolsets, it is of great value to explore alternative biomarkers, involving simple and cost-effective methods with sufficient statistical power, which can correlate with the information provided by existing biochemical markers [141]. To this end, cellular biophysical properties are the effective intrinsic indicators of a multitude of cellular processes, ranging from cell-cycle progression [146] and cell differentiation [147] [148] [149] to malignant transformation [150] [151]. For example, it has been demonstrated that the label-free assessment of cell mass density is as

effective, or even more accurate, descriptor of cellular heterogeneity, compared to the conventional fluorescence markers [152] [153].

As discussed in Section 1.1, QPI is an emerging optical technique for nondestructive testing and minimally invasive analysis of almost transparent biological specimens such as living cells, which allows the extraction of absolute biophysical cell parameters like RI, dry mass and biovolume. For these reasons, the combination between QPI and FC is expected to greatly enlarge the potential of conventional IFC.

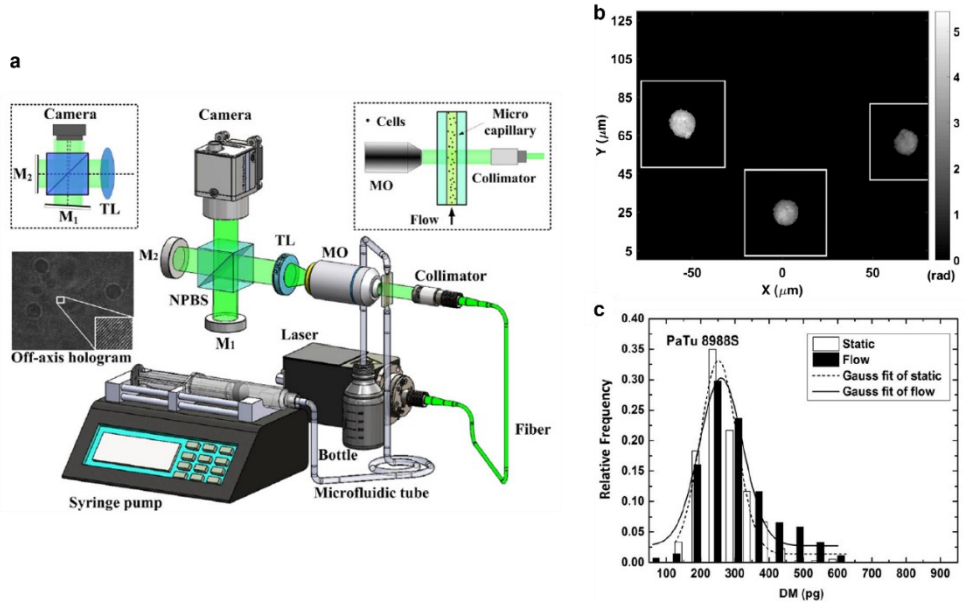

Figure 2.3 HIFC for quantitive characterization of pancreatic tumor cells PaTu 8988S.
(a) Sketch of the HIFC setup. MO, microscopic objective; TL, tube lens; M1 and M2, mirrors; NPBS, non-polarizing beam splitter cube. Insert in upper left corner, configuration of the Michelson interferometer-based self-interference DHM unit; insert at middle left panel, representative recorded digital off-axis hologram; insert in upper right corner, enlarged sketch of the flow field observation area including the micro-capillary inside a cubic silica block. **(b)** QPM with three PaTu 8988S cells after segmentation and digital refocusing. **(c)** Dry mass histograms of PaTu 8988S recorded in static and in flow conditions. (Figure reproduced from Ref. [143])

Actually, the development of label-free IFC has been aided by one of the most powerful properties of DHM, i.e. the possibility of numerically refocusing cells after the experiment instead of recording each of them in their corresponding focal plane, *a priori* calibrated before the experiment. Hence, the DHM recording of single cells could move towards the high-throughput feature typical of the IFC paradigm, without using exogenous markers and providing a high-content quantitative information about the cell biophysical properties. For example, the HIFC system sketched in Figure 2.3(a) has been used to reconstruct the QPMs of flowing pancreatic tumor cells PaTu 8988S, as displayed in Figure 2.3(b), which corresponding histogram of the measured dry mass is reported in Figure 2.3(c) [143]. HIFC has been exploited to characterize RBCs in flow by measuring the Hb content [154], for extracting the quantitative signature of cancer cells [155], for investigating the biophysical properties of WBCs [156], and for identifying shape variations in leukemia cells [157].

However, it is worth noticing that, limited by the fundamental trade-off between the camera's frame rate and its sensitivity, classical optical microscopy, including QPI, lacks the ability to offer sufficient image quality to resolve subcellular structures at high imaging throughput [141]. This explains that the available label-free IFC techniques either can provide the bulk single-cell biophysical knowledge (e.g., cell size, cell shape) at high throughput [147] [148], or have to scale down the throughput by 10^2–10^3 times to preserve high image resolution required for cellular assay [155] [157]. In this regard, the gold-standard label-free IFC technique is a time-stretch interferometer microscope (namely multi-ATOM), which enables single-cell QPI at sub-cellular resolution even operating at a high cell imaging throughput (>10000 cells/s), at least 100 times faster than classical QPI [141] [158].

Despite their significant impact, current commercial FC systems are limited by high cost, large instrumentation size and the constant requirement of highly trained personnel for maintenance (the latter two resulting from its complex system configuration). A typical flow cytometer with cell-sorting function

costs US$200000–1000000. Most cell analysis/sorting tests are typically performed at well-funded, centralized share facility laboratories and hospitals due to the economic reasons. Instead, in global healthcare there is an increasing need of medical equipment with devices able to provide affordable, sensitive, specific, user-friendly, robust, rapid, equipment-free, and deliverable testing for clinical diagnosis [159]. These requests are particularly needed in first-line clinical offices and in developing countries that lack adequate and costly facilities. In the last years, many research efforts have been spent to realize LOC devices for point-of-care applications satisfying these requirements [160], in particular exploiting the advantages of optical imaging techniques for diagnostic purposes as they are high resolution, real-time, and able to measure macroscopic parameters in microscopic devices [161]. Moreover, rapid diagnostics should skip long and cumbersome analytic procedures that eventually request complex laboratory equipment and multistep pretreating. In terms of rapidity and flexibility, a direct diagnosis on human physiological liquids would be greatly beneficial if an imaging microfluidic device were used on samples without any preparation (i.e., urine or blood sampled from human body and directly analyzed). Also, diagnostic analysis of flowing and not-adherent cells needs to be quantitative, label-free, and as fast and accurate as possible [159]. In this scenario, lens-free on-chip DHM offers a flexible, compact and cost-effective alternative for many on-chip diagnostics applications such as whole blood analysis [162]. In fact, lens-free on-chip DHM is an emerging technique that allows imaging of biological samples within a large FOV without using bulky lenses or optical components. Based on a compact, cost-effective and robust architecture, lens-free on-chip DHM offers a tool capable of meeting the emerging needs of microscopic analysis and diagnosis with low mechanical resources for telemedicine applications. Such a setup is shown in Figure 2.4(a). It is based on consistent in-line DHM which achieves a relative high resolution. In this platform, the sample is placed directly on an array of optoelectronic sensors. A partially coherent light source employing LEDs is used to illuminate the sample.

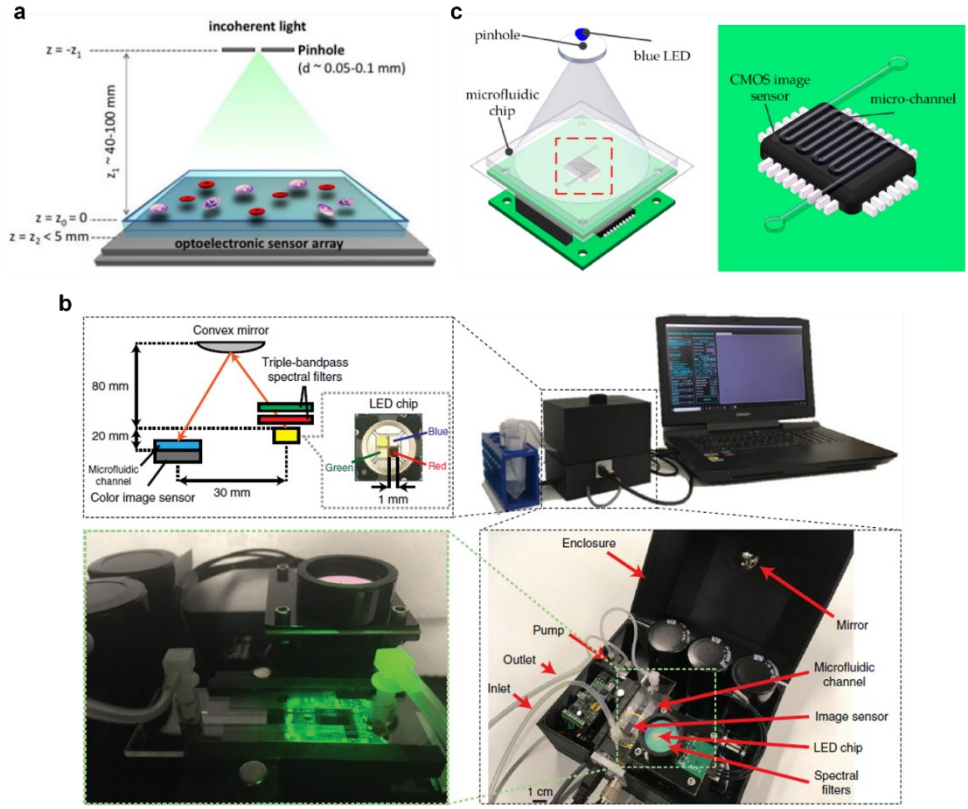

Figure 2.4 DHM miniaturization.

(a) Schematic illustration of a lens-free on-chip DHM system. The objects are placed directly on a digital sensor array with typically $z_2 < 5$ mm distance to its active area. A partially coherent light source, such as an LED, is placed $z_1 \sim 4–10$ cm away from the objects, and filtered by a pinhole of diameter d ~ 0.05–0.1 mm to record the digital inline holograms of objects with unit fringe magnification over a large FOV, e.g., 24 mm^2. **(b)** Photos and schematic illustration of a portable HIFC device. The water sample is constantly pumped through the microfluidic channel at a rate of 100 mL/h during imaging. The illumination is emitted simultaneously from red, green, and blue LEDs in 120-μs pulses and triggered by the camera. Two triple-bandpass filters are positioned above the LEDs, and the angle of incidence of the light on the filters is adjusted to create a <12 nm bandpass in each wavelength to achieve adequate temporal coherence. The light is reflected from a convex mirror before reaching the sample to increase its spatial coherence while allowing a compact and lightweight optical setup. **(c)** Schematic illustration of a lens-free on-chip HIFC device with zoomed-in on the right the S-type micro-channel. (Figure a reproduced from Ref. [162]; Figure b reproduced from Ref. [163]; Figure c reproduced from Ref. [164])

The light produced by the source is filtered through a small hole. During vertical propagation, the beam tends to increase in diameter, thus allowing a coherent illumination of micro-objects in a large FOV. If the density of the objects is not excessively large or if the objects are weakly scattering, as occurs with most biological samples, much of the light does not interact with the objects and therefore acts as a reference beam. Instead, a small sample portion of light is scattered by and thus forms the object wave. The degree of coherence (both spatial and temporal) on the sensor plane allows the object wave and the reference wave to overlap and form an interference pattern, i.e. the hologram. In this system, the high-throughput recording is obtained by the large FOV instead of the FC mode.

A field-portable and cost-effective HIFC system has been proposed for capturing QPMs of micro- and nano-plankton inside a continuously flowing water sample at a throughput of 100 mL/h [163]. The device is based on partially coherent lens-free DHM and acquires the diffraction patterns of flowing micro-objects inside a microfluidic channel without the use of external labeling. Operated by a laptop computer, this portable device, shown in Figure 2.4(b), measures 15.5 cm × 15 cm × 12.5 cm, weighs 1 kg, and costs less than $2500. Therefore, compared to standard IFC, it provides extreme reductions of cost, size and weight while also giving a high volumetric throughput over a large object size range. Finally, a lens-free HIFC system has been implemented on-chip in microfluidic conditions [164], as sketched in Figure 2.4(c). In particular, the system causes cells to flow through a micro-channel in a PDMS microfluidic chip above a contact image sensor (CIS). A near-coherent light source is mounted above the microfluidic chip, and diffraction shadow images of cells generated by the near-coherent light source are then captured by the CIS. Because of the low intensity of near-coherent light caused by a pinhole, the exposure time of the image sensor in the system is longer than 400 ms. Therefore, there is stronger motion blur while the cells are quickly flowing in the micro-channel. To solve this problem, the cells in the micro-channel are imaged simultaneously in a large FOV instead of with a FC method in which

the cells pass through the testing area at high speed. In other words, the method takes advantage of the larger FOV of the CIS to reduce the cell flow velocity. To utilize the large FOV of the CIS, an S-type channel shape is employed. As a result, the CIS captures the maximum possible number of cells in a frame. In addition, the cells in current frame flow out of the micro-channel completely before the next exposure of the CIS. Thus, all the cells in each frame are new cells, and the cells in each individual frame can be evaluated to increase the number of tested cells. Regarding cost, the CIS is commonly used in industrial cameras and mobile phones, so the price is very low (below $10). The microfluidic chip comprises a PDMS channel and a piece of thin glass (0.18 mm), making it very cheap and easy to replace. Using whole blood cells to test the cell counting precision, the reached error less than 2% has outlined the high-precision of this LOC device.

2.4 TPM-FC Paradigm

As discussed in Chapter 1, the 3D quantitative and label-free characteristic is bringing out TPM as promising optical imaging technique to be used individually or combined with other imaging modalities to effectively and efficiently tackle many unresolved but important biological and medical problems in the future. Over the last years, the TPM technique has started to trade into the industry by means of NanoLive Inc. [165] and TomoCube Inc. [166]. Both companies use the TPM-ISC mode to obtain label-free 3D images of entire cells and tissue slices, and promise to open numerous unexplored applications in biology and medicine. This attempt to extend the TPM technique from lab research to public use is contributing to making it even more popular among biologists and physicians all over the world. Another important step toward a remarkable reduction of the production cost is the employment of LEDs as light source, which aims at the same time to increase

the TPM resolution thanks to the higher signal-noise ratio [167] [168]. However, although TPM has been intensively developed over the past 10 years, its applications are still limited to cell biology studies. Thus, it needs to be fully explored for more translational research. Due to the shortcomings of the currently available methods, many long-standing problems remain in the biomedical field, but they can be potentially solved with TPM. For instance, immunocyte phenotyping, stem cell multipotency identification, cancer cell screening, and tissue pathology are promising directions in which TPM may contribute. However, in order to achieve actual success in these important topics, thus making TPM really compatible with the already established clinical procedures, a major improvement must be addressed, i.e. the high-throughput feature [47]. In fact, clinical diagnostics on cells, such as blood testing, usually needs to deal with millions of cells to obtain statistical understanding on the cell populations, as occurs in FC and IFC. Current reported TPM systems work in static modality, have a very limited FOV (~50 μm × 50 μm), and at least tens of measurements are needed to generate one tomogram, which takes a lot of time. To tackle the low-throughput issue, in 2017, for the first time, the TPM tool has been demonstrated working in FC mode, thus implementing the TPM-FC paradigm [107]. In fact, the 3D RI tomogram of a single-cell has been reconstructed while flowing and rotating in a microfluidic channel. Therefore, by exploiting the well-established feature of FC about the single-cell high-throughput analysis, the TPM-FC aims to deeply broaden the great potential of the TPM technique by overcoming its main limitation toward its spreading in the clinical world.

2.4.1 TPM-FC System at ISASI-CNR

The current TPM-FC system built up at ISASI-CNR labs is based on a DH microscope developed in off-axis telecentric configuration employing a Mach-Zehnder interferometric scheme, as sketched in Figure 2.5(a). A laser light (Laser Quantum Torus 532) is used as illumination source , emitting at 532

nm with an output power equal to 750 mW. The laser beam is split by a polarizing beam splitter (PBS) cube into object and reference beams, which are reflected and transmitted, respectively. In addition, to balance the ratio between intensity of object and reference beam, maintaining the same polarization, two half-wave plates are placed in front of and behind the PBS, respectively. Object beam passes through a microfluidic chip (Microfluidic ChipShop 10000107 - 200 μm × 1000 μm × 58.5 mm) and then it is collected by a MO (MO1, Zeiss Plan-Apochromat, 40×, NA=1.3, Oil immersion) and sent to a tube lens (TL1 with focal length 150 mm). Reference beam passes through a beam expander shaped by a MO (MO2, NewPort, 20×, NA=0.40) and a second tube lens (TL2 with focal length 250 mm). Then, both collimated beams are recombined by a beam splitter cube with a small angle between them in order to achieve off-axis configuration and generate the interference pattern digitally recorded by the CMOS camera (Genie Nano-CXP Cameras, 5120×5120 pixels and 4.5 μm pixel size). The camera is equipped by a video recording system ensuring long time acquisition mode. The FOV is 640×640 μm^2 with a spatial resolution of 0.5 μm. Hence, the camera records (along the optical z-axis) at 30 fps a sample of cells while flowing (along the y-axis) and rotating within a microfluidic channel thanks to the hydrodynamic forces of a laminar flow ($\sim$ 50 nL/s) generated by an automatic syringe pump (Syringe Pump neMESYS 290N). The latter is a low-pressure system which allows a high-precision and pulsation-free dosing of liquids at micro and nanoliter scale ensuring a very homogeneous flow inside the microchannel. In fact, the Hagen-Poiseuille equation relates the pressure drop ΔP in a fluid flowing through a long pipe with its volumetric flow rate Q as

$$\Delta P = R_{hyd} Q, \tag{2.1}$$

where R_{hyd} is the hydraulic resistance of the channel. The main assumptions of the equation are that the fluid is viscous and incompressible, and the flow is laminar. These conditions are completely satisfied in microfluidics [169].

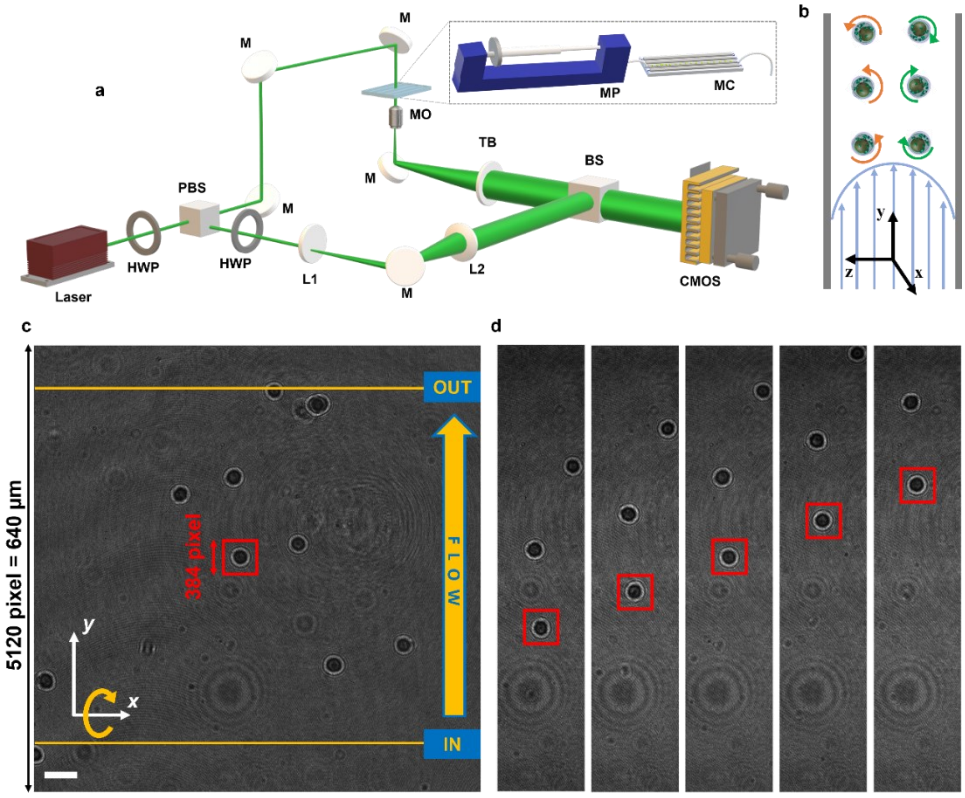

Figure 2.5 TPM-FC recording system at ISASI-CNR.
(a) Sketch of the TPM-FC system. PBS – Polarizing Beam Splitter; WP –Wave Plate; M – Mirror; L1, L2 – Lens; MO – Microscope Objective; MC – Microfluidic Channel; MP – Microfluidic Pump; TL – Tube Lens; BS – Beam Splitter; CMOS – Camera. **(b)** Scheme of rotation of cells due to the velocity gradient and chosen reference coordinate system. Cells flow along the y-axis, rotate around the x-axis, and are illuminated along the z-axis. **(c)** Digital hologram taken from the recorded DHM sequence, with fibroblast cells flowing along the y-axis from the input line to the output line used for detecting them. The scale bar is 50 µm. **(d)** Five cuts of digital holograms of the same fibroblast cell at different time frames.

The general solution for the flow velocity in a channel with a rectangular cross-section is given by [170]

$$(2.2)\ u(x,z) = \frac{16h^3}{\mu\pi^3}\left(-\frac{dp}{dy}\right)\sum_{i=1,3,5,\ldots}^{\infty}(-1)^{\frac{i-1}{2}}\left[1-\frac{\cosh\left(\frac{i\pi z}{2h}\right)}{\cosh\left(\frac{i\pi w}{2h}\right)}\right]\frac{\cos\left(\frac{i\pi x}{2h}\right)}{i^3},$$

where dp/dx is the pressure drop across the channel, and h and w are the height and the width of the channel cross-section $\{x, z\}$, respectively. This analytic solution says that a Hagen-Poiseuille flow is characterized by a parabolic velocity profile, in which the velocity of flow in the center of the channel is greater than that toward the outer walls. As sketched in Figure 2.5(b), due to the parabolic velocity profile, if a cell is close to the wall, its surface will be affected by different velocity values. In particular, the cell side closer to the center of the channel is affected by a higher velocity than the side closer to the wall. The couple of forces acting on the cell generates a torque, and so a rotation is induced. Therefore, several digital holograms are recorded while the cell is rotating with respect to the fixed illumination beam direction, thus fulfilling the TPM recording principle. In particular, TPM-FC frames within the TPM-SRC modality in terms of the missing cone problem, i.e. isotropic reconstruction can be achieved. However, unlike the conventional TPM-SRC tools, TPM-FC comes with some advantages. The biological sample is not altered by the mechanical/optical external forces needed to rotate it. Moreover, the hydrodynamics-based rotation is not limited to handle one single cell for each experiment, thus moving toward the high-throughput property since the difficult and time-consuming recording can be skipped. Furthermore, cells are not fixed at rest on a surface, but they are analyzed in suspension in a buffer solution (e.g., Phosphate Buffered Saline). This latter property is important above all when cells that circulate in the human bloodstream must be characterized by TPM, as their natural condition is considered. An example of recorded digital hologram is displayed in Figure 2.5(c), while a sequence of successive holograms cut in the same vertical region is reported in Figure 2.5(d) to show the cell flow along the y-axis.

2.4.2 Automatic Reconstruction Processing

The first requirement to process a high number of cells is the implementation of an automatic reconstruction code, which has been developed herein. Each

recorded hologram is pre-processed with the aim to detect and track each flowing cell within the FOV. Due to the inherent contrast between cells and their background in the digital hologram, a threshold-based method is exploited to detect the frames in which a cell enters and exits the FOV by passing through the input and output lines shown in yellow in Figure 2.5(c). According to the reference system in Figure 2.5(c), the microfluidic pump ensures that cells flow along the y-axis with a quasi-uniform speed while keeping about the same x-position, as shown in Figure 2.5(d). Therefore, the x-coordinates of the intermediate positions are computed as the mean value between the detected input and output x-coordinates, while the corresponding y-coordinates are computed by assuming a uniform movement between the input and the output lines, i.e.

$$y_k = y_i + \frac{y_f - y_i}{f - i}(k - i), \tag{2.3}$$

where $k = i, \dots, f$ is the intermediate frame index ranging from the detected input frame i and output frame f, and y_i and y_f are the y-coordinates of the fixed input and output lines, respectively. Then, a sliding patch of sizes 384×384 pixels is centered on these raw positions (see red box in Figure 2.5(c,d)). In summary, a video sequence of 5120×5120 pixels holographic images turns into tens of sequences of 384×384 pixels sub-holograms, each of them containing the cell during its rotation. Finally, each sub-hologram is numerically reconstructed by implementing the processing pipeline described in Section 1.1.3 and shown in Figure 2.6(a). In particular, the suppression of undesired diffraction orders is made by Fourier spectrum filtering to select and center the real diffraction order (i.e., hologram demodulation). Afterwards, the demodulated hologram is numerically refocused to provide the in-focus complex amplitude from which the phase-contrast image is obtained by calculating its argument [13]. The residual optical aberrations, superposed to the retrieved phase-contrast image, are subtracted by using a reference hologram, acquired without the sample in the imaged FOV [171]. Then, the 2D windowed FT filtering is employed as denoising method [172]

and the PUMA algorithm is used for the phase unwrapping [18]. Finally, the QPM is centered in the cell transversal position [13]. The processing is then repeated for all the different positions occupied by the cell during its flow along the FOV.

In particular, among other features, DHM allows the accurate *a posteriori* retrieval of the spatial coordinates of an object, thus providing a 3D particle tracking in the entire imaged FOV. Therefore, DHM is often used in different branches of bio-microfluidics, such as the study of the migration and motility of biological samples [13] [173]. Due to this distinctive property, DHM can be easily combined to FC without even the need for controlling *a priori* the cell focus, as instead occurs in conventional IFC. Classical holographic tracking methods are typically composed of two main steps, i.e. numerical refocusing for retrieving the position of the targets along the optical axis, and evaluation of the transverse position of the refocused object. As regards the axial localization (or refocusing), it is possible because a digital hologram contains information about all planes along the optical z-axis. In fact, thanks to the Angular Spectrum method in Eq. (1.19), the demodulated hologram can be numerically propagated along the z-axis. At each z-position, the image contrast of the amplitude of the propagated complex wavefront is computed by means of the Tamura Coefficient (TC), defined as [174]

$$TC\{I\} = \sqrt{\frac{\sigma\{I\}}{\mu\{I\}}}, \tag{2.4}$$

where σ and μ are the standard deviation and average value of a certain image I, respectively. As illustrated in Figure 2.6(b), the TC computed throughout the z-stack defines a convex functional which minimum corresponds to the focal plane of the analyzed cell, as a biological sample is a phase object whose information is mainly contained in the phase modulation of the incident wavefront. The TC-based method allows implementing a fully automatic refocusing method. While the axial localization operates on the amplitude of the complex wavefront, the transversal localization is instead based on the

unwrapped in-focus QPM. The transversal position is computed after segmenting the cell from its background and by computing the weighted centroid, i.e. the cell centroid weighted by the cell phase values [13]. In Figure 2.6(c), the same QPM is reported before (at the top) and after (at the bottom) having been moved in the ROI center, i.e. after aligning the cell weighted centroid with the ROI center to avoid motion artefacts in the tomographic reconstruction. All the TPM-FC codes herein presented have been implemented in Matlab®.

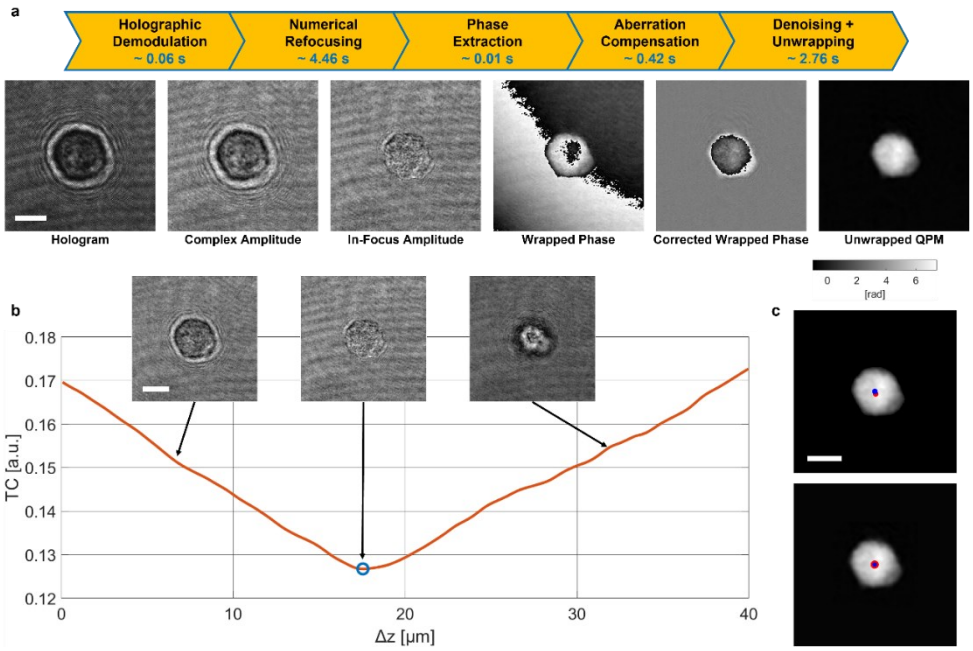

Figure 2.6 Holographic processing for TPM-FC.
(a) Steps of the holographic processing pipeline to compute the QPM of a fibroblast cell from the corresponding holographic ROI (384×384). **(b)** Autofocusing of the cell based on the minimization of the TC computed throughout the z-stack. The focal plane corresponds to the blue circle. Δz is the distance along the optical z-axis from the recording z-position. The amplitude of the complex wavefront propagated at three z-positions is reported at the top, highlighting different image contrasts, as quantified by the TC. **(c)** At the top, segmented non-centered QPM, with the cell weighted centroid (red dot) non corresponding to the ROI center (blue dot). At the bottom, segmented centered QPM, with the cell weighted centroid (red dot) corresponding to the ROI center (blue dot). The scale bars are 10 μm.

2.4.3 Rolling Angles Recovery

In order to perform a 3D tomographic reconstruction, two inputs are requested, i.e. the set of 2D projections and the corresponding viewing angles. In TPM-FC, the 2D projections are the centered QPMs, while the viewing angles correspond to the rolling angles of the cell flowing along the microfluidic channel. However, unlike the conventional TPM setups, in TPM-FC the viewing/rolling angles are not *a priori* known, therefore they must be estimated to reconstruct the cell tomogram. In the previous implementations of TPM-FC, three different numerical methods have been created to recover the unknown rolling angles. The first one was developed for cells with quasi-homogenous RI distribution and demonstrated for RBCs. This approach models RBCs as microlenses [21], thus providing a mathematical relation between the rolling angles and the variation of Zernike coefficients during the cell rotation [107]. The second one was developed for cells having high RI variations and demonstrated for marine algae particles like diatoms. In this case, the maximization of the correlation coefficient between pairs of mirrored phase images permits the rolling angles identification of each pair such that the angles sum is 180° [107]. However, these two recovery methods work efficiently for cells having non-spherical shapes, as in the case of RBCs and diatoms, and above all they exploit information that in general are not always available *a priori*. Therefore, a third approach was investigated for quasi-spherical cells, which exploits information deduced from a theoretical microfluidic model of cell rotation and centroids movement [175]. This last method was also demonstrated for single cells as well as cell clusters. However, it was strongly dependent on the noise level, above all in the case of single cells, and in addition it was very slow since for each cell in each experiment, a complex theoretical microfluidic model had to be created. Therefore, herein an alternative general strategy to recover the unknown rolling angles of the flowing cells is proposed, not depending on the cell shape, the RI content, and complex microfluidic models [108].

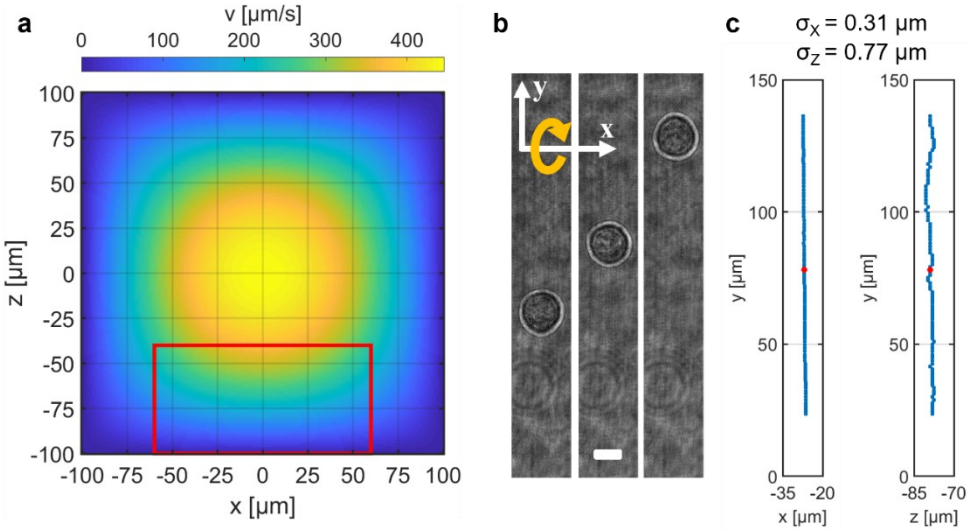

Figure 2.7 Cell roto-translation in TPM-FC.
(a) Parabolic velocity profile in the cross section of the microfluidic channel. The red rectangle is the region in which cells are recorded. **(b)** Three cuts of digital holograms of the same MCF7 cell at different time frames. The shape variation of the cell highlights its rotation around the x-axis while it is flowing along the y-axis. The scale bar is 10 μm. **(c)** Tracking of the cell in (b) within the channel's sections xy and yz, with reported at the top the cell drift along the x- and z-directions as standard deviation of the corresponding positions.

In fact, it exploits only the 3D holographic tracking outcome and the microfluidic properties of the TPM-FC system. This tracking-based rolling angles recovery method was demonstrated on data captured in both the current TPM-FC system and in a previous one, equipped with a microfluidic channel with 200 μm × 200 μm cross section and coupled to a 2048×2048 CCD camera. In Figure 2.7(a), the parabolic velocity profile in the latter channel's cross section is reported, related to Eq. (2.2). The red rectangle in Figure 2.7(a) highlights the region wherein the flowing cells are usually observed and recorded. Within this region, the velocity gradient in the z-direction can be neglected with respect to that in the x-direction. Therefore, the cells can be assumed to rotate around the x-axis while flowing along the y-axis. In Figure

2.7(b), three cuts of the recorded digital holograms of the same human breast cancer cell (MCF7) at different time frames are reported as example, in which it is evident the cell rotation around the x-direction due to the flip of the cell shape along the y-direction. In Figure 2.7(c), the 3D holographic tracking of the cell is displayed by visualizing the trajectory within the *xy*- and *yz*-sections. It is noted that the cell drift, evaluated as the standard deviation of the estimated positions along the x- and z-axes (σ_x and σ_z, respectively) is negligible, being σ_x = 0.31 μm and σ_z = 0.77 μm, which can be expected as the length of the channel along the flow y-axis (i.e., 7 cm) is much greater than the size of the channel's cross section. This demonstrates the quasi-constant positioning of the cell within the channel's cross section *xz*, a key point to assume the continuous and quasi-uniform cell roto-translation. As a consequence, as the angular increment is small because of the high frame rate, it can be safely supposed that the incremental rolling angle around the x-axis between two consecutive frames is proportional to the translation velocity with which the cell is moving between the two corresponding y-positions.

Assume that a sequence of K digital holograms of a flowing cell has been recorded. After calculating the 3D positioning of the cell (x_k,y_k,z_k) for the k-th frame through the holographic tracking strategy, and after reconstructing the corresponding QPMs, the proposed method recovers the rolling angles according to the following two steps.

1. Estimation of the frame index f_{180} at which the 180° of rotation has occurred with respect to the QPM of the frame $k = 1$.
2. By assuming the proportionality between translation and rotation, and a null initial rotation angle $\theta_1 = 0°$ for the frame $k = 1$, the rolling angle is calculated, for each frame $k = 2, 3, \dots, K$, as

$$\theta_k = 180° \frac{y_k - y_1}{y_{f_{180}} - y_1}. \tag{2.5}$$

The key-enabling step is the identification of a phase image rotated by 180° with respect to the first one. The Tamura Similarity Index (TSI) has been

proposed as the QPM similarity metric used to solve this problem, since it is expected to exhibit more robustness against other possible metrics. TSI is based on local measurements of the image contrast through the TC. In particular, let $QPM(k)$ be the phase reconstruction of the k-th frame with sizes $N \times M$, and $S_{i,j}(k)$ a 3×3 patch within $QPM(k)$, centered in the pixel of coordinates (i, j), with $i = 2, \dots, N-1$ and $j = 2, \dots, M-1$. By replacing each pixel of the $QPM(k)$ with the contrast value of $S_{i,j}(k)$ calculated by using TC, a new image of sizes $(N-2) \times (M-2)$ is obtained, namely the local contrast image (LCI), whose generic element is

$$LCI_{i,j}(k) = TC\{S_{i,j}(k)\}, \tag{2.6}$$

with $i = 2, \dots, N-1$, $j = 2, \dots, M-1$, and $k = 1, \dots, K$. Finally, the TSI is obtained as

$$TSI(k) = TC\{LCI(1)./flip\{LCI(k)\}\}, \tag{2.7}$$

where $flip$ is the vertical flipping operator to take into account the mirroring property with respect to the x-axis and ./ denotes an elementwise division. $TSI(k)$ defines a functional whose global minimum point

$$f_{180} = \underset{k}{\operatorname{argmin}}\{TSI(k)\} \tag{2.8}$$

is the sought for index f_{180}. Once f_{180} is estimated, the unknown rolling angles can be computed by means of Eq. (2.5).

To assess the performance of TSI, it has been compared with some of the most used similarity indices, i.e., the Spatial Correlation Coefficient (SCC) [107], the Structural Similarity Index (SSIM) [176], the Universal Image Quality Index (UIQI) [177] and the Gradient Magnitude Similarity Deviation (GMSD) [178]. All these metrics define in turn functionals enable of estimating f_{180} as for the TSI. In particular, for SCC, SSIM and UIQI, the global maximum is of interest while, for the GMSD, the global minimum is relevant. Furthermore, a 3D numerical cell phantom has been simulated in order to reproduce the rotation of a flowing cell within the microfluidic channel. In particular, the numerical

model of the 3D RI distribution of a cell has been created by considering the main four sub-cellular structures, i.e., the cell membrane (RI = 1.350), the cytoplasm (RI = 1.365), the nucleus (RI = 1.380) and some mitochondria (RI = 1.410). The shapes of the structures and the corresponding nominal RIs have been chosen by taking inspiration from measured values reported in literature for the MCF7 cell line [179] [180]. Assumed the straight-ray approximation, after the numerical integration of the 3D RI distribution along different orientations around the same axis and with fixed angular step, synthetic QPMs are obtained. To evaluate the accuracy and the robustness of the similarity metrics, 180 test cases have been simulated, drawn by combining the following possibilities

- 2 possible Gaussian distributions of the RIs for each sub-cellular structure with average values corresponding to the nominal RIs reported above and standard deviations $\sigma_{RI} = \{0.01, 0.02\}$;
- 2 possible cell membrane structures, i.e., spherical and non-spherical;
- 5 possible cell rolling angles sets;
- 9 possible zero-mean Gaussian noises with standard deviations σ_N varying within [0,0.2] rad with uniform step, added to each QPM.

Among the simulated rolling angles sets, three of them, with $\Delta\theta = \{3°, 4°, 5°\}$, provide the exact 180° cell rotation at the frame $f_{180} = 61$, $f_{180} = 46$ and $f_{180} = 37$, respectively. The other two cases are designed by adding small perturbations on rolling angles created with $\Delta\theta = \{3°, 5°\}$, in order to simulate two angle sequences without the exact 180° cell rotation. In the latter two cases, similarity metrics must identify the frames with the rolling angles closest to 180°, which are 180.6° and 180.8° in such simulations, respectively. In Figure 2.8(a), the numerical model of the 3D RI distribution of a cell obtained by simulating the nominal RI values is reported. Figure 2.8(b) shows the QPMs obtained from Figure 2.8(a) by numerical integration along the orientations at 0° and 180°. In this example, the simulated angular step is $\Delta\theta =$

3°, so the 180° of rotation occurs at frame $f_{180} = 61$. Figure 2.8(c) displays the corresponding noisy QPMs obtained by adding the Gaussian noise with $\sigma_N = 0.175$ rad in the case $\sigma_{RI} = 0.01$. Finally, Figure 2.8(d) reports the SSC, SSIM, UIQI, GMSD and TSI similarity metrics, normalized to their respective maxima for visual comparison, for the considered test case. In the legend, the estimated f_{180} of the five methods are reported. Notably, for the considered test case, TSI provides the right f_{180} showing also a sharp extreme point, enabling the determination of f_{180} with a high reliability.

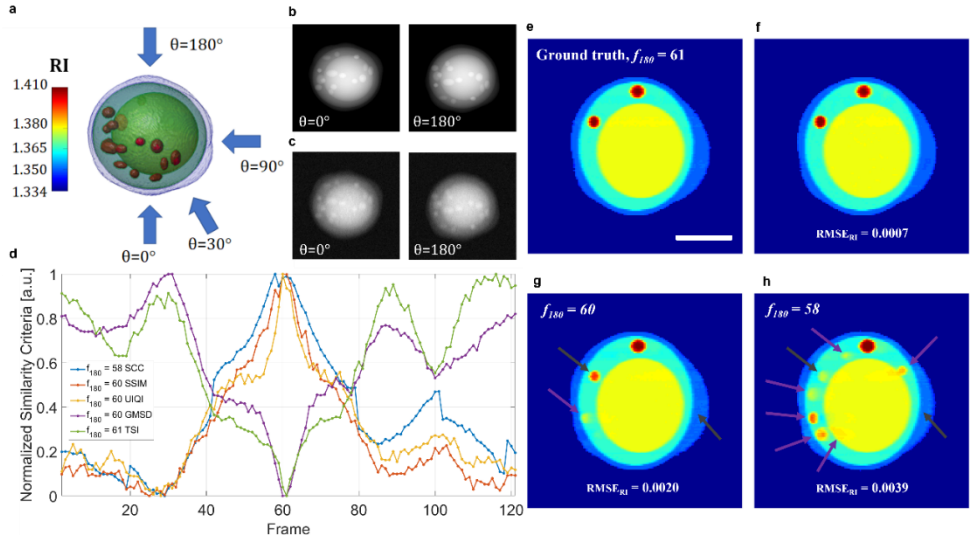

Figure 2.8 Numerical simulation to evaluate the performance of similarity metrics in f_{180} searching.
(a) 3D RI distribution of an MCF7 cell simulated with the nominal RI values and a non-spherical shape. **(b)** QPMs obtained by numerical integration of the cell phantom in (a) along the orientations at 0° and 180° (simulated angular step $\Delta\theta = 3°$, then f_{180} = 61). **(c)** QPMs noisy images ($\sigma_N = 0.175$ rad) obtained in the case of $\sigma_{RI} = 0.01$ corresponding to QPMs in (b). **(d)** Comparison among similarity metrics, normalized between 0 and 1. As reported in the legend, only TSI provides the right result, showing also a sharper extreme point than the other metrics. **(e)** Reference reconstruction obtained with the exact rolling angles. The scale bar is 5 μm. **(f)** Reconstruction obtained with the rolling angles calculated with TSI. **(g)** Reconstruction with wrong estimations of f_{180} obtained with SSIM, UIQI, and GMSD. **(h)** Reconstruction with wrong estimation of f_{180} obtained with SCC. In (f-h), the RMSE values with the reference in (e) are reported.

The overall accuracy for each metric is now reported and indicated as A. The accuracy is calculated as the ratio between the number of correct identifications and the total number of test cases, i.e., 180. The correct identification consists in determining the frame with cell rotation equal to 180° when $\Delta\theta = \{3°, 4°, 5°\}$ or the one with cell rotation closest to 180° for the other two rolling angle sets. The results are $A_{TSI} = 98.33$ %, $A_{SSIM} = 80.56$ %, $A_{GMSD} = 79.44$ %, $A_{UIQI} = 77.22$ % and $A_{SCC} = 67.78$ %. As it can be seen, TSI shows the best results. It fails only in 3 cases, related to higher noise levels. However, in such cases, the error amounts at ±1 frame. The other compared metrics show worse performances with the lowest accuracy reached by the SCC. One can expect this since the SCC has demonstrated to be efficient for non-spherical objects only [107].

It is important to underline that a wrong f_{180} estimation induces errors in any rolling angle and finally provokes artefacts in the tomographic reconstruction. To highlight such tomographic distortions, tomographic reconstructions have been performed from the simulated QPMs sequence in Figure 2.8(b) by using in Eq. (2.5) the rolling angles recovered by the considered similarity metrics and a sequence of y-positions fixed by exploiting the assumed proportionality between translation and rotation. In particular, it is assumed that the particle translates of one pixel for a rotation of 0.1°, accordingly to the microfluidic and recording conditions. Figure 2.8(e) illustrates the reference reconstruction in which the central slice is obtained by implementing the inverse RT through the FBP algorithm with the exact rolling angles. In Figure 2.8(f), the same reconstruction is reported, but obtained by using the rolling angles estimated by the TSI. The considered test case is the one leading to a 180.6° cell rotation. In this case, TSI estimates as 180° the actual 180.6° rotation. A Root Mean Square Error $\text{RMSE}_{\text{RI}} = 0.0007$ is obtained between the reference reconstruction and the reconstruction with recovered rolling angles. Finally, Figure 2.8(g) shows the same reconstruction as before, but obtained when the rotation is estimated by SSIM, GMSD or UIQI. Indeed, the latter three methods achieve the same estimate $f_{180} = 60$, as it can be inferred from Figure 2.8(d).

Similarly, Figure 2.8(h) displays the case when the rotation is evaluated by SCC for which $f_{180} = 58$. For both the considered reconstructions, lower and spreading RI values occur (see black arrows) as well as artefacts caused by the wrong estimations of f_{180} (violet arrows). $\mathrm{RMSE_{RI}}$ increases of one order of magnitude with respect to TSI.

In the experimental condition, the cell's rotation is sampled with an angular step that in general is not an exact divisor of 180°, therefore the cell's projection at which the exact 180° of rotation occurs is not acquired. As also investigated through the numerical cell phantom, this confirms the need of an accurate metric able to precisely identify the frame of the closest rolling angle with respect to 180°. In particular, the cell analysed in Figure 2.9(a-c) is the one reported in Figure 2.7(b), whose holographic tracking results have been shown in Figure 2.7(c). The second cell in Figure 2.9(d-f) is more spherical and it has been selected to show how similarity metrics work for real spherical objects. Also in this case, position drifts along x- and z-axes are very limited, resulting in σ_x = 0.13 μm and σ_z = 0.48 μm, i.e. the cell has quasi-constant positioning within the channel's cross section xz during the flow. The TSI curves are displayed in Figure 2.9(a,d), showing their global minima at the frames $f_{180} = 51$ and $f_{180} = 41$, respectively. Then, all the rolling angles are calculated through Eq. (2.5), thus obtaining that the highest cells orientations, corresponding to the rolling angles calculated at the last frames, are θ_K = 349.0° and θ_K = 356.1°, with $K = 102$ and $K = 81$, respectively. Moreover, in Figure 2.9(b,e), the acquired data are shown in the spectral domain. As the blue spectral lines of the polar plot corresponding to [0°,180°) do not coincide with the red spectral lines corresponding to [180°,360°), the latter acquisition, although being in principle equivalent to the former, is capable to complement [0°,180°), thus allowing better tomographic results. The reconstructed QPMs of the first frame of each sequence and the ones corresponding to the estimated 180° sample rotation are reported within Figure 2.9(a,d). Finally, tomographic reconstructions, obtained by using rolling angles sequences

calculated with the proposed method, are shown in Figure 2.9(c,f), in which the isotropy of the TPM-FC reconstruction can be inferred.

It is worth remarking that the proposed tracking-based rolling angles recovery method can be also applied in the case of the microfluidic channel with a rectangular cross section 200 μm × 1000 μm. In fact, in this case, the property of cell rotation around the sole x-axis is even more assured as, due to the larger width (i.e., 1000 μm) with respect to the height (i.e., 200 μm), the side walls of the channel contribute much less to the cell rotation around the z-axis with respect to a channel with square cross section.

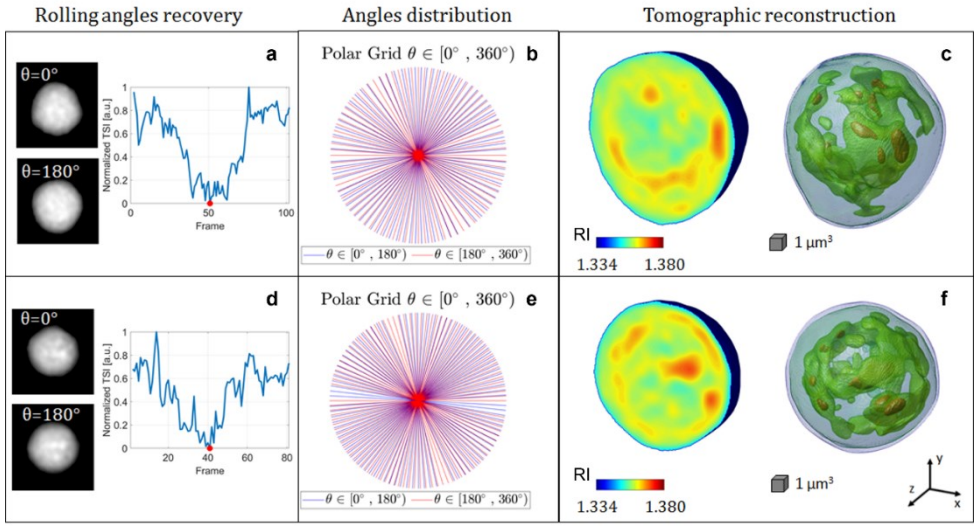

Figure 2.9 Tomographic reconstructions of a non-spherical (a-c) and a quasi-spherical (d-f) MCF7 cell.
(a,d) TSI-based recovery method to identify the f_{180} frame (red circles) and the corresponding QPMs at 0° and 180°. **(b,e)** Polar grid plot with the distribution of detected rolling angles in [0°,180°) (blue lines) and the distribution of detected rolling angles in [180°,360°) (red lines). **(c,f)** 3D slice-by-slice tomographic reconstructions (on the left) and corresponding iso-levels representations (on the right).

2.4.4 TPM-FC in High-Throughput Modality

Among the TPM techniques, TPM-FC is the only one that can potentially perform high-throughput recording and analysis thanks to the FC modulus. Even if other tomographic IFC systems have been proposed [181], the type of data that TPM-FC can collect is much more informative than conventional IFC (i.e., 3D, label-free, and quantitative). This means that reaching the high-throughput property is more challenging in a TPM-FC system with respect to an IFC one. In IFC, the recorded image can be directly analyzed after being collected, while, in TPM-FC, the recorded holograms must be firstly processed to extract the corresponding QPMs, recover the unknown rolling angles, and finally reconstruct the tomogram to analyze. For this reason, a fully automatic reconstruction code is requested, as described in Sections 2.4.2 and 2.4.3. Moreover, the holographic processing is time- and resource-consuming, therefore its speeding-up is strongly needed, as will be described in Section 3.1. Furthermore, in TPM-FC, each cell is represented by a 3D array instead of a 2D array as in conventional IFC, thus a problem of huge memory occupation exists. A strategy to perform a quasi-lossless tomographic compression will be proposed in Section 4.5. Finally, while in conventional IFC one single 2D image is recorded per cell, in TPM-FC tens or hundreds of holograms must be recorded per cell in order to reconstruct its 3D RI tomogram. For this reason, in principle the achievable throughput can be one or two orders of magnitude lower than IFC. However, in IFC, one cell at time must be imaged in its focal plane, thus the cells are made to flow in single file under focusing conditions. Instead, in TPM-FC, the 3D holographic particle tracking can be exploited to record more than one cell per frame while flowing in the same FOV. In this case, an upper bound must be fixed about the cell concentration as a too high value could produce mutual hydrodynamic interactions able to deform the cells or change their rotation, thus losing the tomographic condition. Here numerical fluid dynamic simulations have been combined to experimental TPM-FC data in order to model this problem and assess an upper bound of the potential throughput of the TPM-FC system [109].

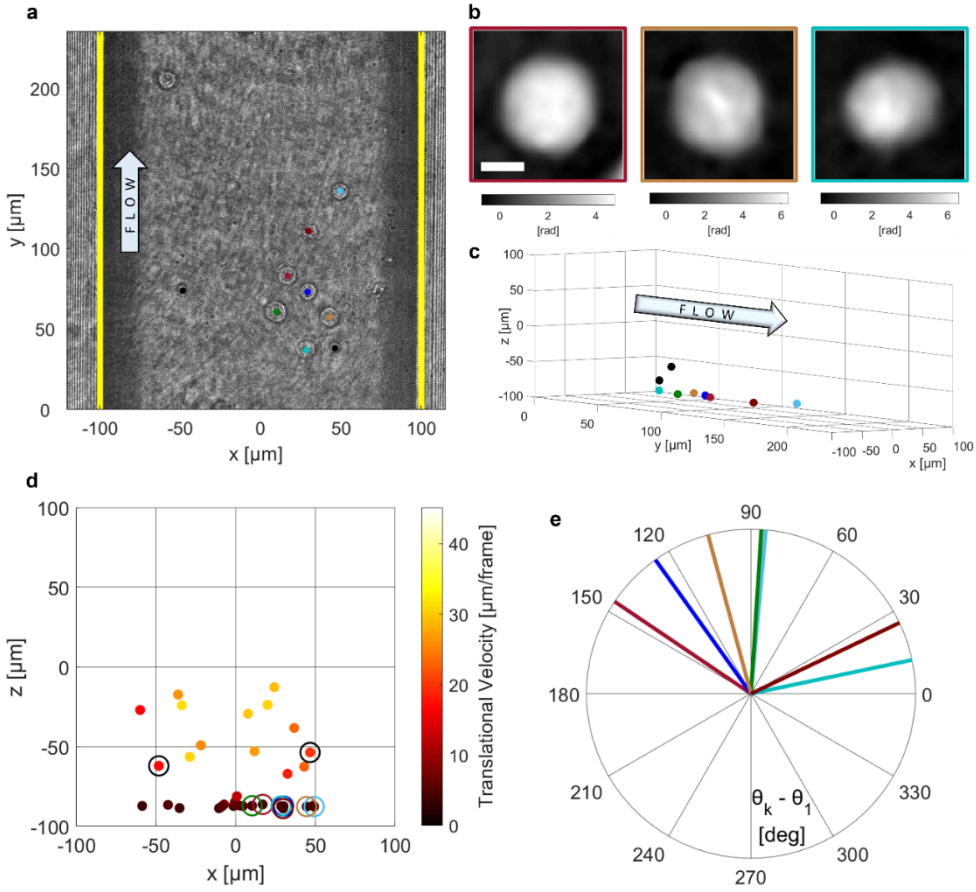

Figure 2.10 Experimental measurements of cells flowing and rolling in a microfluidic channel.
(a) Digital hologram taken from the recorded DH sequence, with highlighted the transversal positions of some flowing cells (dots). The yellow lines are the channel's edges. **(b)** QPMs of three cells in (a). The scale bar is 5 µm. **(c)** 3D positions inside the microfluid channel of the cells highlighted in (a). **(d)** Channel's cross section positions and translational velocities of 35 cells. The circles correspond to the cells highlighted in (a). **(e)** Rolling angles θ_k of the cells highlighted at the *k*-th frame in (a) by coloured dots, with respect to the rolling angles θ_1 at which each cell appears for the first time in the FOV (i.e., θ_1=0°).

At this aim, again the microfluidic channel with 200 µm × 200 µm cross section has been used but coupled to a 1024×1024 CCD camera and a 20× MO in order

to image also the channel's walls inside the FOV. In the TPM-FC experiment, ISK cells have been used, i.e. a well-differentiated endometrial cancer (EC) cell line. An example of 1024×1024 digital hologram taken from the recorded DH sequence is displayed in Figure 2.10(a), while the QPMs about some cells in the reported frame are shown in Figure 2.10(b). The 3D cell positions have been computed through the holographic tracking algorithm, as illustrated by the colored dots in Figure 2.10(a). It is worth noting that the QPMs are not informative when the cell is too far away from the holographic recording plane along the optical z-axis. Therefore, in such case, the x- and y-positions are estimated with lower accuracy directly from the digital holograms by assuming a uniform movement along the flow direction (black dots in Figure 2.10(a)). In order to study the flow properties by means of these experimental data, the x- and z-positions must be referred to the reference system of the microfluidic channel, while at this stage the x-positions refer to the holographic FOV and the z-positions refer to the holographic recording plane. To cope with this issue, the presence of the channel's edges within the imaged FOV has been exploited. In particular, the edges have been refocused through the TC method, thus obtaining the distance between the channel's bottom and the holographic recording plane as well as the x-positions of the channel's edges, highlighted in yellow in Figure 2.10(a). Hence, in Figure 2.10(c), the 3D positions of the cell localized in Figure 2.10(a) have been reported in the 3D space of the microfluidic channel.

As discussed in Section 2.4.3, the laminar flow inside the microchannel is characterized by a parabolic velocity profile within the channel's cross-section (i.e., the xz-plane). For this reason, cells are expected to move faster along the flow direction (i.e., the y-axis) the closer they are to the center of the channel with respect to both the x- and z-axis. This property is verified on average by the experimental measurements about the translational speeds of 35 cells reported in the channel's cross section displayed in Figure 2.10(d).

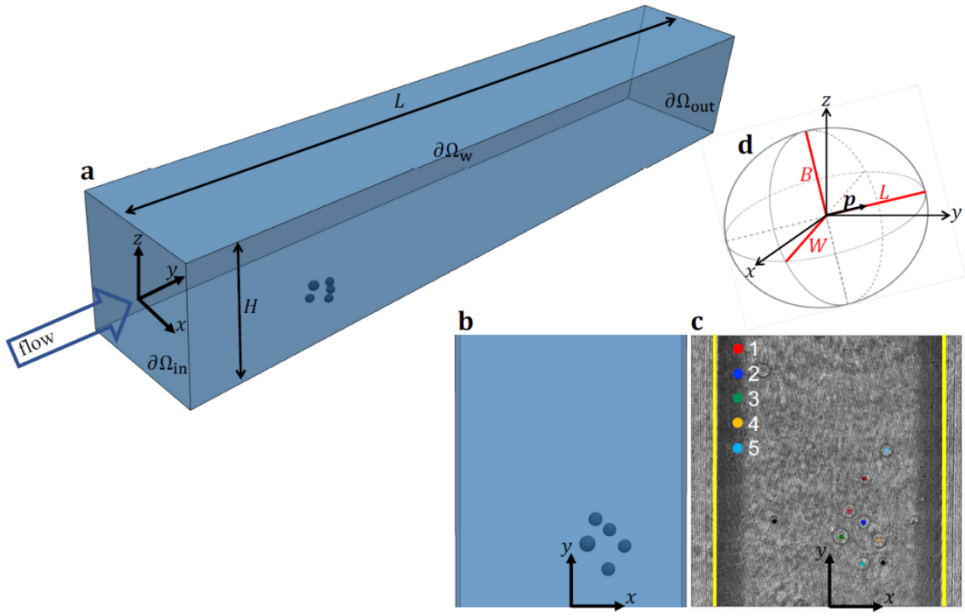

Figure 2.11 Fluid dynamic modellation of an axperimental test case.
(a) Scheme of the computational domain employed in the numerical simulations. **(b)** Top-view zoom-in with the 5 modelled cells flowing in (a). **(c)** Experimental digital hologram used to simulate the 5 cells in (a,b). **(d)** Scheme of a scalene ellipsoid highlighting the semiaxes L, B, W, and the orientation unit vector $\boldsymbol{p}$.

Table 1 Values of the volume and aspect ratio of the ellipsoidal particles considered in the numerical simulations.

Cell number	Volume [μm³]	L/B	L/W
1	1035.7	1.05	1.07
2	908.8	1.05	1.13
3	1618.6	1.07	1.10
4	916.2	1.12	1.18
5	957.7	1.07	1.17

In addition, as the holographic recording plane is near to the channel's bottom, the cells for which the QPMs can be reconstructed mainly rotate around the x-axis, since the gradient along the z-axis is greater than that along the x-axis. Their rolling angles have been retrieved by means of the tracking-based method described in Section 2.4.3 [108]. The rolling angles reached by the colored cells at the k-th frame imaged in Figure 2.10(a) are reported in Figure 2.10(e) with respect to the rolling angles at which each cell appears for the first time in the FOV, which has been arbitrarily set to 0°.

In order to assess whether adjacent cells flowing through a microfluidic channel can have an effect on each other during tomographic recordings, the worst case within the recorded holographic sequence has been selected, i.e. the most adjacent group of 5 cells reported in Figure 2.10(a). The computational domain reported in Figure 2.11(a) has been considered, namely, a portion of a squared cross-section microfluidic channel with side $H = 200$ μm. A saline solution carrying ISK cells is fed to the channel with a flow rate $Q = 1$ μL/min. In the simulations, the selected 5 cells (see Figure 2.11(a) and the top-view zoom in Figure 2.11(b)) are modelled as ellipsoidal elastic particles, whose semiaxes are computed by matching the optically measured values of the volume and the aspect ratios of the cells identified with numbers from 1 to 5 in Figure 2.11(c), which reports a frame taken from the experimental video (the same as in Figure 2.10(a)). Also cell initial relative positions mimic those shown in Figure 2.11(c). In Figure 2.11(d), a scheme of an arbitrarily oriented scalene ellipsoid is displayed, highlighting the semiaxes L, B, W, and the orientation unit vector $\boldsymbol{p}$, i.e., a unit vector identifying the orientation of the ellipsoid major semiaxis L, whereas in Table 1 they are reported the quantitative values of the volume and aspect ratio of the ellipsoidal particles considered in the numerical simulations. It is worth remarking that, since all the values of the aspect ratios L/B and L/W are quite close to 1, the cells are quasi-spherical.

The motion of the suspension carrying the cells is governed by the mass and momentum balance equations on both the cells and the suspending liquid.

Preliminarily, the Reynolds number is evaluated, measuring the relative importance of inertial and viscous forces, as

$$Re = \rho \bar{u} H / \eta, \tag{2.9}$$

with $\rho \sim 1000$ kg/m^3 the liquid density, $\bar{u} = Q/H^2 = 3.33 \times 10^{-4}$ m/s the liquid average velocity, $H = 2 \times 10^{-4}$ m the channel characteristic dimension, and $\eta \sim 10^{-3}$ Pa s the liquid viscosity. Since Re is in the order of 10^{-2}, inertial effects are neglected. Furthermore, let assume that both the phases are incompressible, thus the mass and momentum balance equations read

$$\begin{aligned} \boldsymbol{\nabla} \cdot \boldsymbol{u} &= 0 \\ \boldsymbol{\nabla} \cdot \boldsymbol{T} &= 0' \end{aligned} \tag{2.10}$$

with $\boldsymbol{u}$ the velocity vector and $\boldsymbol{T}$ the stress tensor. According to the Newtonian constitutive equation, in the suspending medium it can be written

$$\boldsymbol{T} = -p\boldsymbol{I} + 2\eta \boldsymbol{D}, \tag{2.11}$$

with p the pressure, $\boldsymbol{I}$ the identity tensor, and $\boldsymbol{D} = (\boldsymbol{\nabla u} + \boldsymbol{\nabla u}^{\mathrm{T}})/2$ the symmetric part of the velocity gradient tensor. Concerning the cells, let assume they obey the neo-Hookean constitutive equation, thus

$$\boldsymbol{T} = -p\boldsymbol{I} + \boldsymbol{\tau}, \tag{2.12}$$

where $\boldsymbol{\tau}$ is the extra-stress tensor, for which the neo-Hookean constitutive equation reads

$$\overset{\nabla}{\boldsymbol{\tau}} = 2G\boldsymbol{D}, \tag{2.13}$$

with $\overset{\nabla}{\boldsymbol{\tau}} = D\boldsymbol{\tau}/Dt + \boldsymbol{\nabla u}^{\mathrm{T}} \cdot \boldsymbol{\tau} + \boldsymbol{\tau} \cdot \boldsymbol{\nabla u}$ the so-called upper-convected time derivative and G the shear elastic modulus of the material. In the presented simulations, $G = 0.9$ kPa is considered as a characteristic value for ISK cells [182]. The balance equations describing the system are supplied with the following boundary conditions

$$\boldsymbol{u}|_{\partial\Omega_{\mathrm{w}}} = \boldsymbol{0}, \tag{2.14}$$

$$\boldsymbol{u}|_{\partial\Omega_{\mathrm{in}}} = \boldsymbol{u}|_{\partial\Omega_{\mathrm{out}}}, \tag{2.15}$$

(2.16) $$-(\boldsymbol{T}\cdot\boldsymbol{n})|_{\partial\Omega_{\mathrm{in}}}=(\boldsymbol{T}\cdot\boldsymbol{n}-\Delta p\boldsymbol{n})|_{\partial\Omega_{\mathrm{out}}}.$$

The Eq. (2.14) expresses the no-slip and no-penetration conditions for the liquid velocity on the channel wall $\partial\Omega_{\mathrm{w}}$, whereas Eq. (2.15) and Eq. (2.16) express the periodicity of velocity and traction in the suspending liquid between the channel inlet $\partial\Omega_{\mathrm{in}}$ and the outlet $\partial\Omega_{\mathrm{out}}$, with Δp the pressure drop between the two sections (to be computed) and $\boldsymbol{n}$ the outwardly directed unit vector normal to the boundary. The periodicity condition means that the computational domain is part of a channel that repeats indefinitely along the flow direction y. Of course, this means that the actual length L of the computational domain must be chosen such that the 5 cells hydrodynamically interact among them but do not feel their periodic images along y. This is verified for $L=1.2$ mm. At the channel inlet, the flow rate of the suspending liquid $Q=1$ μL/min is imposed as

(2.17) $$-\int_{\partial\Omega_{\mathrm{in}}}\boldsymbol{u}\cdot\boldsymbol{n}=Q.$$

The boundary conditions on each interface between the suspending medium and a cell are the continuity of velocity and traction across the interface. Since both the cells and the suspending medium are inertialess, no initial conditions on the velocities are required. Only an initial condition for the extra-stress in the cells needs to be specified, and the cells are assumed to be initially stress-free, i.e.

(2.18) $$\boldsymbol{\tau}|_{t=0}=\boldsymbol{0}.$$

Finally, it is worth mentioning that all the results reported and discussed below refer to an initial orientation of the cells such that $\boldsymbol{p}_0=\{\sqrt{3}/3,\sqrt{3}/3,\sqrt{3}/3\}$, yet other values of $\boldsymbol{p}_0$ have been considered, showing no significant effects neither on cell dynamics nor on the quantitative values of the results shown in what follows. The equations reported above are solved with the arbitrary Lagrangian Eulerian (ALE) finite element method (FEM) using well-known stabilization techniques, such as SUPG and log-conformation [183]. Both the matrix fluid and the suspended particles are discretized by a mesh

made of quadratic tetrahedra. During the simulations, the elements of the mesh progressively deform because of cell deformation, rotation, and translation in the channel. Any time the quality of the mesh elements in the computational domain becomes unacceptable in terms of a threshold, a remeshing is performed and the solution is projected from the old mesh to the new one [184] [185]. For the reported simulations, a mesh with about 2.5×10^4 tetrahedra and a time-step of 0.01 s has been found to be adequate. The simulations have been performed through the commercial software COMSOL Multiphysics™ V5.5 on 2 cores of a DELL Power Edge M710HD blade with 2 Intel Xeon E5649 hexacore processors @ 2.53 GHz and 48 GB of RAM, yielding a computational time of about 2 days.

In Figure 2.12(a), the trajectories along the y flow direction of the 5 cells highlighted in Figure 2.11(c) are reported. The solid lines refer to the results of the numerical simulations, whereas the symbols represent the experimental data. The initial y-position of cell 5, $y_{\mathrm{P5},0}$, namely, the position of such cell when it appears in the experimental observation window, is taken as a reference, so the values on the vertical axis are computed as a difference with respect to $y_{\mathrm{P5},0}$. Each data set is characterised by a colour referring to the colour code in Figure 2.11(c). By comparing the numerical and the experimental results, a fair quantitative agreement can be observed, thus the cell model adopted in numerical simulations, based on ellipsoidal particles with shapes, dimensions, and mechanical properties chosen as illustrated above, describes quite effectively the actual behavior of the cells observed in the experiments, including their hydrodynamic interactions. In Figure 2.12(b-f), the history of the z-positions of the cells under investigation is illustrated. In this case, it is apparent that the experimental data are affected by a larger uncertainty. In fact, the symbols are quite scattered and do not arrange along a smooth curve (the thin solid lines connecting them have the scope of guiding the eye). On the other hand, the numerical results follow trends showing either a slight increase or a decrease of the cell vertical position, which can be attributed to the hydrodynamic interactions among the particles.

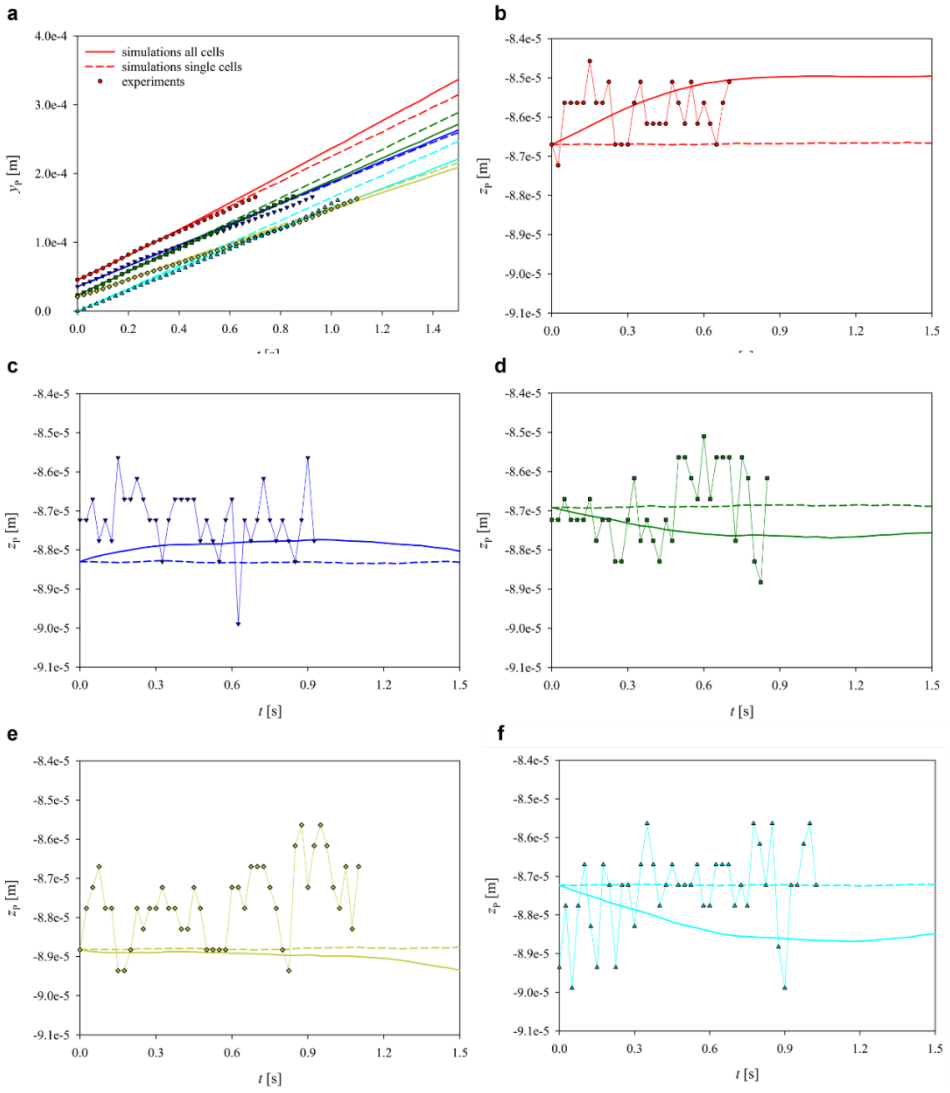

Figure 2.12 Temporal histories of the positions of the 5 cells highlighted in Figure 2.11(c) computed through numerical simulations in the presence (solid lines) and in the absence (dashed lines) of the other cells, and experiments (symbols).
(a) Cell y-positions. All the values are computed with reference to the initial y-position of cell 5, $y_{P5,0}$. **(b-f)** Cell z-positions. The colour of each data set refers to the colour code in Figure 2.11(c).

In addition, it can be observed that, unlike Figure 2.12(a), the initial z_P-values considered in numerical simulations do not match the initial experimental values. Indeed, given the uncertainty on cell vertical positions, the numerical initial z_P-values are searched in the range of the experimentally observed ones that could yield a satisfactory agreement on the y_P-data shown in Figure 2.12(a). To evaluate the effects of hydrodynamic interactions on cell dynamics, numerical simulations of the behavior of cells 1 to 5 have been performed in the absence of the others, keeping the same geometrical and constitutive parameters used in the complete simulation. The dashed lines in Figure 2.12 report the results of such simulations. Regarding the motion along the flow direction (see Figure 2.12(a)), two comments can be made. On the one hand, there are some quantitative differences between the trajectories of the cells with and without the other ones. In particular, cell 1 is slightly slower when it is alone, i.e., hydrodynamic interactions push it forward along the flow direction, whereas cells 2 and 5 are slightly faster when the other cells are absent, i.e., hydrodynamic interactions slow them down along the flow direction, and cells 3 and 4 show almost no difference between the two cases. On the other hand, the observed differences are moderate, thus the hydrodynamic interactions arising in the complete system do not alter cell translational dynamics dramatically. Regarding cell motion in the vertical direction (see Figure 2.12(b-f)), it is apparent that, when the particles are isolated, there is no displacement along such direction. Indeed, in the absence of hydrodynamic interactions, the portion of the channel under investigation is too short to observe lateral migration towards the channel centerline in the given flow conditions [186]. Finally, it is worth mentioning that cell displacement in the transversal x-direction is substantially irrelevant both in the experimental and in the numerical case, thus it is not reported here for brevity. In Figure 2.13, the simulated orientational dynamics of the cells are reported when they are considered all together (solid lines) and one by one (dashed lines). In particular, the y-component of the orientation unit vector $\boldsymbol{p}$ is shown in Figure 2.13(a), whereas its z-component is shown in Figure

2.13(b) (the x-component is not reported as it automatically comes from the condition that the magnitude of $\boldsymbol{p}$ is equal to 1). As it is apparent, all the curves start from $\sqrt{3}/3$, since $\boldsymbol{p}_0 = \{\sqrt{3}/3, \sqrt{3}/3, \sqrt{3}/3\}$ for all the cells, yet there are no significant effects on the cell rotational velocity when different $\boldsymbol{p}_0$-values are considered. Two main observations can be made by looking at Figure 2.13. First, all the cells perform more than one complete rotation in the imaged FOV, during which they displace less than 200 μm in the flow direction (see Figure 2.12(a)). This is also consistent with the experimental observation that, within the y-axis FOV of 235 μm, the necessary full cell rotation is obtained. Moreover, it is worth mentioning that, given the cell mechanical properties and the flow conditions considered in the simulations, cell deformation is completely negligible, so no deformation effects are expected to affect the tomographic reconstruction of the cells. Second, by comparing for each cell the solid line with the corresponding dashed one, it can be observed that, even if hydrodynamic interactions have a quantitative effect on cell rotational behavior, cells are still able to perform a complete rotation within the observation window.

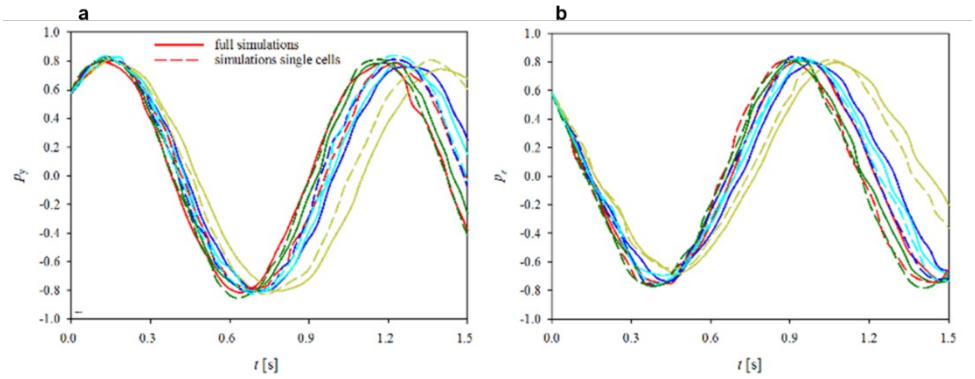

Figure 2.13 Temporal histories of components of the orientation unit vector $\boldsymbol{p}$ for the 5 cells highlighted in Figure 2.11(c) computed through numerical simulations in the presence (solid lines) and in the absence (dashed lines) of the other cells.
(a) Cell y-components. **(b)** Cell z-components.The colour of each data set refers to the colour code in Figure 2.11(c).

This means that, despite the spatial proximity, it is possible to reconstruct the 3D RI tomograms of the analysed 5 cells, as indeed displayed in Figure 2.14. At this aim, the FBP algorithm has been employed. For this reason, the throughput of the tomographic measurement can be increased by analyzing more cells simultaneously. In particular, the xy-section of the microfluid channel imaged by the employed DH microscope measures 200 μm × 235 μm. By cropping a central region of analysis of size 160 μm × 215 μm and by considering that, in the studied worst case, 5 cells occupy a region of size 60 μm × 60 μm, the throughput of the system can be increased up to 50 cells per frame, which means that up to 30 tomograms per second can be recorded inside an active area of 160 μm × 215 μm since each cell takes on average 40-45 s to cross the FOV. It is important to note that, for the tested flow rate, the results of numerical simulation do not report mechanical deformation of the cells. This means that the high throughput could be further potentially improved by increasing the flow rate. In fact, to reconstruct the tomogram, a single full rotation is enough, while in the presented experiments, cells experience on average 1.5 rotations. Hence, by setting the right flow rate, cells could take 25-30s to undergo a full rotation inside the imaged FOV, thus leading to an upper bound of 50-60 tomograms per second. At the same time, a larger FOV can be designed in order to further increase the throughput. For example, in the TPM-FC system in Figure 2.5, a very large FOV of 640×640 μm^2 has been reached. Of course, other more efficient microfluidic solutions can be investigated at the aim of fulfilling the high-throughput need. Among them, the inertial focusing in microfluidics [187] can be exploited to force the cells to enter in the microfluidic channel in a precise and known position, thus controlling exactly the cell flow and rotation. In fact, in this solution, cells would flow and rotate in single file at controlled velocities, thus matching the best condition for obtaining a unique full rotation of the cell in the imaged FOV in the shortest possible time by avoiding cell deformation. Moreover, this solution would extremely simplify, speed up and make more accurate the overall processing for the tomographic reconstruction, from the cell

detection/tracking to the rolling angles estimation. Finally, the very large FOV (i.e., 640 μm × 640 μm) could be exploited in an optimized way to create parallel tracks for the cell roto-translation by means of parallel inertial focusing [187], thus filling the gap with conventional IFC in terms of throughput.

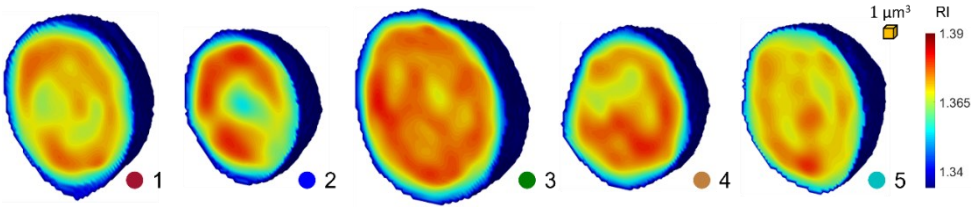

Figure 2.14 TPM-FC reconstructions at high concentrations.
Central slice of the 3D RI tomograms of the 5 adjacent cells in Figure 2.11(c).

CHAPTER

3 Artificial Intelligence for Single-Cell Analysis in TPM-FC

A cell's phenotype is the culmination of several cellular processes through a complex network of molecular interactions that ultimately can result in a unique morphological signature [188]. Visual cell phenotyping is the characterization and quantification of these observable cellular traits in images. Microscopy has become a fundamental tool for cell biology because it overcame the limitations of the human eye and allowed to observe single cells in their microenvironments. However, advanced single-cell analysis based on visual cell phenotyping often involves multistep workflows challenging to those who are not computational experts [136]. Therefore, momentum to enable a broader group of biomedical researchers and clinicians to carry out complex and automatic single-cell analyses is growing. A revolution in the biophysical cytometry has been introduced by AI [189]. In particular, AI has been demonstrated fitting perfectly to IFC as each of these two techniques takes advantage from the other's capabilities [190]. In fact, AI requires a large number of informative examples for training a model and IFC can quickly produce millions of single-cell images. The combination between AI and IFC has opened up new avenues for innovation across a wide variety of high-throughput cell biology applications, which are moving toward well-defined protocols for the final clinical approval [191]. A remarkable boosting of the AI-based cell phenotyping has been recently provided by QPI, thanks to the wealth of label-free biophysical information that can be measured in the QPM of a single cell [192]. For example, hematologic disorders have been diagnosed

[193] [194] [195], infectious like COVID-19 have been detected [196] [197], and the cell cycle stages [198] and the cell states [199] have been classified. Further biomedical applications based on HIFC include the classification of 3-part leukocytes [200], human PBMCs and leukemic cells [141], healthy and pathological leukocytes [201], healthy and cancer cells [155] [202] [203], as well as the detection of RBCs infected by P. falciparum [204] and cancer cells in blood [205] [206], and the assessment of the drug resistance in cancer cells [207]. Very recently, the use of AI has started to be investigated also in the 3D case of static TPM [208] [209]. However, despite these important advantages, DHM-based systems are not as widely used as other microscopy modalities, such as brightfield or fluorescence microscopes, mainly because a heavy holographic processing, time and resource-consuming, must be implemented in order to retrieve the phase information. Therefore, in recent years, AI has been exploited not only for solving automatic classification problems with high accuracy in the DHM world, but also to greatly lighten the computational time and the hardware resource requested by the holographic processing [210] [211], which is highly demanded for LOC implementations [212].

In this Chapter, AI-based applications herein developed for the single-cell analysis in the TPM-FC field are described. After presenting a DL approach proposed here for speeding up the holographic processing for TPM-FC [213], several classification problems are solved in three different scenarios. In particular, DL is exploited to identify cancer cells directly from the holographic diffraction patterns recorded in FC mode [214]. Then, phenotyping of flowing cancer cells is performed by means of ML through the fractal characterization of their phase signature [215] [216]. Finally, a ML tool for recognizing the drug resistance in cancer cells is fed for the first time by features extracted from the tomograms [217].

3.1 Speeding up the Holographic Processing

In Section 2.4, the TPM-FC paradigm has been introduced and its promising features have been highlighted with respect to conventional TPM, with particular focus on the possibility of reconstructing the 3D RI tomograms of single cells at high-throughput. At this aim, an automatic processing has been implemented to reconstruct tomographic data from the holographic recording (see Section 2.4.2). However, to reach the high-throughput property, a very large number of digital holograms has to be recorded, thus the numerical holographic reconstruction process becomes the bottleneck that prevents reliable and exploitable applications at LOC scale due to the demanding algorithms and the huge computational time. Depending on the hologram size (i.e., the number of pixels of the sensor camera) and the imaging configuration (i.e., in-line or off-axis), the entire processing pipeline to reconstruct one single QPM from the recorded digital hologram can take minutes on a basic desktop computer. To cope with this computational limitation, recently, DCNNs have been employed to speed up the holographic processing pipeline [210] [218]. In particular, the numerical refocusing step is addressed as a DCNN-based in-focus distance regression problem [219] [220], or through DCNNs for classification [221]. The phase aberration compensation has been solved by using a simplified version of the U-Net model for the background detection and subtraction [222]. Instead, DCNNs inspired by the ResNet model have been employed for both the automatic phase aberration compensation [223] and phase unwrapping process [224]. Recently, by suitably adapting the encoder-decoder models, it has been demonstrated that the entire holographic reconstruction process can be skipped, thus enabling the direct reconstruction from raw holograms without any prior knowledge about the imaging parameters [225] [226] [227] [228] [229]. Despite the remarkable results achieved in these works in terms of the accuracy for recovering the QPMs from digital holograms, such DCNN architectures usually employ tens of millions of learnable parameters and need a remarkable amount of memory to store

them. Instead, here, for the first time in DHM, the multi-scale context aggregation network (CAN) [230] [231] is proposed at the aim of speeding up the numerical holographic processing for TPM-FC [213]. At this purpose, the TPM-FC system in Figure 2.5 has been employed for experiments of fibroblast cells of the NIH-3T3 cell line. As detailed in Figure 2.6(a), the overall conventional holographic processing to obtain the unwrapped QPM from the recorded digital hologram takes about 7.71 s by using an Intel® Core™ i9-9900K CPU with a 64Gb RAM through the Matlab® 2021a environment. This time must be multiplied for the hundreds of digital holograms needed to be processed to obtain the 3D tomograms of one single cell, thus strongly limiting the high-throughput feature. To cope with this issue, the CAN architecture sketched in Figure 3.1 has been trained as end-to-end DCNN to reconstruct an unwrapped QPM from the corresponding recorded digital hologram [213].

The CAN is a fully convolutional network as the resolution of the input (i.e., $M \times M$) is not changed throughout the layers of the network up to the output layer. The network has a depth $d = 8$ and all the convolutional layers CL_S, with $1 \leq S \leq d$, have a width w. In particular, the layers CL_S, with $1 \leq S \leq d-1$, are based on w 3×3 kernels and are followed by a Leaky ReLU nonlinearity, while the last layer CL_d employs w 1×1 kernels with no nonlinearity. Let x_S be the output of a convolutional layer CL_S, with $1 \leq S \leq d-1$. The input y_S of the successive Leaky ReLU layer is computed through an adaptive normalization process as follows

$$y_S = \lambda_S x_S + \mu_S BN(x_S), \tag{3.1}$$

where BN is the batch normalization operator and $\lambda_S, \mu_S \in \mathcal{R}$ are learnable scalar weights. Thanks to the adaptive normalization step, the batch normalization layer is strengthened and the overall model can better approximate the phase retrieval operator. More important, the fully-resolution intermediate layers allow aggregating the global context of the input image through a multi-scale analysis due to the several dilation factors r_S of the convolutional layers CL_S.

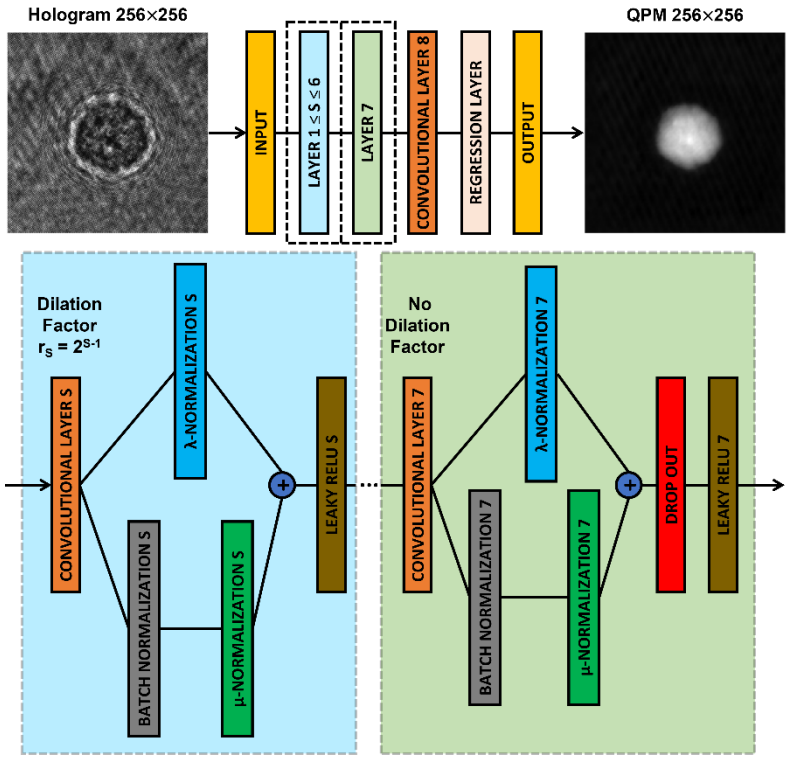

Figure 3.1 CAN model.
Sketch of the CAN architecture for the end-to-end prediction of the QPM from the recorded digital hologram. The Layers 1-7 are zoomed in the dotted boxes.

In particular, the dilation factor r_S increases as 2^{S-1} for $S = 1, \dots, d-2$, while the layer CL_{d-1} has no dilation. Hence, the receptive field expands exponentially with the network's depth, thus including the multi-scale global context despite the compactness of the CAN architecture. In fact, the number of learnable parameters of the model with the described configuration is very low with respect to the tens of millions of parameters of the classical encoder-decoder networks like the U-Net. Furthermore, the network requests a small memory during the forward step because there are no skip connections across non-consecutive layers. For these reasons, the CAN model is expected to be accurate (due to aggregation of the multi-scale global context), fast (due to the

compactness of the architecture), and particularly suited for on board computing (due to the small memory requested) [230]. Of course, these three properties depend on the setting of the width w and the input size M. In Table 2, the comparison among different network configurations has been reported to identify a suitable trade-off. In fact, the memory occupation increases with the width w, while the prediction time increases with both the width w and the input size M. Obviously, the smallest and fastest configuration is $w = 32$ and $M = 64$, which allows reaching a video-rate QPM prediction with a 214 kB memory occupation. However, as shown in Figure 2.5(c), the whole cell information is contained in a 384×384 ROI, which means that a down sampling up to 64×64 leads to an excessive loss of resolution. On the other hand, the most accurate configuration is $w = 128$ and $M = 512$, which however requires megabytes for the memory occupation and seconds for the QPM prediction. Therefore, an intermediate configuration is more suitable in respect to the proposed TPM-FC recording system. In fact, $w = 64$ and $M = 256$ have been chosen, since they allow computing a QPM in 168 ms by occupying only 818 kB of memory (due to just 223183 parameters) with a negligible resolution loss with respect to the original ROI size.

Table 2 Comparison among different CAN configurations. Prediction times (in milliseconds) obtained by varying the width w (and then the memory occupation) and the input size M. The selected configuration is highlighted in green.

	w = 32 214 kB	**w = 64 818 kB**	**w = 128 3231 kB**
M = 64	36	43	57
M = 128	49	69	36
M = 256	94	168	333
M = 512	258	547	1207

The dataset for training the neural network has been created by considering the NIH-3T3 fibroblast cell line. For multiple flowing cells, hundreds of 5120×5120 holograms have been recorded. For each cell within the FOV, a 384×384 ROI has been cropped from the recorded hologram around the cell to preserve all the diffraction information useful for the autofocusing operator, as shown in Figure 2.5(c). Hence, the corresponding QPM has been computed through the conventional holographic processing. Then, the hologram and the corresponding QPM have been resized to 256×256, thus becoming the input and the target of the network, respectively. In particular, the training set and the validation set have been created by randomly selecting respectively 4000 and 1000 images from 100 flowing and rotating cells. To train the network, some hyperparameters have been tuned. In particular, the Leaky ReLU coefficient has been set to 0.2, and a Dropout operation has been added to the Layer 7 with 0.5 factor to improve the generalization property of the network. Moreover, a mini-batch with 100 observations has been used. Finally, the ADAM optimizer has been employed to learn the parameters by minimizing the Mean Absolute Error (MAE) computed as follows by the final Regression Layer

$$MAE = \frac{1}{K}\sum_k \frac{1}{P}\sum_p \left| z_{k,p} - \hat{z}_{k,p} \right|, \tag{3.2}$$

where K is the number of observations in the mini-batch, P is the number of pixels p in an image, z is an output image, and $\hat{z}$ is the corresponding target image. It is worth noting that, in addition to the input size M and the width w, performances of CAN also depend on the setting of the depth d. To select the best d, a mini-training of the network has been repeated at different depth values, i.e. the training of the network realized for 50 epochs with a quarter of the overall dataset and a mini-batch made of 25 observations. The original CAN architecture was demonstrated to obtain the best results with $d = 9$ in approximating image processing operators [230]. Instead, in the presented phase retrieval problem, $d = 8$ has been fixed in order to avoid the too large dilation factor $r_7 = 64$ (instead of the maximum $r_6 = 32$ in the $d = 8$ case) that

could have caused an excessive smoothing of the QPM output at the cost of even more parameters.

The CAN model has been trained for 100 epochs by using the aforementioned desktop computer. The training step has required about 92h. However, as shown in Figure 3.2(a), the loss function curves of both the training and validation sets drop quickly after a few epochs, and they saturate around the 50th epoch. Therefore, the training time can be safely halved. The correctness in the QPM restoration has been evaluated by computing the SSIM between the target QPM and the predicted QPM reported at the original 384 × 384 size.

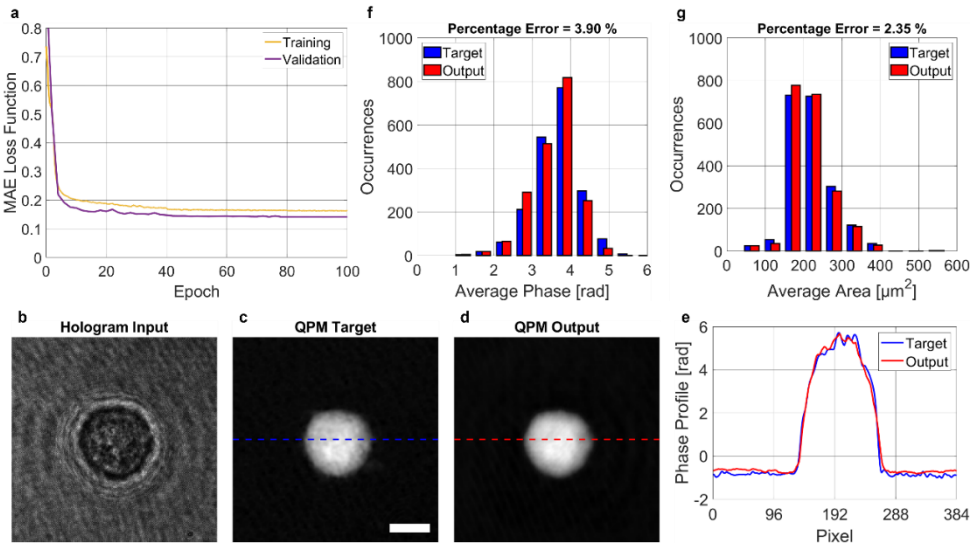

Figure 3.2 Assessment of the QPM reconstruction by DL.
(a) MAE loss function computed at different epochs from the training set (yellow) and the validation set (violet). **(b-d)** Input, target, and output, respectively, of the trained CAN model containing a test cell. The SSIM between the target and the output is 0.961. The scale bar is 10 μm. **(e)** Phase profiles of the QPM target (blue) and QPM output (red) selected from the lines highlighted in (c,d), respectively. **(f,g)** Comparison between the histograms of the average phase and the average area, respectively, computed from the QPM targets (blue) and the QPMs outputs (red) of each cell belonging to the test set. The percentage error between the measured features is reported at the top.

In particular, the trained CAN model allows reaching a 0.962 ± 0.013 accuracy measured over the 4000 images of the training set and a 0.961 ± 0.015 accuracy measured for the 1000 images of the validation set. Moreover, a test set has been created by randomly selecting other 2000 images (not used to feed the network during the training step), achieving 0.961 ± 0.013 of accuracy, thus indicating the substantial capability of generalization of this network. In Figure 3.2(b-d), an observation belonging to the test set is shown, made of the input (i.e., the holographic ROI), the target (i.e., the QPM obtained by the standard processing), and the output (i.e., the QPM computed by the network), respectively, in which an average SSIM of 0.961 is obtained.

Beyond the numerical assessment of the regression performance, a comparison between phase profiles is also reported in Figure 3.2(e). This clearly shows the proficiency of the CAN in the realm of DHM to preserve not only the mere cell morphology, but also the quantitative content of its 2D phase-contrast map. It is worth to remark that such process is also very fast. In fact, the trained model takes about 0.17 seconds to get the unwrapped QPM from the hologram, which is 45 times faster than the conventional holographic processing. This property is crucial in FC systems, since it allows analyzing a much larger number of cells in the same time-period, thus enabling statistically relevant studies about specific cell populations. In fact, from the QPMs, 2D label-free features can be measured for diagnostic purposes. As a consequence, a further way to validate the proposed architecture consists in checking whether the QPM outputs lead to the same features that would be measured from the corresponding QPM targets. To this aim, the 2000 cells belonging to the test set have been segmented from the background within the QPMs. The average phase and the average area have been computed for each cell in both the target and the output cases, which corresponding histograms are compared in Figure 3.2(f,g), respectively. To quantify the matching between the histograms, the percentage error has been computed as follows

$$Err = 100\,\frac{1}{N}\sum_{i=1}^{N}\left|\frac{f_i-\hat{f}_i}{\hat{f}_i}\right|, \tag{3.3}$$

where N is the number of observation, f is a feature computed from the output image, and $\hat{f}_i$ is the same feature computed from the corresponding target image. In the case of the average cell phase, a 3.90% error is obtained, while in the case of the average cell area, a 2.35% error is obtained.

In order to further assess the performances of the CAN architecture in correctly reconstructing the QPM, in Figure 3.3 some particular cases are shown in which the network works surprisingly well, thus supporting its generalization property. In fact, the model has been trained by using single live spherical-like cells centered in their ROIs, as displayed in Figure 3.2(b-d).

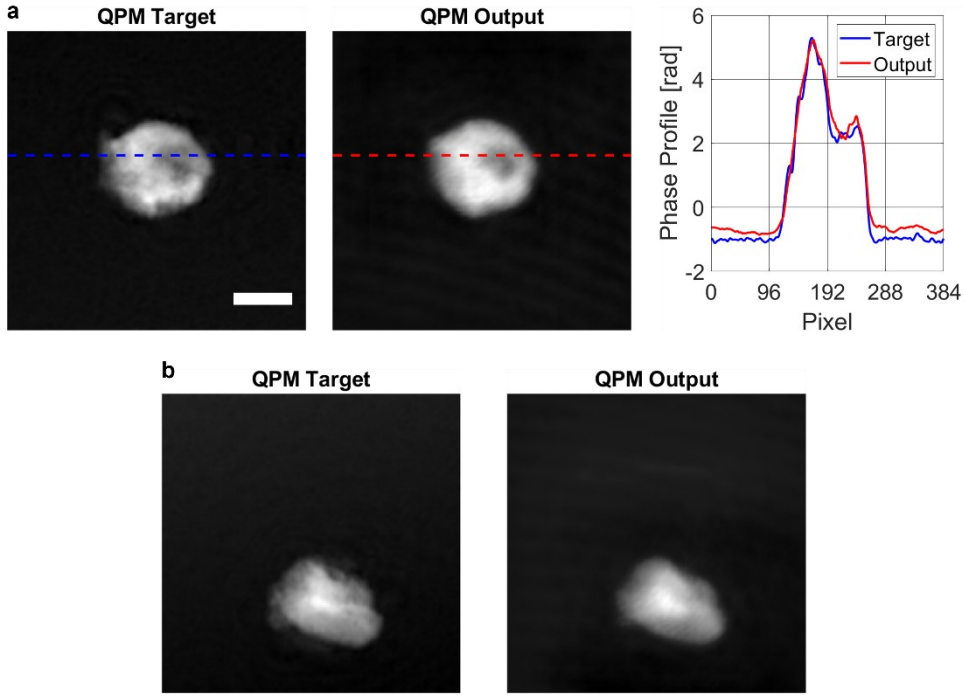

Figure 3.3 Assessment of the CAN performances in some particular cases. **(a)** QPM target and QPM output of a dead cell, with the phase profile corresponding to the highlighted lines. **(b)** QPM target and QPM output of a distorted cell, not centered in its ROI. The scale bar is 10 μm.

An example is reported in Figure 3.3(a), in which the QPMs of a dead cell are shown after reconstruction with the conventional method and the proposed one. A healthy cell has a convex phase profile, while a dead cell loses its content, thus resulting in an internal phase concavity [32]. The phase profiles plotted in Figure 3.3(a) highlight that the network prediction is accurate in reproducing also the phase concavity, even though the network model had never received this kind of image as an example during the training step. Moreover, as the cells are suspended in the microfluidic flow, they usually have a spherical shape. However, when the cell suffers a stress condition, it could exhibit a distorted shape, and the reconstruction architecture should be able to reproduce it in order to be reliable for diagnostics. Remarkably, also in this case the network correctly predicts the QPM, as shown in Figure 3.3(b). It is worth remarking that, besides being not spheroid-like shaped, the cell in Figure 3.3(b) is not centered in its ROI, unlike all the cells used in the training set. The highlighted special cases, in addition to the results reported in Figure 3.2, underline that the network has learned the right mathematical operator that converts a hologram into the corresponding QPM.

To test the potentiality of the proposed network in the TPM-FC framework, 65 tomograms have been reconstructed by using both the standard and the DCNN-based approaches to recover the QPMs. In particular, 65 cells correspond to 14462 recorded holograms, whose QPM retrieval takes about 31 hours by using the standard processing and only 41 minutes by exploiting the CAN model, i.e. the CAN inference can do the same task using only the 2% of the time required to the conventional method. In Figure 3.4(a), the central slices of the 3D RI tomograms of the same cell are displayed, respectively reconstructed from the QPMs obtained in the standard processing modality and through the proposed network. A great similarity has been reached, as also underlined by the good agreement between the RI profiles reported in Figure 3.4(b). A further proof is the high symmetry of the corresponding RI violin histogram in Figure 3.4(c), corresponding to an SSIM = 0.997 computed between the two tomograms.

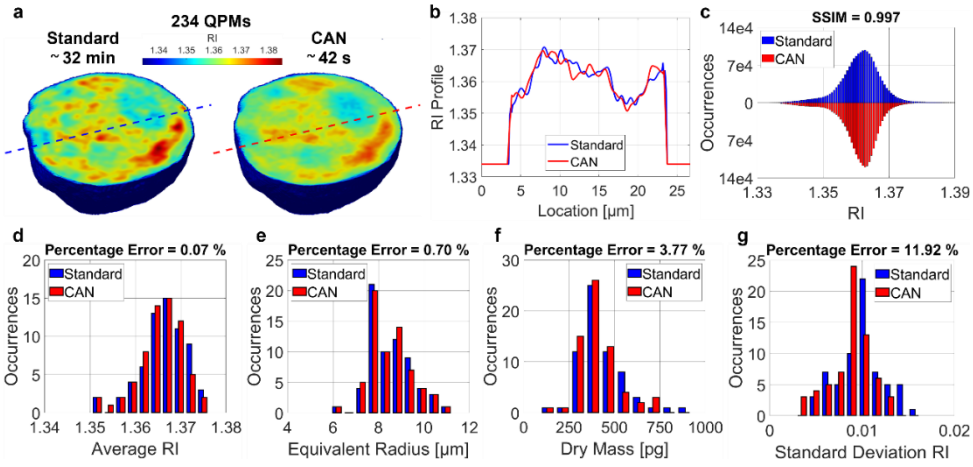

Figure 3.4 Assessment of the tomographic reconstruction by DL.
(a) Central slice of the 3D RI tomogram reconstructed from 234 QPMs retrieved (on the left) in the standard way in about 32 min and (on the right) by the CAN model in about 42 s. **(b)** RI profile corresponding to the lines highlighted in (a) from the standard tomogram (blue) and the CAN tomogram (red). **(c)** Violin histogram of the 3D RI distribution about the standard tomogram (blue) and the CAN tomogram (red) in (a), which SSIM is reported at the top. **(d-g)** Comparison between the histograms of the average RI, the equivalent radius, the dry mass, and the standard deviation RI, respectively, computed from 65 standard tomograms (blue) and CAN tomograms (red). The percentage error between the measured features is reported at the top.

As well as in the 2D case, also in the 3D case it is important to preserve the truthfulness of the statistical measurements, especially their adherence to the quantitative ground-truth. To this aim, the histograms of the average RI and the equivalent radius (i.e., the radius of a sphere having the same volume of the analysed cell) calculated for the 65 reconstructed tomograms are reported in Figure 3.4(d,e), where a 0.07% and a 0.70% percentage errors are obtained, respectively. An important quantitative feature that can be inferred from the 3D RI tomogram is the dry mass, obtained by multiplying the dry mass density defined in Eq. (1.48) to the cell volume. The dry mass can be considered a bioindicator of the health state of the cell as it is related to its biophysical properties. Therefore, the fast and accurate quantification of the dry mass for

a large number of cells could encourage further developments of diagnostic applications in biomedicine based on TPM-FC [5]. For this reason, the low percentage error of 3.77% obtained in the case of the dry mass reported in Figure 3.4(f) by using the CAN architecture acquires even more importance. As a counterweight to the abovementioned advantages of the reported results, a limitation can be recognized in the partial loss of internal RI contrast. This effect is clearly visible in the central slice comparison in Figure 3.4(a), and is quantified as a percentage error of 11.92% about the RI standard deviation in Figure 3.4(g), where a shift to lower values of the histogram obtained from DCNN processing can be noticed with respect to the standard one. Finally, 9 3D RI tomograms are reported in Figure 3.5 to show a greater variety of cases about the typical tomographic performances in terms of both reproducibility and computational time.

In order to assess the ability of the network in preserving high frequency features, in Figure 3.6 an NIH-3T3 cell is analyzed, in which LDs are clearly visible inside and distinguishable from the surrounding cytoplasm. In fact, in the QPM target shown in Figure 3.6(a), two LDs can be recognized at the highest phase values. The same LDs can be equally well observed in the corresponding QPM output in Figure 3.6(b), even if with a slight reduced contrast, as shown in the phase profile reported in Figure 3.6(c). As a consequence, the same property can be found in the corresponding 3D case in Figure 3.6(d-f). In particular, the two LDs are well defined at the highest RIs in the standard tomogram in Figure 3.6(d). Instead, they become more widespread in the CAN tomogram in Figure 3.6(e), as can be also inferred from the RI profiles reported in Figure 3.6(f). However, despite the loss of contrast, both Figure 3.6(e) and Figure 3.6(f) point out that LDs can be segmented even in the 3D RI tomogram reconstructed through the neural network. Moreover, the SSIM between the two tomograms is very high (i.e., 0.996), thus confirming that the global content is preserved and only the fine details at the high frequencies are lost.

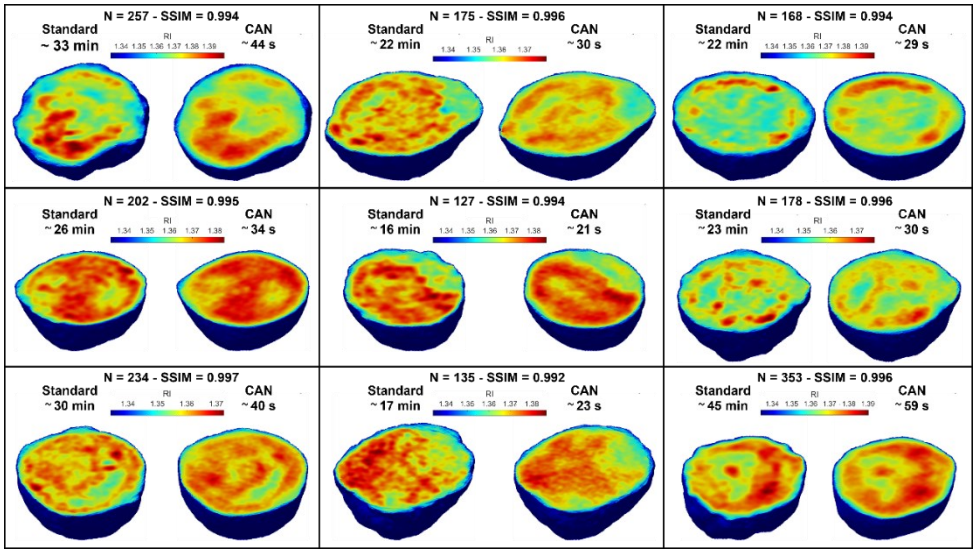

Figure 3.5 3D tomographic reconstructions.
Comparison between the central slices of 9 3D RI tomograms reconstructed by using the QPMs obtained through the standard holographic processing (on the left) and the CAN model (on the right). For each cell, the number of QPMs, the SSIM between the tomograms, and the computational time of the standard phase retrieval and the CAN-based phase retrieval are reported at the top.

Therefore, the 11.92% error in Figure 3.4(g) can be related to the loss of details (i.e., high frequencies) due to the employment of the network, which partially limits an intracellular analysis. However, in Figure 3.4(d-f), the CAN architecture has been demonstrated to provide a fast and accurate measurement of the global cellular features from the 3D RI tomograms, which can be exploited for diagnostic purposes. Therefore, using the network output or the result of the conventional pipeline would provide similar results in terms of global features and thus the same diagnostic response.

In order to analyze a possible diagnostic application, the ability of the network in preserving the 3D morphological differences between a healthy and a distorted cell is assessed in Figure 3.7. The QPMs target and the QPMs output of the distorted cell shown in Figure 3.3(b) have been used to reconstruct the

corresponding standard and CAN tomograms, respectively. The 3D shape of the distorted cell obtained through the standard method in Figure 3.7(a) is very similar to the corresponding one obtained through the CAN method in Figure 3.7(b). Moreover, the 3D shape of the distorted cell is significantly different from the quasi-spherical shape of a healthy cell displayed in Figure 3.7(c,d), obtained from the standard and CAN tomograms, respectively. An example of quantitative descriptor of the 3D morphology is the sphericity, which is 1 in the case of a perfect spherical cell otherwise is less than 1 in the case of a non-spherical cell.

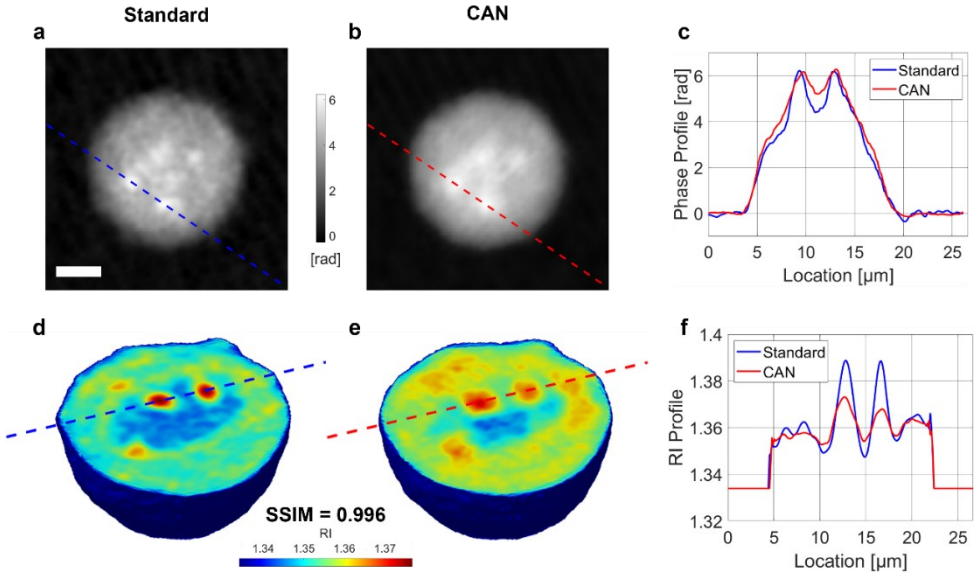

Figure 3.6 Assessment of the CAN performances in visualizing intracellular LDs.

(a,b) QPM target and QPM output, respectively, with two LDs visible at the highest phase values. The scale bar is 5 µm. **(c)** Phase profile of the QPM target (blue) and QPM output (red) selected from the lines highlighted in (a,b), respectively, passing through LDs. **(d,e)** Central slice of the 3D RI tomogram reconstructed by the standard method and the CAN method, respectively, with two LDs visible at the highest RI values. The SSIM between the tomograms is reported below. **(f)** RI profile corresponding to the lines highlighted in (d,e) from the standard tomogram (blue) and the CAN tomogram (red), respectively, passing through LDs.

In fact, it is defined as the ratio between the surface area of a sphere having the same volume of the analyzed cell and the surface area of the cell. The box plot in Figure 3.7(e) regarding the sphericity of the standard and CAN tomograms of 65 healthy cells allows to quantify the 3D morphological similarity between the standard and CAN shapes. The slightly greater median value and the smaller standard deviation of the CAN sphericity, with respect to the standard one, can be explained again with the loss of details about the external surface introduced by the DCNN (see Figure 3.7(a-d)) that leads to smaller surface areas. However, the red asterisks in Figure 3.7(e) point out that the 3D morphological difference between the distorted and healthy cells can be easily recognized also in the CAN case, thus preserving the diagnostic potentiality of the TPM-FC tool.

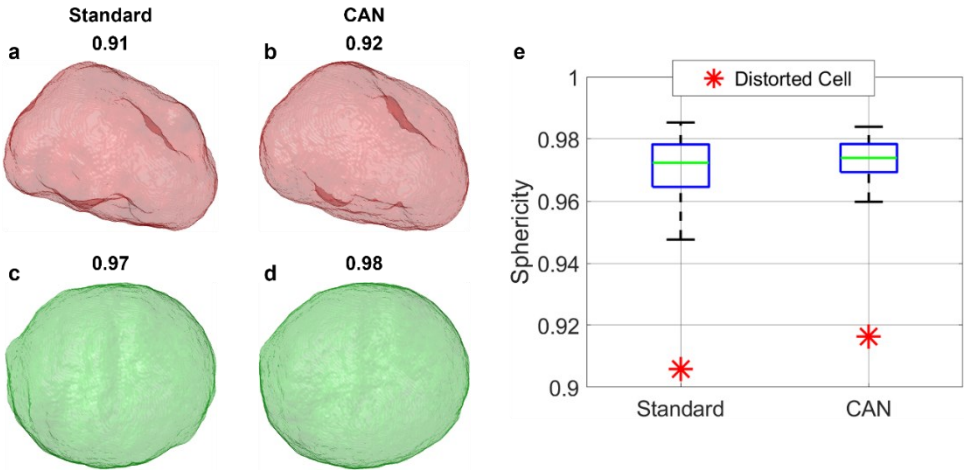

Figure 3.7 Assessment of the CAN performances in discerning between healthy and distorted cells.
(a,b) External shape of the 3D RI tomogram of a distorted cell reconstructed by the standard method and the CAN method, respectively. **(c,d)** External shape of the 3D RI tomogram of a healthy cell reconstructed by the standard method and the CAN method, respectively. In (a-d), the sphericity is reported at the top. **(e)** Box plot of the sphericity of the standard and CAN tomograms of 65 healthy cells compared to the sphericity of the distorted cell in (a,b) (red asterisk).

In Figure 3.8, the CAN performances at different widths w have been assessed. In particular, a mini-training of the $w = 32$, $w = 64$, and $w = 128$ architectures has been performed in order to compare their outputs. The central slice of the same cell shown in Figure 3.4(a) is reported in Figure 3.8(a) after reconstructing the tomogram by means of these three trained models. As also visible in the RI profiles displayed in Figure 3.8(b), the accuracy of the network in reconstructing the correct 3D RI tomogram increases with the width w, as expected. To quantify this property, the 65 tomograms are reconstructed again and, for each of them, the average RI, the equivalent radius, the dry mass, and the standard deviation RI are measured. The percentage errors between these features measured in the standard case and the same ones measured in the three CAN cases are reported in Figure 3.8(c), in which it can be noted the decreasing trend of the error as the width w increases. It is worth noting that, as the training dataset has been reduced by a quarter, the percentage errors reported in Figure 3.8(c) regarding the $w = 64$ architecture are bigger than the corresponding ones computed through the same architecture and reported in Figure 3.4(d-g). Nevertheless, the percentage errors of dry mass and standard deviation RI even reach a lower value in the case of the $w = 128$ model trained with the reduced dataset with respect to the $w = 64$ model trained with the entire dataset, i.e. 3.23% and 11.05%, respectively. However, a larger width w results in a greater number of parameters. In such a case, with the same hardware resources, the training and the prediction time would become longer, and the network would require a bigger memory occupation, as discussed in Table 2. Therefore, this means that the width of the network must be tuned according to the specifications of the tool to be implemented. Definitely, the proposed DCNN model provides enough compactness and computing velocity to be fit into on-chip SRAM, opening to the possibility of performing onboard computations, which is a highly demanded property for LOC devices with low processing hardware resources.

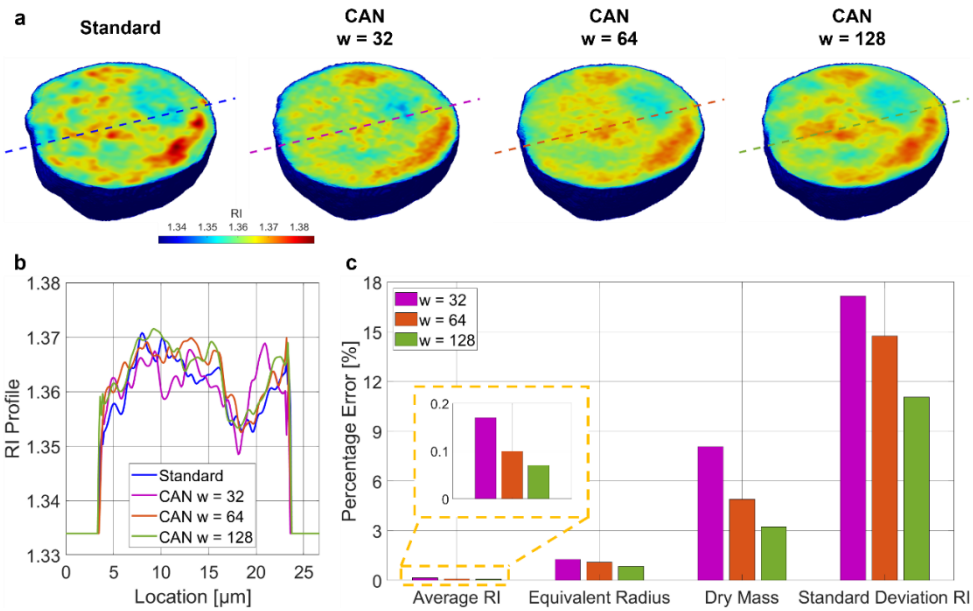

Figure 3.8 Assessment of the CAN performances after a mini-training of the architecture at different widths w.
(a) Central slice of a 3D RI tomogram reconstructed by the standard method and the CAN method with $w = 32$, $w = 64$, and $w = 128$. **(b)** RI profile corresponding to the lines highlighted in (a). **(c)** Percentage errors between the average RI, the equivalent radius, the dry mass, and the standard deviation RI measured in 65 standard tomograms and the same features measured in the corresponding CAN tomograms obtained with $w = 32$, $w = 64$, and $w = 128$. The percentage errors of the average RI are zoomed in the inset.

3.2 Classifying Cells from their Holographic Diffraction Patterns

Neuroblastoma (NB) is the most common paediatric solid tumor of the sympathetic nervous system [232].

[redacted] In pediatric patients, the risks linked to tissue biopsy sometimes may exceed benefits.

Over the last years, the sampling and analysis of non-solid biological tissue (e.g. blood), named LB, has been aimed to overcome these limitations (see conclusions in Chapter 5 for more details). [redacted] CTCs represent a snapshot of overall tumor bulk (primary tumor and metastases) [239]. CTCs detach from the primary tumor

and disseminate to distant sites via blood singularly or in clusters [240]. [redacted] Advanced technologies combining microfluidic platforms with label-free DHM and AI may represent a useful tool to efficiently discriminate tumor cells from other cell types or within a background of blood cells. Nowadays, many clinical tests are based on in-flow running of biological matter so that a long computational apparatus is not really workable when a decision-making is needed, for example in sorting devices. Indeed, in case of diagnostic strategies based on microfluidic systems, it would be a desirable configuration method working quasi real-time on flowing samples.

Reducing the computational time to obtain a preliminary phenotyping result will be the route to pursue. In the DHM framework, one possibility would be a fast processing of a digital hologram based on DCNN, as discussed in Section 3.1. However, another solution would be based on the direct employment of the recorded digital hologram. A raw digital hologram stores the complex amplitude of the sample in the form of a modulated fringe pattern. In principle, to associate an object to a certain population, its information does not really need to be decoded from the recorded pattern, provided that a suitable AI model is properly trained with a fair number of examples. Based on this idea, the possibility to directly use raw recorded digital holograms for carrying out cells classification tasks through learning approaches has been here investigated, thus skipping the entire holographic reconstruction process [214]. In this prospective study, two NB cell lines are classified by means of

their holographic diffraction patterns, i.e., the CHP134, consisting of the patient's tumor previously treated with chemotherapy and irradiation therapy, and the SKNSH, established by primary bone marrow tumor. Actually, in DH, the possibility to solve classification problems by using digital holograms as input of a learning-based classifier has been recently explored [244] [245] [246]. Here, for the first time this approach is implementing for phenotyping of NB CTCs in FC mode.

The pipeline used to classify the NB cells consists of three main steps.

- First, DH video frames containing cells from the two cell lines are collected with two different methodologies. In-flow DH frames recorded through the TPM-FC system in Figure 2.5 (microfluidic channel with 200 μm × 200 μm cross section coupled to a 2048×2048 CCD camera with 5.5 μm pixel size recording at 35 fps and a 40× MO, oil immersion, NA=1.30) are used as training and validation sets, while DH frames collected on Petri dishes are used as test set. The in-flow frames give about 80-100 different views of the same cell, thus augmenting the dataset, while the advantage of using Petri dishes is the ability to obtain many different cells in few frames, thus evaluating the robustness of the classifiers more accurately.

- Second, using transfer learning on COCO dataset [247], a Mask R-CNN model is trained on a subset of the training set cells. The Mask R-CNN is used to segment cells from both the in-flow video frames and the Petri dish images, in order to build the training, validation and test sets. A visual inspection is applied on the masks to remove the output False Positives.

- Finally, the single cells obtained in the previous step are fed to a binary classifier in order to discriminate between the two different NB cell lines. Here, both feature-based ML algorithms and a DL model have been tested. In particular, a shallow Multilayer Perceptron (MLP) and Logistic Regression (LR) have been used on a set of 10 manually

extracted features [248]. For the DL approach, a LeNet-like DCNN has been employed. The DCNN learns the features automatically during the training stage using an augmented dataset, which has been obtained by rotating each cell 36 times in the image plane, in order to obtain a rotationally invariant classifier.

More precisely, the dataset consists of 12 in-flow DH video sequences for training and validation, from which a total of 21852 frames have been extracted. In each DH video sequence, cells belong to the same phenotype, therefore each detected cell is automatically labelled with the corresponding class. Moreover, in order to test the network generalization capabilities, 120 cells have been recorded in Petri dish. Three frames from the in-flow video sequences related to CHP134 and SKNSH cell lines are shown in Figure 3.9(a,b), respectively, while two static images recorded in Petri dish are shown in Figure 3.9(c). In order to build a prototype for the fast NB cell classification, real-time detection and segmentation of cells is required. Therefore, these processes have been automated by employing a Mask R-CNN [249]. Mask R-CNN is a state-of-the-art DCNN used for the task of instance segmentation, that is, it is able to detect the bounding boxes that delimit object instances belonging to a target class while also being able to output a mask which precisely segments the object inside each bounding box. In this case, a Mask R-CNN pre-trained on the COCO dataset has been used [247]. The head of the network has been replaced with a 2-class classification head in order to only predict cells vs. background. This architecture has been trained for 40 epochs in Keras in Python 3 [250] to identify and segment cells (independently from their class) by using 200 cells manually extracted from the training set. The network has been then run on the holographic frames, thus obtaining 983 CHP134 cells and 918 SKNSH cells for the training set, 413 CHP134 cells and 584 SKNSH cells for the validation set, and 301 CHP134 cells and 207 SKNSH cells for the test set.

As regards the classification stage, a DL model has been firstly considered. In particular, a binary classification model based on a DCNN is applied to distinguish among cells of the CHP134 and of the SKNSH lines.

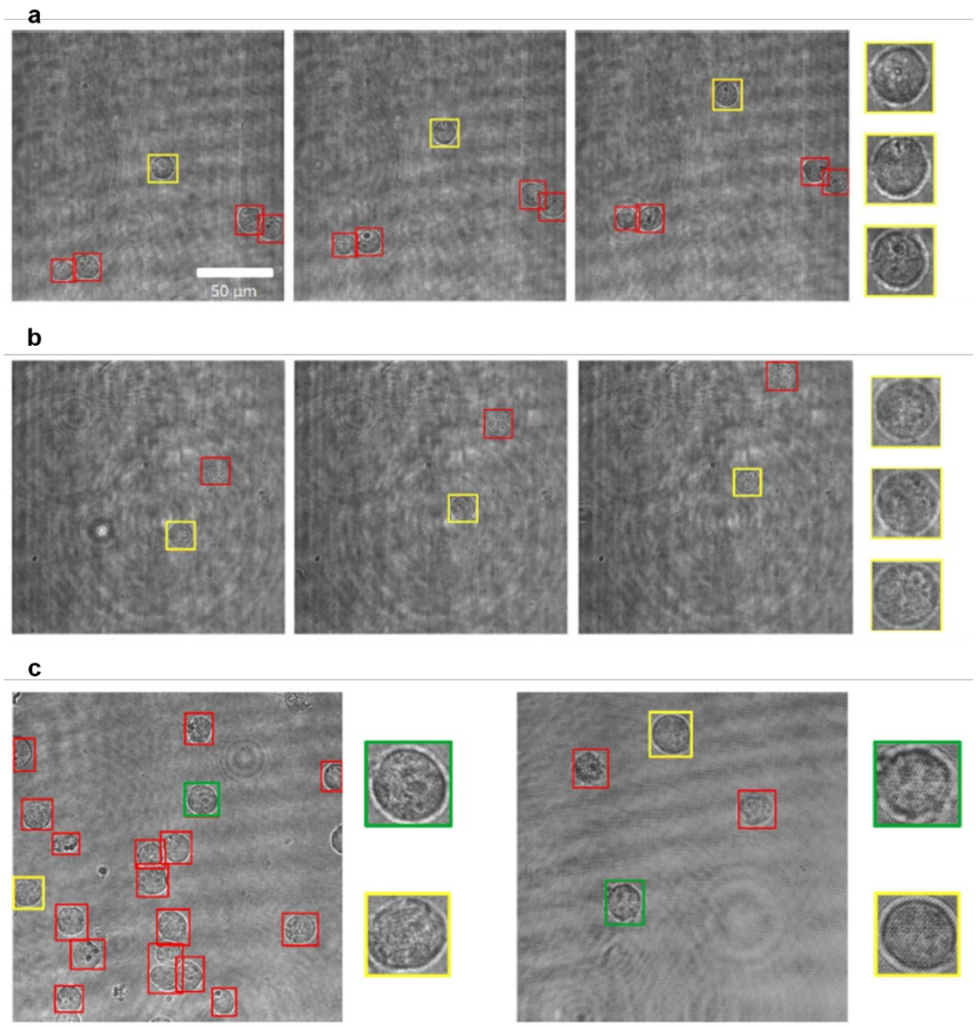

Figure 3.9 DH frames of NB cancer cells.

(a,b) Three successive frames with CHP134 and SKNSH cells, respectively, recorded in flow condition with an interval of 10 frames. **(c)** CHP134 (on the left) and SKNSH (on the right) cells recorded on a Petri dish. In (a-c), a zoomed cell view cropped from the holograms is shown on the right.

The employed DCNN is an adaptation of the well-known LeNet-5 [251], as shown in Figure 3.10(a). The network is made of two main parts, i.e. a feature extractor and a classifier head. The input to the network has size 256×256 pixels, with each pixel being normalized in the range [0,1]. The feature extractor is made of consecutive blocks of convolutional and max-pooling layers, in an alternating fashion. All the convolutional blocks have a 3×3 kernel size, while all the pooling blocks perform down sampling using a window of size 2×2. The 4 convolutional layers have respectively 32, 64, 128 and 128 filters. All the convolutional layers use a ReLU as activation function. The network head is instead composed of 2 fully-connected layers, the first comprising 512 neurons, while the last one has 1 single neuron with a sigmoid activation function, in order to obtain a probability class score (if the value is less than 0.5, the cell is predicted as belonging to the CHP134 class, otherwise as belonging to the SKNSH one). To avoid overfitting, two main strategies have been adopted. The first one is the use of data augmentation on the training set. Each cell from the training set has been rotated 36 times by 10° in the image plane. This helps the network to compute rotational-invariant features during the training phase and prevents overfitting by obtaining a training set that is effectively 36 times larger than the original one. The second technique is the use of a dropout layer between the two fully connected layers. The dropout layer randomly disables some of the connections between the two layers during training, forcing the network to be more robust to random noise and thus reducing overfitting to the training data. The LeNet-like DCNN has been trained using binary cross-entropy as a loss function. The dropout factor has been set to 0.5. The Adam optimization algorithm has been used with a learning rate of 0.0001. With these settings, the network has been trained for 40 epochs with a batch size of 32 images, using the validation accuracy to perform early stopping, i.e. to choose the epoch which performed best on the validation set. The LeNet-like DCNN has been implemented in Keras in Python 3. The training has been performed on a NVIDIA GeForce GTX 970 GPU with a 4 GB of VRAM.

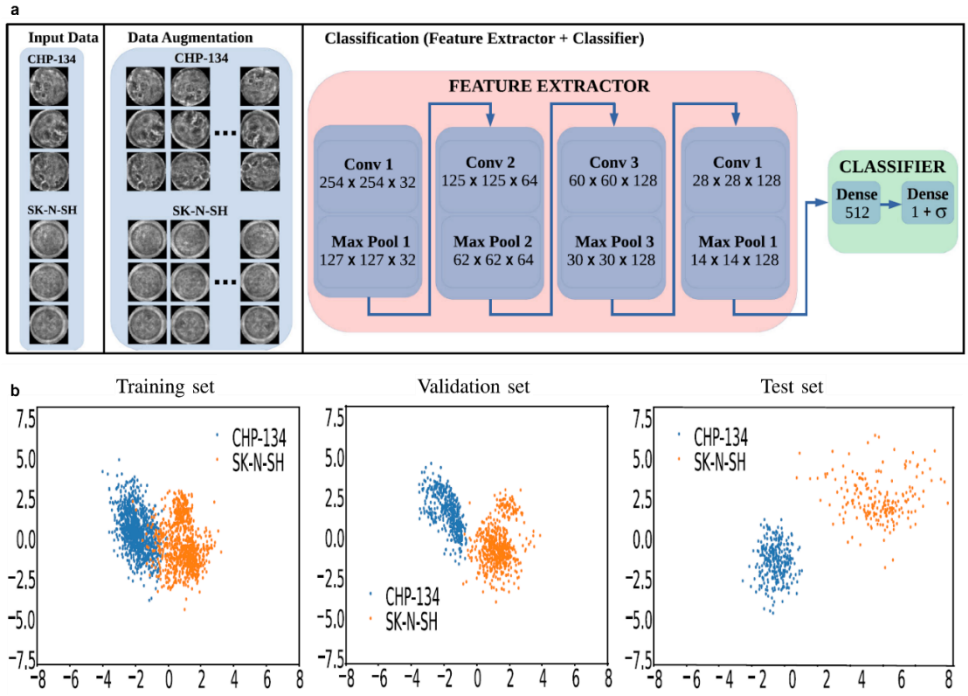

Figure 3.10 AI-based classification of CHP134 and SKNSH NB cancer cells.
(a) DL pipeline. The cell masks are extracted from each holographic frame by using a Mask R-CNN (left). Data augmentation is then performed by rotating each extracted cell by 10° for 36 times in the image plane (center). The LeNet-like DCNN architecture is finally trained, consisting of a feature extraction backbone and a classifier head (right). The backbone is made of a series of convolutional and max pooling layers. ReLU activation is used after each convolutional layer. The classifier head consists of two fully-connected layers of 512 and 1 neurons, respectively. A sigmoid activation function σ is applied to the last layer to obtain the class probability. **(b)** First two PCA components over training set, validation set, and test set. The two cell lines (CHP134 in orange and SKNSH in blue) are quasi perfectly separable.

In addition to the DL model, two feature-based ML algorithms have been employed for the classification task, i.e. the shallow MLP and the LR. First, 10 morphological/texture features are extracted from each cell image [248]. The features extracted are the first order pixel statistics of standard deviation, kurtosis and skewness, second order texture statistics of contrast, correlation,

homogeneity and energy, and the shape parameters of area, eccentricity and perimeter. Before the training step, all the collected features are normalized by subtracting the mean of the whole datasets (training, validation and test sets) and then scaled to unit variance. The Principal Component Analysis (PCA) algorithm [252] has been applied to the 10 extracted features, and the first two principal components are shown in Figure 3.10(b). Among the several architectures of the shallow MLP tested, the best one consists of an input layer of 10 neurons related to the 10 different features extracted from the cells, one hidden layer with *tanh* activation function made of 32 neurons, and an output layer made of 1 neuron and a sigmoid function to obtain the class membership score. The network has been trained in Keras using Adam optimizer with a learning rate of 0.001. Furthermore, looking at the 10 extracted features, it is possible to apply a LR to separate cells from the two lines in the feature space using a hyperplane. After a fine-tuning step to obtain the best accuracy on training and validation sets, Newton has been chosen as solver and no regularization has been applied.

ML and DL approaches outline different performances. As regards DCNN learning, both the training and validation accuracy quickly reach a plateau of 100% from the 30th epoch. Therefore, the best weights to evaluate the network on the test set have been chosen at epoch 30 of the training. As a result, the test accuracy is also 100%. Instead, the MLP takes more epochs to reach the 100% of accuracy on both training and validation sets. The test accuracy is of 92.2% with only 38 classification errors by misclassifying SKNSH cells. Finally, the LR on the 10 extracted features reaches 92.5% of accuracy on the test set.

In conclusion, the attained results demonstrate that a highly phenotyping accuracy of CHP134 and SKNSH NB cancer cells is achievable even with raw holograms, thus avoiding the phase retrieval reconstruction process. In particular, the combination between Mask R-CNN and LeNet-like DCNN applied to these two cell lines has reached the best accuracy in real-time classification during biological samples holographic acquisition. Therefore,

this strategy could be useful in the case of biomedical applications based on microfluidic systems where high-throughput is needed. Finally, it is worth remarking that, although the proposed approach completely skips the holographic reconstruction process, the use of DH imaging is decisive to achieve the above results. In fact, since both phase and amplitude information are encoded within a hologram, this pattern is more informative than a diffracted pattern obtainable with a single beam [253]. Moreover, using an interferometric system is advantageous also for post-classification tasks. Indeed, once a cell is classified and associated to a certain population, it could be of interest to achieve additional morphometric information *a posteriori* (e.g., its dry mass, biovolume, thickness, shape information).

3.3 Classifying Cells from their Phase Signatures

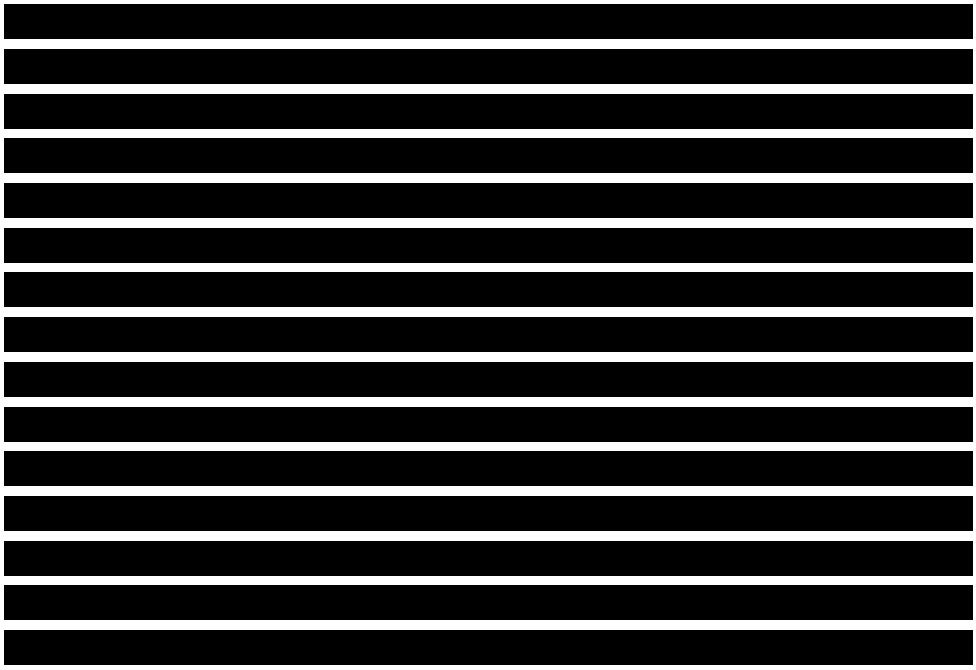

[redacted]

[redacted]

[redacted]

[redacted]

[redacted]		[redacted]	[redacted]
[redacted]	[redacted]	[redacted]	[redacted]
[redacted]	[redacted]	[redacted]	[redacted]
	[redacted]	[redacted]	[redacted]
	[redacted]	[redacted]	[redacted]
	[redacted]	[redacted]	[redacted]

[redacted]

[redacted]

[redacted]

[redacted]

[redacted]

[redacted]		[redacted]		[redacted]	
		[redacted]	[redacted]	[redacted]	[redacted]
[redacted]	[redacted]	[redacted]	[redacted]	[redacted]	[redacted]
[redacted]	[redacted]	[redacted]	[redacted]	[redacted]	[redacted]
	[redacted]	[redacted]	[redacted]	[redacted]	[redacted]
	[redacted]	[redacted]	[redacted]	[redacted]	[redacted]
[redacted]		[redacted]	[redacted]	[redacted]	[redacted]

[redacted]

[redacted]

[redacted]

[redacted]

[redacted]

[redacted]

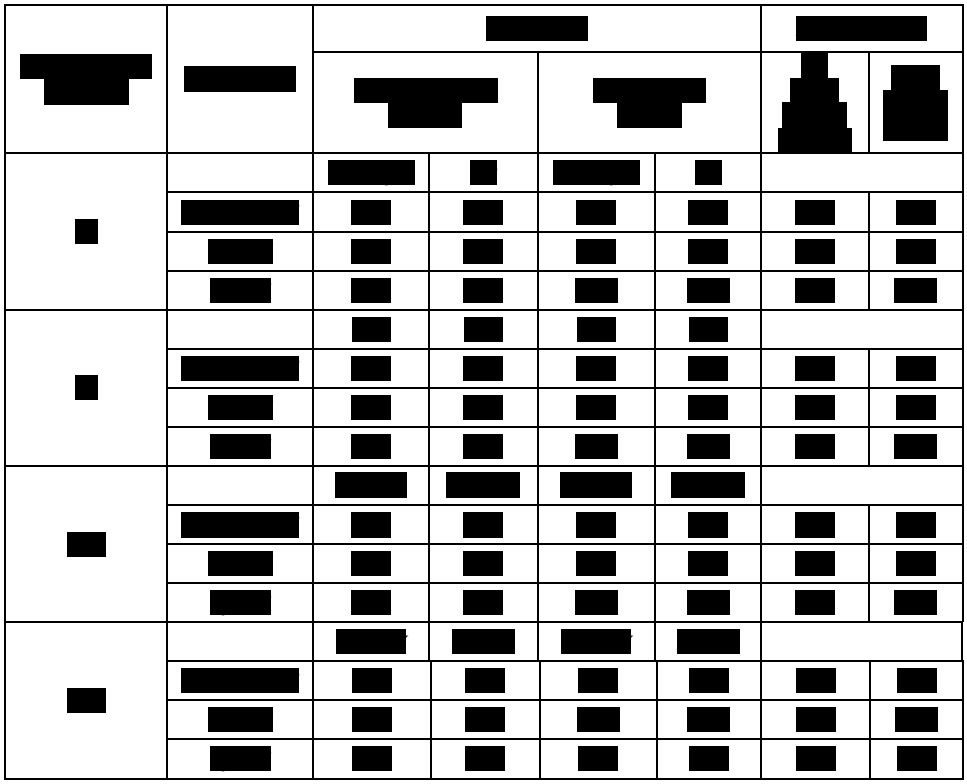

[redacted]

[redacted]

[redacted]	[redacted]				
	[redacted]	[redacted]	[redacted]	[redacted]	[redacted]
[redacted]	[redacted]	[redacted]	[redacted]	[redacted]	[redacted]
[redacted]	[redacted]	[redacted]	[redacted]	[redacted]	[redacted]
[redacted]	[redacted]	[redacted]	[redacted]	[redacted]	[redacted]

[redacted]

[redacted]

3.4 Classifying Cells from their 3D RI Tomograms

EC is the sixth most diagnosed cancer in women worldwide [268]. In the past few decades, the incidence of EC has increased in many countries [269]. Although surgical treatment is effective for early-stage cancers, it is more complex for high-risk and advanced diseases. In these latter cases, the best therapeutical approach is chemotherapy, which mainly exploits platinum-based drugs. Among them, cisplatin is believed to effectively affect EC proliferation and apoptosis. Unfortunately, the recurrent or advanced disease that develops in a minority of patients reduces the therapeutical efficacy because of chemoresistance [270]. Hence, in such cases, an accurate evaluation of the drug sensitivity of the patient can allow planning a more effective individualized chemotherapy. So far, the chemotherapy sensitivity in EC patients has been mainly evaluated by the tumour physicians based on the presence of tumour biomarkers, gynaecological examinations, magnetic resonance or CT imaging [271], without however obtaining very satisfactory results [272]. Therefore, in recent years, an alternate method based on a biological model of the tumour tissue has been proposed to visually predict drug resistance. In particular, the chemotherapy resistance is assessed into nude mice after subcutaneous transplantation of tumour tissue or purified tumour cells. However, this approach turns out to be expensive and time-consuming, thus limiting its clinical applications due to a low success rate, too [273]. Cell line models are another preclinical tumor model to examine drug sensitivity by evaluating the metabolic activity of cells through methyl

thiazolyl tetrazolium (MTT) assays as a reflection of cell viability or analyzing the RNA-sequencing to detect multiple drug resistance genes. However, tumors are genetically diverse, and the cells in the tumor are likely to have a small population that is drug-resistant. MTT can only be used to evaluate purified tumor cells, which require a long time to establish, and the sensitivity of RNA sequencing is relatively low. A promising solution to this challenging clinical issue can be found in the well assessed discovery about distinctive morphological changes in drug resistant cancer cells [274] [275] [276], which means that the sensitivity of tumor cells to different kinds of chemotherapy could be accessed through the analysis of parameters from cell morphology. Then, single-cell analysis becomes the key-technique to fully exploit this property, and IFC is the eligible tool to accomplish this task. However, in FIFC, the 2D morphological information can be altered by the exogenous staining (photobleaching and photodamaging), and quantitative information about the cell biophysical properties cannot be measured from the recorded images, thus limiting the understanding of complex phenomena like drug resistance. Hence, a label-free and quantitative IFC is needed to study drug resistance. Recently, it has been demonstrated that changes of living cells corresponding to different chemotherapeutic sensitivity could be quantitatively evaluated using QPMs [272]. Furthermore, ML has been exploited for detecting epithelial ovarian cancer cells (A2780) with the drug-resistance property [207]. In particular, a 92.2% classification accuracy has been reached by training an SVM classifier with 20 features extracted from the QPMs of about 2000 cells recorded through a HIFC system. In recent years, the employment of AI for solving classification problems based on QPI has rapidly increased. Thanks to the label-free and quantitative information provided by QPMs, the combination between AI and QPI is showing fruitful results. Of course, a remarkable boosting of the classification performance is expected by the employment of 3D TPM in place of 2D QPI, since the 3D spatial distribution of the cell RI can be exploited. However, so far few examples exist in this direction [208] [209].

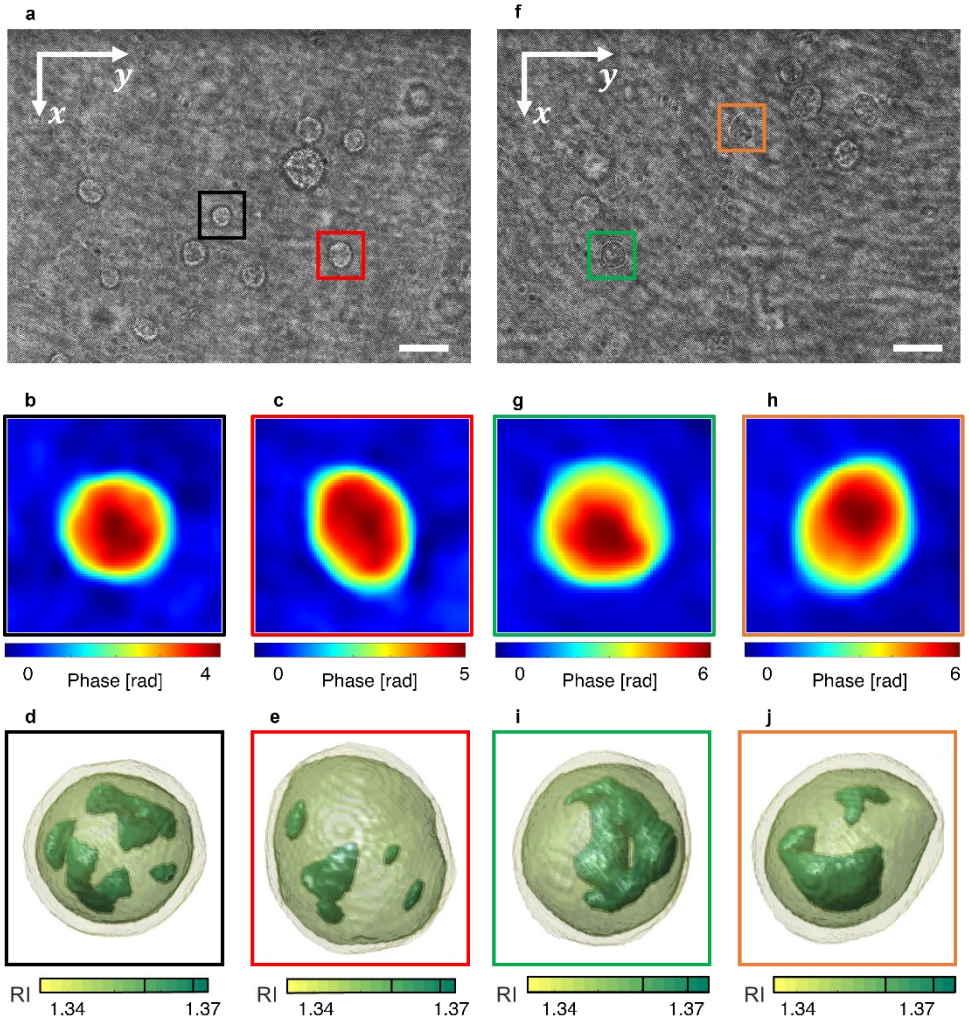

Figure 3.16 TPM-FC recording and reconstruction of two ISK cells (a-e) and two ISK-CisR cells (f-j).
(a,f) Recorded holograms of cells flowing along the y-axis and rotating around the x-axis. The scale bar is 20 μm. **(b,c,g,h)** Centered QPM ROIs containing the cells highlighted in (a,f). **(d,e,i,j)** Three-isolevels representation of the 3D RI tomograms of the cells in (b,c,g,h), respectively. For each cell, the intermediate thresholds have been set as the 65% and the 90% of the maximum RI value, as reported in the colorbars below.

The main limitation is the difficulty in creating large datasets for training an AI model. For this reason, the high-throughput property of TPM-FC is expected to provide a solution to overcome this obstacle. Here, for the first time, the TPM-FC has been exploited to characterize the 3D RI tomograms of suspended cells and classify them by means of ML models [217]. In particular, this strategy is followed for solving the challenging problem of detecting non-drug resistant and drug resistant cells within the same EC cell line (i.e., ISK cells and ISK-CisR cells, respectively). The ISK cell line is a well-differentiated adenocarcinoma, oestrogen receptor α (ERα)(+), ERβ(+), and progesterone receptor (PR)(+) cell line derived from the American Type Culture Collection. The drug-resistant characteristic of ISK-CisR cells has been induced by exposing ISK cells to cisplatin for 10 months. The TPM-FC system in Figure 2.5 (microfluidic channel with 200 μm × 200 μm cross section coupled to a 1024×1024 CCD camera with 5.5 μm pixel size recording at 20 fps and a 20× MO, NA=0.50) has been employed to reconstruct the 3D RI tomograms of 89 ISK cells and 89 ISK-CisR cells. Two frames from the recorded holographic videos are shown in Figure 3.16(a,f) about the ISK and ISK-CisR cells, respectively, while the corresponding QPMs and 3D RI tomograms are displayed in Figure 3.16(b,c,g,h) and Figure 3.16(d,e,i,j), respectively.

From the 3D tomograms, 67 features have been extracted, which can be grouped as morphological and texture features, as summarized in Table 7. In particular, there are 26 morphological features, such as volume, surface, sphericity, and equivalent diameter. The remaining texture parameters can be divided into four categories of statistical features based on the histogram, GLCM, neighborhood grey-tone difference matrix (NGTDM), and grey-level size zone matrix (GLSZM). Instead, from one single 2D QPM for each reconstructed tomogram, 54 corresponding features have been measured to compare the classification performance. More details and a list of all the features are provided in Appendix A.2. In Figure 3.17, the histograms of 5 corresponding 3D and 2D features are displayed. From the histograms, it can be seen that there are some differences in the feature data distribution

between the two cancer cells, especially the gradient feature in Figure 3.17(d,i). However, by comparing the overall distribution of 3D features with respect to the 2D ones, a slightly higher difference between the two populations can be inferred. Moreover, the distributions of ISK cells' 3D features are more concentrated, while ISK-CisR cells are relatively dispersed.

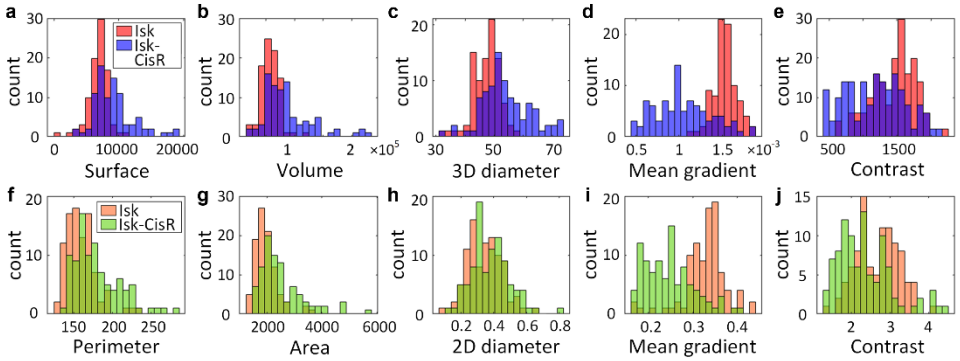

Figure 3.17 Histograms of different 3D features (a-e) and 2D features (f-j) of EC cells.
(a) Surface. **(b)** Volume. **(c)** 3D diameter. **(d)** Mean gradient. **(e)** GLCM contrast. **(f)** Perimeter. **(g)** Area. **(h)** 2D diameter. **(i)** Mean gradient. **(j)** GLCM contrast.

Table 7 Feature extraction from 3D RI tomograms and 2D QPMs.

Feature Type	# Features from 3D tomograms	# Features from 2D QPMs
Morphology	26	13
Histogram	6	6
GLCM	19	19
NGTDM	5	5
GLSZM	11	11
Total	*67*	*54*

To further explore and understand the performance of the extracted features, three different univariate analysis methods have been used, i.e. variance analysis [277], Pearson correlation coefficient [278], and Chi-square test [279]. Variance represents the divergence of the data distribution. A lower variance means that the feature data are relatively concentrated, and their contribution to the classifier is smaller. The significance level α in this method has been set as 0.01. Pearson correlation coefficient is a simple way to understand the correlation between a certain feature and its responding variable. Herein, a feature has been considered statistically significant whether no correlation with the other ones is observed, i.e. the Pearson correlation coefficient is always less than 0.2. At last, a two-sided p-value less than 0.05 from the Chi-square test has been considered statistically significant. The result of the significance evaluation of features is shown in Figure 3.18(a). There are differences in the results obtained by different methods. The number of significant features evaluated by the Pearson method is much more than by the Chi-square test, although 0.2 is a very strict standard for the Pearson method. The numbers of non-significant features by variance analysis are the same in 3D and 2D. However, the proportion of significant parameters in the 3D features set is higher than the corresponding proportion in the 2D features set for all the methods. This is a remarkable result suggesting that 3D features, which contain more cell information, can distinguish cells' drug resistance better. In Figure 3.18(b,c), the heat maps of correlation coefficients between extracted features are reported. The darker the color, the stronger the correlation between them, and the less informative they are when used jointly, indicating that they can yield more similar contributions to the cells classification task. The diagonal elements of the matrix are autocorrelation of each feature and thus have value 1. In Figure 3.18(b), the subsets in the yellow box show a large correlation between several 3D morphology features. In Figure 3.18(c), two subsets of 2D morphology and GLCM features show a large correlation. This means that features in the boxes describe more similar cell information, but it does not mean that their classification performances are

worse than other features. Overall, the correlation between 2D features is higher than 3D features.

Several ML methods have been used to classify the feature data of the two kinds of EC cells, such as Trees, Naïve Bayes, k-nearest neighbor (KNN), support vector machine (SVM), LR, and linear discriminant analysis (LDA). The ensemble learning strategy of the random subspace method (RSM) [280] has been used to randomly select partial features to train the classifiers in order to reduce redundant features' influence on classification results.

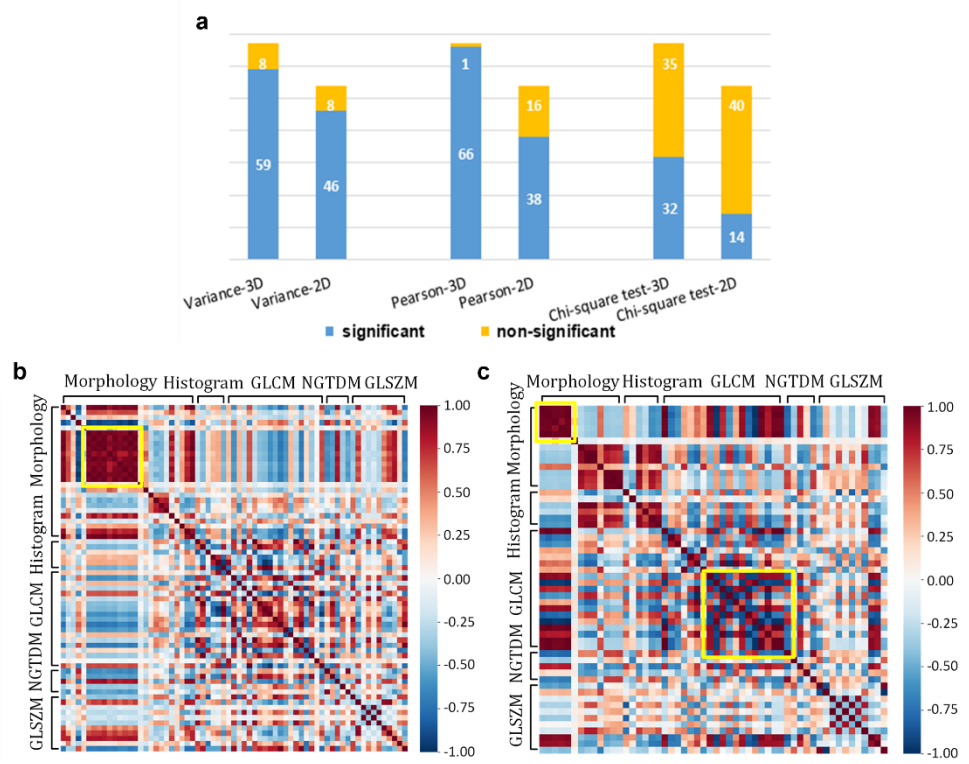

Figure 3.18 Significance analysis of the 3D and 2D features extracted from EC cells.
(a) Number of significant and non-significant 3D and 2D features tested by three different univariate analysis methods. **(b,c)** 5 correlation matrix of 67 3D features and 54 2D features, respectively, visualized as heat maps. The diagonal elements of the matrix are autocorrelation of each parameter.

The performances of the classifiers have been evaluated by the predicted results and receiver operating characteristic (ROC) analysis. Specificity, sensitivity, and accuracy of predicted results, and area under ROC curve (AUC) have been applied as the evaluation parameters.

As the feature number of the 3D RI tomograms is 67, the data set for ML is a matrix with 178×67 data points. The 54 features extracted from the corresponding 2D QPMs form a 178×54 dataset. The order difference between different features is large, influencing classification learning. So, the feature sets have been first standardized between 0 and 1 using the linear normalization method. For more accurately training and testing the datasets and avoiding the overfitting problem, 5-fold cross-validation has been used in the training process. Each dataset is divided into 6 subsets. For each round, there are 4 subsets for training and 1 subset for validation in the training process, and the left 1 subset for testing the trained classifier. The final performance of each classification method is calculated by averaging the results of 6 rounds. Table 8 shows the performance of different classification methods on 3D and 2D features. In Table 8, the LDA classifier achieves the best performance for 3D image classification with the highest score on the four evaluation parameters, while SVM achieves the highest score for 2D feature data. Although the best performance of 2D features is not as good as that of 3D features, 2D features still get better classification results by Trees and Naïve Bayes classifiers. The sensitivity is generally higher than specificity for all the classifiers with 2D features, but 3D features does not show this rule, which indicates that 3D feature data are more robust. Then, the RSM has been applied to the LDA classifier to test the classification performances when a different number of features is selected. As shown in Figure 3.19, the classification accuracy of the feature set with numerousness from 10 to 54 for 2D features and 10 to 67 for 3D features has been tested. As can be seen from the curves, the classification accuracy increases as the number of features increases when the number is relatively small.

Table 8 Comparison of the performance of different classifiers with 3D / 2D image features.

Classifier	Performance			
	Specificity	**Sensitivity**	**Accuracy**	**AUC**
Trees	0.79 / 0.86	0.82 / 0.83	0.803 / 0.847	0.84 / 0.86
Naïve Bayes	0.72 / 0.76	0.82 / 0.87	0.770 / 0.816	0.85 / 0.90
KNN	0.79 / 0.83	0.92 / 0.86	0.854 / 0.847	0.93 / 0.90
SVM	0.88 / 0.88	0.97 / 0.86	0.921 / 0.874	0.96 / 0.93
LR	0.89 / 0.88	0.98 / 0.82	0.933 / 0.800	0.96 / 0.84
LDA	0.91 / 0.84	0.98 / 0.88	0.944 / 0.863	0.97 / 0.90
Subspace-LDA (50 features / 40 features)	**0.94** / 0.86	**0.98** / 0.89	**0.961** / 0.879	**0.98** / 0.94

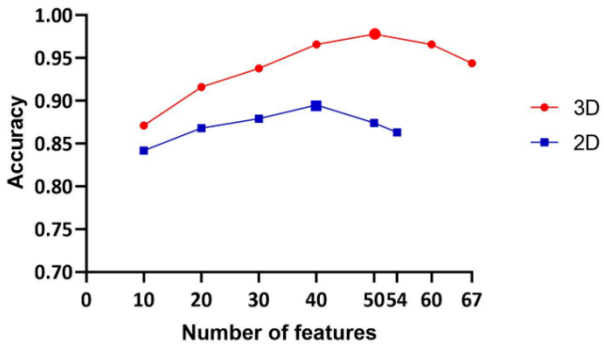

Figure 3.19 LDA classification accuracy of the different subspace of features selected by RSM.
In the 3D case, the maximum 96.1% accuracy is obtained with 50 features, while, in the 2D case, the maximum 87.9% accuracy is reached with 40 features.

However, after a certain number of features, increasing the number reduces the classification accuracy, indicating that the features have become redundant. In this case, the optimal number for 2D features is about 40 and for 3D features is about 50, as detailed in the last row in Table 8. It can be seen

that using the RSM to select multiple subsets of features can improve the classification performance for both 2D and 3D features. Remarkably, the 3D feature set allows recognizing the drug-resistant cells with 96.1% accuracy, 94% sensitivity, and 98% specificity.

In summary, chemotherapy is important in the treatment of EC. Identifying drug resistance in EC cells is critical for chemotherapeutic treatment. However, there is no rapid and effective method to identify drug-resistant cancer cells for now. Here it has been proved for the first time that TPM-FC combined to ML allows identifying two EC cells (i.e., drug-sensitive ISK cells and drug-resistant ISK-CisR cells) with the best classification accuracy of 96.1% reached by the LDA classifier fed by 50 3D features selected through RSM [217].

AVGVSTVS FRIDERICVS ROMANORVM IMPERATOR SEMPER

CHAPTER

4 Stain-Free Intracellular Specificity in TPM-FC

Traditional tools of histopathology will evolve soon, and the future of early diagnosis and precision medicine will pass through the accurate screening of single cells. A key challenge that will allow the next jump forward is achieving a more informative label-free microscopy. As discussed in previous Chapters, the gold standard imaging tool in cell biology is FM, in which stains or fluorescent tags are used to make the biological sample visible on a selective basis. Nevertheless, due to the FM limitations, avoiding staining permits one to access non-destructive, rapid, and chemistry-free analysis in biology and medicine. However, the advantages of label-free QPI and TPM are counterbalanced by the lack of direct intra-cellular specificity. Recently, significant progresses have been reported to introduce specificity in QPI by AI. Generative networks for cross-modality imaging and virtual staining are good examples in this sense. Networks for improving data analysis have been reported and commercialized as well, as in the case of the Nikon NIS.AI software suite that virtually stains and can segment the organelles from label-free images of cells in adhesion. In NIS.AI, conventional segmentation of 2D labelled images is used to pre-train the network, which can then emulate the process when requested by the users.

To illustrate the state of the art for intracellular specificity, the summary diagram shown in Figure 4.1 compares various label-free and fluorescent techniques. Unlike the label-free bioimaging (blue box), the FM bioimaging (yellow box) has intracellular specificity because organelles are marked, but it is qualitative and limited by the staining itself.

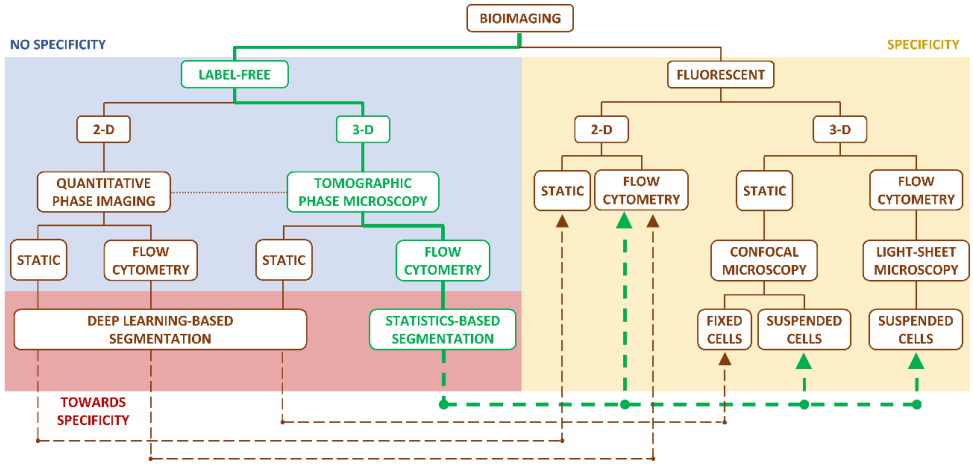

Figure 4.1 Comparison between label-free and fluorescent bioimaging in microscopy.
The methods in the red box allow to fill the specificity gap between the (blue box) label-free and (yellow box) FM techniques. The dashed lines highlight the FM techniques that could be replaced by the label-free ones. DL has been employed to virtually stain unlabelled tissues [281] [282] [283] as well as single cells [284] [285] in QPMs. The concept of virtual staining has then been extended to 3D RI tomograms of adherent samples, thus showing an AI-based RI to fluorescence mapping for the identification of the stain-free nucleus [286] and other endogenous subcellular components [287]. The computational techniques here proposed (green pathway) fill a blank in the bioimaging realm because, in terms of specificity, they make the TPM-FC consistent with both the 2D FIFC, the 3D FM confocal microscopy, and the 3D FIFC.

The methods in the red box allow to fill the specificity gap between the label-free and FM techniques (dashed lines). In particular, a Generative Adversarial Network has been employed to virtually stain unlabelled tissues (PhaseStain [281]) as well as single cells (PICS [284] and HoloStain [285]) in QPMs, i.e. in a 2D imaging case. Digital staining through the application of DCNNs has been successfully applied to multi-modal multi-photon microscopy in histopathology of tissues [282]. A neural network has also been used to translate autofluorescence images into images that are equivalent to the bright-field images of histologically stained versions of the same samples, thus achieving virtual histological staining [283]. In the 3D imaging case, organelles

of unlabelled and adhered cells have been identified using a DCNN [286] [287] to introduce specificity in TPM reconstructions, thus making 3D label-free TPM equivalent to the well-established 3D confocal microscopy, but only for static analysis of fixed cells at rest on a surface. Instead, the specificity property of FM confocal microscopy has not been replicated yet on static suspended cells in a label-free manner. In addition, the light-sheet FM has been recently integrated to microfluidic circuits, thus creating a 3D FM flow cytometer [288] [289], but the label-free technique equivalent in terms of specificity does not exist yet.

In this Chapter, computational methods herein developed for segmenting stain-free intracellular organelles in 3D RI tomograms reconstructed by TPM-FC are described. In particular, it is discussed the segmentation of endogenous organelles like the nucleus [290], nucleolus [290], and LDs [291], even exploiting the intracellular biolens signature [292] [293], as well as exogenous particles like nanoGraphene Oxide (nGO) [294]. As sketched by the green dashed lines in Figure 4.1, the proposed technology allows filling a blank in the bioimaging realm because, in terms of specificity, TPM-FC is the only tool able to become consistent with 3D FIFC. But, unlike the 3D FIFC, TPM-FC can provide direct measurements at the stain-free intracellular level of intrinsic 3D parameters (morphology, RI, and their derivatives, like dry-mass) correlated to cell physiology and health state. Finally, a method for compressing the 3D RI tomogram into a greatly smaller 1D sequence with a negligible intracellular information loss is herein introduced [295].

4.1 Nucleus Specificity

Among all intracellular structures, the nucleus is the principal one in the eukaryotic cell since it contains most of the genetic material and it is responsible for the cellular lifecycle. Identifying the nucleus through label-free

3D imaging is a challenging task since the nuclear size and RI can vary among different cell lines, within the same cell line, and even within the same cell, depending on the lifecycle's phases. In addition, different subcellular structures show similar RI values [296], thus making any threshold-based detection method ineffective. So far, the only method for segmenting the nucleus from RI tomograms has been proposed in static TPM and is based on the employment of a DCNN, which is trained by means of FM confocal images of single-cells with the nucleus stained by exogenous labels [286]. However, any network that learns from examples of fluorescence emissions is inherently biased by the labelling process itself (e.g., photobleaching and photodamaging) and thus cannot perform better than the ground-truth. Moreover, in the case of flowing biological cells in suspension, a voxel-level registration between 3D RI and 3D fluorescence is not obtainable, so that DCNNs cannot learn from examples of tomograms pairs. In the absence of a deterministic ground-truth, the method proposed here, named as Computational Segmentation based on Statistical Inference (CSSI), avoids the learning step and exploits a robust ad hoc clustering algorithm for segmenting the nucleus in 3D TPM-FC, i.e., it recognizes statistical similarities among groups of nucleus voxels [297]. The output of the CSSI algorithm is the best convex hull that overlaps to the cell nucleus, i.e., the smallest convex region that on average contains it. Although this approximation error is expected to be low as the nucleus has mostly a convex shape, hereafter the segmented region will be referred as nuclear organelle convex hull (OCH).

To validate the CSSI method, it has been firstly tested and assessed on a 3D numerical cell phantom simulation, modelled with the cell membrane, nucleus, cytoplasm, and mitochondria, as shown in Figure 4.2(a) (see Appendix A.3 for more details). As reported by the histogram in Figure 4.2(b), a RI distribution has been assigned to each of the four sub-cellular structures. This 3D numerical cell phantom has been used to assess the proposed CSSI algorithm for nucleus segmentation. However, nucleus segmentation is only one case of a more general technique which in principle can segment any kind

of subcellular structure with a suitable spatial resolution, because it only exploits the hypothesis of knowing the location of a group of voxels belonging to the organelle to be segmented, considered as the initial reference set. In fact, the CSSI method is based on the Wilcoxon-Mann-Whitney (WMW) test [298] [299], that is a statistical test used to reject or not the hypothesis for which a test set has been drawn from the same distribution as the designed reference set. In particular, the steps depicted in the scheme in Figure 4.2(c) are performed as follows.

- Rough clustering of the organelle voxels, exploiting the WMW test to infer the statistical similarity between different voxel clouds (i.e. the test sets) and a certain voxel cloud (i.e. the initial reference set) which contains the voxels supposed to belong to the organelle of interest.
- Filtering of the outlier organelle voxels when they are too far away from the centroid of the rough organelle cluster in terms of both geometric and statistical distances.
- Refinement of the filtered organelle cluster to improve its external shape by adding/removing smaller voxel clouds.
- Filling of the holes and smoothing of the corners of the refined organelle cluster by common morphological operators.

Notice that, whenever the WMW test is used, the reference set is randomly selected from the last estimation of the organelle cluster until that moment, to match its dimensionality with that of the test set, thus preserving the fairness of the statistical test. Due to this random selection, by repeating several times the described steps, at each iteration $j = 1, 2, \dots, K$, a slightly different estimation of the OCH can be obtained. The output of each iteration is a binary valued 3D volume whose non-null values correspond to the voxels associated with the organelle. Therefore, the sum of all the K outputs provides a tomogram of occurrences, from which the probability that a voxel belongs to the organelle can be inferred

through a normalization operation. Finally, the OCH is identified by a suitable probability threshold. A detailed description of the CSSI algorithm is reported in Appendix A.4. Here the problem of stain-free nucleus segmentation is considered, therefore the initial reference set is associated to the central voxels of the cell. Indeed, for many kinds of suspended cells, the central voxels belong to the nucleus. This property occurs especially in the case of cancer cells.

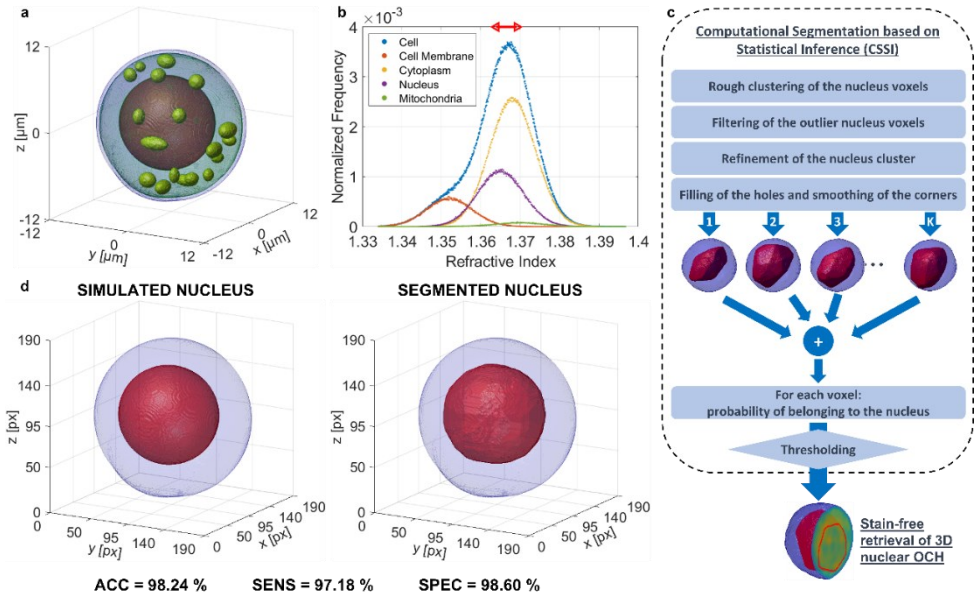

Figure 4.2 Numerical assessment of the CSSI algorithm applied to segment the 3D nuclear OCH from a 3D numerical cell phantom.
(a) Isolevels representation of the 3D cell model, simulated with four sub-cellular components, i.e., cell membrane, cytoplasm, nucleus, and 18 mitochondria. **(b)** Histogram of the RI values assigned to each simulated sub-cellular structure in (a). The red arrow at the top highlights the RI values assigned to the transition region between the nucleus and cytoplasm. **(c)** Block diagram of the CSSI method to segment the nuclear OCH from a stain-free 3D RI tomogram. **(d)** Visual comparison between the simulated 3D nucleus and the 3D nuclear OCH segmented from the simulated RI tomogram in (a). The simulated nucleus and the segmented nucleus are marked in red within the blue cell shell. The clustering performances obtained in this simulation are reported below (see their definitions in Table 9).

This is confirmed by the 2D images of the SKNSH NB cells recorded through a 2D FIFC system (i.e., Amnis ImageStream®), as shown in Figure 4.3, by the 3D morphological parameters reported in the literature for human breast cancer MCF7 cells imaged through a 3D FM confocal microscope [179], and more generally by the increase of the nucleus-cytoplasm ratio demonstrated in cancer cells [300] [301] [302] [303] [304]. On the left in Figure 4.2(d), the sole simulated nucleus is reported in red within the blue cell shell, while on the right the nucleus segmented from the 3D numerical cell phantom through the CSSI algorithm is displayed. The visual comparison in Figure 4.2(d) suggests that the proposed CSSI method allows segmenting a nucleus region very close to the original one, as also confirmed by the great quantitative performances reported below the tomograms. Moreover, to numerically assess the proposed 3D CSSI algorithm, it has been applied to reconstruct the nuclei of 1000 numerical cell phantoms simulated by randomly drawing their morphological and RI parameters from the distributions described in Appendix A.3.

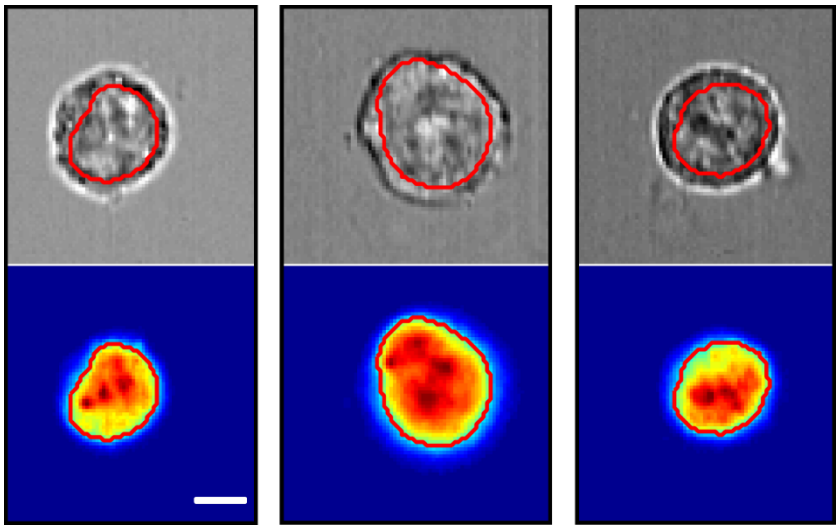

Figure 4.3 2D FIFC images of SKNSH cells recorded by Amnis ImageStream®. Three cells recorded simultaneously in brightfield images (top) and fluorescent images with the stained nucleus (bottom). The contour of the nucleus segmented by using the fluorescence information is overlapped in red. Scale bar is 5 μm.

The overall CSSI performances are summarized in the first column of Table 9 by means of 9 metrics, which corresponding histograms are displayed in blue in Figure A.8. It is worth pointing out that, in order to simplify the description of the CSSI algorithm and highlight its results about the stain-free nucleus identification, so far the presence of the nucleolus within the 3D numerical cell phantoms has been neglected. The extended analysis with the simulation of the nucleolus reported in Appendix A.5 highlights that the presence of nucleoli inside the nucleus does not substantially deteriorate the performances of the CSSI nucleus segmentation algorithm (see the second column of Table 9 and the corresponding orange histograms in Figure A.8). For example, the accuracy passes from an average value of $ACC = 96.28\ \%$ in the case without the nucleolus to an average value of $ACC = 95.86\ \%$ in the case with nucleolus.

As regards the experimental assessment of the CSSI algorithm, the TPM-FC system in Figure 2.5 (microfluidic channel with 200 μm × 200 μm cross section coupled to a 2048×2048 CMOS camera with 5.5 μm pixel size recording at 35 fps and a 40× MO, oil immersion, NA=1.30) has been employed to record the holograms of five human SKNSH NB cancer cells and three human MCF7 breast cancer cells. The tomographic reconstructions obtained by the FBP algorithm has been used in this study as initial guess of the LT algorithm described in Section 1.3.5, here exploited for enhancing the quality of the 3D RI tomograms [86]. The proposed CSSI method has been used to retrieve the 3D nuclear OCHs inside the reconstructed tomograms. The isolevels representation of an SKNSH cell is shown in Figure 4.4(a), highlighting in red the 3D segmented nuclear OCH within the blue cell shell. Moreover, its central slice is displayed in Figure 4.4(b), in which the segmented nucleus is marked by the red line, while in Figure 4.4(c) the corresponding 3D RI histogram is reported in green, separating in red and in blue the contributions of the 3D nuclear OCH and the 3D non-nucleus region, respectively. To experimentally assess the 3D segmentation technique, the segmented 3D TPM-FC reconstruction has been projected back to 2D where the experimental 2D FIFC images are available for comparison.

Table 9 Performances in computing the nuclear OCH (without and with nucleoli) and a single nucleolar OCH over the same dataset of 1000 3D numerical cell phantoms. TP (True Positive) is the number of voxels that are correctly classified as organelle, TN (True Negative) is the number of voxels that are correctly classified as non-organelle, FP (False Positive) is the number of voxels that are wrongly classified as organelle, and FN (False Negative) is the number of voxels that are wrongly classified as non-organelle.

Metric	Mathematical Definition	Mean ± Standard Deviation [%]		
		Nuclear OCH		Single Nucleolar OCH
		Without Nucleoli	With Nucleoli	
True Positive Rate (Sensitivity or Recall)	$\mathrm{TPR} = \mathrm{SENS} = \frac{\mathrm{TP}}{\mathrm{TP} + \mathrm{FN}}$	94.97 ± 5.01	92.08 ± 5.47	88.84 ± 5.11
True Negative Rate (Specificity)	$\mathrm{TNR} = \mathrm{SPEC} = \frac{\mathrm{TN}}{\mathrm{TN} + \mathrm{FP}}$	96.92 ± 2.59	97.69 ± 2.05	99.88 ± 0.06
Positive Predictive Value (Precision)	$\mathrm{PPV} = \frac{\mathrm{TP}}{\mathrm{TP} + \mathrm{FP}}$	93.75 ± 4.28	95.07 ± 3.74	89.86 ± 4.19
Negative Predictive Value	$\mathrm{NPV} = \frac{\mathrm{TN}}{\mathrm{TN} + \mathrm{FN}}$	97.61 ± 2.46	96.29 ± 2.82	99.87 ± 0.07
Accuracy	$\mathrm{ACC} = \frac{\mathrm{TP} + \mathrm{TN}}{\mathrm{TP} + \mathrm{TN} + \mathrm{FP} + \mathrm{FN}}$	96.28 ± 1.71	95.86 ± 1.65	99.75 ± 0.07
Balanced Accuracy	$\mathrm{BA} = \frac{\mathrm{TPR} + \mathrm{TNR}}{2}$	95.95 ± 2.17	94.89 ± 2.31	94.36 ± 2.54
F1 Score	$\mathrm{F1} = \frac{2\mathrm{TP}}{2\mathrm{TP} + \mathrm{FP} + \mathrm{FN}}$	94.17 ± 2.42	93.36 ± 2.33	89.16 ± 2.34
Matthews Correlation Coeff. (Phi Coeff.)	$\mathrm{MCC} = \frac{\mathrm{TP} \times \mathrm{TN} - \mathrm{FP} \times \mathrm{FN}}{\sqrt{(\mathrm{TP} + \mathrm{FP})(\mathrm{TP} + \mathrm{FN})(\mathrm{TN} + \mathrm{FP})(\mathrm{TN} + \mathrm{FN})}}$	91.60 ± 3.36	90.53 ± 3.28	89.13 ± 2.30
Fowlkes–Mallows Index	$\mathrm{FM} = \sqrt{\mathrm{PPV} \times \mathrm{TPR}}$	94.26 ± 2.27	93.47 ± 2.22	89.25 ± 2.27

In particular, the segmented RI tomogram is digitally rotated from 0° to 150° with 30° angular step around x-, y-, and z-axes, and then its silhouettes along the z-, x-, and y-axes, respectively, are considered to create 2D TPM-FC segmented projections, as sketched in Figure 4.4(a). According to the ray optics approximation in Eq. (1.1), the phase measured by DH is directly proportional to the integral of the RI values along the direction perpendicular to the plane of the camera. In this way, 18 unlabelled QPMs are obtained. As shown in a re-projected QPM on the left in Figure 4.4(d), it is cumbersome to recognize a sub-cellular structuring since no label is employed. However, thanks to the proposed 3D CSSI algorithm, the region occupied by the nucleus can be also marked (red line) in the 2D TPM-FC projection within the outer cell (blue line). This process has been exploited to further assess the proposed segmentation algorithm, by comparing the 3D results obtained through the TPM-FC technique with a conventional 2D FIFC system (i.e. Amnis ImageStream®). The latter has been used to record 11549 2D FIFC images of flowing SKNSH single cells, in which the nuclei have been stained through fluorescent dyes. On the right in Figure 4.4(d), the bright-field image of an SKNSH cell has been combined with the corresponding fluorescent image of the marked nucleus, therefore the false-color visualization makes the nucleus easily distinguishable (red line) with respect to the outer cell (blue line). Amnis ImageStream® can record a single random 2D image for each cell since it goes through the FOV once. Instead, TPM-FC allows the 3D tomographic reconstruction of a single cell. Through the reprojection process, the transition of the reconstructed cell within the Amnis ImageStream® FOV has been simulated at different 18 3D orientations with respect to the optical axis. In this way, the Amnis ImageStream® recording process has been digitally replicated and the dataset of 2D TPM-FC images has been increased avoiding a high correlation between the reprojections of the same cell, thanks to the choice of a big angular step (i.e., 30°).

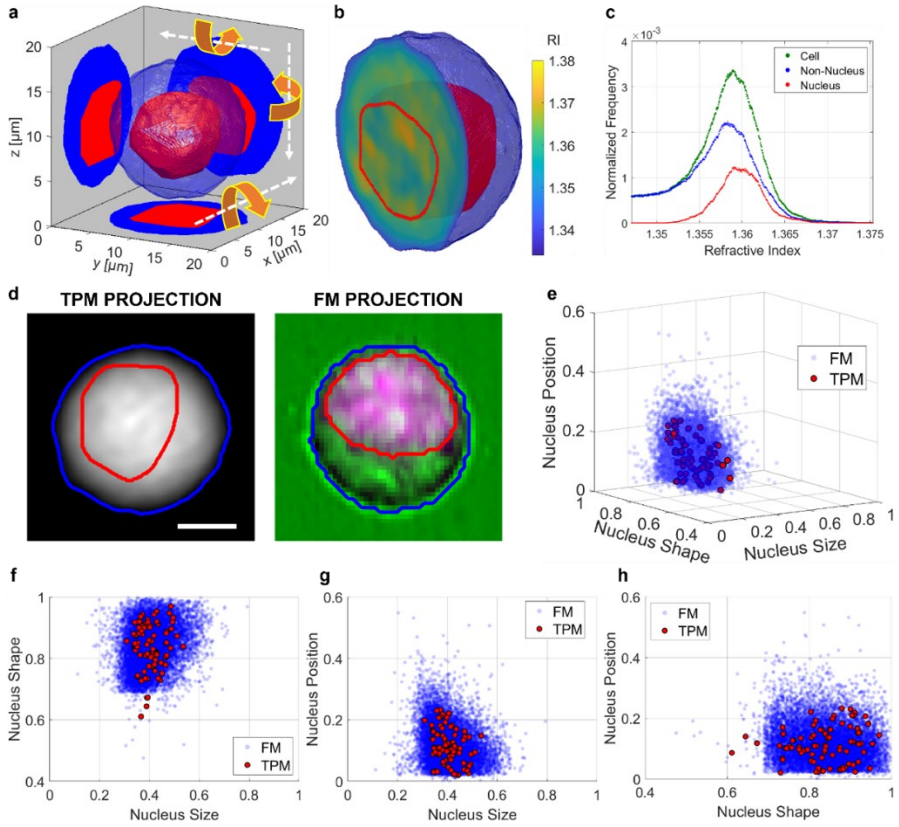

Figure 4.4 Experimental assessment of the CSSI algorithm in segmenting the 3D nuclear OCHs from unlabelled TPM-FC reconstructions of 5 SKNSH cells, by comparison with the morphological parameters of a 2D FIFC system.
(a) 3D segmented nucleus (red) within the 3D cell shell (blue) of an SKNSH cell reconstructed by TPM-FC. The segmented tomogram is rotated around the *x*-, *y*-, and *z*-axes (orange arrows) and then reprojected along the *z*-, *x*-, and *y*-axes (white arrows), thus obtaining 2D TPM segmented projections in *xy*-, *yz*-, and *xz*-planes, respectively. **(b)** Central slice of the isolevels representation in (a), with nucleus marked by the red line. **(c)** RI histogram of the SKNSH cell in (a,b) reconstructed by 3D TPM-FC (green), along with the RI distributions of its 3D nuclear OCH (red) and non-nucleus region (blue) segmented by CSSI algorithm. **(d)** 2D segmented projection with nucleus (red line) and non-nucleus (blue line) regions, obtained (on the left) by reprojecting 3D unlabelled TPM-FC RI reconstruction in (a,b) and (on the right) by recording 2D labelled FIFC images. The scale bar is 5 μm. **(e)** 3D scatter plot of nucleus size vs. nucleus shape vs. nucleus position measured in 11549 FIFC (blue dots) and 90 TPM (red dots) 2D projections. **(f-h)** 2D scatter plots of nucleus size vs. nucleus shape, nucleus size vs. nucleus position, and nucleus shape vs. nucleus position, respectively, containing the same points in (e).

Hence, in the 3D scatter plot in Figure 4.4(e), some 2D morphological parameters representative of nucleus size, nucleus shape, and nucleus position have been compared, i.e. nucleus-cell area ratio (NCAR), nucleus aspect ratio (NAR), and normalized nucleus-cell centroid distance (NNCCD), respectively, measured from both 90 TPM images (red dots) and 11549 FIFC images (blue dots). In particular, the NAR has been computed as the ratio between the minor axis and the major axis of the best-fitted ellipse to the nucleus surface, while the nucleus-cell centroid distance refers to 2D centroids and has been normalized to the radius of a circle having the same area of the cell, thus obtaining NNCCD. The 3D scatter plot highlights the very good agreement between TPM-FC and FIFC 2D nuclear features since the TPM-FC red dots are completely contained within the FIFC blue cloud. In addition, by using the one-sample multivariate Hotelling's T2 test [305] between TPM-FC and FIFC measurements about NCAR, NAR, and NNCCD, a high p-value has been obtained, i.e. 0.962, according to which it is not rejected with high confidence level the hypothesis that TPM-FC and FIFC 2D nuclear features have been drawn from the same distributions. This quantitative comparison is summarized in Table 10. Moreover, to better visualize the 3D scatter plot in Figure 4.4(e), it has been split into three different 2D scatter plots, shown in Figure 4.4(f-h).

Table 10 2D morphological parameters of SKNSH cells measured in labelled nuclei segmented from 11549 2D FIFC images and in unlabeled nuclei segmented by CSSI algorithm from 90 2D reprojections of five TPM-FC reconstructions.

		Mean Value		*p-value*
		TPM-FC	*FIFC*	*Hotelling's T^2 test*
nucleus size	*nucleus-cell area ratio*	0.404	0.406	0.962
nucleus shape	*nucleus aspect ratio*	0.839	0.838	
nucleus position	*normalized nucleus-cell centroid distance*	0.116	0.118	

As regards the MCF7 cells, an example of RI reconstruction and CSSI nucleus segmentation is shown in Figure 4.5(a,b). In particular, the nucleus shell is marked in red within the blue cell shell in the isolevels representation of Figure 4.5(a), which segmented central slice is displayed in Figure 4.5(b). Moreover, in Figure 4.5(c), its 3D RI histogram is displayed in green, also separating the RI distribution of the 3D nuclear OCH (red) and the 3D non-nucleus region (blue).

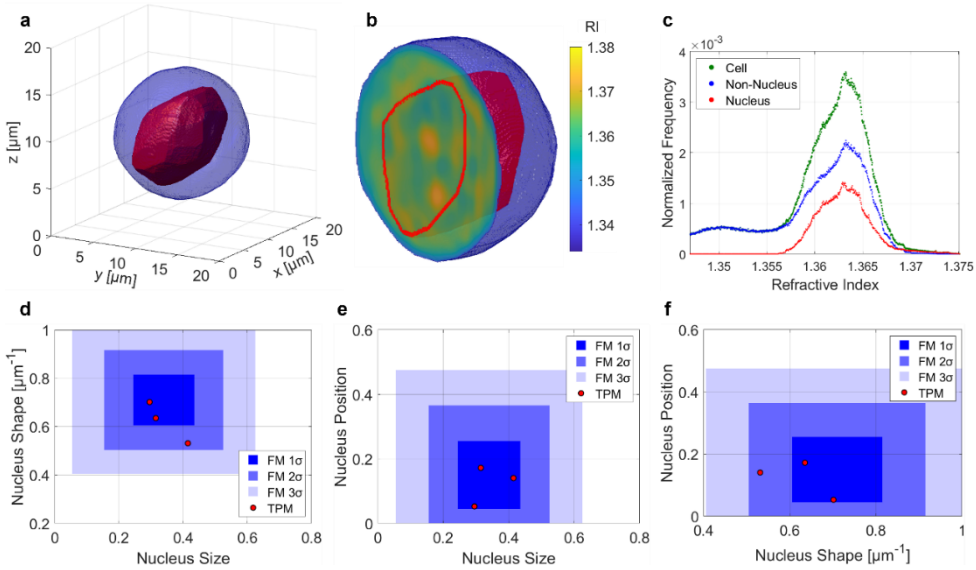

Figure 4.5 Experimental assessment of the CSSI algorithm in segmenting the 3D nuclear OCHs from unlabelled TPM-FC reconstructions of 3 MCF7 cells, by comparison with the morphological parameters of a 3D FM confocal microscope.

(a) 3D segmented nuclear OCH (red) within unlabelled 3D cell shell (blue) reconstructed through TPM-FC. **(b)** Central slice of the isolevels representation in (a), with nucleus marked by the red line. **(c)** RI histogram of the MCF7 cell in (a,b) reconstructed by 3D TPM-FC (green), along with the RI distributions of its 3D nuclear OCH (red) and non-nucleus region (blue) segmented by CSSI algorithm. **(d-f)** Scatter plots of nucleus size vs. nucleus shape, nucleus size vs. nucleus position, and nucleus shape vs. nucleus position, respectively, measured in three segmented TPM-FC MCF7 nuclei (red dots) along with the corresponding FM intervals (blue rectangles) around the average values, with half-width 1σ, 2σ, and 3σ (σ is the standard deviation of the measurements).

In this case, the experimental assessment is based on a quantitative comparison with the 3D morphological parameters measured in [179], in which a confocal microscope has been employed to find differences between viable and apoptotic MCF7 cells through 3D morphological features extraction. In that study, 206 suspended cells were stained with three fluorescent dyes to measure average values and standard deviations of 3D morphological parameters about the overall cell and its nucleus and mitochondria. A synthetic description of 3D nucleus size, shape, and position is given by nucleus-cell volume ratio (NCVR), nucleus surface-volume ratio (NSVR), and normalized nucleus-cell centroid distance (NNCCD), respectively. In particular, in this case, the nucleus-cell centroid distance refers to 3D centroids and has been normalized with respect to the radius of a sphere having the same cell volume, thus obtaining NNCCD. Moreover, it is worth underlining that NCVR and NSVR are direct measurements reported in [179], while NNCCD is an indirect measurement since it has been computed by using the direct ones in [179]. In the 2D scatter plots in Figure 4.5(d-f) regarding nucleus size, shape, and position, the three TPM-FC measurements (red dots) are reported along with three blue rectangles, which are the intervals $\mu \pm 1\sigma$, $\mu \pm 2\sigma$, and $\mu \pm 3\sigma$, with μ the average value and σ the standard deviation of the same parameters measured by 3D FM confocal microscopy. These scatter plots highlight a very good agreement between the 3D nucleus identified in labelled static MCF7 cells by confocal microscopy and the 3D nucleus segmented in unlabelled flowing MCF7 cells by the proposed CSSI algorithm. In fact, all the TPM-FC values are located in the 1σ-interval around the FM average values, except for shape measurement, that is anyway located in the 2σ-interval around the FM average value (Figure 4.5(d,f)). The values shown in Figure 4.5(d-f) are summarized in Table 11.

Table 11 3D morphological parameters of MCF7 cells measured in labeled nuclei segmented from 3D FM confocal images [179] and in unlabeled nuclei segmented by CSSI algorithm from three TPM-FC reconstructions.

		FM	*TPM cell 1*	*TPM cell 2*	*TPM cell 3*
nucleus size	*nucleus-cell volume ratio*	0.3396 ± 0.0939	0.296	0.415	0.315
nucleus shape	*nucleus surface-volume ratio [μm^{-1}]*	0.713 ± 0.103	0.702	0.531	0.635
nucleus position	*normalized nucleus-cell centroid distance*	0.152 ± 0.108	0.053	0.141	0.172

In summary, in this study an entirely new strategy for bridging the gap between FM and TPM in terms of subcellular specificity has been introduced and discussed. In particular, for the first time it has been demonstrated the capability to identify the cell nucleus from 3D RI tomograms in stain-free cells analyzed in FC modality. To provide a general overview of the differences, advantages, and limitations of the main methods that aim at introducing nucleus specificity, the most significant efforts towards this goal have been compared in Table 12 by just pointing out the field of application of each listed technique in respect of what was claimed in the related work. Therefore, each cell of Table 12 is filled with flags or crosses depending on whether the corresponding method possesses or lacks a certain attribute, each of them being highly pursued in the bioimaging field. The CSSI method is very promising to promote label-free TPM with nucleus specificity since it addresses all the required attributes shown in Table 12. In particular, the proposed CSSI algorithm allows TPM-FC to reach the same results of 2D FIFC, but without using dyes and preserving its high-throughput property. Furthermore, the TPM reprojections are much more informative than the FM images (see Figure 4.4(d)).

Table 12 Properties of the methods for the nucleus identification.

	Label-free	3D	Flow Cytometry	Specificity
QPI	✓	✗	✓	✗
TPM	✓	✓	✓	✗
FIFC	✗	✗	✓	✓
FM Confocal Microscopy	✗	✓	✗	✓
Light-Sheet FM [288] [289]	✗	✓	✓	✓
PhaseStain [281] **– PICS** [284]	✓	✗	✗	✓
HoloStain [285]	✓	✗	✓	✓
TPM + DL [286] [287]	✓	✓	✗	✓
TPM-FC + CSSI [297]	✓	✓	✓	✓

Indeed, the phase values contain a quantitative measurement about both the 3D sub-cellular morphology and RI distribution, which can be associated to the cell biology, instead of the 2D FM images, from which the sole 2D morphological parameters can be inferred. Similarly, besides the 3D morphological analysis of the 3D FM confocal microscopy, in the proposed technology a complete 3D label-free quantitative characterization of the RI-based fingerprint at the sub-cellular single-cell level is possible, as reported in the histograms in Figure 4.4(c) and Figure 4.5(c). Furthermore, the confocal microscope can only image static samples. Instead, in the range of FM methods, recently a light-sheet FM strategy has been implemented to retrieve 3D volumetric imaging of single cells while they are flowing in microfluidic circuits. Although promising compared with confocal microscopy, light-sheet FM combined to FC is still qualitative and limited by the staining drawbacks as the *a priori* knowledge of the target proteins, the phototoxicity and photobleaching.

As demonstrated here, the CSSI approach is an ad hoc clustering algorithm based on the computation of statistical similarities among groups of voxels

inside the same cell. CSSI strength lies in completely avoiding training neural networks through FM images, which leads to the abovementioned advantages. At the same time, the proposed approach comes with two main drawbacks. The computational times are significantly higher than DCNN inference times. Moreover, the accuracy of the estimated associations depends on the statistical significance of the tests the algorithm performs. Thus, as demonstrated above, a poor tomographic resolution can limit the accuracy in identifying small subcellular structures. However, a combined approach between DL and statistical inference is expected to be successfully attempted in the future. For instance, CSSI could be used to generate a dataset of tomograms pairs to train a DCNN to emulate the CSSI process and obtain real-time inference in nucleus identification in flowing cells.

It is worth pointing out that, to date, the CSSI is the sole method able to retrieve the 3D nuclear specificity in stain-free suspended single-cells in FC mode, thus providing quantitative measurements at the sub-cellular level with statistical significance on a large number of cells by potentially exploiting the high-throughput property. Finally, the CSSI algorithm could be prospectively transferred to other scenarios. In fact, as the CSSI method is based on the sole property of having different statistical distributions of the reconstructed quantity among the several intracellular organelles, it can be also applied to other flow cytometric tomographic phase imaging techniques [106]. In particular, the WMW statistical test can be considered a non-parametric hypothesis test able to disclose differences between the medians of two statistical distributions. Therefore, if each intracellular organelle is associated to a distinct RI statistical distribution, the proposed CSSI method is in principle able to segment an organelle whether the difference between its RI median value and the RI median values of all the other intracellular organelles is greater than the RI precision of the employed tomographic system. For this same reason, the CSSI is expected to work well when the signal-to-noise ratio is high enough to make perceptible the differences between the RI statistical distributions of the several cell organelles. In fact, in the simulations and

experimental segmentations herein reported, the tomograms have been put in the worst case that still ensures to respect this property, i.e. the RI values have been rounded to the third decimal place, since this minimal condition of RI resolution is respected by most of the TPM setups (being easily obtainable). Of course, a higher signal-to-noise ratio (i.e., a better RI resolution) is expected to improve the CSSI performances.

4.2 Nucleolus Specificity

The CSSI algorithm introduced in Section 4.1 is based on the computation of statistical similarities among groups of voxels inside the same cell by starting from an initial guess on the organelle location. To implement it, the sole property that must be satisfied consists in having different statistical distributions of the reconstructed quantity among the several intracellular organelles, as occurs for example in the RI case [5]. For this reason, the same strategy, based on statistics approach, can be also exploited to segment other cell organelles. In particular, the steps of the CSSI algorithm described in Appendix A.4 have been developed on the basis of this statistics working principle at the aim of identifying a single compact organelle having a distinctive RI distribution inside the cell, and it has been demonstrated for segmenting the nucleus. Here, it is shown that the same algorithm can be implemented to segment another single compact organelle, like the nucleolus in case a cell has a single nucleolus (e.g., in slowly cycling cells [306]) [297]. As regards the nucleolus location, two different situations have to be analyzed, namely case 1 and case 2. To describe them, in Figure 4.6 and Figure 4.7, a numerical cell phantom is considered with 15 mitochondria and a spherical nucleolus with a 27 times smaller volume than the surrounding nucleus. In the case 1 in Figure 4.6, the nucleolus is not in the center of the cell, as shown by the violet sphere in Figure 4.6(a). In the case 2 in Figure 4.7, the nucleolus is

located in the center of the cell, as displayed by the violet sphere in Figure 4.7(a). As reported in the RI histograms in Figure 4.6(b) and Figure 4.7(b), the RI values assigned to the nucleoli simulated in the cases 1 and 2, respectively, are greater than the corresponding outer nuclei but still included in their RI distributions in order to consider the worst case condition for segmentation. As regards the case 1, the CSSI algorithm starts looking for nuclear voxels from the central cube (i.e., the yellow reference cube C_R in Figure 4.6(c) overlapped to the red simulated nucleus).

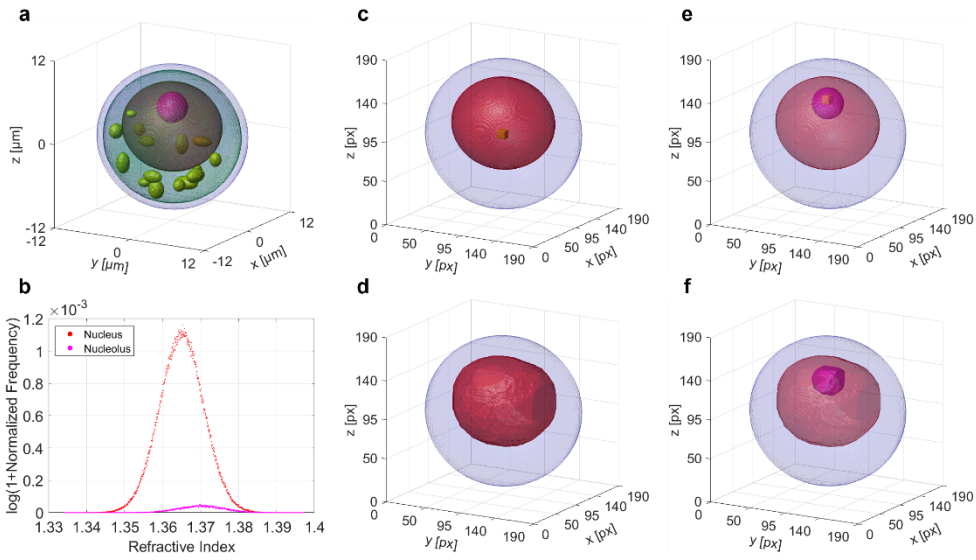

Figure 4.6 Numerical assessment of the CSSI algorithm applied to segment a single 3D nucleolar OCH when far from the center of the 3D numerical cell phantom (case 1).
(a) Isolevels representation of the 3D cell model, simulated with five sub-cellular components, i.e., cell membrane, cytoplasm, nucleus, nucleolus, and 15 mitochondria. **(b)** Histogram of the RI values assigned to the nucleus and the nucleolus in (a). **(c,d)** Respectively, simulated nucleus and corresponding nuclear OCH (red) segmented by the CSSI algorithm despite the presence of the not-centered nucleolus in (a). In (c), the starting central reference cube C_R of the CSSI algorithm is overlapped in yellow. **(e,f)** Respectively, simulated nucleolus and corresponding nucleolar OCH (violet) segmented by the CSSI algorithm after the nucleus identification (red) in (d). In (e), the starting reference cube C_R of the CSSI algorithm is overlapped in yellow in the zone of the segmented 3D nuclear OCH in (d) having the highest RIs.

As the CSSI algorithm is able to segment the nuclear OCH, i.e. the best convex hull that on average overlaps to the cell nucleus, the hole left by the presence of the nucleolus is automatically closed. Consequently, the correct nucleus segmentation shown in Figure 4.6(d), directly comparable with the simulated nucleus in Figure 4.6(c), can be obtained. Then, as the nucleolus has the highest RIs inside the nucleus, the CSSI algorithm can be easily adapted to search for its voxels by setting as starting reference cube C_R the cube having the highest average RI within the segmented nucleus (i.e., the yellow cube in Figure 4.6(e) overlapped to the simulated nucleolus). As displayed in violet in Figure 4.6(f), the CSSI output is the nucleolar OCH, i.e. the best convex hull that on average overlaps to the cell nucleolus simulated in Figure 4.6(e). Instead, the case 2 is exactly the opposite of case 1. In fact, if the nucleolus is in the center of the cell (violet simulated region in Figure 4.7(c)) and the CSSI algorithm normally starts from the central reference cube C_R (yellow cube in Figure 4.7(c)), the first output is the nucleolar OCH, as reported in violet in Figure 4.7(d). In such a case, it can be easily inferred that the segmented region is the nucleolus rather than the nucleus due to its much smaller size. Then, the second step consists in searching for the nucleus by starting from a reference cube C_R that is adjacent to the outer side of the segmented nucleolus (e.g., the yellow cube in Figure 4.7(e)). Again, the nuclear OCH is correctly segmented, as shown in red in Figure 4.7(f) with respect to the red simulated nucleus in Figure 4.7(e).

Therefore, starting from the same 1000 3D numerical cell phantoms used to assess the CSSI performances, 500 phantoms for the case 1 and 500 phantoms for the case 2 have been simulated by using the same distributions presented in Appendix A.5 by fixing one single nucleolus per cell. In the third column of Table 9, the values of 9 metrics are reported to quantify the CSSI performances in segmenting the stain-free nucleolus, which are just slightly worse than the stain-free nucleus ones because of the much smaller number of voxels representative of this organelle.

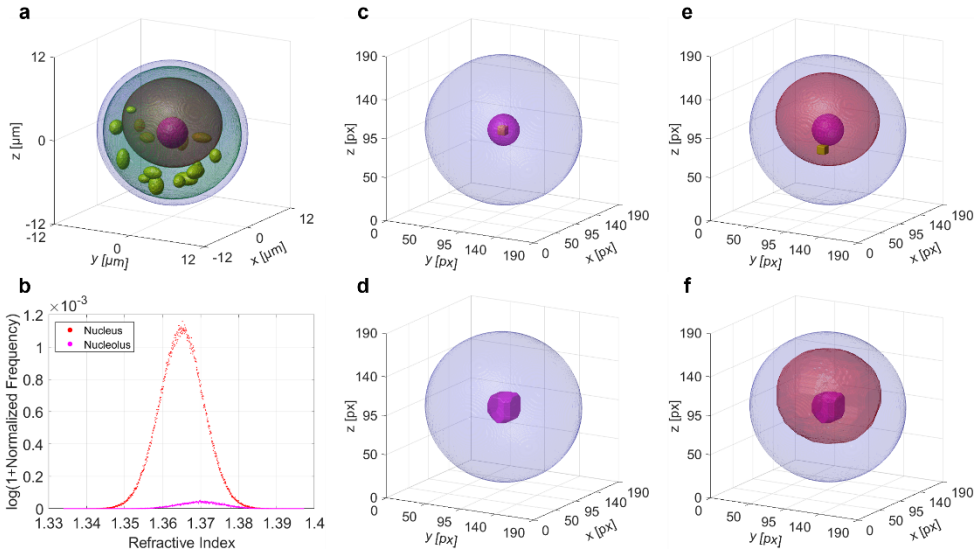

Figure 4.7 Numerical assessment of the CSSI algorithm applied to segment a single 3D nucleolar OCH when in the center of the 3D numerical cell phantom (case 2).

(a) Isolevels representation of the 3D cell model, simulated with five sub-cellular components, i.e., cell membrane, cytoplasm, nucleus, nucleolus, and 15 mitochondria. **(b)** Histogram of the RI values assigned to the nucleus and the nucleolus in (a). **(c,d)** Respectively, simulated nucleolus and corresponding nucleolar OCH (violet) segmented by the CSSI algorithm because, by starting from the central reference cube C_R overlapped in yellow in (c), the centered nucleolus in (a) is found. **(e,f)** Respectively, simulated nucleus and corresponding nuclear OCH (red) segmented by the CSSI algorithm after recognizing that the region segmented in (d) is the nucleolus due its small size. In (e), the starting reference cube C_R of the CSSI algorithm is overlapped in yellow in the adjacent zone to the outer side of the segmented 3D nucleolar OCH in (d).

In fact, the principal factor that could limit the success of the CSSI algorithm in case of a single compact organelle is a low imaging spatial resolution with respect to the size of the analyzed organelle, which means that the organelle is represented by a very low number of voxels. In such a case, to take into account a lower number of voxels representing a certain organelle, the resolution factor ε can be reduced. However, it cannot be excessively decreased otherwise the opposite effect is obtained, i.e. a bad segmentation of

the organelle due to a too low statistical power of the WMW test. The statistical power is indeed the probability of correctly classifying a voxel as non-organelle when it actually does not belong to that organelle, and it is well known that the statistical power of a hypothesis test increases with the number of observations. To demonstrate this property, a 3D numerical cell phantom with 15 mitochondria has been simulated and used to create 8 possible resolution scenarios, i.e., inside it, the same spherical organelle has been simulated with a radius changing from 15 to 50 pixels (step of 5 pixels). In Figure 4.8(a), three of these phantoms are shown corresponding to the 50, 30, and 15 pixels radii. For each of these 8 resolution scenarios, the CSSI algorithm has been implemented by using three resolution factors, i.e. ε=10 px, ε=8 px, and ε=6 px, which segmentation results are reported in Figure 4.8(b-d), respectively, for the 50, 30, and 15 pixels radii. In order to quantitatively compare the CSSI segmentation at different organelle sizes (i.e., imaging spatial resolutions) and resolution factors ε, the F1 scores have been computed through the formula in Table 9. In Figure 4.8(e), it is evident that by fixing a too low resolution factor (i.e., ε=6 px), the segmentation performances significantly drop because of the low statistical power of the WMW test. Instead, the segmentation performances are much higher in the ε=10 px and ε=8 px cases, which means that starting from the resolution factor ε=8 px, the statistical power (i.e., the number of observations) of the WMW test is enough to guarantee a good segmentation output. Moreover, as can be expected, the zoom-in of the F1 score plot in Figure 4.8(f) highlights a growing trend of the classification performances with the organelle pixel size (i.e., with the imaging spatial resolution). In particular, the ε=8 px curve shows the best behavior since it has the lowest slope, which means that, by reducing the imaging spatial resolution, the segmentation performance decreases more slowly than the ε=10 px case. In fact, after reaching a sufficient statistical power by selecting ε>6 px, the ε=8 px resolution factor allows following better the external organelle shape due to a better spatial resolution despite the number of observations is lower than the ε=10 px case.

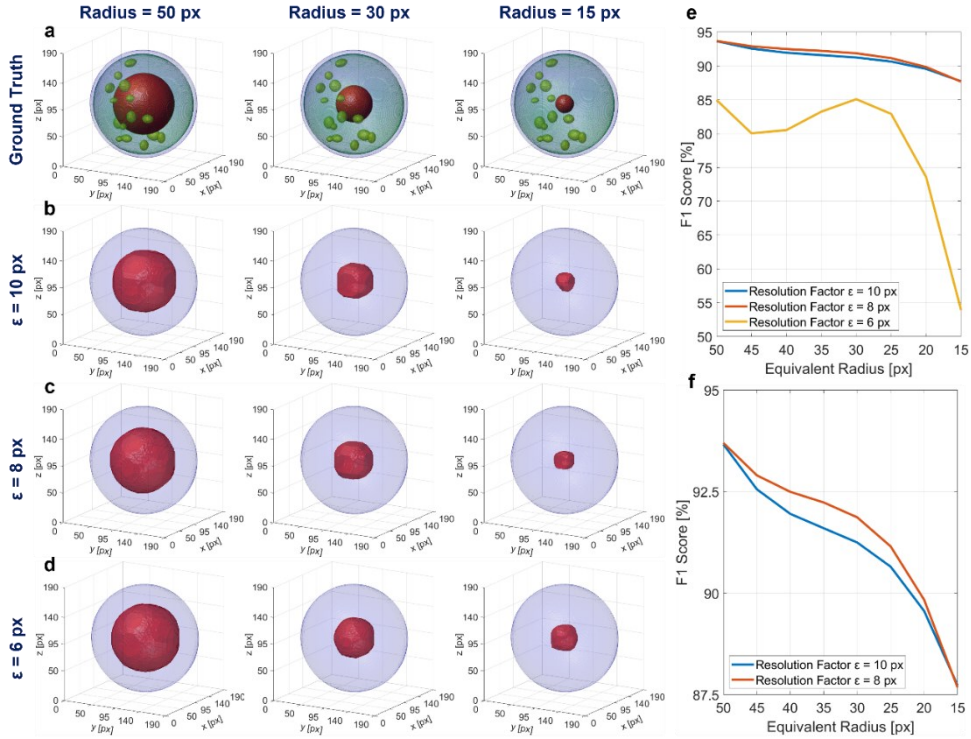

Figure 4.8 CSSI performances in segmenting a generic organelle with respect to the imaging spatial resolution (i.e., its number of voxels) and the CSSI resolution factor *ε*.
(a) Three 3D numerical cell phantoms with 15 mitochondria (green) and a spherical organelle (red) having an equivalent radius of 50 px (left), 30 px (center), and 15 px (right). **(b-d)** CSSI segmentation of the red organelles in (a) by using the resolution factors ε=10 px, ε=8 px, and ε=6 px, respectively. **(e)** F1 score in segmenting the red organelle in (a) by using the resolution factors ε=10 px, ε=8 px, and ε=6 px while changing its equivalent radius (i.e., the imaging spatial resolution) between 15 px and 50 px. **(f)** Zoom-in of the ε=10 px and ε=8 px curves in (e).

It is worth pointing out two other important points. First, by using a resolution factor ε at least equal to 8 px, an organelle with an equivalent radius less than 15 pixels cannot be examined since the organelle would be covered by very few distinct cubes. Furthermore, the CSSI computational time increases in a nonlinear way with the resolution factor ε, therefore ε=10 px has been selected

as a good trade-off to analyze the simulated and experimental tomograms in this study. Hence, remarkably the CSSI algorithm can be used to segment other single compact organelles different from the nucleus but, in case they are very small, the imaging spatial resolution must be able to provide an equivalent radius greater than 15 pixels to implement the CSSI algorithm with at least a resolution factor ε=8 px. Otherwise, the statistics of the WMW test are not robust and this greatly worsens the segmentation performances. Instead, in case of multiple organelles, the same working principle based on the statistical similarities can be exploited. However, the algorithm implemented in Appendix A.4 must be slightly modified to avoid the constraints herein used to gather all the candidate cubes at the aim of segmenting a single compact region, i.e. the nucleus.

4.3 Identification of Lipid Droplets

4.3.1 Segmentation in 3D RI Tomograms

LDs are ubiquitous intracellular organelles specialized in triacylglycerols and steryl esters storage, found in some prokaryotes and in most eukaryotic cells, where they reside primarily in the cytoplasm [307]. Initially described exclusively as storage organelles, LDs are now recognized as dynamic entities that play several other pivotal roles in intracellular homeostasis. For example, LDs provide a defense mechanism against numerous stress conditions (e.g., lipotoxicity, endoplasmic reticulum (ER) stress, oxidative stress, mitochondrial damage during autophagy), and control certain proteins' expression by supporting their maturation, storage and turn-over [308]. In addition to ER from which they derive, LDs dynamically interact with most intracellular organelles, including mitochondria, peroxisomes, lysosomes, Golgi apparatus, and nuclei [308], which contribute to the final 3D spatial organization of LDs inside the cellular volume. Although the mechanisms

linking specific LD structural characteristics to a certain function are still not completely understood, a vast number of evidences shows that variation in LDs number, size, ultrastructure, motility, lipid/protein content and interactions with other organelles significantly influences many cellular processes [308] [309]. Consequently, their dysregulation may have implications in diseases, and evaluation of LDs-related parameters may be exploited as a biomarker. Indeed, LDs have been described to have a role in various pathologies, including diabetes [310], atherosclerosis [311], fatty liver disease [312], neurodegenerative diseases [313] and cancer [314] [315]. Moreover, they are recognized as structural markers of inflammation, since a remarkable increase in LDs number and size rapidly occurs in immune cells in response to inflammatory stimuli [316] [317]. Most recent evidence shows that monocytes from COVID-19 affected patients display an increased LDs accumulation with respect to healthy blood donors, suggesting a possible involvement of these organelles in the SARS-CoV-2 pathogenesis [318]. However, the limitations of currently available techniques for LDs characterization still prevent from completely understanding their functions and exploiting their potential for clinical purposes. In particular, development of new non-destructive techniques is required, which provide fast LDs detection, quantification, and characterization, ensuring powerful statistical data, with the aim of discovering novel insights on this prominent issue. Among the various techniques used for LDs investigation, TEM and FM are probably the most exploited for this purpose [319] [320]. The LDs ultrastructure can be easily determined by TEM due to their homogeneous spherical shape and their recognizable electron density [321]. However, only small areas of a sample can be analyzed by TEM, thus strongly limiting the ensemble study of LDs inside the cell, and the method requires skilled and highly trained operators. FM is a somewhat more user-friendly technique, with a growing number of fluorescent lipophilic dyes used for LDs detection, most popular being Nile Red, Bodipy® 493/503, LipidTOX and Oli Red O [322]. These reagents come with the advantage of being easy to use, thus

allowing tracing LDs dynamics, even by the live cell imaging. These dyes may also be used in FC, allowing higher throughput, but providing no information on LDs volumetric distribution. It is important to note that fluorescent dyes are subjected to photobleaching, may interfere with cell function, especially during long exposure times, and induce phototoxicity. These limitations have prompted the development of label-free methods for live imaging.

Among label-free approaches, DHM is a valuable non-destructive tool for LDs analysis, as their RI substantially differs from the surrounding cell inner structure, and the DH method relies on the RI difference as a contrast agent. The first demonstration in visualizing and measuring LDs in live cells by DH was reported in the last decade [323]. Recently, TPM has been applied for LDs 3D imaging within mammalian cells [324] [325] [326] and microalgae [327], for 4D tracking of the LDs dynamics in live hepatocytes [328], and for recording time-lapses of living foam cells [329]. Nevertheless, the up-to-date available label-free techniques allow to investigate LDs only in static, adherent cells, strongly limiting both throughput and reliability of the information regarding the LDs volumetric organization, the latter being significantly affected by the cell culture mode. Furthermore, imaging methods developed for operating on adhesion samples exclude the possibility to investigate populations that naturally exert their functions in circulation, such as cells in bodily fluids. Although TPM apparatuses are really powerful, they cannot furnish in simple way high-throughput analysis, that can instead be achieved only by imaging techniques capable to operate in FC modality. Instead, an imaging modality for phenotyping the cells in flow-through is highly demanded for investigating the sample in an environment that well mimics physiological conditions and can guarantee statistically significant assays by investigating a high number of cells in a single experiment. For this reason, here, for the first time, LDs are visualized and quantitatively measured in 3D in live cell suspensions through TPM-FC while they are flowing along a simple and commercially available microfluidic channel [291].

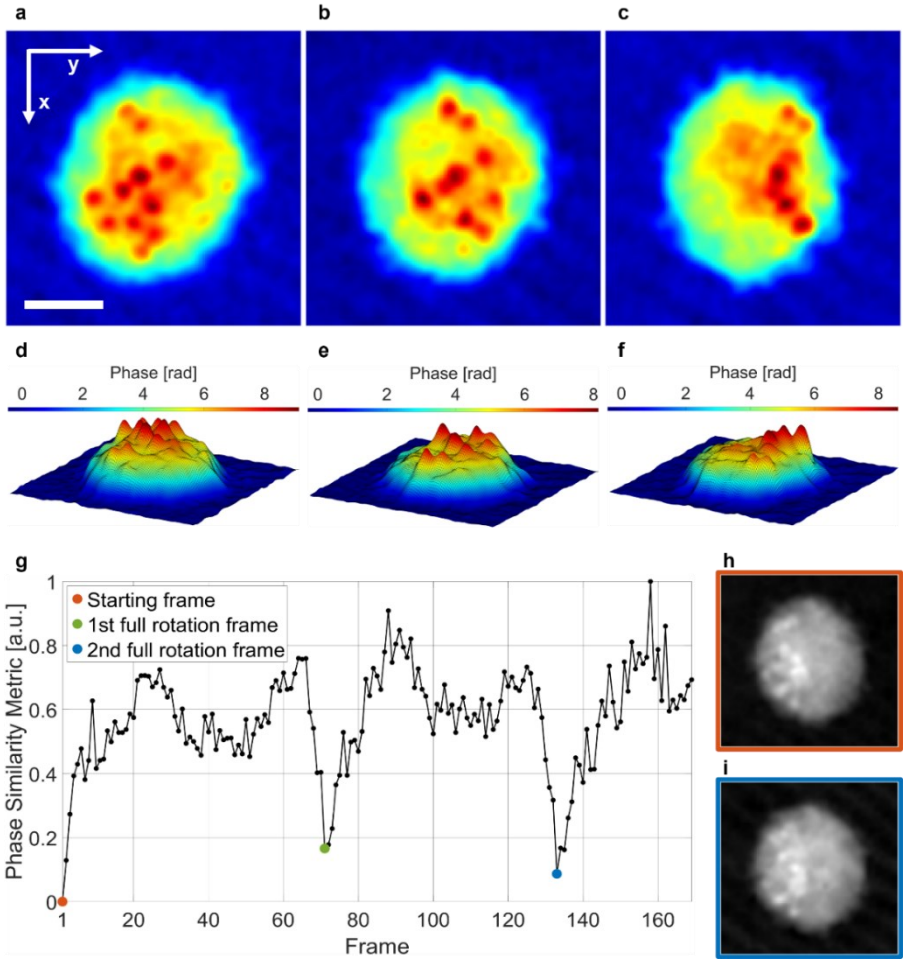

Figure 4.9 LDs in A2780 QPMs.

(a-c) Three QPMs of an A2780 cell while flowing along the y-axis and rotating around the x-axis. The spots with the biggest phase values (dark red) are the LDs. Scale bar is 5 μm. **(d-f)** Pseudo-3D visualization of the 2D QPMs in (a-c), respectively, in which the LDs are well-separated from the outer cell because of their greater height. **(g)** Trend of the phase similarity metric, which is null in the starting frame of the QPM sequence (orange dot) and is minimum when the first (green dot) and the second (blue dot) full cell rotations have occurred. **(h)** QPM at the first frame and **(i)** QPM after two full rotations, in which LDs are located in the same positions.

By means of the TPM-FC system in Figure 2.5, 54 human ovarian cancer cells (A2780) and 34 monocytes (THP1) have been recorded. Three typical QPMs of an A2780 cell are reported in Figure 4.9(a-c), in which the rotation around the x-axis of the cell flowing along the y-axis can be observed. In fact, as the RIs of the LDs are higher than the other organelles, they can be recognized within the QPMs as the red spots. To mark this property, the same QPMs are shown in a pseudo-3D visualization in Figure 4.9(d-f), in which the height codifies the phase values. Hence, LDs correspond to the isolated peaks, which change their position because of the cell rotation in the microfluidic channel. As discussed in Section 2.4.3, to recover the unknown rolling angles of the flowing cell, a full rotation is detected through a suitable phase image similarity metric, and then a proportion with the positions along the flow direction is implemented [108]. However, this method suffers when the similarity metric does not have a trend with pronounced minima. In that case, an error can be committed in retrieving the unknown rolling angles, which propagates to the tomographic reconstruction. Instead, the presence of intracellular LDs provides a great help in making more accurate the rolling angles recovery and then the 3D RI tomogram. In fact, as shown in Figure 4.9(a-c), the LDs are phase peaks which move in the QPM sequence according to the cell rotation, thus providing a highly distinguishable marker for the phase similarity. This property is highlighted in the phase similarity metric reported as example in Figure 4.9(g). It is computed by comparing all the QPMs with the first one of the sequence. Hence, it is 0 in the first frame, while the other local minima, which are well defined thanks to the LDs, correspond to full rotations (i.e., 360°). Indeed, a full rotation can be easily detected when LDs come back to their starting positions, as shown in Figure 4.9(h,i). Once the unknown viewing/rolling angles are estimated, the pairs consisting of the QPMs and the corresponding rolling angles are given in input to the FBP algorithm in order to reconstruct the 3D RI spatial distribution at the single cell level.

In Figure 4.10(a), the central slice of the 3D reconstructed tomogram of one typical A2780 cell is shown. The LDs presence is clearly visible. Moreover, it can be noted from the colour scale of the plot that LDs reach RI values much higher than the surrounding medium. In fact, the corresponding RI histogram in Figure 4.10(b) goes up to 1.500, that is a very high value for these types of cells, thus suggesting that a threshold-based method is enough for numerical segmenting the LDs and thus to extract the quantitative measurement of each LD. In Figure 4.10(c-e), three isolevels representations of the same 3D tomogram are reported after having segmented LDs with three different thresholds numerical value (i.e., 1.400, 1.420, and 1.440, respectively). All three results are plausible, since separate particles have been isolated in the same cell location. Obviously, the greater the RI threshold, the smaller the volume of particles identified. Hence, a criterion to set the LDs-threshold is requested. The RI values of LDs change based on the type of cell, the temperature, and the wavelength [330]. Segmenting intracellular organelles is always problematic in a label-free technique since an exogenous calibrated marker is missed. In the 2D case, a DL approach has been employed to identify LDs inside the QPMs [331]. Instead, in the 3D case, to segment LDs in microalgal cells [327] and in foam cells [329], the RI threshold has been selected according to the FM image of the same cell obtained from the channel mounted on the static TPM system. However, this is not possible in TPM-FC. Instead, to fix an average RI threshold, here independent 2D FM measurements about the number and the diameter of LDs have been exploited (see Appendix A.6), as well as the high number of cells reconstructed through the TPM-FC technique. The TPM-FC configuration selected for these experiments has a lower spatial resolution than the 2D FM images in order to provide a very large FOV. Therefore, as shown in Figure 4.10(c-e), in this experiment LDs cannot be resolved when they are too close each other. For this reason, the number of LDs measured through the TPM-FC is expected to be smaller than the FM technique.

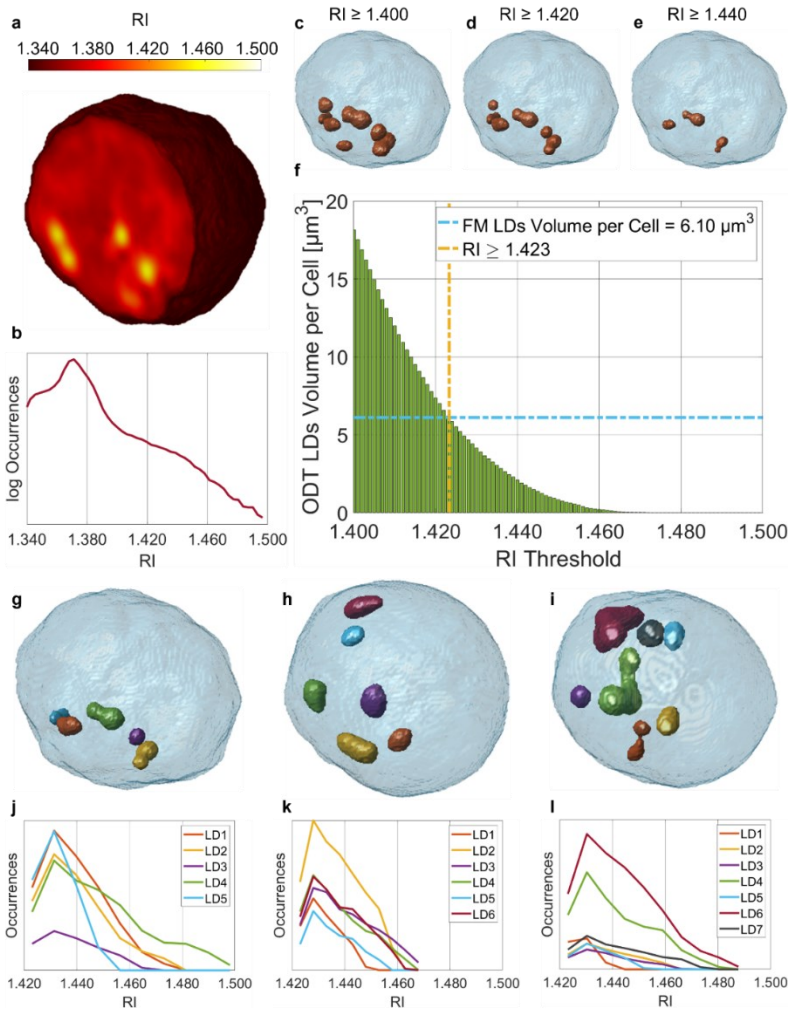

Figure 4.10 Segmentation of the LDs within the 3D RI tomograms of A2780 live cells.

(a) Central slice of the 3D RI tomogram of an A2780 live cell, in which LDs take the highest RI values. **(b)** Histogram in logarithmic scale of the 3D RI distribution of the cell in (a). **(c-e)** Isolevels representation of the tomogram in (a), in which LDs (orange) have been segmented by using the RI thresholds reported above. **(f)** Average volume per cell of the LDs segmented in 54 TPM-FC tomograms of A2780 live cells by using different RI thresholds. The selected LDs-threshold (yellow line) allows computing the same average volume measured in 2D FM images (blue line). **(g-i)** Isolevels representation of separated LDs or LDs clusters segmented in 3 A2780 tomograms by using the LDs-threshold selected in (f), and **(j-l)** corresponding RI histograms. (a-e,g,j) are the same cell.

However, the overall volume of LDs must be unchanged. Within the 2D FM images, the average LDs volume per cell can be computed indirectly by multiplying the average number of LDs and their average diameter, thus obtaining 6.10 μm^3 in the A2780 case. Instead, as reported in Figure 4.10(f), the LDs average volume per cell can be measured directly from the 54 tomograms by varying the RI threshold, thus obtaining the expected decreasing curve. The LDs-threshold can be finally selected in such a way to guarantee the same average volume, which is RI ≥ 1.423 in the A2780 case. By using the computed LDs-threshold, all the 54 tomograms of the A2780 cells have been segmented. In Figure 4.10(g-i), three of these segmented tomograms are displayed by painting separated LDs or LDs clusters with different colours, and the corresponding RI distributions in 3D are reported in Figure 4.10(j-l), which are very similar to each other.

In recent years, TPM has emerged because it allows label-free quantitative measurements at the single-cell level of features about both the 3D morphology and the RI statistics, which are related to the cell biophysical properties (e.g., dry mass). The implementation of the TPM-FC system further allows the replication of the same measurement on a large number of cells, thus reaching a statistical significance, which can be exploited for characterizing a certain phenomenon. Therefore, in Figure 4.11, the histograms of several properties about the hundreds of reconstructed LDs are reported. In particular, in Figure 4.11(a-e), the mean value, the standard deviation, the entropy, the kurtosis, and the skewness of the 3D RI distribution about each LD are respectively shown. The equivalent radius displayed in Figure 4.11(f) is the radius of a sphere having the same volume of the analyzed LD. The dry mass reported in Figure 4.11(g) is the mass of the biological sample without its water content, calculated as in Eq. (1.48).

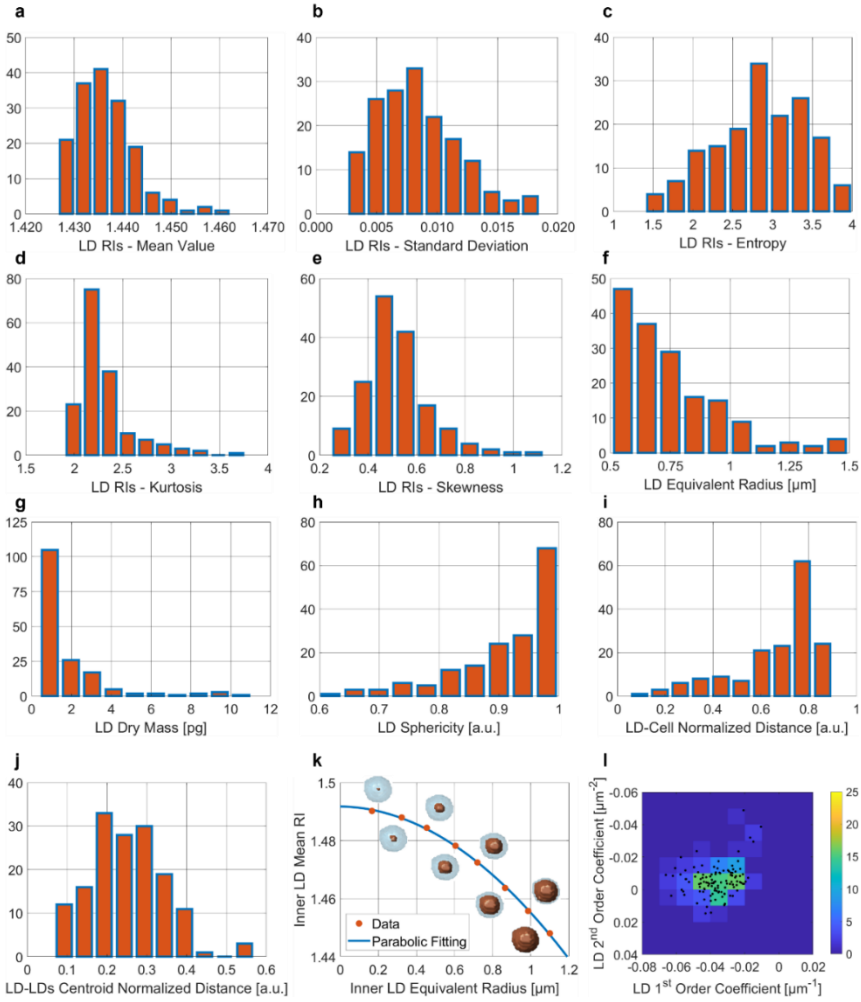

Figure 4.11 LDs features extracted from 54 A2780 3D RI tomograms.
(a-e) Histograms of respectively the mean value, standard deviation, entropy, kurtosis, and skewness of the 3D RI distributions of each LD. **(f-h)** Histograms of respectively the equivalent radius, the dry mass, and the sphericity of each LD. **(i)** Histogram of the distance between each LD centroid and the corresponding cell centroid, normalized to the cell equivalent radius. **(j)** Histogram of the distance between each LD centroid and the centroid of all the LDs inside the same corresponding cell, normalized to the cell equivalent diameter. **(k)** Mean RIs (orange dots) of concentric inner zones (orange regions) selected inside the same LD, with overlapped in blue the parabolic fitting. **(l)** Bivariate histogram of the first and second order coefficients of the parabolic fitting in (k) measured in all the LDs (black dots).

The sphericity shown in Figure 4.11(h) is instead computed as the ratio between the surface area of a sphere with same volume of the LD and its actual surface area, thus providing a quantification of the particle's shape (sphericity is 1 if the particle is a perfect sphere, otherwise it is smaller than 1 the more the particle has a non-spherical shape).

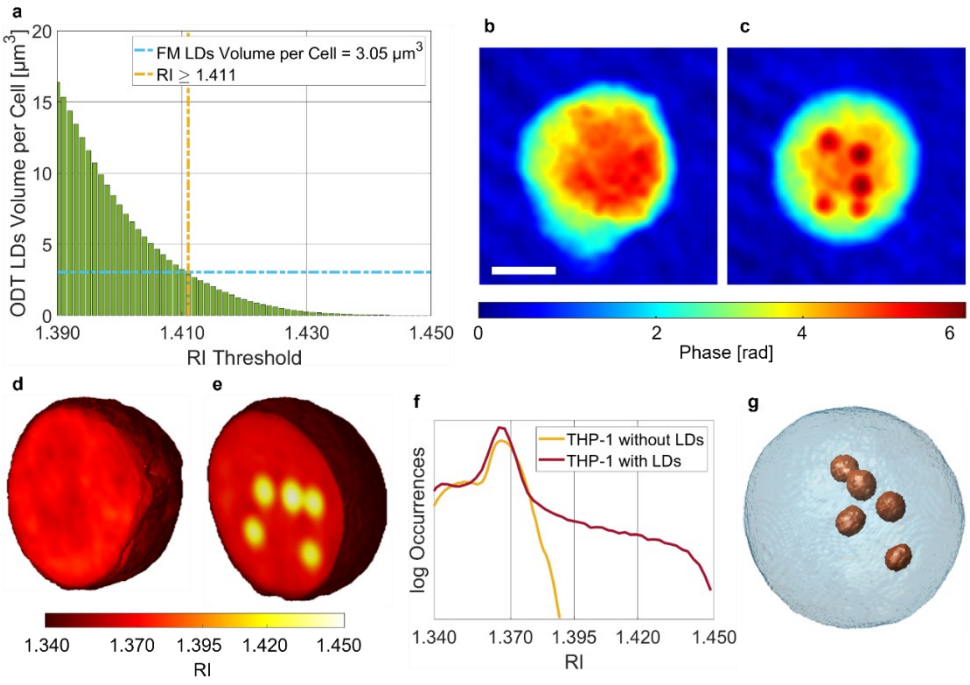

Figure 4.12 Segmentation of the LDs within the 3D RI tomograms of THP1 live cells.
(a) Average volume per cell of the LDs segmented in 34 TPM tomograms of THP1 live cells by using different RI thresholds. The selected LDs-threshold (yellow line) allows computing the same average volume measured in 2D FM images (blue line). **(b,c)** QPMs of two THP1 cells, one without LDs (b) and the other one with LDs (c) (dark red spots). Scale bar is 5 μm. **(d,e)** Central slices of the 3D RI tomograms of the cells in (b,c), respectively, in which LDs take the highest RI values. **(f)** Histogram in logarithmic scale of the 3D RI distribution of the cells in (d) (yellow) and (e) (red). **(g)** Isolevels representation of the tomogram in (e), in which LDs (orange) have been segmented by using the LDs-threshold selected in (a).

Furthermore, the proposed TPM-FC allows reconstructing the 3D tomograms of suspended cells rather than adhered cells, therefore the 3D spatial arrangement of LDs inside the cell can be accessed and investigated. In particular, in order to set parameters about this assay, the distance between the centroid of each LD and the centroid of the cell that contains it has been computed, normalized to the cell equivalent radius. It is worth to remark that the corresponding histogram, reported in Figure 4.11(i), shows a bimodal distribution. The central region of a cancer cell is usually occupied by the nucleus [302] and LDs are usually expected to be found inside the cytoplasm [332]. For this reason, most of LDs are about the 80% of the cell equivalent radius away from the cell centroid. However, there is a minor amount of LDs closer to the cell centroid, which can be explained considering that LDs are sometimes found also within the nucleus [333]. Moreover, the 3D tomograms in Figure 4.11(g-i) have confirmed the property of LDs of concentrating in the same region of the cytoplasm [334], which has been also observed in the 2D FM images. To quantify this property, for each cell, the centroid of all the LDs has been computed, and its distance from each LD has been calculated, normalized to the cell equivalent diameter. The corresponding histogram is displayed in Figure 4.11(j), which provides a characterization of the spread of the LDs positions around their own ensemble centroid. From a structural point of view, LDs are formed by an inner core which mainly stores triacylglycerols and steryl esters and are surrounded by a phospholipid monolayer studded with LD-specific proteins [335]. Therefore, the RI is expected to change passing from the outer zone to the inner zone of the LD. For this reason, concentric volumes inside the same LD have been considered. In Figure 4.11(k), it is shown a sequence of the same LD as the size of the internal structure decreases (orange regions) along with the corresponding mean RIs (orange dots). The mean RI increases passing from the overall volume, made of both the membrane and the inner core, to the sole inner core. Moreover, the computed data are perfectly fitted by a parabolic curve.

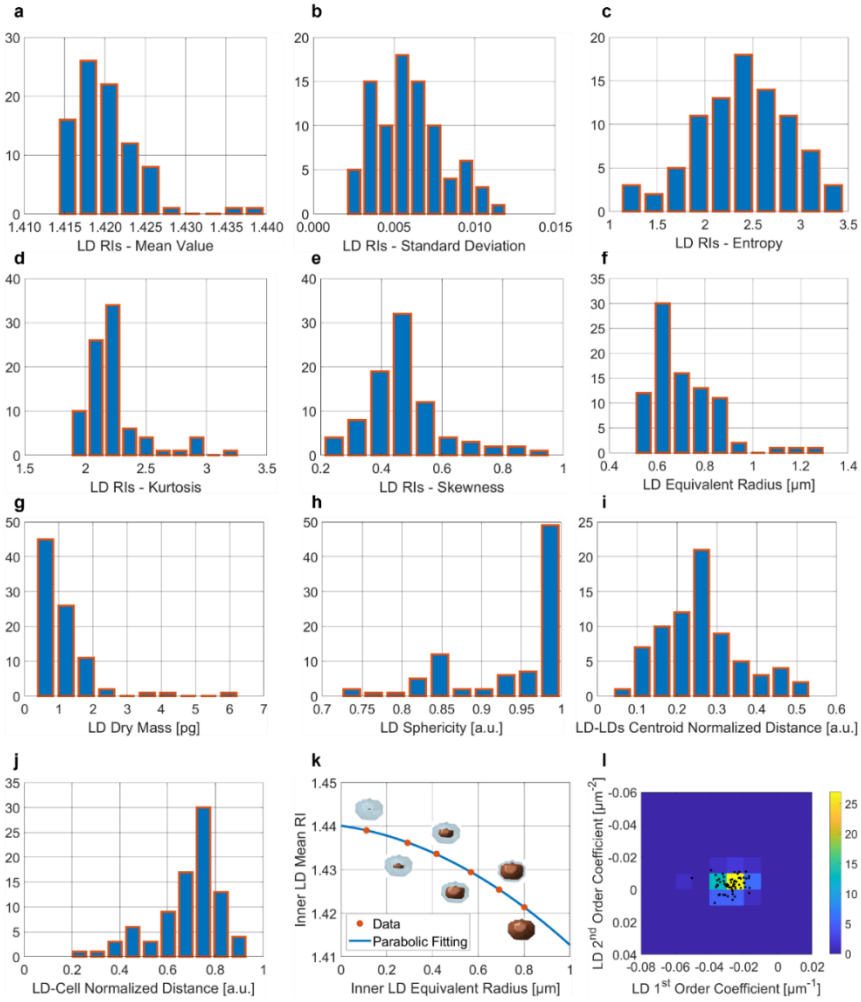

Figure 4.13 LDs features extracted from 34 THP1 3D RI tomograms.
(a-e) Histograms of respectively the mean value, standard deviation, entropy, kurtosis, and skewness of the 3D RI distributions of each LD. **(f-h)** Histograms of respectively the equivalent radius, the dry mass, and the sphericity of each LD. **(i)** Histogram of the distance between each LD centroid and the corresponding cell centroid, normalized to the cell equivalent radius. **(j)** Histogram of the distance between each LD centroid and the centroid of all the LDs inside the same corresponding cell, normalized to the cell equivalent diameter. **(k)** Mean RIs (orange dots) of concentric inner zones (orange regions) selected inside the same LD, with overlapped in blue the parabolic fitting. **(l)** Bivariate histogram of the first and second order coefficients of the parabolic fitting in (k) measured in all the LDs (black dots).

Table 13 Average values and standard deviations of the features about each LD segmented in 54 A2780 and 34 THP1 live cells.

	A2780	**THP1**
RI Mean Value	1.437 ± 0.006	1.420 ± 0.004
RI Standard Deviation	0.008 ± 0.003	0.006 ± 0.002
RI Entropy	2.851 ± 0.570	2.389 ± 0.501
RI Kurtosis	2.310 ± 0.280	2.236 ± 0.238
RI Skewness	0.520 ± 0.134	0.479 ± 0.131
Volume [μm^3]	2.267 ± 2.430	1.678 ± 1.272
Equivalent Radius [µm]	0.751 ± 0.215	0.708 ± 0.141
Surface Area [μm^2]	8.873 ± 7.038	7.109 ± 3.672
Sphericity [a.u.]	0.914 ± 0.086	0.940 ± 0.074
Dry Mass [pg]	1.757 ± 1.920	1.085 ± 0.861
LD-Cell Normalized Distance [a.u.]	0.666 ± 0.178	0.686 ± 0.139
LD-LDs Centroid Normalized Distance [a.u.]	0.251 ± 0.093	0.261 ± 0.104
1^{st} Order Coefficient Parabolic Fitting [μm^{-1}]	-0.037 ± 0.011	-0.028 ± 0.007
2^{nd} Order Coefficient Parabolic Fitting [μm^{-2}]	-0.006 ± 0.010	-0.003 ± 0.004

Therefore, the parabolic fitting has been performed for all the LDs, and their first order and second order coefficients have been reported in Figure 4.11(l) (black dots), overlapped to the corresponding bivariate histogram. This analysis confirms the higher density of the inner LD core with respect to its surrounding region. In general, the plots shown in Figure 4.11(k-l) can be used as a tool to inspect the inner LD RI distribution.

By using the same pipeline, about two hundreds of THP1 cells have been analyzed. As shown in Figure 4.12(a), by comparing the average LDs volume per cell with the 2D FM measurement, the LDs-threshold RI ≥ 1.411 has been selected. This threshold allowed identifying LDs in 34 THP-1 live cells. In Figure 4.12(b,c), the QPMs of a monocyte without LDs and with LDs are respectively shown, while the central slices of the corresponding 3D RI tomograms are reported in Figure 4.12(d,e), respectively. In both 2D and 3D cases, the LDs are clearly recognizable as distinguishable spots with the highest phase or RI values, respectively. For this reason, in the histogram of the 3D RI distribution in Figure 4.12(f), the two cells can be easily identified. Indeed, as expected, only the monocyte with LDs, which isolevels representation is displayed in Figure 4.12(g), shows an inflated distribution of RIs, due to a large number of occurrences for higher RI values. The 3D RI tomograms of the 34 THP1 monocytes have been exploited to measure the same features about LDs described in the case of A2780 cells, as shown in Figure 4.13. The average values and the standard deviations of these parameters are resumed in Table 13 for both the A2780 and THP1 cells. On average, LDs in A2780 cells have a greater RI mean value, standard deviation, entropy, kurtosis, and skewness than the THP1 monocytes. Moreover, as they are bigger in size too, they also have a greater dry mass. Again, the histogram of the LD-cell normalized distance shows a bimodal distribution, as displayed in Figure 4.13(j). In general, the 3D disposition inside the cell is about the same in both cases.

4.3.2 Detection through Biolensing Effect

Recently, it has been found that biological samples behave as optical elements. The essential biophotonic probes, based on a single-cell hierarchy, include biolasers, waveguides, and biolenses [22] [336]. Ambition for integrating these elements into the performance of photonics arises from the need for such biocompatible and available micro components. In particular, it has been

proved that many cell types, including RBCs, exhibit the biolensing effect and thus can behave as active micro-lenses, characterized by flexible focal lengths and magnifications, making them available for many applications, e.g., imaging, light coupling, and lithography [21] [337] [338]. Such a concept is useful for diagnosis at single-cell level. In fact, changes in biolens performance can be correlated directly to the living cell morphology and to the typical biochemical activities [30] [339] [340] [341] [342]. Herein, monocytes and lymphocytes, which are similar in RIs but different in sizes, have been exploited to prove the biolensing effect of the whole cell in TPM-FC [343]. In particular, the TPM-FC system in Figure 2.5 has been employed for recording the holograms of 221 monocytes and 189 lymphocytes. The holographic processing described in Section 2.4.2 has been implemented for refocusing the complex amplitude of the recorded cells. As WBCs have been recorded in flow modality, their shape is quasi-spherical as they are suspended in a buffer medium, therefore they can be treated as micro-size biolenses. Notably, as sketched in Figure 4.14(a), a sphere of RI n and diameter d, surrounded by a medium of RI n_m, and distant l from borders with the air, behaves as a lens with focal distance f given by

$$f = \frac{nd}{4(n-n_m)}\frac{1}{n_m} + l\left(1 - \frac{1}{n_m}\right), \tag{4.1}$$

which, for small distances l (in comparison to the first term), can be approximated as

$$f \approx \frac{nd}{4(n-n_m)}\frac{1}{n_m}. \tag{4.2}$$

This means that larger spheres of equal n exhibit longer focal distances than the smaller spheres if $(n - n_m) > 0$. Here, the complex amplitude propagated along the optical axis has been investigated to compare focal distances of lymphocytes and monocytes. The cell plane has been found as the axial coordinate z_{TCmin} where TC, calculated for intensity, reaches the minimum. Subsequently, the image plane has been localized as the distance z_{TCmax} where TC, calculated for intensity, reaches its maximum [174].

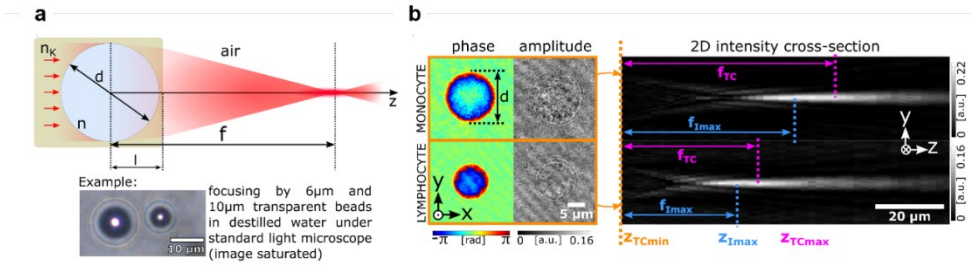

Figure 4.14 Focusing fingerprint by sphere-shaped lenses.
(a) Focusing by micro-spheres. **(b)** On the left, amplitude and phase profiles of round-shaped WBCs (monocytes and lymphocytes) and, on the right, propagated intensity profiles with corresponding focal distances.

Thus, the focal distance f_{TC} has been calculated as the difference between these two planes, i.e.

$$f_{TC} = z_{TCmax} - z_{TCmin}. \tag{4.3}$$

Secondly, the focal distance f_{Imax} has been calculated as the distance between the cell plane z_{TCmin} and the plane of maximal intensity z_{Imax} (i.e. the plane where intensity reaches its global maximum), i.e.

$$f_{Imax} = z_{Imax} - z_{TCmin}. \tag{4.4}$$

In Figure 4.14(b), f_{TC} and f_{Imax} are shown for one lymphocyte and one monocyte. As expected from Eq. (4.2), both the focal distances are higher in the case of monocytes since they have larger sizes but similar RIs than lymphocytes.

Possible applications of the cell biolensing effect in FC modality would be in the field of label-free discrimination of different cell populations in cytometric approach. There is a great demand in finding morphological biomarkers that avoid the use of fluorescent labels in order to reduce the time consumption of sample preparation and also avoid phototoxicity to allow faster and more efficient downstream analysis. Biolens modelling would be a valuable route to marker-free samples clustering because the focused light encodes information

both on shape and RI distribution inside the cell volume. Such modelling would in principle avoid the feature calculation from the whole 2D QPM. Indeed, a realistic implementation of a cytometer based on biolensing properties does not necessary need the whole DH image processing pipeline but it would be necessary the recording of the intensities by putting the camera in a well-defined range of distances and propagating the field at a nominal distance, thus strongly reducing the processing time. The use of AI would speed up the entire processing to allow video rate image analysis. In the optimized system, the expected throughput for data acquisition would be potentially the same of current IFC systems (thousands of cells per second). Moreover, also cell sorting would be feasible when video rate image analysis is supported by AI [212] [133].

However, as well as the whole cell, it has been proved that also LDs could act as intracellular micro-lenses [344]. As discussed in Section 4.3.1, as LDs are involved in a lot of pathologies, label-free methods capable to provide a fast and high-throughput detection of LDs inside single cells are strongly requested in order to aid biomedical diagnostic applications. Here a novel strategy based on HIFC for revealing in simple way the presence of intracellular LDs in each suspended living cell flowing along a microfluidic channel is investigated [345]. In particular, LDs are detected by evaluating the way their presence changes the focusing properties of the whole biolens (i.e. the hosting cell). As first step of this study, an advanced numerical simulation combined to the TPM-FC experiments has been performed in order to investigate this phenomenon. In particular, two living cell lines have been considered, that are A2780 human ovarian cancer cells as positive case, i.e., cells with high amount of LDs [291] [346], and Jurkat T-lymphocyte WBCs as negative case since, in physiological conditions, the number and the size of their LDs are very low [317] [347]. In fact, in case WBCs are in healthy conditions, LDs are not completely absent, but their number and size are low. When LDs have sizes comparable with the wavelength, they cannot be detected due to sensitivity of the presented system, that depends on the trade-

off between LDs size and axial resolution. For this reason, Jurkat T-lymphocytes have been considered as negative case. Finally, another line of WBCs, i.e., human monocytes THP1, has been recorded by the TPM-FC system before and after the appearance of LDs, in order to test the ability of the proposed approach in correctly identifying the presence of LDs. Therefore, here it has been demonstrated that the time and resource consuming 3D TPM-FC reconstruction and the nontrivial downstream segmentation of LDs can be avoided for the purpose of identifying them inside single flowing cells, since a much simpler and faster 2D HIFC system can solve this same task by exploiting the LDs biolens features.

The TPM-FC system in Figure 2.5 has been used to reconstruct the 3D RI tomograms of the A2780 ovarian cancer cell and the Jurkat T-lymphocyte cell reported in Figure 4.15(a,f), respectively. In the isolevels representation of the tomographic reconstruction displayed in Figure 4.15(b,g), the LDs are only visible in the A2780 cell, in which they have been segmented at the highest RIs (corresponding to the highest phase values in Figure 4.15(a)), as described in Section 4.3.1 [291]. The BPM forward model has been implemented to simulate the in-focus complex wavefront produced by the RI tomogram [348]. The simulated QPMs about the overall A2780 cell, the sole LDs segmented from the A2780 cell, and the Jurkat T-lymphocyte cell are shown in Figure 4.15(c,d,h), respectively. Moreover, the corresponding experimental QPMs numerically retrieved from the recorded holograms about the A2780 and the Jurkat T-lymphocyte cell are displayed in Figure 4.15(e,i), respectively, to show the reliability of the BPM.

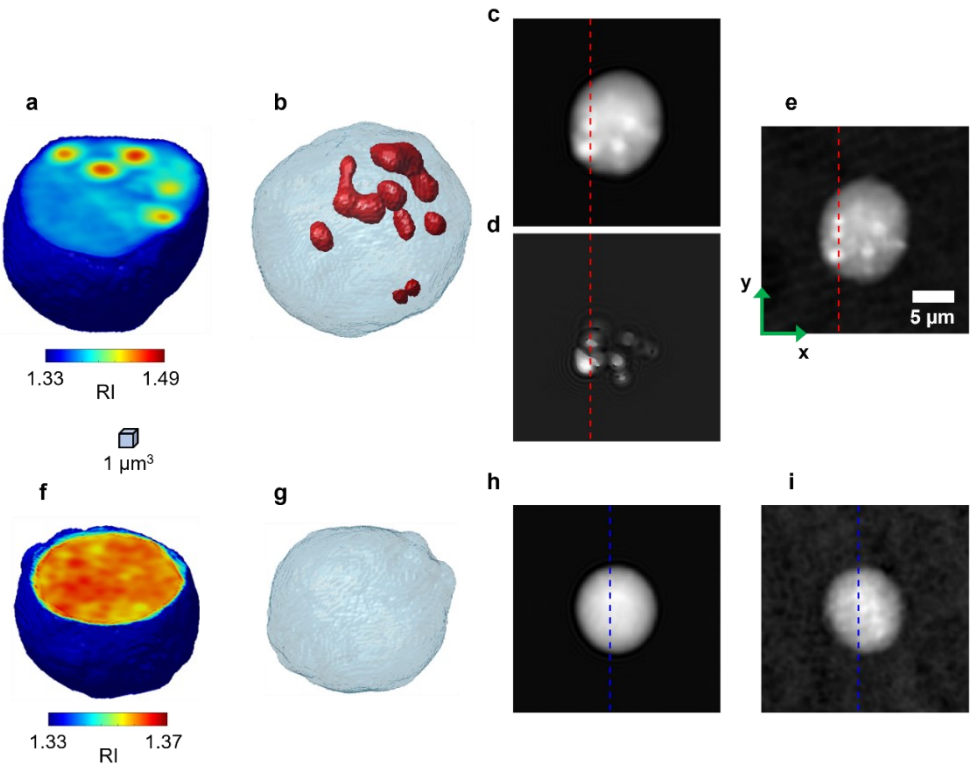

Figure 4.15 Simulation of the light beam propagation through an experimental tomogram of an A2780 ovarian cancer cell (a-e) and a Jurkat T-lymphocyte WBC (f-i) obtained by TPM-FC.
(a,f) Slice of the 3D RI tomogram reconstructed by means of the TPM-FC method. **(b,g)** Isolevels representation of the reconstructed tomograms in (a,f), respectively. In (b), LDs have been segmented at the highest RIs (red volume). In (g), LDs are missing. **(c,d,h)** QPM simulated through the BPM forward model starting from all the RIs in (a), the RIs of the sole segmented LDs in (a,b), and all the RIs in (f). **(e,i)** QPM numerically retrieved from the first frame of the experimental DH sequence used for reconstructing tomograms in (a,f), respectively. The experimental QPMs in (e,i) correspond to the simulated ones in (c,h), respectively. In (c-e), the red lines pass for the maximum phase value in (e). In (h,i), the blue lines pass for the maximum phase value in (i).

Then, both the simulated and recorded in-focus complex wavefronts have been propagated at different distances along the optical z-axis by means of the

Angular Spectrum method (see Eq. (1.19)). For each *z* position, the intensity of the propagated complex field has been considered. To deepen the effect due to the presence of LDs, within the QPMs in Figure 4.15(c-e), the vertical lines passing for the maximum phase value found in the experimental QPM in Figure 4.15(e) have been selected. In the same way, within the QPMs in Figure 4.15(h,i), the vertical lines passing for the maximum phase value found in the experimental QPM in Figure 4.15(i) have been selected. Hence, in Figure 4.16(a-e), for each *z* propagation distance, the intensity values extracted respectively from the QPMs in Figure 4.15(c-e,h,i) along the selected lines are reported. It can be noted that the intensity mapping has a remarkable difference between the A2780 and lymphocyte case. In fact, in both the simulated and the experimental intensity mapping about the A2780 cell (see Figure 4.16(a,c), respectively), there are small maximum values in the initial part of the optical *z*-axis (see the arrows before 10 μm), while they miss in both the simulated and the experimental intensity mapping about the Jurkat T-lymphocyte cell (see Figure 4.16(d,e), respectively). These maximum regions are due to LDs that behave as biolenses. In fact, due to their smaller sizes, LDs focalize much before the entire cell in a distinguishable region within the intensity mapping because of their higher RIs. This is confirmed by the intensity mapping in Figure 4.16(b) related to the sole LDs, in which the maximum areas are in the same *z* region as the overall cell in Figure 4.16(a,c), as underlined by the arrow (note that spurious frequencies are related to the numerical error in the QPM simulation visible in Figure 4.15(d) due to the high RI contrast between the LDs and the surrounding medium).Instead, in the Jurkat T lymphocyte case, there is only the maximum region at longer *z* distances due to the focalization of the overall cell, which can be in turn considered as a bigger quasi-spherical lens. Note that the focalization of the overall cell is missing in the A2780 case since a lateral line has been selected.

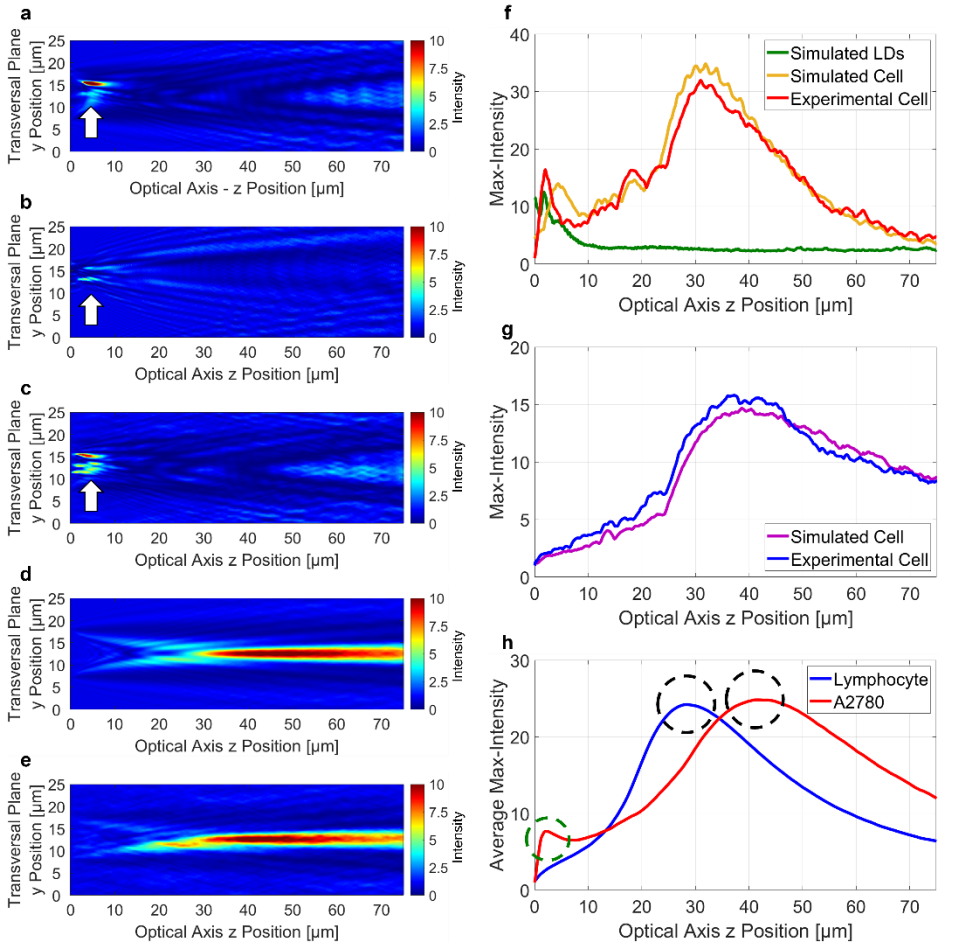

Figure 4.16 Alteration of the focalization property of the whole cell due to the presence of LDs.

(a-e) Intensity values of the complex wavefront propagated along the optical *z*-axis, taken from the *y* lines selected in Figure 4.15(c-e,h,i) regarding the simulated QPM of the overall A2780 cell, the simulated QPM of the sole A2780 LDs, the experimental QPM of the overall A2780 cell, the simulated QPM of the overall Jurkat T-lymphocyte cell, and the experimental QPM of the overall Jurkat T-lymphocyte cell, respectively. Arrows in (a-c) highlight the perturbation of the cell biolens features by LDs. **(f,g)** Max-intensity of the complex wavefront propagated along the optical *z*-axis about the analyzed A2780 cell and Jurkat T-lymphocyte cell, respectively. **(h)** Average max-intensity computed among all the Jurkat T-lymphocyte cells (blue line) and A2780 cells (red line). The high peaks (black circles) are related to the focalization of the overall cell. The small peak (green circle) is related to the focalization of LDs.

To consider the effect of the overall QPM without selecting a specific line, for each *z* distance, the maximum intensity value of the propagated complex wavefront has been computed, thus obtaining the max-intensity curves in Figure 4.16(f,g) about the analyzed A2780 and lymphocyte cell, respectively. In Figure 4.16(f), two main peaks are visible about the experimental cell, the farthest and highest one due to the focalization of the outer cell, and the closest and lowest one (before 10 μm) due to the perturbation introduced by LDs, as also confirmed by the max-intensity curve related to the sole LDs. Instead, in Figure 4.16(g), only the farthest peak related to the focalization of the whole cell can be observed. Essentially, in order to summarize the concept behind the detection of LDs, it can be useful to consider that LDs are themselves biolenses and therefore the optical properties of the overall biological optical system consists in the whole cell (primary biolens) and a number of smaller embedded biolenses (i.e. intracellular LDs). It is important to underline that the LDs detection accuracy is strictly related to the sensitivity of the max-intensity measures to provide the peak, as reported in Figure 4.15(f-h). This sensitivity depends on the trade-off between LDs size and axial resolution, i.e. LDs having sizes comparable with the wavelength cannot be detected. This suggests that such biological-lens system is more complex in respect to the single lensing effect of the cell itself.

To assess the perturbation introduced by the LDs to the biolens features of the whole cell, as summarized in Table 14, 537 QPMs of 202 Jurkat T-lymphocytes and 575 QPMs of 60 A2780 ovarian cancer cells have been recorded through the TPM-FC system, used here as HIFC system, while flowing and rotating along the microfluidic channel. In Figure 4.16(h), the max-intensity curves computed for each 2D QPM have been averaged inside the Jurkat T-lymphocyte cell line (blue) and the A2780 cell line (red), at the aim of analyzing the focalization property of these two populations on a greater number of cells. The two average max-intensity curves show again a maximum peak due to the focalization of the overall cell (black circles), while, as expected from the biological point of view, the smaller peak due to the presence of LDs

is instead localized at the initial *z* distances only in the A2780 case (green rectangle). For this reason, it is expected that the variation of the cell focalization property caused by LDs could be exploited for a fast detection of cells with LDs inside by means of HIFC. At this aim, the Jurkat T-lymphocyte WBC and the A2780 ovarian cancer cell studied in Figure 4.15 have been considered again, and the comparison between their max-intensity curves has been displayed in Figure 4.17(a).

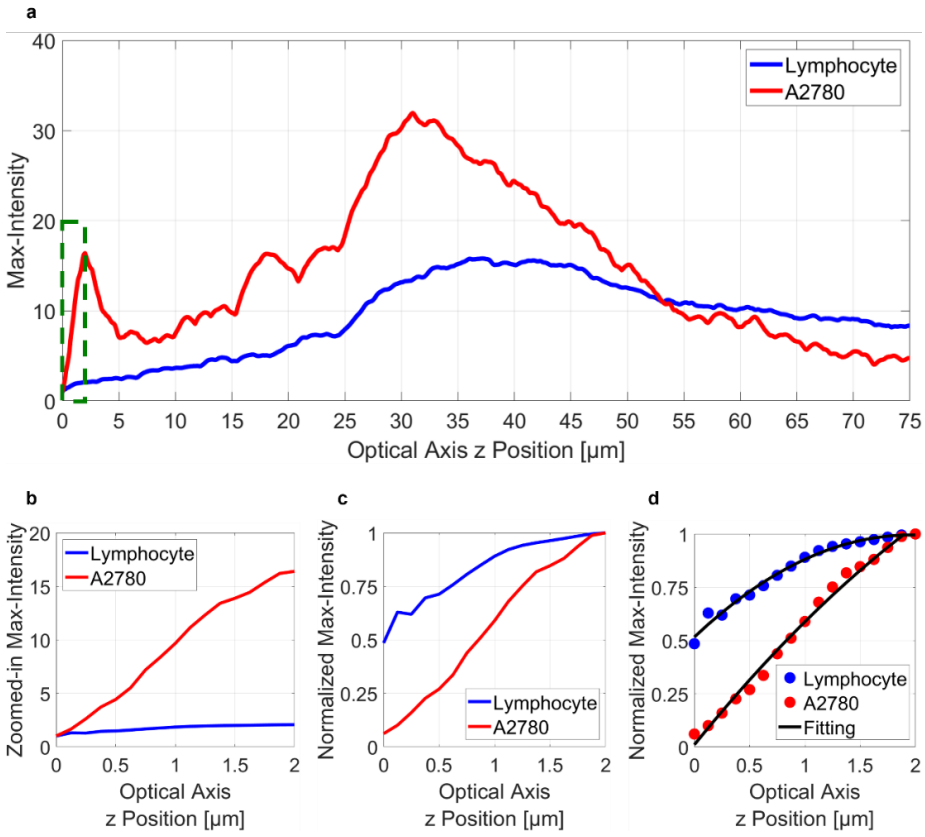

Figure 4.17 Quantitative characterization of the alteration of the cell biolens features by LDs.
(a) Comparison between the max-intensity curve of the Jurkat T-lymphocyte cell (blue line) and the A2780 cell (red line) analyzed in Figure 4.15. **(b)** Zoom-in of the max-intensity curves in (a) in the [0,2] µm region (green box). **(c)** Zoomed-in max-intensity curves in (b) normalized to their maxima. **(d)** Normalized max-intensity curves (dots) with overlapped the 2nd order polynomial fitting (black line).

As shown in Figure 4.17(b), to deepen the perturbation due to LDs, analysis about the max-intensity curve has been limited only to the first 2 μm along the optical *z*-axis, since it is the region between the focal plane of the cell and the location of the LDs peak in the max-intensity curve. In fact, this region is expected to provide the best detection accuracy in the shortest possible time, since this is the region in which the difference between the cases with and without LDs (red and blue curve, respectively) is maximized, and at the same time the depth of the *z*-stack along which the QPM is numerically propagated by means of the Angular Spectrum formula is very small (i.e., the numerical *z*-scanning is fast). To avoid errors related to the different cell sizes and not to the presence of LDs, the two zoomed-in max-intensity curves have been normalized to their maxima in the range from 0 to 2 μm, thus obtaining the normalized max-intensity curves displayed in Figure 4.17(c). As the maximum value of the zoomed-in max-intensity curve about the A2780 cell is much greater than the Jurkat T-lymphocyte one (see Figure 4.17(b)), the average value of the normalized max-intensity curve about the A2780 cell is much smaller than the Jurkat T-lymphocyte one (see Figure 4.17(c)). Moreover, the presence of LDs leads to different slopes in the initial regions of the max-intensity curves. For this reason, the normalized max-intensity curves have been fitted through a 2nd order polynomial, as reported in Figure 4.17(d)). Hence, in order to characterize the normalized max-intensity curves reported in Figure 4.17(c,d), two parameters have been considered, i.e., the average value and the quadratic coefficient of the 2nd order polynomial fitting. In the scatter plot of Figure 4.18(a), the QPMs of the recorded Jurkat T-lymphocyte and A2780 cells have been represented by means of their max-intensity average values and quadratic coefficients. Remarkably, these two parameters can provide a great separation between these two cell lines due to the presence or not of LDs, as also demonstrated by the boundary line computed through the LDA [349].

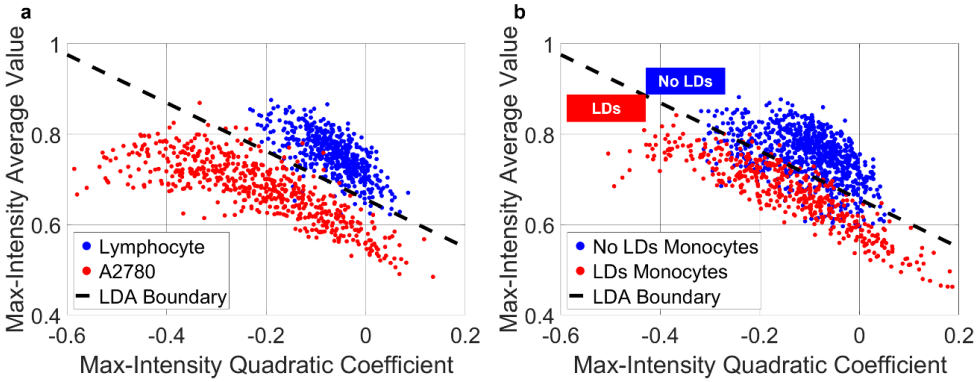

Figure 4.18 Identification of cells with LDs from the in-flow QPMs represented through their max-intensity average values and quadratic coefficients. **(a)** Scatter plot of Jurkat T-lymphocyte (blue dots) vs. A2780 (red dots) cells, separated by the line boundary computed through the LDA (black line). **(b)** Scatter plot of monocytes without (blue dots) and with (red dots) LDs, separated by the LDA boundary found in (a).

Table 14 Dataset of Jurkat T-lymphocyte and A2780 ovarian cancer cells collected through the TPM-FC.

	# QPMs	**# Cells**
Lymphocyte	537	202
A2780	575	60

To test the proposed method in recognizing cells with LDs from the experimental QPMs, another dataset has been considered, made of monocytes THP1 recorded before and after the appearance of LDs. In fact, within the WBCs, a remarkable increase in the number and size of LDs in response to stress conditions has been demonstrated [308]. For this reason, in order to promote the appearance of many and large LDs, no external agent has been exploited, but monocytes population without LDs has been left in culture for some days reducing the culture medium perfusion and thus inducing a stress condition. In particular, as summarized in Table 15, 864 QPMs related to 96

monocytes without LDs and 450 QPMs related to 50 monocytes with LDs have been considered. In Figure 4.18(b), the same LDA boundary found in the lymphocytes vs. A2780 scatter plot has been exploited to recognize the presence of LDs inside monocytes. It is worth remarking that, although the LDA has been set on a different problem, also in this case the presence of LDs has been correctly identified in most of the experimental QPMs by only exploiting the perturbation that intracellular LDs introduce to the biolens features of the whole cell. In fact, in Figure 4.18(b), an accuracy of 81.2% has been obtained in detecting or not LDs inside the 1314 analyzed QPMs. Depending on the size and RI, LDs in some angular positions in 2D QPMs can be difficult to be detected or even non detectable at all. For example, the LDs can be occluded by the complexity of the nuclei's structure. A possible solution would be recording more than one QPM of the same cell during its rotation, as occurs in the proposed system. In fact, cell rotation can allow to obtain one or more directions along which the LDs are more easily detectable, still without the need to retrieve the 3D RI tomograms. For example, in the presented case study, as reported in Table 15, only 9 QPMs per cell have been recorded. Nevertheless, by using a max-voting strategy, remarkably the accuracy increases up to 100% in detecting or not LDs inside the 146 analyzed cells.

Table 15 Dataset of monocytes THP1 collected through the TPM-FC system before and after the appearance of LDs.

	# QPMs	**# Cells**
No LDs Monocyte	864	96
LDs Monocyte	450	50

4.4 Internalized nanoGraphene Oxide for Drug Delivery Monitoring

Recently, nanographene and its derivatives have captured much attention due to their electronic properties [350] [351] and promising applications in biomedicine field, even including approaches to fight or detect infections caused by the new coronavirus SARS-CoV-2 (COVID-19) [352] [353]. Indeed, graphene and graphene oxide (GO) have been used in making DNA-based optical sensors for drug delivery [354] and for the detection of nucleic acids [355], proteins [356], virus [357], metal ions [358] and small molecules [359]. Furthermore, nGO is a promising candidate as vaccine carrier and adjuvant for efficient intracellular vaccine protein delivery [360] [361]. Different techniques are continuously developed and refined to study the interactions of Graphene Family Materials (GFMs) with biological samples. The MTT assay is used for the nonradioactive and spectrophotometric quantification of the cell proliferation, the viability in cell populations, and the in vitro toxicology [362]. A careful validation of MTT assay procedures is needed in experiments where GFMs are one of the constituents, to avoid a potential bias in concluding results of cytotoxicity studies [363]. In fact, GO is a universal fluorescence quencher [360] [364]. Hence, the use of fluorescence techniques for revealing, quantifying, and visualizing GO can be affected by the fluorescent quenching due to the interactions of nanoparticles (NPs) with fluorophores and organic dyes [365]. Thus, fluorescence-based methods are not suitable for toxicity testing of carbon-based nanomaterials. The gold standard technique to study nanomaterials-cells interaction or even mapping the GO intracellular distribution exploits electron-based microscopy, such as TEM. Furthermore, many interesting developments have been achieved recently about other imaging modalities for measuring intracellular processes as in confocal microscopy [366], multimodal optical-electron imaging [367], and hybrid Raman fluorescence spectral imaging [368] [369]. However, despite all the above-mentioned methods provide imaging and measurements in cells, very

few studies have been devoted to visualize the 3D spatial distribution of NPs uptake in a quantitative way. Confocal microscopy would be the elective optical tool to this aim. Indeed, it has been demonstrated that Confocal Raman imaging can be used for tracking the nGO cellular uptake in living cells avoiding any additional fluorescent or plasmonic tag [370]. However, while it is quite easy to perform 3D confocal scanning of cells on a flat surface, it is impossible on suspended or flowing cells. FC has been demonstrated being a suitable technology to provide quantitative measurements of the cellular uptake of NPs [371] [372], because the SSC has been correlated to the cellular granularity [371]. Unfortunately, such technology does not allow retrieving the exact localization of NPs inside the cell volume. Alternatively, the fluorescence signal of labelled NPs provides a more robust analysis [372], but fluorescent tags can influence the particle properties and behavior. DH has been recently adopted as a valuable full-field, label-free, non-invasive and high-resolution tool for nanomaterial toxicity and cell interaction studies by morphologic characterization [373] [374]. Biophysical and morphological parameters such as cell volume, thickness, density, dry mass, RI variation in time, and bio-distribution of NPs inside cell cytoplasm can be measured by phase-contrast images, without the use of chemical compounds that could interfere with nanomaterials. The ability of DH to evaluate the bio-distribution of nGO internalized in adhered live cells for 24 h and 48 h has been demonstrated [375]. However, in the previous studies, analysis was limited to 2D spatial distribution of internalized nGO inside adhered cells, while there is still a strong lack of understanding of its true 3D spatial distribution within suspended cells. TPM-FC could be exploited for this purpose. However, nGO and their aggregates strongly scatter visible light, therefore phase-contrast microscopy cannot be effective in retrieving their 3D spatial distribution. To overcome this issue, here an alternative strategy has been proposed for revealing the 3D spatial intracellular distribution of nGO, namely Tomographic Amplitude Microscopy (TAM) in FC [294]. In particular, for the first time, here it has been demonstrated that a 3D tomogram can be obtained

by using the amplitude maps (AMs) computed from the recorded digital holograms in place of QPMs, thus furnishing a complete visualization in 3D of the internalized nGO aggregates. By using fibroblast cells after 24 h and 48 h of nGO internalization, some geometrical descriptors have been here proposed to characterize the 3D intracellular spatial distributions of these NPs inside the reconstructed TAM-FC tomograms.

Murine embryonic fibroblasts NIH-3T3 cells have been chosen to analyze the effects of nGO in-vitro. NIH-3T3 cells have been grown in DMEM supplemented with 10% FBS (both Life Technologies, Carlsbad, CA), 2 mM L-glutamine (Sigma, St. Louis, MO), 100 U/mL penicillin, and 100 μg/mL streptomycin. Then, the fibroblasts have been seeded at a cell density of 5×10^4 cells/mL in a 35 mm Petri dish (WillCo) and incubated at 37 °C and in a humidified 5% CO2 atmosphere in an incubator (Esco). To investigate the 3D intracellular distribution of nGO, 50 μg/mL of nGO at intermediate oxidation degree (nGO2 [375]) has been added in the complete DMEM medium. Then, the cell culture has been monitored at different time points at 24 h and 48 h. At time points of 24 h and 48 h, cells have been detached by trypsin-EDTA and injected into a microfluidic channel to collect holographic images of flowing and rotating cells. The TAM-FC system employed for experiments corresponds to the TPM-FC system in Figure 2.5 (microfluidic channel with 200 μm × 200 μm cross section coupled to a 2048×2048 CCD camera recording at 30 fps with 5.5 μm pixel size and a 40× MO, oil immersion, NA=1.30). The sole difference between TAM-FC and TPM-FC can be found in the numerical post-processing for the tomographic reconstruction. The holographic reconstruction processing described in Section 2.4.2 has been implemented to obtain the in-focus complex wavefront, from which the AMs and QPMs have been recovered. Then, after recovering the unknown rolling angles as in Section 2.4.3 [108], for each flowing and rotating cell, TPM-FC reconstruction has been performed. Unlike cells, nGO is a strong scattering material in the visible spectrum, which causes alterations within the periodic interference fringe pattern recorded by DH. When the amount of internalized graphene is low, this disruptive

phenomenon is localized in a little region within the cell, as highlighted in Figure 4.19(a,f,k) by the blue inserts within the digital holograms of three NIH-3T3 cells treated with nGO for 24 h. The effect of the nGO cluster can be observed as a dark spot in the red inserts within the retrieved QPMs shown in Figure 4.19(b,g,l). Moreover, this dark spot appears in several images of the QPM sequence, changing its position every time because of the cell rotation. After performing the TPM-FC reconstruction on first two cells in Figure 4.19, the 3D visualization of accumulated nGO is obtained by setting a suitable threshold that allows its recognition at the lowest RI values, as shown in Figure 4.19(c,h) by black regions within the red cell shells. Instead, a third NIH-3T3 cell recorded with the same experimental conditions (i.e. after 24 h from the nGO adding in the DMEM medium) is reported in Figure 4.19(k-o), where the high light absorption caused by the nGO accumulation has led to a greater loss of information among all the holograms of the recorded sequence. Indeed, the effect of light absorption in some sample areas causes the loss fringes in the hologram, as shown in the blue insert in Figure 4.19(k). This loss of information in digital holograms provokes distortions in most of the corresponding QPMs, thus making the visualization of nGO grains unfeasible in the TPM-FC reconstruction. In fact, in Figure 4.19(m), the TPM-FC reconstruction lacks the nGO cluster, even if the graphene internalization is clearly visible in some QPMs of the sequence, as displayed in Figure 4.19(l). To overcome this drawback, here the AMs have been adopted instead of the QPMs to reconstruct the 3D tomogram, because they can collect much better the light absorption information. Figure 4.19(d,i,n) shows the AMs for the three analyzed test cases, in which the nGO grains are still visible in any image of the sequence but without the abrupt jumps that characterize the corresponding QPMs. The FBP algorithm has been implemented with the AMs and the same angles calculated by means of the recovery method explored for TPM-FC [108]. Therefore, this technique has been indicated as TAM-FC.

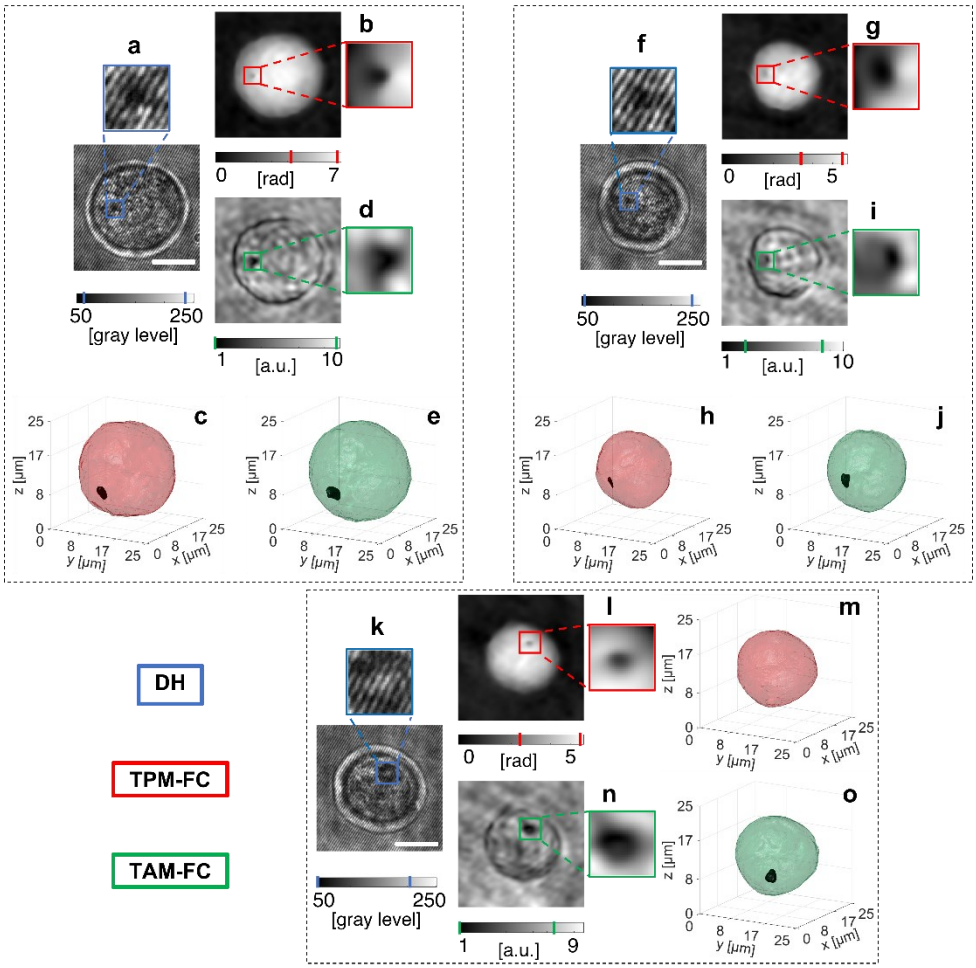

Figure 4.19 3D graphene reconstruction through TPM-FC and TAM-FC methods in three NIH-3T3 cells after 24h-treatment with nGO.
(a,f,k) Holographic ROIs with the NIH-3T3 cells, altered by the internalized nGO (blue insert). **(b,g,l)** Numerically retrieved QPMs, with highlighted in the red insert the dark spot due to nGO disturbance in (a,f,k). **(c,h,m)** Isolevels representation of the 3D TPM-FC reconstructions. In (c,h), the nGO accumulation (black) is segmented from the outer cell (red), while this is not possible in (m). **(d,i,n)** Numerically retrieved AMs, with highlighted in the green insert the dark spot due to nGO disturbance in (a,f,k). **(e,j,o)** Isolevels representation of the 3D TAM-FC reconstructions, in which the nGO accumulation (black) is segmented from the outer cell (green). Scale bars are 10 µm. Colorbars intervals refer to the inserts.

While in TPM-FC the reconstructed tomogram is the quantitative 3D spatial distribution of cell RI, in TAM-FC the reconstructed tomogram can only be considered as a 3D visualization of intracellular regions having different light attenuation coefficients. However, the lack of artifacts in the AMs allows the complete identification of the 3D graphene spatial distribution within the tested NIH-3T3 cells by means of TAM-FC also in the third analyzed cell for which TPM-FC fails, as reported in Figure 4.19(o). Moreover, as proof of the effectiveness of the proposed approach, the TAM-FC reconstructions about the other two test cases in Figure 4.19(e,j) show remarkable similarities with the TPM-FC ones in Figure 4.19(c,h), respectively, but at the same time it is clear that TAM-FC improves the 3D visualization of the nGO cluster, which instead is incomplete in TPM-FC because of the loss of information in the generative QPMs.

It is worth pointing out that the higher the quantity of internalized nGO, the less the ability to provide an effective TPM-FC reconstruction. Therefore, in case of huge nGO internalization, the proposed TAM-FC reconstruction method is the key-approach for detecting accurately the 3D spatial distribution of nGO within cells. To prove this, an NIH-3T3 cell has been studied after a 48h-treatment, in which a massive nGO internalization can be observed. This is evident in the four frames taken from the recorded holographic sequence displayed in Figure 4.20(a). Graphene has arranged as a ring within the cell around the nucleus (nuclear decoration [372] [375]), thus occupying a large cell volume. Consequently, phase retrieval fails for any hologram of the sequence, thus preventing the TPM-FC reconstruction, as displayed in Figure 4.20(b). In fact, when the cluster absorbs too much light, the signal collected by the sensor is too low to properly detect the object wavefront modulation of the fringe's carrier. As a result, information in that area is lost, and in turn the QPM signal cannot be retrieved. The phase signal is discontinuous in this sense, since it varies from defined values to undefined values.

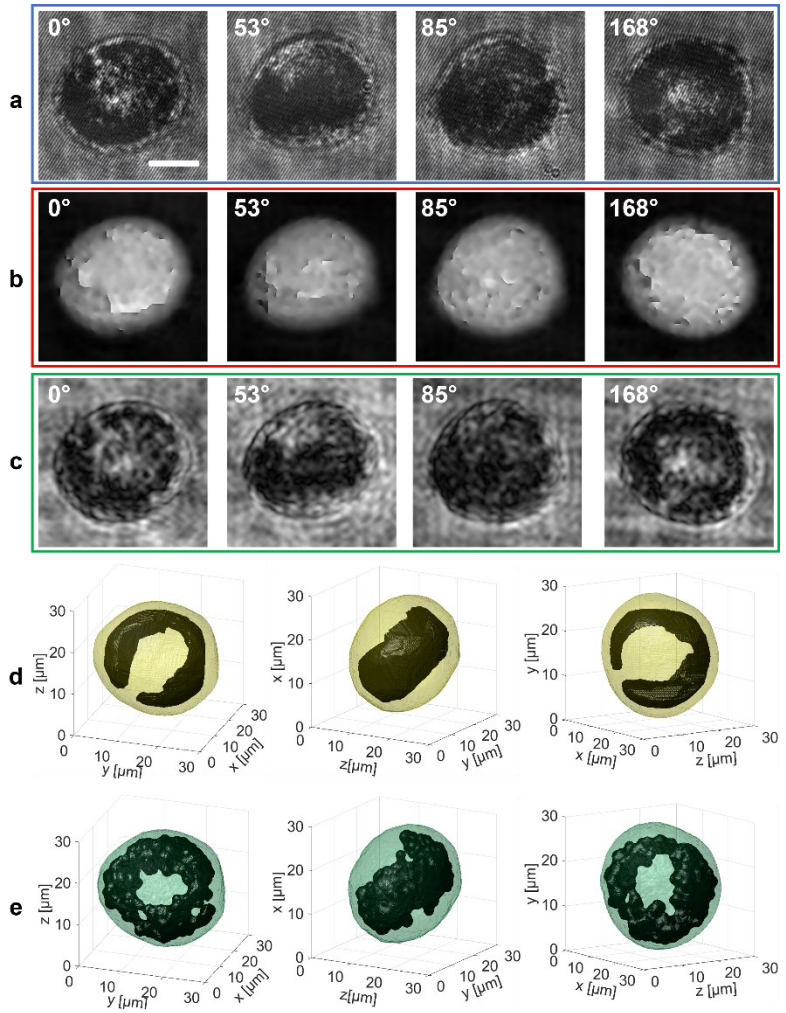

Figure 4.20 3D graphene reconstruction in an NIH-3T3 cell after 48h-treatment with nGO.

(a) Four frames taken from the recorded holographic sequence of the rolling cell, from which a ring-shaped nGO spatial distribution can be inferred. **(b)** QPMs numerically retrieved from (a), in which the phase jumps are not corrected by the unwrapping algorithm. **(c)** AMs numerically retrieved from (a), in which the dark regions are due to the light attenuation of the internalized graphene. **(d,e)** Three views of the isolevels representation of the tomogram reconstructed through SFS and TAM-FC algorithms, respectively, in which the internalized nGO (black), segmented and isolated from the outer cell (yellow and green, respectively), distributes as a 3D ring, as observed in 2D images in (a-c). Scale bar in (a) is 10 μm. In (a-c), the estimated viewing angles are reported at the top.

If phase unwrapping is performed to obtain the quantitative optical thickness map, this will show unreliable values in that area and the unwrapping error might propagate also in different areas [17]. Thus, one cannot rely on the QPM in the presence of highly absorbing clusters for achieving quantitative information. Instead, the dark ring region is properly preserved in the AMs in Figure 4.20(c), thus the TAM-FC approach is able to recover the 3D visualization of internalized nGO with high accuracy, as shown by three different views of the TAM-FC reconstruction in Figure 4.20(e). To further demonstrate the effectiveness of TAM-FC algorithm, a comparison with a well-established 3D shape reconstruction method has been performed, namely Shape From Silhouette (SFS) [376], already demonstrated to recover the 3D visualization of live cell [377]. Here, the SFS algorithm has been performed separately on the overall cell to reconstruct the cell shell, and on the nGO distribution obtained from AMs. The result, reported in Figure 4.20(d), clearly shows low resolution in defining the nGO shape if compared to the TAM-FC reconstruction in Figure 4.20(e).

The tomographic results reported here allow a much more complete understanding of the nGO internalization process in respect to the previous 2D methods [375]. In fact, by means of the proposed TAM-FC, a 3D visual analysis is immediately available, thus furnishing insights on how nGO is clustering and spatially distributing within the cell volume. Besides, beyond this very useful full 3D direct visualization, quantitative 3D measurements have been here extracted for a full nGO characterization. These quantitative parameters can be the bases for the definition of biomarkers for nGO-cell interaction in terms of 3D spatial intracellular deployment of nGO. At the aim to define some 3D morphological parameters to investigate nGO positioning and shapes, the TAM-FC reconstructions at 24 h of Figure 4.19(e,j,o) are reported again in Figure 4.21(a-c) and named cell 1, cell 2 and cell 3, respectively.

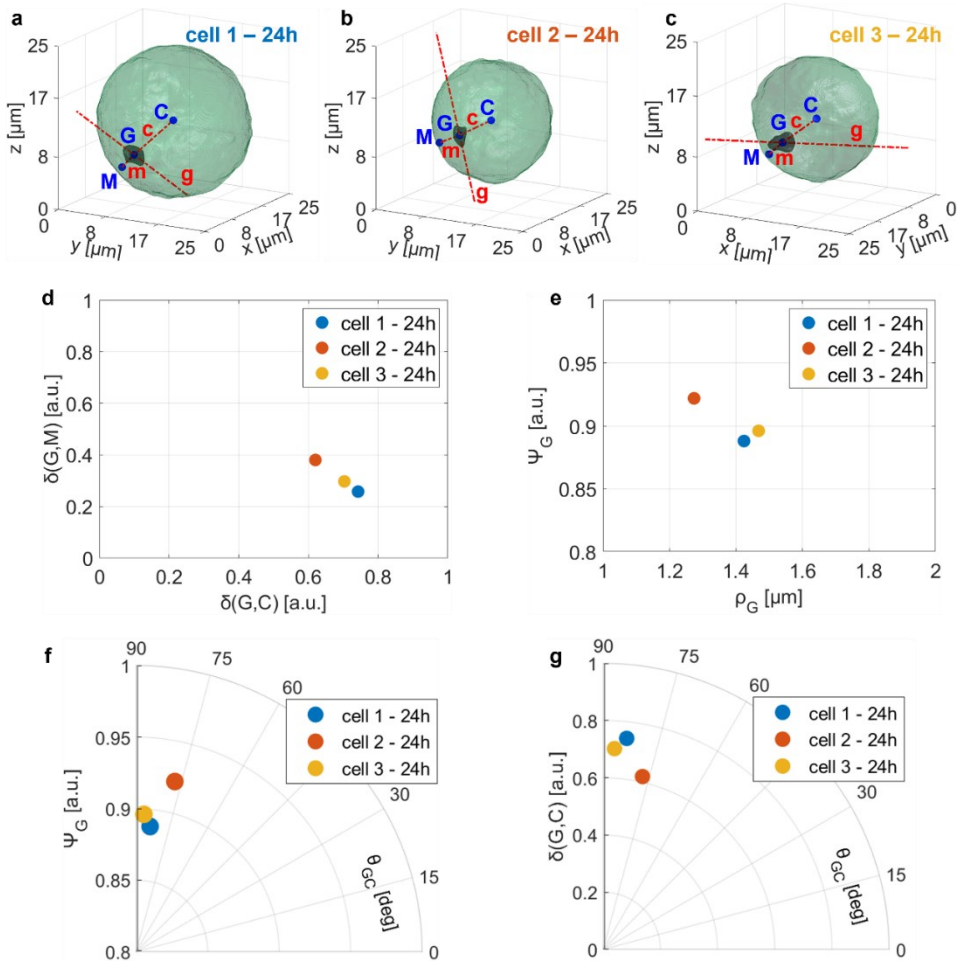

Figure 4.21 3D quantitative Euclidean analysis from TAM-FC reconstructions of nGO uptake in NIH-3T3 cells after 24h-treatments.

(a-c) TAM-FC reconstructions of three 24h-cells (green) and their nGO clusters (black). C is the cell centroid, G is the graphene centroid, and M is the nearest point of the external cell membrane to point G. Line c joins points C and G, and line m joins points M and G. Line g passes for point G and is orientated like 3D nGO cluster. **(d)** Cartesian plot of graphene-cell normalized distance $\delta(G,C)$ vs. graphene-membrane normalized distance $\delta(G,M)$. **(e)** Cartesian plot of graphene sphericity Ψ_G vs. graphene equivalent radius ρ_G. **(f)** Polar plot in which the radial coordinate is the graphene sphericity Ψ_G and the angular coordinate is the graphene-cell angle θ_{GC}. **(g)** Polar plot in which the radial coordinate is the graphene-cell normalized distance $\delta(G,C)$ and the angular coordinate is the graphene-cell angle θ_{GC}.

In particular, they have been measured the graphene-cell normalized distance $\delta(G,C)$, the graphene-membrane normalized distance $\delta(G,M)$, the orientation of the detected nGO cluster (i.e. the graphene-cell angle θ_{GC}), its sphericity Ψ_G, and its equivalent radius ρ_G. In all three cases, nGO clusters are about in the same relative position between cell centroid and cell membrane, as shown by the $\delta(G,C)$ vs. $\delta(G,M)$ plot in Figure 4.21(d), and moreover they are closer to the cell membrane, as displayed in Figure 4.21(a-c). Their sphericity Ψ_G decreases with a bigger graphene equivalent radius ρ_G, as reported in Figure 4.21(e), and with a bigger graphene-cell angle θ_{GC}, as shown by polar plot in Figure 4.21(f). In addition, as also visible in Figure 4.21(a-c), nGO clusters are oriented about orthogonally with respect to cell radius, but graphene-cell angle θ_{GC} slightly decreases with the graphene-cell normalized distance $\delta(G,C)$, as reported in the polar plot in Figure 4.21(g). Hence, passing from 24 h to 48 h, as the volumes of nGO clusters increase, their sphericities reduce since they stretch orthogonally with respect to cell radius, in order to finally form a unique 3D ring structure, as visible in Figure 4.21(e).

Furthermore, the test case reported in Figure 4.20 needs a more sophisticated morphological analysis. The 3D shape of nGO in Figure 4.20(e) has been modeled as a toroid having its same volume, as shown by the inset in Figure 4.22(a). The toroid provides a rough estimation of the nuclear size, since the 3D nGO ring distributes around nucleus without accessing it, because nGO particles are larger than the functional diameter of the nuclear pores [375]. This information is very valuable in a label-free technique such as DHM, in which the intracellular identification is still an open and challenging issue, since no dyes are used to make nucleus visible and easily detachable from the surrounding cytoplasm. Moreover, the toroidal modelling can be exploited for an additional quantitative analysis about 3D nGO distribution by unrolling its shape through the conversion in spherical coordinates, i.e. azimuthal angle, elevation angle and radial distance, as reported in yellow in Figure 4.22(a).

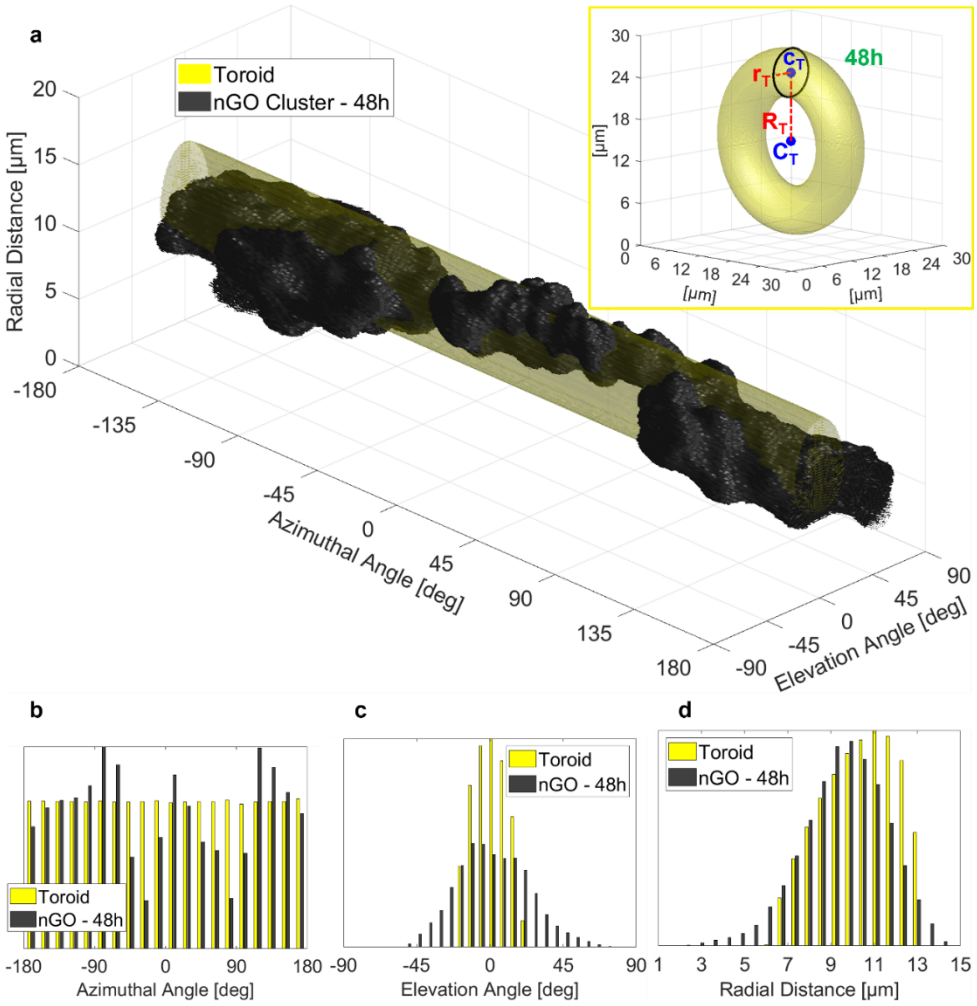

Figure 4.22 3D quantitative Euclidean analysis from TAM-FC reconstructions of nGO uptake in NIH-3T3 cells after 48h-treatments.

(a) Modelled toroid (yellow) and 3D nGO ring structure (black) unrolled by converting the cartesian coordinates in spherical coordinates. In the insert, toroid used to model 3D nGO ring structure of the 48h-cell. C_T is the centre of the toroid and c_T is the centre of its generator circle (black), which radius is r_T (inner radius). The outer radius R_T is the distance between centres C_T and c_T. **(b-d)** Comparison between the histograms of the modelled toroid (yellow) and the 3D nGO ring structure (black) about the azimuthal angle, the elevation angle and the radial distance, respectively.

Table 16 Morphometric features measured in the TAM-FC reconstructions of four NIH-3T3 cells, analysed after 24 h and 48 h from the nGO adding in DMEM medium.

	24 h cell 1	*24 h cell 2*	*24 h cell 3*	*48 h*
	Figure 4.19(e)	*Figure 4.19(j)*	*Figure 4.19(o)*	*Figure 4.20(e)*
Cell Volume [μm³]	6006.59	3053.92	3092.40	9478.44
Cell Equivalent Radius [μm]	11.28	9.00	9.04	13.13
Graphene Volume [μm³]	12.10	8.66	13.25	2339.69
Graphene Equivalent Radius [μm]	1.42	1.27	1.47	8.24
Graphene-Cell Volume Ratio [%]	0.20	0.28	0.43	24.68
Graphene Surface Area [μm²]	28.69	22.12	30.22	1933.38
Graphene Sphericity [%]	0.89	0.92	0.90	0.44
Graphene 1st Principal Axis [μm]	3.47	2.85	3.60	-
Graphene 2nd Principal Axis [μm]	2.90	2.47	2.64	-
Graphene 3rd Principal Axis [μm]	1.72	1.77	2.08	-
Graphene-Cell Distance [μm]	8.35	5.51	6.25	1.79
Graphene-Membrane Distance [μm]	2.90	3.38	2.64	-
Graphene-Cell Normalized Distance [a.u.]	0.74	0.62	0.70	-
Graphene-Membrane Normalized Distance [a.u.]	0.26	0.38	0.30	-
Graphene-Cell Angle [deg]	83.63	77.17	86.76	-
Toroid Outer Radius [μm]	-	-	-	9.88
Toroid Inner Radius [μm]	-	-	-	3.47
Azimuthal Angle Percentage Error [%]	-	-	-	24.40
Elevation Angle Percentage Error [%]	-	-	-	54.82
Radial Distance Percentage Error [%]	-	-	-	30.72

The same calculation has been performed on the nGO shape, reported in black in Figure 4.22(a), enabling a quantitative evaluation about the surface irregularity through histograms of spherical coordinates in Figure 4.22(b-d). A detailed discussion about the geometrical analysis is provided in Appendix A.7.

To summarize all the quantitative descriptors, a set of parameters measured from the TAM-FC reconstructions discussed in Figure 4.19(e,j,o) and Figure 4.20(e) is reported in Table 16, including those described in Figure 4.21, Figure 4.22, and in Appendix A.7. In particular, the graphene volume increases of two orders of size in passing from 24 h to 48 h. As a consequence, the cell

equivalent radius grows by few microns, since a large amount of graphene is internalized. These volumetric measurements could be very useful to study the cytotoxicity effects due to nGO uptake, for example to kill sick cells, such as tumour cells [378].

4.5 Encoding Tomographic Data via 3D Zernike Descriptors

In the last decade, very promising results of TPM in biomedicine have demonstrated the effectiveness of this technology as a novel imaging modality for single-cell studies (see Chapter 1). The recent demonstration of TPM-FC has added the missing milestone for employing this technology in high-throughput modality, as discussed in Section 2.4, and several applications have been herein demonstrated. Depending on the number and the velocity of cells simultaneously imaged in the FOV, the throughput can vary from tens to thousands of cells per minutes. While this is a unique opportunity for in-depth single-cell analysis with high statistical relevance, it also poses a non-negligible problem in terms of data management. In the case of TPM-FC, usually tens to hundreds QPMs have to be reconstructed in focus for each cell to estimate its 3D RI tomogram. Of course, reducing the number of probing directions relaxes data managing and computational burden but trading off resolution. The huge amount of data has pushed the scientific community to improve computational processing in terms of costs and speed through AI [211]. The latest result herein reported regards the use of DL to make the holographic reconstruction process up to 45 times faster (see Section 3.1) [213]. Recently, it has been demonstrated the possibility to achieve potentially more than 10000 tomograms per second, using only 4 views acquired simultaneously with an angle-multiplexing illumination strategy and exploiting DL to recover the missing information [379]. It is evident that,

storing and managing 3D data in a fast and accessible way will be necessary to make TPM-FC technology truly exploitable in clinical applications. This issue can be framed within the wide field of volumetric image analysis. In fact, a large variety of image coding techniques exist [380], such as transform based techniques like Discrete Wavelet Transforms (DWTs). Other approaches use a different paradigm based on video coding methodologies such as H.264/MPEG-4 AVC and H.265/MPEG-HHEVC [381] to compress 3D and 4D medical image datasets. Despite very recent and highly performing 3D coding strategies [382] [383] [384], at present, the most commonly used volumetric image analysis methods are based still on 3D DWTs [385]. An alternative scheme, based on the 3D extension of Zernike polynomials, was proposed by Canterakis [386] with the aim to have an all-round tool for 3D image analysis and recognition. It was demonstrated that the 3D Zernike representation is a natural extension of spherical harmonics based descriptors, providing complete orthonormal affine invariants and guaranteeing very high coding performance, especially for objects having spherical-like symmetries. Indeed, this methodology was successfully employed in a wide range of applications, ranging from the conventional 3D shape compression and retrieval [387] and, very recently, to 3D protein shape investigation [388].

Considering that in the natural environment of cells, such as in continuous flow, their 3D shape can be considered almost spherical, here the Zernike polynomials basis in 3D space is introduced for representing single-cell tomograms. In particular, it is described the possibility to encode 3D tomographic data into a sequence (i.e. a 1D numerical string) of the corresponding 3D Zernike Descriptors (3DZD) without significant loss of information [295]. In this way, the 3DZD can encode tomographic data with a-priori chosen fidelity. Squeezing single-cells tomograms via 3DZD has not been investigated before. Moreover, an intrinsic relation between Zernike polynomials and single-cell QPI has been recently discovered, showing that cells can be modeled as biological opto-fluidic microlenses [21]. Here, such modelling is extended to 3D TPM. Since the cell's QPM is the 2D projection of

the 3D real object (i.e. the tomogram), the 3D extension of Zernike polynomials can be also considered as the generalization of the microlens volumetric shaping. This concept opens to a new paradigm for managing tomograms through 3D Zernike polynomials, not only limited to the compression and reconstruction of 3D tomographic data but interpreting the 3DZD and related aberrations as the fingerprint of the subcellular structures. The 3DZD-based reconstruction is firstly demonstrated with a simulated tomographic cell phantom (i.e. a ground truth), with the aim to define the Zernike polynomials order needed to reach a reconstruction's fidelity score, fixed as < 1% of the Normalized Root Mean Square Error (NRMSE) between the reconstruction and the ground truth. Moreover, a performance analysis of the proposed Zernike based encoding scheme is reported, in comparison with the most used volumetric image compression strategy based on the 3D DWTs. Then, the method is validated on several single-cell tomograms data, recorded by TPM systems in static [389] as well as in the most relevant case of flow cytometry conditions, i.e. TPM-FC. This breakthrough methodology can pave the way for novel approaches in tomographic data management and storage, since it allows to replace 3D data with 1D sequences (i.e. the 3DZD), reducing the problem dimensionality while maintaining the same degree of data richness.

In optical imaging, Zernike polynomials are commonly used to study wavefront aberrations [390], but they have been recently exploited to model QPMs of living cells [22]. In analogy to the 2D case, the 3D version of Zernike polynomials and the relative coefficients, i.e. 3DZD, can be used to represent single-cell 3D RI distributions. Let $T(\mathbf{x})$ be a tomographic reconstruction. Its reconstruction using the 3D Zernike basis functions $Z_{nl}^{m}(\mathbf{x})$ is

$$T(\mathbf{x}) \approx \tilde{T}(\mathbf{x}) = \sum_{n,l,m} \Omega_{nl}^{m} Z_{nl}^{m}(\mathbf{x}), \tag{4.5}$$

where $\tilde{T}(\mathbf{x})$ is the approximated tomogram, $\mathbf{x} = (x, y, z)^T$ are the Cartesian coordinates, n, l, m are integer indexes such that $n \epsilon [0, N]$, $l \leq n$ with $n - l$ even numbers and $m \in [-l, l]$, and N is the maximum polynomial order. The Ω_{nl}^{m} value are the 3DZD that can be calculated by solving the equivalent linear

system after vectorizing the terms in Eq. (4.5), i.e. in the similar way to the 2D case for the wavefront aberrations computing [390]. All details about the mathematical derivation of 3D Zernike basis functions in Eq. (4.5) and the computation of the 3DZD are reported in Appendix A.8. Theoretically, the exact reconstruction of a tomogram can be achieved if and only if $N \to \infty$, so the left side of the Eq. (4.5) holds with the sign of equality.

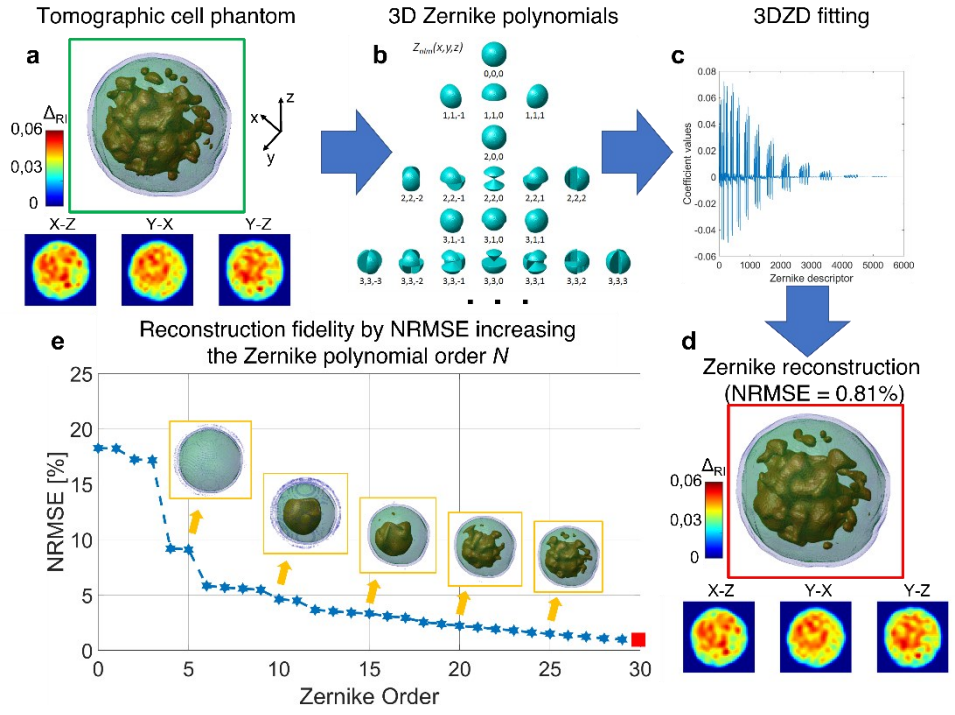

Figure 4.23 Proof of 3DZD encoding for high fidelity recovery of tomographic data.

(a) Isolevel image of a tomographic cell phantom with three inset images reporting the central slices along orthogonal directions. **(b)** Shapes visualization of the first 20 Zernike polynomials (up to order $N = 3$). **(c)** 3DZD obtained by fitting the tomographic cell phantom with Zernike polynomials up to order $N = 30$ (corresponding to 5456 descriptors). **(d)** Tomogram recovery by using the 3DZD, reporting a fidelity score of $NRMSE = 0.81\%$. The retrieved isolevel image and relative central slices show high visualization fidelity too if compared to (a). **(e)** NRMSE vs. Zernike order. Inset figures report isolevel images reconstructed by fixing the Zernike polynomials order up to 5, 10, 15, 20, 25, showing the retrieval of tiny details when the order of basis functions employed for fitting grows.

Of course, one can obtain only an approximation of the tomogram by using a finite value of N. Here the aim is to find the value of N such that the reconstruction via 3DZD is as faithful as possible to the ground truth $T(\mathbf{x})$. To do this, the NRMSE between the 3DZD reconstruction and the original tomogram has been used, and the desired fidelity has been fixed at $NRMSE < 1\%$ to guarantee the quasi lossless data encoding. Figure 4.23 reports the demonstration of the ability of 3DZD to reproduce a simulated tomographic cell phantom of sizes $50 \times 50 \times 50$ pixels by using 3D Zernike polynomials up to order $N = 30$, which corresponds to 5456 Zernike basis functions and related 3DZD. In particular, Figure 4.23(a) shows the isolevel RI distribution of the simulated phantom with three inset images reporting the central slices along the three main orthogonal directions. Figure 4.23(b) displays only the first 20 Zernike basis functions, corresponding to the order $N = 3$, while Figure 4.23(c) reports the estimated 3DZD. The isolevels RI distribution and the related central slices of the recovered tomograms calculated by using the right side of the Eq. (4.5), i.e. $\tilde{T}(\mathbf{x})$, and resulting in a $NRMSE = 0.81\%$, are reported in Figure 4.23(d). Finally, Figure 4.23(e) shows the trend of the tomogram recovery fidelity in terms of NRMSE using the 3DZD when the order of Zernike polynomials employed for the fitting grows. Notice that, tiny details (i.e. substructures with smaller sizes) become visible for high order Zernike polynomials (greater than 20) as highlighted by the inset isolevels images in Figure 4.23(e).

In order to further evaluate the performance of the proposed method, the comparison among the 3DZD-based representation and some 3D DWTs is reported in Figure 4.24, in case of two different sizes of the simulated tomographic cell phantom, i.e. $50 \times 50 \times 50$ pixels, used for the results reported in Figure 4.23, and $100 \times 100 \times 100$ pixels. In particular, three wavelet basis sets are considered, namely Symlet 4, Daubechies 4, and Coiflet 4, up to six decomposition levels. For this analysis, two complementary performance metrics are considered, i.e. the above used NRMSE and the percentage of the memory space saving, calculated as

(4.6) $$space\ saving = 100\frac{\#voxels - \#3DZD}{\#\text{voxels}},$$

where the symbol # is the operator that quantifies the cardinality of a set. In the case of the results in Figure 4.23, $\#voxels = 50^3$ and $\#3DZD = 5456$, hence resulting in a $space\ saving = 95.64\%$ with a corresponding $NRMSE = 0.81\%$. Figure 4.24(a,b) report the comparison, respectively in terms of NRMSE and space saving, among the 3DZD encoding method (dashed green lines) and the considered 3D DWTs (by varying the decomposition level from 1 to 6) in the case of $\#voxels = 50^3$. Notice that, to reach a $NRMSE < 1\%$, all wavelet basis functions need to be used with a decomposition level 1, as reported in Figure 4.24(a), which corresponds to a lower space saving (i.e., 82.44%) in respect to the 3DZD strategy, as reported in Figure 4.24(b). Conversely, to guarantee a space saving value greater than 95%, the 3D DWTs have to be used with at a decomposition level greater than 1, as reported in Figure 4.24(b), but the corresponding NRMSE increases up to 2.94%, as reported in Figure 4.24(a). Moreover, notice that the wavelet basis Coiflet 4 is not able to exceed a space saving value greater than 90% even with the highest decomposition level. In summary, the proposed 3DZD representation shows superior performance respect to the selected 3D DWTs, in terms of the coupled metrics NRMSE and space saving. Among the three wavelet basis sets, Symlet 4 shows the best overall performance, therefore it is considered for the comparison with the 3DZD approach when the sizes of the simulated tomogram increase up to $\#voxels = 100^3$. In this case, from Figure 4.24(c,d), it can be observed that the 3DZD method achieves a $space\ saving > 99\%$ (i.e., 99.45%) but still preserving the fidelity score with a $NRMSE < 1\%$ (i.e., 0.95%). On the contrary, the Symlet 4 can approximate better the simulated phantom ($NRMSE = 0.10\%$) at decomposition level 1, as reported in Figure 4.24(e), but with a space saving of 85.11%, as reported in Figure 4.24(f). Instead, by fixing a space saving greater than 99%, achievable with a decomposition level 3, just a $NRMSE = 3.19\%$ can be reached.

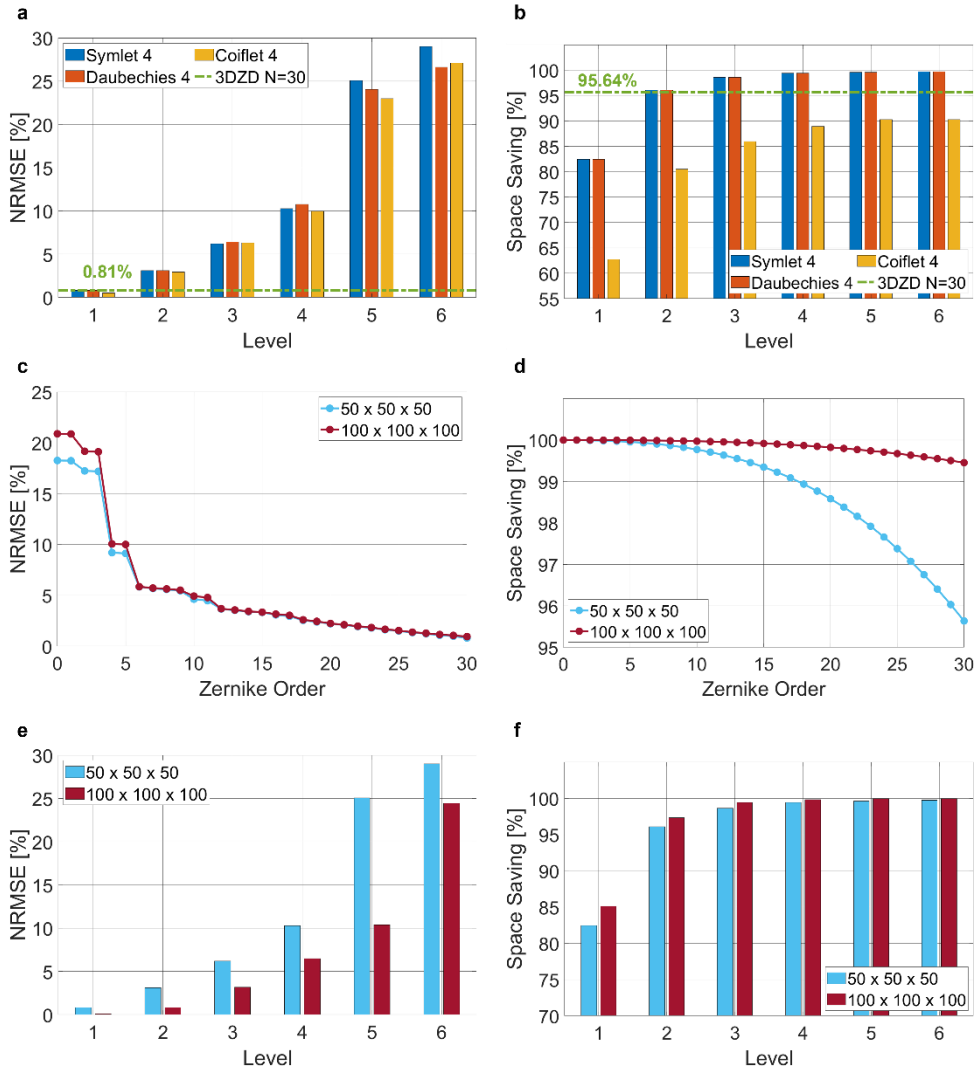

Figure 4.24 Performance analysis of the 3DZD method vs. 3D DWTs. **(a,b)** NRMSE and space saving, respectively, obtained by encoding the tomogram through three different 3D DWTs (i.e., Symlet 4, Daubechies 4, and Coiflet 4) at six decomposition levels. The dashed green lines correspond to the NRMSE and space saving, respectively, of the 3DZD approach at the order $N = 30$. **(c,d)** NRMSE and space saving, respectively, obtained by fitting the tomogram through different orders of the 3DZD at two spatial resolutions (i.e., $50 \times 50 \times 50$ and $100 \times 100 \times 100$). **(e,f)** NRMSE and space saving, respectively, obtained by fitting the tomogram through different decomposition levels of the Symlet 4 at two spatial resolutions (i.e., $50 \times 50 \times 50$ and $100 \times 100 \times 100$).

The validation of the proposed approach is achieved in the case of experimental data on living cells, acquired using different TPM systems, i.e. TPM-FC and TPM-ISC, and processed by different tomogram reconstruction algorithms, i.e. the conventional FBP algorithm and the LT method, respectively. In all cases, to perform a fair comparison in terms of NRMSE and visual inspection, the spatial resolution of original tomographic data is set at $50 \times 50 \times 50$ and the 3D Zernike polynomials are used up to the order $N = 30$, i.e. calculating $\#3DZD = 5456$ corresponding to a fixed $space\ saving = 95.64\%$. Figure 4.25 reports three quasi-spherical cells approximated with the 3DZD recovery method. Among them, the THP-1 monocyte in Figure 4.25(a) and the SKOV3 ovarian cancer cell in Figure 4.25(b) have been acquired by the TPM-FC system in Figure 2.5 and reconstructed with the FBP method, while the tomographic data of the Yeast cell in Figure 4.25(c) has been collected with a TPM-ISC system [389] and reconstructed with the LT algorithm [391]. Notice that the NRMSE for the cells in Figure 4.25(a,b) is less than 1%, while the approximation of the Yeast cell in Figure 4.25(c) provides a $NRMSE = 1.80\%$.

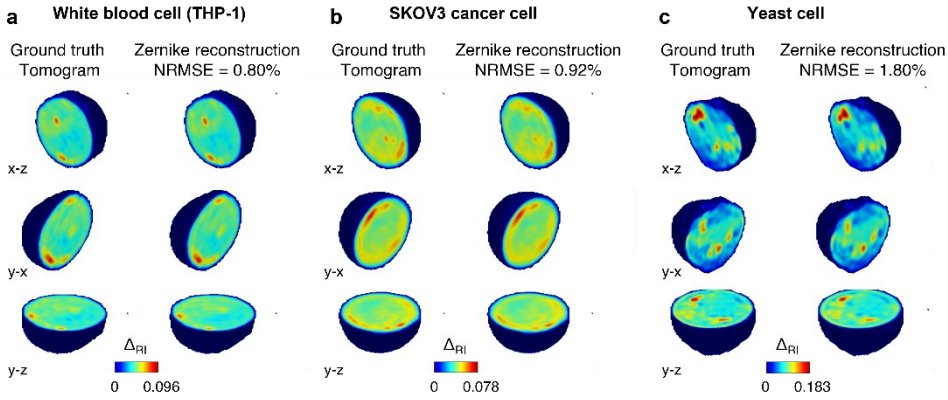

Figure 4.25 Comparison between experimental tomographic data and the corresponding 3DZD reconstructions for a THP-1 cell (a), a SKOV3 cancer cell (b), and a Yeast cell (c).
Left side: central slices of tomographic reconstructions of cells from experimental data. Right side: central slices of tomograms recovered via 3DZD. The NRMSE values are reported at the top.

This is mainly caused by the about double RI contrast. Of course, it is possible to push the value of NRMSE below the desired fidelity score by increasing the polynomials order N. The proposed 3D Zernike representation guarantees very high coding performance especially for objects having spherical-like symmetries as in Figure 4.25. To evaluate the performance also in cases of non-spherical cells, the 3DZD reconstruction of two different cells is reported in Figure 4.26(a,b), namely a RBC and a cluster of two SKNSH NB cancer cells, both acquired with the TPM-FC system in Figure 2.5 (microfluidic channel with 200 µm × 200 µm cross section coupled to a 2048×2048 CMOS camera with 5.5 µm pixel size recording at 35 fps and a 40× MO, oil immersion, NA=1.30) and reconstructed using the FBP approach. In both cases, a remarkable fidelity score is still achieved, as reported by the NRMSE values on the top.

The results reported in Figure 4.25 and Figure 4.26 aim to demonstrate the ability of the proposed 3DZD representation to approximate cells' tomographic data with high accuracy and achieving a very high *space saving* $> 95\%$ corresponding to a data compression ratio ~22.9.

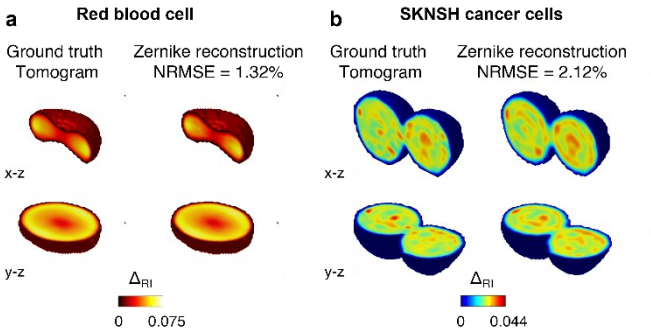

Figure 4.26 Assessment of the 3DZD method in the case of two non-spherical cells, namely a RBC (a) and a cluster of two SKNSH NB cancer cells (b).
Left side: central slices of tomographic reconstructions of cells from experimental data. Right side: central slices of tomograms recovered via 3DZD. The NRMSE values are reported at the top.

However, the effective tomographic data manipulation by using the 1D strings of 3DZD instead of the original 3D tomograms needs to be proved also for cell lines characterization. To demonstrate also this key-enabling potentiality of the proposed method, in Figure 4.27 it is reported the comparison about the histograms of the most common used morphometric features that can be calculated from single-cell tomographic data, i.e. the average RI, the biovolume and the dry mass. In particular, these features are calculated from 66 original tomograms (i.e. ground truth images) of NIH-3T3 mouse cell line recorded through the TPM-FC system in Figure 2.5 (reconstructed by the FBP algorithm) and from the corresponding reconstructions obtained using the 3DZD representation. A $NRMSE = 1.55\% \pm 0.28\%$ is obtained, calculated as the average NRMSE and the related standard deviation from the 66 3DZD reconstructions. Notice that the relative difference between average values of each pair of histograms is less than 0.5% for the average RI and the dry mass and about 2% for the biovolume, thus demonstrating the effectiveness of the proposed method also to represent a cell line accurately.

Tomographic data encode all the information needed to study the subcellular structures, exploiting the 3D distribution of the RI as an endogenous biomarker to identify organelles at the single-cell level. However, the statistical characterization of a cell population requires the collection of thousands of images that, in the case of conventional 2D IFC systems, requires storing and managing one snapshot per cell, that is to say a memory usage of megabytes. Instead, in the case of single-cell tomograms, one can expect to store from gigabytes to terabytes of data, without considering the potentially high computational cost needed to implement advanced algorithms for the identification of sub-populations and/or rare cells. On the one hand, this could be considered a hardware limitation only, which can be mitigated by employing highly-performance computers and GPUs. On the other hand, all LOC-oriented applications, which usually require software installed into on-chip SRAM and a small memory footprint, would remain excluded from a massive adoption of the new TPM-FC technology and related advantages.

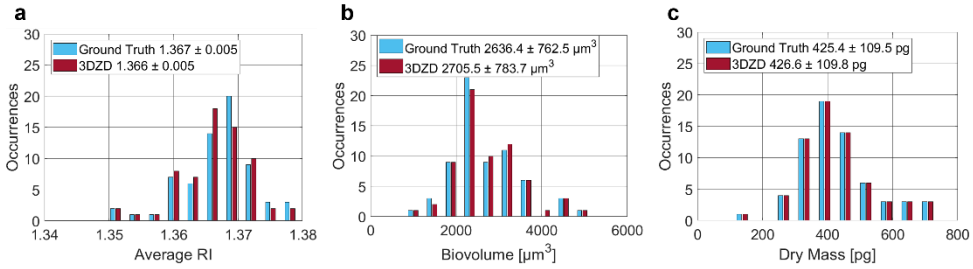

Figure 4.27 Quantitative characterization of the NIH-3T3 cell line reconstructed through 3DZD.
Histograms of **(a)** average RI, **(b)** biovolume, and **(c)** dry-mass, calculated from both experimental tomograms and corresponding reconstructions via 3DZD.

The results presented here demonstrate, for the first time in the field of TPM-FC, the possibility to squeeze single-cell tomograms by using the 3D version of Zernike polynomials. They open the route to a potentially killer methodology to store, manipulate and process volumetric images, especially for LOC systems. Moreover, the possibility to replace volumetric data with the corresponding 3DZD sequence allows to address clinical challenges related to label-free single-cell phenotyping, for which the current solution is based on DL classification [209]. In principle, by the proposed method, it would be possible to switch from deep 3D image classification to deep 1D sequence classification, preserving the same degree of data richness and allowing a very remarkable memory and computational time reduction for the training of DCNNs. Finally, the possibility to employ 3DZD as morphological biomarkers to identify specific subcellular structures may be achieved as a direct generalization from the 2D case, in which the Zernike fitting is used to characterize aberrations of cells [21]. Just like the introduction of compressed formats for audio and video files promoted their widespread sharing by a community of billions users independently on the hardware resources they had access to, it is believed that lightening the weight of cells' 3D tomograms will unlock the massive employment of this technology by the widest audience of researchers, biologist and physicians.

CHAPTER

5 Conclusions

This Ph.D. Thesis aimed to achieve a remarkable step toward the development of the TPM-FC technology. Starting from the first proof of concept of TPM-FC, herein many aspects of this tool have been tackled in order to fully exploit its theoretical potential and fix its main drawbacks for a practical implementation. Therefore, the attained results pave the way toward the first real world clinical applications of TPM-FC.

- From the technological point-of-view, herein it has been demonstrated the feasibility of high-throughput TPM-FC, thanks to the optimization of the opto-fluidic recording system and to
  - ✓ the implementation of an automatic method for retrieving the unknown positions and viewing angles of the flowing/rolling cells within the microfluidic channel [108];
  - ✓ the speeding-up of the holographic processing via DL [213];
  - ✓ the quasi-lossless compression of the RI tomograms by 3D Zernike polynomials [295];
  - ✓ the study of the hydrodynamic mutual interactions among cells inside the microfluidic channel [109].
- In terms of clinical applications, herein the TPM-FC system has been exploited for
  - ✓ the DL classification of human NB cancer cells (SKNSH vs. CHP134) based on the raw holographic diffraction patterns [214];

- ✓ the ML classification of human monocytes WBCs vs. NB cancer cells and the downstream tumor phenotyping (CHP212 vs. SKNBE2 vs. SHSY5Y vs. SKNSH) based on the phase-contrast signature [215] interpreted by means of fractal geometry [216];
- ✓ the ML classification of drug resistance in human EC cells (ISK vs. ISK-CisR) based on the 3D RI spatial distribution [217].

➢ The main gap with FM in terms of lack of chemical intracellular specificity in label-free TPM-FC has been herein filled by means of computational strategies, thus providing reliable biomarkers for clinical applications, such as

- ✓ the nucleus, commonly recognized as cancer biomarker, segmented through a statistical method [297];
- ✓ the nucleolus, containing most of the genetic material, segmented through a statistical method in TPM-FC [297], but also identified in plant cells through an alternative static TPM based on the induced cell dehydration [6];
- ✓ the LDs, recently related to a lot of pathologies, detected by means of a RI threshold inside 3D tomograms [291] or by exploiting changes of the focalization property of the whole cell, considered as a biolens [343], due to the presence of LDs inside 2D QPMs [345];
- ✓ the nGO internalized by the cell, useful for diagnostic and therapeutical purposes like drug delivery, visualized by means of TAM-FC, i.e. a variant of TPM-FC in which the AMs are employed in place of QPMs for the tomographic reconstruction [294].

The technological nature of TPM-FC, combined to the reported results, make it eligible for introducing a breakthrough in several clinical applications based on single-cell analysis, both diagnostic and therapeutic, thanks to the possibility of high-throughput recordings of high numbers of single cells, from which the most informative quantitative content can be extracted, i.e. the 3D

RI tomogram, also at the stain-free intracellular level. Among several possible applications, these remarkable properties, combined to the ability of working in microfluidic environment, bode well that TPM-FC will be able to offer a practical solution in the next future to the fascinating but not yet realized LB paradigm [392].

Histological evaluation, coupled to the analysis of genetic alterations from tissue biopsies, is the current standard method for cancer risk stratification and therapeutic choice. However, tissue biopsies have many limitations, like high invasive nature, subjective evaluation of an individual pathologist, and high procedural costs in the case of molecular pathology. Conversely, LB has been emerging in the last years as a blood test to search for cancer cells (CTCs) or cancer-derived free molecules (DNA, RNA, exosomes, etc) that are circulating in the blood. LB can be used to identify cancer at an early stage, to guide the patient treatment, to evaluate the treatment efficacy, or to validate whether cancer has relapsed [241]. LB is a non-invasive, easily repeatable, and potentially low-cost approach, thus it is revealing as a promising alternative to solid biopsy. In particular, CTCs are vital cells exfoliated from primary tumors and metastatic sites that enter the bloodstream. Their detection and characterization via LB has been deeply investigated for the development of novel protocols in management of cancer patients [393]. CTCs clinical trials are currently employed in breast, prostate, lung, and colorectal cancers [394] [395]. The study of CTCs and evolving CTC technologies are offering also additional models to accelerate oncologic drug development [396].

To date, the potential clinical value of CTCs has been established, but still some limitations should be addressed before CTCs-based LB becomes a routine test in clinical practice. Most of the commonly used approaches for CTCs detection, enumeration, and isolation are based on the recognition of a known, specific CTCs marker, such as a surface antigen, a DNA mutation, a gene expression profile, or even a certain functional property that discriminates CTCs from the rest of the circulating blood cells. The only Food and Drug Administration-approved diagnostic protocol for CTCs detection regards the CellSearch®

system, which bases the CTCs identification and enumeration on the surface epithelial cell adhesion molecule (EpCAM) expression [397]. However, even though the knowledge on CTCs biology is increasing, the main limitations of the current techniques based on the CTCs molecular and functional properties are (a) the fragility and rarity of CTCs (1-10 cells per 10 mL), (b) the *a priori* knowledge of the exact protein composition on the CTCs surfaces, (c) the lack of universal markers able to identify all heterogeneous CTCs in the bloodstream, and (d) the lack of validated, standardized approaches in pre-analytical, analytical, and post-analytical phases of CTCs detection [241]. For these reasons, so far the development of innovative, comprehensive, and standardized methods for CTCs isolation and detection is still unaccomplished.

Currently, label-free imaging methods combined with AI algorithms are revealing as a promising approach for LB [155] [248] [398] [399]. In particular, the sole QPI has been demonstrated able to distinguish between tumor cells and corresponding non transformed cell lines. Great effort has been spent in the integration of DH imaging with compact LOC and microfluidic devices to expand the potentialities of such imaging modality. The most valuable opportunity is the label-free analysis of flowing samples [156] [159] [253] [106]. A proof of principle on the use of fast and high-throughput DH to discriminate between CTCs and the other components of a blood stream has been provided [205] [400]. But, although promising, this approach did not fully exploit the precious content of information of the holographic pattern. Instead of using one single QPM that provides pseudo-3D information deriving from an integral imaging process, a high-resolution 3D representation of the inner distribution of the cell's RI is obtainable by adopting a TPM approach. Herein, the novel TPM-FC has been demonstrated and discussed, thus achieving full 3D label-free characterization in continuous flow at the single-cell level. In order to manage the huge amount of label-free biophysical information provided by the TPM-FC from a wide range of cell populations found in blood, AI becomes pivotal for capturing low number of CTCs without

the requirement for a specific biological marker. AI can extend the range of diagnostic problems one can tackle in automatic way and is designed to make the diagnostic response objective, that is, not dependent on the level of experience or specific skills of the pathologist.

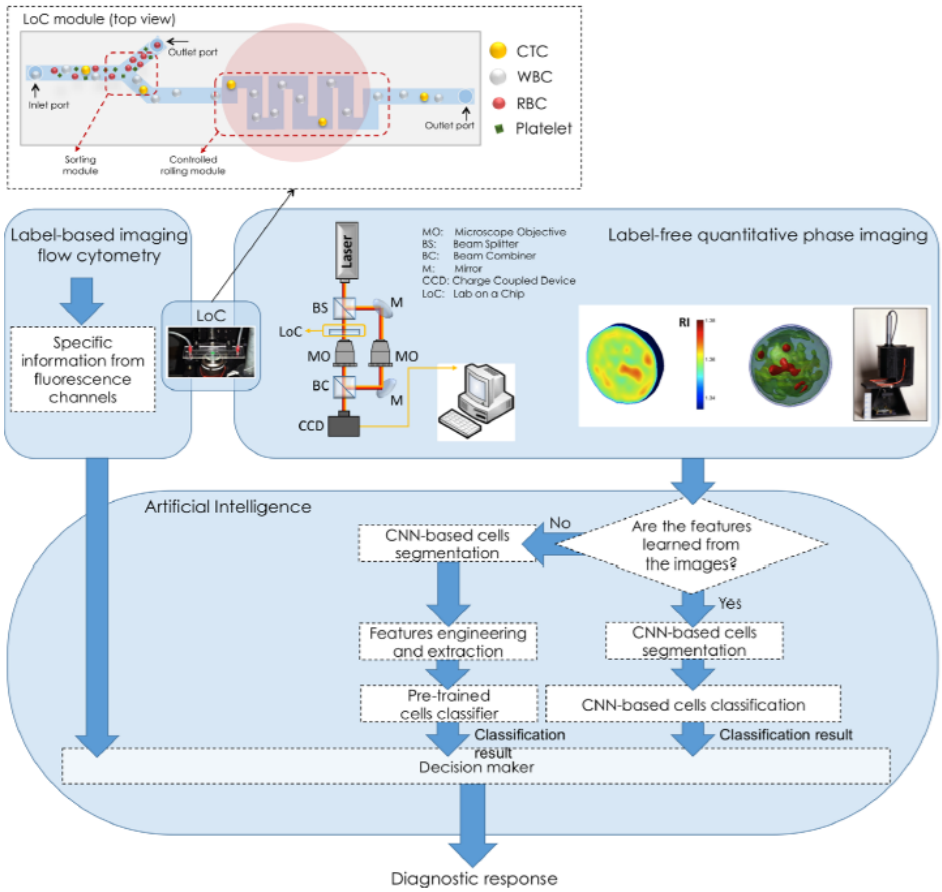

Figure 5.1 Integration between label-free TPM-FC, LOC flow engineering, and AI for the advanced single-cell analysis of blood streams.
The core of the scheme is a microfluidic LOC system able to sort the lighter blood components (RBCs and platelets) and put in rotation CTCs and WBCs to perform QPI measurements at different angles for realizing the TPM-FC reconstructions. All the retrieved 2D and 3D label-free data are then processed by AI approaches to classify CTCs populations (e.g., using DCNN). When available, prior information from fluorescence channels can be exploited to generate a reliable diagnostic response. (Figure reproduced from Ref. [241])

At this scope, AI is hungry for informative data and, in the context of cell type discrimination, high-throughput TPM-FC is in turn the most appropriate candidate to satisfy this need. Hence, the integration of label-free TPM-FC, AI, and microfluidics on board of LOC represents the most promising platform for searching, detecting and isolating CTCs into the bloodstream at the aim of realizing the LB paradigm [241]. As sketched in Figure 5.1, the ideal system would be made of several modules. A microfluidic chip performs a first filtration of the blood sample, thus removing the lighter blood components (i.e., RBCs and platelets). The CTCs and WBCs, which have similar morphologies, continue to flow along the microfluidic channel and, after focusing them in a fixed position inside the cross section and after inducing their rotation, they are recorded through the TPM-FC system. The TPM-FC processing is implemented to retrieve the 2D QPMs and 3D RI tomograms of the collected single cells. Computational approaches are applied to bypass the lack of exogeneous markers and retrieve the intracellular biomarkers. When possible, the label-free quantitative characterization of the single cells can be enriched by the specific characterization provided by a second fluorescent channel within a multimodal recording system. Then, AI is exploited to handle the huge amount of collected information, thus identifying CTCs from WBCs and phenotyping them in order to recognize their cancer origin. The last modulus is an AI-based IACS system that, according to the classification output, collects the CTCs and makes them available for a downstream analysis (e.g., genetic), possible when the label-free property is met.

The results obtained in this Ph.D. Thesis represent a remarkable starting point toward the implementation of such a system, and research in the near future will be devoted to integrate the missing pieces. The microfluidic modulus must be better engineered in order to achieve a higher throughput, comparable with that of conventional IFC. The optical component of the TPM-FC system must be perfectly matched to the microfluidic component in order to maximize contrast and resolution and reduce the waste of hardware resources. Then, the numerical processing must be able to handle the greater number of cells and

provide a fast analysis. The DCNN-based speeding up of the holographic processing demonstrated here must be coupled to another DCNN, trained to provide a real-time detection of the flowing cell within the recorded holographic video sequence. The eukaryotic cell is very complex in terms of internal structure, therefore other computational strategies are requested for identifying the several intracellular organelles in addition to the reported nucleus, nucleolus, and LDs (e.g., lysosomes, Golgi apparatus, mitochondria). As regards the classification step, here different possibilities have been investigated, based on the raw holographic patterns, the phase signature, and the 3D RI distribution. Actually, in general a best solution does not exist, which means that the adopted strategy must be chosen according to the selected problem. However, the TPM-FC tool keeps all three possibilities open, which can be also combined if necessary. Of course, the range of CTCs is extremely wide, therefore a great effort must be spent in the definition of a very distinctive fingerprint at the single-cell level through the combination between AI and TPM-FC. Furthermore, the last modulus realizing the cell sorting must be added. Finally, the proposed system must be miniaturized for starting the clinical practice, and, at this aim, the problem about the memory storage must be fixed, using for example a compression strategy like that proposed here for the 3D tomograms.

Development of such innovative instrumentation for biomedical applications, whose expected cost will be extremely competitive in respect to the actual approaches for LB, can really push toward a new generation of clinical tools that will have a very huge market worldwide. There are a lot of efforts to improve in the near future this integrated and intelligent LOC platform because it is expected that the detection of CTCs in blood would provide a great aid to the early diagnosis of cancers and the development of personalized therapies. Finally, it is also important to outline that label-free modality does not produce chemical waste, thus drastically reducing the impact both on the management and usage of chemicals, which makes this technology a totally green issue.

AVGVSTVS FRIDERICVS ROMANORVM IMPERATOR SEMPER

Appendix

A.1 Fractal Analysis at Single-Particle Level

In order to describe the set of 13 fractal features here proposed for better extrapolating the phase signature of a single cell for its characterization and discrimination, the wrapped QPM ψ of the microplastic displayed in Figure A.1(a) is considered as example since this fractal analysis has been here introduced for the first time for identifying microplastics among diatoms in water environment [216]. From the wrapped QPM ψ, the object support S_ψ is computed by conventional segmentation, as shown in Figure A.1(b), while the hole support Γ_ψ reported in Figure A.1(c) is obtained by the logic *or* between the support frontier (obtainable by means of edge estimation operators) and the binarization of ψ using a zero threshold. The wrapped QPM ψ, the object support S_ψ, and the hole support Γ_ψ, respectively shown in the example in Figure A.1(a-c), have $l = 256$ pixels per side. Over the years, several parameters have been defined to quantify the fractality of an object. One of the most important is the fractal dimension. The topological dimension of an object is the miminum number of coordinates to describe its points. Therefore, it is 0 for a point, 1 for a line, 2 for a plane object and 3 for a solid object. Instead, fractal dimension measures how an object fills the space and, unlike the topological one, can take non-integer values. A possible definition of fractal dimension is the Minkowski–Bouligand dimension, which can be easily understood through the most used method to compute it, i.e. the box-counting method [401]. An image of size l can be rescaled of a factor $\varepsilon = l/r$, i.e. it can be covered by ε^2 distinct boxes of size $r = 1, 2, 4, 8, \dots, l$. For example, the red grid in Figure A.1(b,c) is associated to a scale factor $\varepsilon = 8$, since the microplastic of size $l = 256$ has been divided in $\varepsilon^2 = 64$ distinct boxes of size

$r = 32$. Let n be the number of distinct boxes that contain at least a non-zero value in the hole support Γ_ψ ($n = 31$ in the proposed example). Of course, n depends from the scale factor ε and, according to the Minkowski–Bouligand definition [402], the fractal dimension D can be expressed as

$$D = \lim_{1/\varepsilon \to 0} \frac{log\, n(\varepsilon)}{log\, \varepsilon}, \tag{A.1}$$

where the logarithm can have any base. In the log-log plot in Figure A.1(d), red dots are the values $n(\varepsilon)$ measured over the hole support Γ_ψ in Figure A.1(c). The box-counting method computes fractal dimension D as the slope of the linear fitting to data $n(\varepsilon)$, i.e. red line in Figure A.1(d). In this example, $D = 1.634$ is obtained. Instead, in the ideal case of a full square of size l, $n(\varepsilon) = \varepsilon^2$ for any $\varepsilon = 1, 2, 4, 8, \dots, l$, hence the fractal dimension corresponds to the topological one $D = 2$, as reported in green in Figure A.1(d). It is worth pointing out that, in the described box-counting method, the scale factor ε can assume only powers of 2 values within the $[1, l]$ interval since the image processing operations take place in the discrete space. Instead, in continuous space, ε can take all the real values within $[1, +\infty)$ interval, from which limit in Eq. (A.1) follows.

However, the sole fractal dimension is not able to describe a fractal image. Indeed, it is possible that two distinct images have the same fractal dimension. Therefore, another parameter used in addition to fractal dimension is lacunarity, which is a measure of the distribution of the hole sizes in an image [255]. Lacunarity is commonly computed through the gliding box algorithm [403]. Like the fractal dimension measurement, also the lacunarity is based on a multi-scaled analysis of the image. However, in this case the image is scanned by gliding rather than distinct (i.e. non overlapping) boxes at different scale factors $\varepsilon = 1, 2, 4, 8, \dots, l$. For a fixed ε, let $H(\varepsilon)$ be a $r \times r$ matrix with 1 values. The $A(\varepsilon)$ and $B(\varepsilon)$ maps are computed as the 2D convolution of $(1 - \Gamma_\psi)$ and S_ψ with $H(\varepsilon)$ mask, respectively. Let $m(a, \varepsilon)$ be the probability distribution associated with the $A(\varepsilon)$ map, with $a = 1, 2, \dots, r^2$, obtained after dividing the

frequency distribution by the number of non-zero elements in $B(\varepsilon)$, and let $p_1(\varepsilon)$ and $p_2(\varepsilon)$ its first and second order moments, respectively. The lacunarity Λ at scale ε is defined as [403]

$$\Lambda(\varepsilon) = \frac{p_2(\varepsilon)}{p_1^2(\varepsilon)}. \tag{A.2}$$

For example, in the hole support in Figure A.1(c), $\Lambda(8) = 1.066$ is obtained. In the semi-log plot in Figure A.1(e), red dots are the values of $\Lambda(\varepsilon)$ measured over the map Γ_ψ of Figure A.1(c). Instead, the red line in Figure A.1(e) is the exponential fitting of the curve $\Lambda(\log_2(\varepsilon))$, which is calculated as $y = b_0 + b_1 e^{b_2 x}$. The lacunarity index $L = b_2$ is defined as a synthetic descriptor of lacunarity. It depends on the fill ratio F, which is defined as the ratio between the number of non-zero values within the hole support Γ_ψ and the area of the object support S_ψ ($F = 0.510$ in Figure A.1(c)). Since the calculation of the lacunarity is made on the negative of the hole support, i.e. $\left(1 - \Gamma_\psi\right)$, images with only one single hole covering the entire support have fill ratio $F = 0$ and lacunarity $\Lambda(\varepsilon) = 1$ for any $\varepsilon = 1, 2, 4, 8, \dots, l$, from which lacunarity index $L = 0$. Hence, a low lacunarity index L indicates a big lacunarity.

However, two images with the same fill ratio F could have different lacunarity index L, according to the regularity of their geometry [403]. Regularity can be interpreted as a measure of how the zero and non-zero elements are uniformly distributed with respect to the hole support. With the same fill ratio F, lacunarity index L changes according with the regularity [403]. A synthetic descriptor of regularity is here proposed, namely regularity index R, as follows. Let C be the centroid of the support map S_ψ, which generic point is P. Let Z and $\bar{Z}$ be the generic zero and non-zero points within the hole support Γ_ψ, respectively. The elements of vectors $\underline{d}_{x,P}$, $\underline{d}_{x,Z}$ and $\underline{d}_{x,\bar{Z}}$ are computed as the differences between the x-coordinates of point C and points P, Z and $\bar{Z}$, respectively, and the elements of vectors $\underline{d}_{y,P}$, $\underline{d}_{y,Z}$ and $\underline{d}_{y,\bar{Z}}$ are computed as the differences between the y-coordinates of point C and points P, Z and $\bar{Z}$, respectively. Histograms of vectors $\underline{d}_{x,P}$, $\underline{d}_{x,Z}$ and $\underline{d}_{x,\bar{Z}}$ and histograms of

vectors $\underline{d}_{y,P}$, $\underline{d}_{y,Z}$ and $\underline{d}_{y,\bar{Z}}$, normalized to their maxima, are compared in Figure A.1(f,g), respectively. Let $R_{x,Z}$, $R_{y,Z}$, $R_{x,\bar{Z}}$ and $R_{y,\bar{Z}}$ be the Pearson Correlation Coefficients [278] between normalized histograms of vectors $\underline{d}_{x,Z}$ and $\underline{d}_{x,P}$, $\underline{d}_{y,Z}$ and $\underline{d}_{y,P}$, $\underline{d}_{x,\bar{Z}}$ and $\underline{d}_{x,P}$, $\underline{d}_{y,\bar{Z}}$ and $\underline{d}_{y,P}$, respectively. The regularity index R is defined as the module of the average value among the four correlation coefficients. To reach the maximum value $R = 1$, both the zero elements and the non-zero elements in the hole support Γ_ψ must have the same spatial distribution of the support elements in map S_ψ. In the example in Figure A.1(b,c), maps have high regularity index, hence $R = 0.895$ is obtained.

Moreover, for both curves $n(\varepsilon)$ and $\Lambda(\varepsilon)$,

$$dn\,(\varepsilon) = \frac{\nabla\, log_2\, n(\varepsilon)}{\nabla\, log_2\, \varepsilon} \qquad d\Lambda\,(\varepsilon) = \frac{\nabla \Lambda(\varepsilon)}{\nabla \varepsilon} \tag{A.3}$$

are calculated, where ∇ is the gradient operator, and they are shown through red dots in the semi-log plot in Figure A.1(h,i), respectively. Both curves are characterized through their contrast, computed as the ratio between their standard deviations and their average values, thus obtaining the fractal dimension contrast C_D and lacunarity contrast C_L, respectively. In order to clarify how these parameters characterize the fractality of a pattern, the case of a non fractal object, i.e. a full square of size l, can be considered for comparison. In this case, it results $dn\,(\varepsilon) = 2$ for any $\varepsilon = 1, 2, 4, 8, \dots, l$, as reported by the green line in Figure A.1(h). Instead, in the case of an empty image, it results $d\Lambda(\varepsilon) = 0$ for any $\varepsilon = 1, 2, 4, 8, \dots, l$, as reported by the green line in Figure A.1(i). Therefore, it is also worth measuring the RMSEs, E, between red and green curves in both Figure A.1(h,i), thus obtaining the fractal dimension RMSE, E_D, and the lacunarity RMSE, E_L, respectively.

Another parameter here employed to describe the fractality of the hole support Γ_ψ is the vertex density V, although it is not a classical fractal

parameter. It is defined as the ratio between the number of corners of the hole support Γ_ψ and the number of pixels of its support S_ψ.

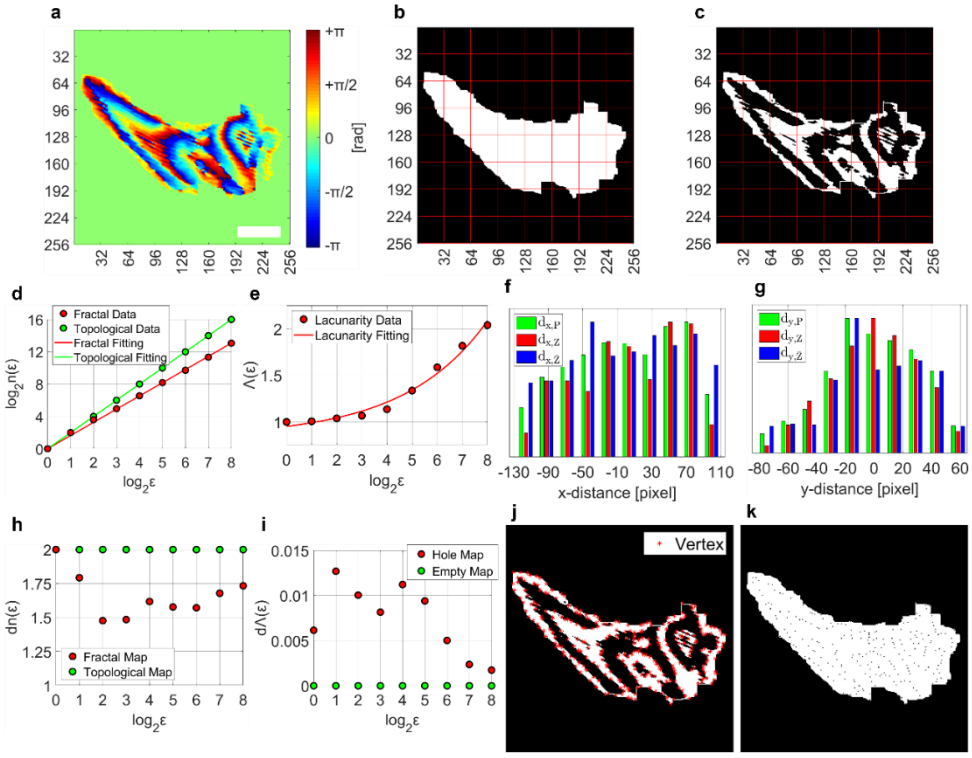

Figure A.1 Fractal characterization of a microplastic.
(a-c) Wrapped QPM ψ, object support S_ψ and hole support Γ_ψ, respectively. Red grid in (b,c) is associated to a scale $\varepsilon = 8$, since maps are covered by distinct boxes of size $r = 32$. Scale bar is 5 μm. **(d)** In red, counted boxes n at different scales ε (dots) along with their linear fitting (solid line) for the hole support in (c). In green, counted boxes n at different scales ε (dots) along with their linear fitting (solid line) for an ideal full square of size $l = 256$ (fractal dimension=topological dimension= 2). **(e)** Lacunarity Λ at different scales ε (dots) along with their exponential fitting (solid line) for the hole support in (c). **(f)** Histograms of x-distances $\underline{d}_{x,P}$, $\underline{d}_{x,Z}$ and $\underline{d}_{x,\bar{Z}}$ and **(g)** histograms of y-distances $\underline{d}_{y,P}$, $\underline{d}_{y,Z}$ and $\underline{d}_{y,\bar{Z}}$, normalized to their maxima, used to compute regularity index R of the hole support in (c). **(h)** In red and in green, curves $dn\ (\varepsilon)$ obtained from red and green counted boxes $n(\varepsilon)$ in (d), respectively. **(i)** In red, curve $d\Lambda\ (\varepsilon)$ obtained from red data in (e). In green, curve $d\Lambda\ (\varepsilon)$ obtained from lacunarity curve $\Lambda(\varepsilon)$ of an empty image of size $l = 256$. **(j)** Hole support Γ_ψ with vertices highlighted in red and **(k)** the vertex map V_ψ obtained from its binarization. Distances are expressed in pixels.

From the example in Figure A.1(j), in which corners are marked by red asterisks, $V = 1.730\%$ is obtained. Moreover, as shown in Figure A.1(k), a vertex map V_ψ is created, in which pixels that have been identified as corners are set to 0 within the object support S_ψ. Finally, the described lacunarity analysis is applied on the vertex map V_ψ as well, thus computing its vertex regularity index, R_V, vertex lacunarity index, L_V, vertex lacunarity contrast, C_{L_V}, and vertex lacunarity RMSE, E_{L_V}.

For the sake of clarity, the meaning of the proposed regularity index R is detailed with an example. In particular, starting from the object support S_ψ of Figure A.1(b), three hole supports Γ_ψ are simulated having the same fill ratio $F = 0.500$. In the hole support $\Gamma_{\psi,1}$ in Figure A.2(a), the object support is replaced with a chessboard. In the hole support $\Gamma_{\psi,2}$ in Figure A.2(f), the outer space is filled with 1 and the inner space is filled with 0. In the hole support $\Gamma_{\psi,3}$ in Figure A.2(k), the left side is filled with ones and the right side is filled with zeroes. Each of the three simulated hole supports follows a different idea of regularity. However, here it is exploited the idea of regularity expressed by the hole support $\Gamma_{\psi,1}$ in Figure A.2(a). Let $C \equiv (x_C, y_C)$ be the centroid of the object support S_ψ, which generic point is $P \equiv (x_P, y_P)$. Instead, within the hole support Γ_ψ, let $Z \equiv (x_Z, y_Z)$ and $\bar{Z} \equiv (x_{\bar{Z}}, y_{\bar{Z}})$ be generic inner zero and non-zero points, respectively. The elements of vectors $\underline{d}_{x,P}$, $\underline{d}_{y,P}$, $\underline{d}_{x,Z}$, $\underline{d}_{y,Z}$, $\underline{d}_{x,\bar{Z}}$ and $\underline{d}_{y,\bar{Z}}$ are respectively computed as

$$\begin{aligned} d_{x,P} &= x_P - x_C \,;\, d_{y,P} = y_P - y_C \\ d_{x,Z} &= x_Z - x_C \,;\, d_{y,Z} = y_Z - y_C \\ d_{x,\bar{Z}} &= x_{\bar{Z}} - x_C \,;\, d_{y,\bar{Z}} = y_{\bar{Z}} - y_C \end{aligned} \quad \text{(A.4)}$$

Let $h(\cdot)$ be the histogram of a vector, normalized to its maximum. The quantities

$$\begin{aligned} R_{x,Z} &= corr\left(h(\underline{d}_{x,Z}), h(\underline{d}_{x,P})\right) \,;\, R_{y,Z} = corr\left(h(\underline{d}_{y,Z}), h(\underline{d}_{y,P})\right) \\ R_{x,\bar{Z}} &= corr\left(h(\underline{d}_{x,\bar{Z}}), h(\underline{d}_{x,P})\right) \,;\, R_{y,\bar{Z}} = corr\left(h(\underline{d}_{y,\bar{Z}}), h(\underline{d}_{y,P})\right) \end{aligned} \quad \text{(A.5)}$$

are computed, where $corr(\cdot,\cdot)$ is the Pearson Correlation Coefficient between two vectors [278], which ranges from -1 to 1 ($corr = -1$ indicates perfect negative correlation, $corr = +1$ indicates perfect positive correlation, and $corr = 0$ indicates no correlation between two vectors). Finally, the regularity index is defined as

$$R = \left|\frac{R_{x,Z}+R_{y,Z}+R_{x,\bar{Z}}+R_{y,\bar{Z}}}{4}\right|. \tag{A.6}$$

Hence, the normalized histograms $h(\underline{d}_{x,P})$ and $h(\underline{d}_{y,P})$ are used as a reference, since P is a generic point of the object support S_ψ with centroid C. On this basis, a hole support Γ_ψ is regular if both its zero elements Z and non-zero elements $\bar{Z}$ have the same spatial distribution of points P within object support S_ψ. For this reason, to analyze the hole support $\Gamma_{\psi,1}$, the normalized histograms $h(\underline{d}_{x,P})$ and $h(\underline{d}_{x,Z})$, $h(\underline{d}_{y,P})$ and $h(\underline{d}_{y,Z})$, $h(\underline{d}_{x,P})$ and $h(\underline{d}_{x,\bar{Z}})$, and $h(\underline{d}_{y,P})$ and $h(\underline{d}_{y,\bar{Z}})$, are respectively compared in Figure A.2(b-e). At the top of Figure A.2(b-e), the corresponding correlation coefficients $R_{x,Z}$, $R_{y,Z}$, $R_{x,\bar{Z}}$ and $R_{y,\bar{Z}}$ are respectively reported to evaluate the similarity between the distributions of points. Due to the simulated chessboard, in this example the zero elements Z and the non-zero elements $\bar{Z}$ follow exactly the same distribution of the support points P, therefore all the correlation coefficients are 1. As a consequence, the hole support $\Gamma_{\psi,1}$ has maximum regularity index $R = 1$. The same analysis reported in Figure A.2(b-e) is repeated in Figure A.2(g-j) and Figure A.2(l-o) for hole supports $\Gamma_{\psi,2}$ and $\Gamma_{\psi,3}$, respectively. In particular, the zero elements rather than the non-zero elements of the hole support $\Gamma_{\psi,2}$ in Figure A.2(f) are distributed like the object support (high correlation coefficients in Figure A.2(g,h) and low correlation coefficients in Figure A.2(i,j)). Instead, the y-coordinates rather than the x-coordinates of both zero and non-zero elements of the hole support $\Gamma_{\psi,3}$ in Figure A.2(k) are distributed approximately like the object support (high correlation coefficients in Figure A.2(m,o) and low correlation coefficients in Figure A.2(l,n)). However, hole supports $\Gamma_{\psi,2}$ and $\Gamma_{\psi,3}$ have about the same regularity

index, i.e. $R = 0.508$ and $R = 0.538$, respectively. Moreover, with the same fill ratio F, a different regularity index R leads to a different lacunarity index L. In fact, as reported at the top of Figure A.2(a,f,k), hole supports $\Gamma_{\psi,1}$, $\Gamma_{\psi,2}$ and $\Gamma_{\psi,3}$ have lacunarity index $L = 0.005$, $L = 0.292$ and $L = 0.097$, respectively.

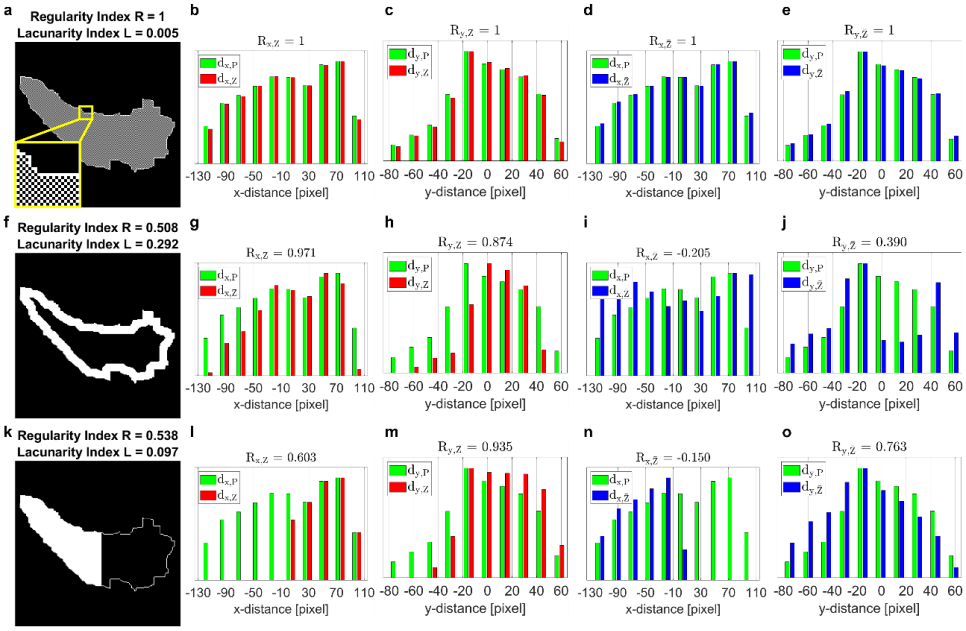

Figure A.2 Concept and definition of regularity index *R*.

(a,f,k) Three hole supports $\Gamma_{\psi,1}$, $\Gamma_{\psi,2}$ and $\Gamma_{\psi,3}$, respectively, simulated starting from the same microplastic object support, with the corresponding values of regularity index R and lacunarity index L at the top. In (a), the chessboard inner structure is highlighted in the yellow insert. **(b,g,l)** Comparison between the x-distances normalized histograms of the support points P (green) and the zero elements Z (red) within maps in (a,f,k), respectively. **(c,h,m)** Comparison between the y-distances normalized histograms of the support points P (green) and the zero elements Z (red) within maps in (a,f,k), respectively. **(d,i,n)** Comparison between the x-distances normalized histograms of the support points P (green) and the non-zero elements $\bar{Z}$ (blue) within maps in (a,f,k), respectively. **(e,j,o)** Comparison between the y-distances normalized histograms of the support points P (green) and the non-zero elements $\bar{Z}$ (blue) within maps in (a,f,k), respectively. In (b-e,g-j,l-o), correlation coefficients between the normalized histograms are reported at the top.

[redacted]

A.2 Feature Extraction from 2D QPMs and 3D RI Tomograms

For classifying EC cells, 54 features have been extracted from the 2D QPMs and 67 features have been measured from the 3D RI tomograms [217]. As shown in Figure A.4, there is a huge increment of information from 2D region to 3D volume, thus introducing more complex features. The perimeter and area in the 2D region correspond to the surface and volume in 3D space for morphological features. Among the texture features, histogram features are the first order statistical parameters calculated from the image histogram, i.e. mean, variance, skewness, kurtosis, energy, and entropy. GLCM is a matrix obtained by counting the number of the two grayscales at a certain direction and distance and describes the image texture by calculating the statistics of the grayscale matrix. The image has been divided into 16 gray scales, and each GLCM-feature value is the average of statistical features from 13 different directions, as shown in Figure A.4. NGTDM describes the relationship between a pixel and its surrounding pixel values. GLSZM counts the number of a certain gray level with a certain region size. Table A.1 shows the list of both 2D and 3D feature categories.

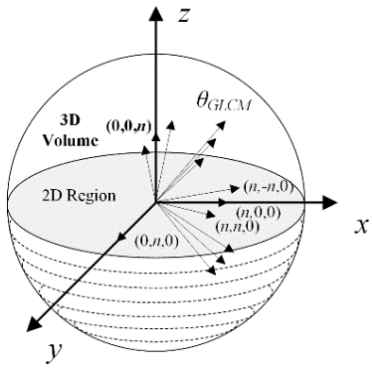

Figure A.4 3D volume for feature calculation.
The 13 directions for calculating the GLCM-feature values are reported.

Table A.1 List of features for characterizing 2D QPMs and 3D RI tomograms of EC cells.

Feature Type	2D	3D
Morphology		
Perimeter	√	-
Area	√	-
Volume	√	-
Major axis length	√	-
Minor axis length	√	-
Diameter	√	-
Eccentricity	√	-
Area at 25% phase	√	-
Max phase	√	-
Mean phase at 25%	√	-
Max gradient	√	-
Mean gradient	√	-
Mean gradient at 25%	√	-
Surface	-	√
Volume	-	√
Volume-RI	-	√
Ratio of surface to volume	-	√
Surface ratio of the same volume sphere	-	√
Max-slice perimeter	-	√
Mean slice perimeter	-	√
Max slice area	-	√
Mean slice area	-	√
Max slice major axis length	-	√
Mean slice major axis length	-	√
Max-slice minor axis length	-	√
Mean slice minor axis length	-	√

Max slice diameter	-	√
Mean slice diameter	-	√
Max slice eccentricity	-	√
Mean slice eccentricity	-	√
Max slice gradient	-	√
Max slice average gradient	-	√
Mean slice gradient	-	√
Mean slice max gradient	-	√
Max slice variance	-	√
Mean slice variance	-	√
Sum RI at 10%	-	√
Sum RI at 50%	-	√
Sum RI at 90%	-	√
Histogram features		
Mean	√	√
Variance	√	√
Skewness	√	√
Kurtosis	√	√
Energy	√	√
Entropy	√	√
Grey-level co-occurrence matrix (GLCM)		
Autocorrelation	√	√
Cluster prominence	√	√
Cluster shade	√	√
Contrast	√	√
Correlation	√	√
Difference entropy	√	√
Difference variance	√	√
Dissimilarity	√	√
Energy	√	√

Entropy	√	√
Homogeneity	√	√
Information measure of correlation 1	√	√
Information measure of correlation 2	√	√
Inverse difference	√	√
Maximum probability	√	√
Sum average	√	√
Sum entropy	√	√
Sum of squares	√	√
Sum variance	√	√
Neighbourhood grey tone difference matrix (NGTDM)		
Coarseness	√	√
Contrast	√	√
Busyness	√	√
Complexity	√	√
Texture Strength	√	√
Grey level size zone matrix (GLSZM)		
Small zone emphasis	√	√
Large zone emphasis	√	√
Low gray level emphasis	√	√
High gray level emphasis	√	√
Small zone low gray level emphasis	√	√
Small zone high gray level emphasis	√	√
Large zone low gray level emphasis	√	√
Large zone high gray level emphasis	√	√
Gray level nonuniformity	√	√
Zone size nonuniformity	√	√
Zone percentage	√	√
Zone size variance	√	√
Zone size entropy	√	√

A.3 3D Numerical Cell Phantom

In [179], a confocal microscope has been employed to find differences between viable and apoptotic MCF7 cells through 3D morphological features extraction. In particular, 206 cells were stained with three fluorescent dyes in order to measure the average value and standard deviation of 3D morphological parameters about the overall cell and its nucleus and mitochondria. These measurements have been here exploited to simulate a 3D numerical cell phantom [297], by setting 1 px = 0.12 μm. It is made of four sub-cellular structures, i.e., cell membrane, cytoplasm, nucleus, and mitochondria. Cell, nucleus, and mitochondria have been shaped as ellipsoids, then the cell external surface has been made irregular, and finally the cytoplasm has been obtained through a morphological erosion of the cell shape. Moreover, in each simulation, the number of mitochondria has been drawn from the uniform distribution $U_1\{a_1, b_1\}$. A 3D numerical cell phantom is displayed in Figure 4.2(a), in which 18 mitochondria have been simulated. To each simulated 3D sub-cellular component, a RI distribution has been assigned, as shown by the RI histogram in Figure 4.2(b). Measuring accurate RI values at sub-cellular level is still a deeply debated topic [404] [405]. Hence, realistic RIs cannot be replicated since they are not yet well known, therefore the unfavorable case for the testing purpose segmenting the nucleus from cytoplasm has been simulated, i.e., overlapped subcellular distributions of the RI values have been modelled. In particular, for each cell membrane voxel, its RI is drawn from distribution $N_1(\mu_1, \sigma^2)$. Instead, without knowing if the nucleus RIs are greater than the cytoplasm ones or vice versa, in each simulation, cytoplasm and nucleus are randomly assigned to distributions $N_2(\mu_2, \sigma^2)$ or $N_3(\mu_3, \sigma^2)$. It is worth remarking that, to strengthen the numerical assessment, the randomness of the RI assignments among the different simulations has been increased, because each voxel belonging to cell membrane, nucleus, and cytoplasm is drawn from gaussian distributions N_1, N_2, and N_3 (or N_1, N_3, and N_2), respectively, which average values μ_1, μ_2, and μ_3 are in turn drawn from

other gaussian distributions for each voxel extraction, i.e. $N_{\mu_1}(\mu_{\mu_1}, \sigma_\mu^2)$, $N_{\mu_2}(\mu_{\mu_2}, \sigma_\mu^2)$, and $N_{\mu_3}(\mu_{\mu_3}, \sigma_\mu^2)$, respectively. Instead, as regards mitochondria, each of them has a RI gaussian distribution $N_4(\mu_4, \sigma^2)$ which average value μ_4 is drawn from the gaussian distribution $N_{\mu_4}(\mu_{\mu_4}, \sigma_\mu^2)$ for each mitochondrion and not for each voxel. Moreover, a RI transition zone straddling the nucleus to cytoplasm is created, thus avoiding any discontinuity that could somehow facilitate the segmentation. In particular, after drawing all nucleus and cytoplasm values, RIs that are in the middle of their average values are assigned to the voxels of the transition zone, as highlighted by the red arrow at the top of Figure 4.2(b). This transition zone is obtained through morphological erosion and dilation of the nucleus ellipsoid, by using a spherical structuring element, which radius is drawn from the uniform distribution $U_2\{a_2, b_2\}$ px for each simulation, thus resulting in an internal nucleus volume that is about 85-95 % of the total nucleus volume. In the example in Figure 4.2(a,b), a 3 px radius has been selected. All the described parameters are reported in Table A.2.

Table A.2 Parameters used for simulating the 3D numerical cell phantoms.

$\mu_{\mu_1} = 1.352$	$\mu_{\mu_3} = 1.368$	$\sigma = 0.005$	$a_1 = 10$
$\mu_{\mu_2} = 1.365$	$\mu_{\mu_4} = 1.370$	$\sigma_\mu = 0.003$	$b_1 = 20$
$a_2 = 1$	$a_3 = 1$	$a_4 = 25$	$a_5 = \mu_N + \frac{1}{3}[q_{0.95}(N) - \mu_N]$
$b_2 = 3$	$b_3 = 10$	$b_4 = 30$	$b_5 = \mu_N + \frac{2}{3}[q_{0.95}(N) - \mu_N]$

A.4 CSSI Algorithm

In order to describe the steps of the proposed CSSI algorithm [297] sketched in Figure 4.2(c), the 3D numerical cell phantom shown in Figure 4.2(a,b) is used.

1. The 3D RI tomogram of the analyzed cell is centered in its $L_x \times L_y \times L_z$ array, that is then divided into distinct cubes, each of which has an edge measuring ε pixels, as shown in the central *xz*-slice in Figure A.5(a).

The ε parameter is the resolution factor at which the 3D array is firstly analyzed. It must be an even number and, after dividing each side of the 3D array by ε, an odd number must be obtained. Therefore, each distinct cube contains ε^3 voxels (i.e. RI values). The cubes completely contained within the cell shell are the investigated cubes C_I (yellow cubes within the blue cell shell in Figure A.5(a)). The central cube is not an investigated cube, since it is taken as a reference cube C_R (green cube in Figure A.5(a)), which vertices have x-, y-, and z-coordinates taken from pairs (V_{1x}, V_{2x}), (V_{1y}, V_{2y}), and (V_{1z}, V_{2z}), respectively. In Figure A.5(b), the 3D array from which the central *xz*-slice of Figure A.5(a) has been selected is displayed.

As discussed in Section 4.1, the CSSI algorithm is based on the WMW test [298] [299]. It is a rank-based non-parametric statistical test, thus distributions do not have to be normal. With a certain significance level γ, it allows rejecting or not the null hypothesis H_0 for which two sets of values have been drawn from the same distribution. The significance level γ is the probability of making an error of 1st species, i.e. of rejecting the null hypothesis H_0 when it is true. The confidence level is defined as 1-γ, i.e. it is the probability of not rejecting the null hypothesis H_0 when it is true. An important parameter in a statistical test is the p-value, which ranges from 0 to 1. The p-value is the observed significance level, i.e. the smallest significance level at which H_0 is rejected. It can be also defined as the probability of obtaining results at least as extreme

as the results actually observed, when the null hypothesis H_0 is true. Therefore, a low p-value leads to reject the null hypothesis H_0, because it means that such an extreme observed result is very unlikely when the null hypothesis H_0 is true. In fact, if the p-value$\geq\gamma$, H_0 is not rejected with significance level γ, while if p-value$<\gamma$, H_0 is rejected with significance level γ. Therefore, the greater the p-value the greater the confidence level with which two sets of values have been extracted from the same population. Hence, the proposed algorithm performs multiple comparisons between the investigated cubes C_I and the reference one C_R through the WMW test, because the C_R voxels are assumed belonging to the subcellular structure of interest, thus if a certain C_I has been drawn from its same distribution, then also the C_I voxels belong to the subcellular structure of interest. Without loss of generality, here the method is described in the case of the nucleus segmentation. As discussed in Section 4.1, for many kinds of suspended cells (e.g., cancer cell lines) the central voxels of the cell belong to the nucleus, therefore the reference cube C_R is associated to the central cube of the 3D RI tomogram.

2. An adaptive threshold T_P is set according to the p-values computed through the WMW test between the investigated cubes C_I and the reference cube C_R. It is chosen as the maximum value less than or equal to τ, such that for at least one C_I it happens that p-value$\geq T_P$.
3. A first rough clustering is performed through repeated M-iterations loops, to create a preliminary nucleus set $\mathcal{N}^P$. For each of them
    a. A temporary set $\mathcal{N}^T$ is created with the RIs of the sole reference cube C_R.
    b. At each of M iterations
        i. A reference set $\mathcal{R}$ is created by randomly drawing ε^3 values from the temporary set $\mathcal{N}^T$.

ii. For each investigated cube C_I, the corresponding p-value is computed with respect to the reference set $\mathcal{R}$ through the WMW test.

iii. The investigated cubes C_I such that their p-value$\geq$ T_P are added to the temporary set $\mathcal{N}^T$.

c. After an M-iterations loop, all the investigated cubes C_I added to the temporary set $\mathcal{N}^T$ are moved to the preliminary nucleus set $\mathcal{N}^P$, and then the temporary set $\mathcal{N}^T$ is reset.

d. Steps a-c are repeated until at least n investigated cubes C_I have been stored within the preliminary nucleus set $\mathcal{N}^P$, which is shown in Figure A.5(c).

4. A filtering operation is performed to delete outlier cubes from the preliminary nucleus set $\mathcal{N}^P$, thus creating a filtered nucleus set $\mathcal{N}^F$. Let $C_{\mathcal{N}^P,i}$ be a cube within $\mathcal{N}^P$, with $i = 1,2,\dots,n$.

a. The reduced nucleus set $\mathcal{N}_i^{P-}$ is created after removing the cube $C_{\mathcal{N}^P,i}$ from the preliminary nucleus set $\mathcal{N}^P$, with $i = 1,2,\dots,n$.

b. A p-value vector $\bar{p}$ of length n is created, which i-th element is the p-value computed through the WMW test between the cube $C_{\mathcal{N}^P,i}$ and the reduced nucleus set $\mathcal{N}_i^{P-}$.

c. A distance vector $\bar{d}$ of length n is created, which i-th element is the Euclidean distance between the centre of cube $C_{\mathcal{N}^P,i}$ and point B, i.e., the centroid of the preliminary nucleus set $\mathcal{N}^P$.

d. The p-value vector $\bar{p}$ is sorted in ascending order, thus obtaining the sorted p-value vector $\bar{p}^S$, shown in Figure A.5(d).

e. The distance vector $\bar{d}$ is sorted in ascending order and normalized to its maximum, thus obtaining the sorted distance vector $\bar{d}^S$, shown in Figure A.5(e) by blue dots.

Both vectors $\bar{p}^S$ and $\bar{d}^S$ are used to remove outlier cubes within the preliminary nucleus set $\mathcal{N}^P$. In fact, a cube $C_{\mathcal{N}^P,i}$ is considered an outlier if it is far from the centroid B and has a low p-value with respect to the other cubes in $\mathcal{N}^P$.

f. A fourth-degree polynomial is fitted to the sorted distance vector $\bar{d}^S$, thus obtaining the vector $\bar{d}^{SF}$ and its first difference $\overline{D}^{SF}$, that are reported in red in Figure A.5(e,f), respectively.

g. Let m be the index of the lowest value with null slope in vector $\overline{D}^{SF}$, as highlighted by the black dot in Figure A.5(f). If in the vector $\overline{D}^{SF}$ there is no point with null slope, m is chosen as the index of the global minimum.

h. After computing thresholds T_1, T_2, T_3, T_4, and T_5, the filtered nucleus set $\mathcal{N}^F$ reported in Figure A.5(g) is formed by cubes $C_{\mathcal{N}^P,i}$ that satisfy one of the following conditions

$$\begin{aligned} &1)\ \frac{d_i^{SF}}{d_{max}^{SF}} \le T_1 \\ &2)\ T_1 < \frac{d_i^{SF}}{d_{max}^{SF}} \le T_2\ \&\ p_i^S > T_4, \\ &3)\ T_2 < \frac{d_i^{SF}}{d_{max}^{SF}} \le T_3\ \&\ p_i^S > T_5 \end{aligned} \tag{A.7}$$

where & is the logical *and* operator, d_i^{SF} and p_i are elements of vectors $\bar{d}^{SF}$ and $\bar{p}^S$, respectively, with $i = 1,2,\dots,n$, and d_{max}^{SF} is the maximum value of vector $\bar{d}^{SF}$.

However, to build a filtered nucleus set $\mathcal{N}^F$, a strong spatial and statistical filtering has been made, in order to store only cubes that belong to the nucleus with high probability, thus leading to a strong underestimation of the nucleus

region. Moreover, to increase the statistical power of the WMW test, the resolution factor ε should not be too small. As a consequence, the ε-cubic structuring element leads to a low spatial resolution.

5. A refinement step is performed, in order to transform the filtered nucleus set $\mathcal{N}^F$ into a refined nucleus set $\mathcal{N}^R$, shown in Figure A.5(h). For each cube $C_{\mathcal{N}^F,i}$ within the filtered nucleus set $\mathcal{N}^F$,
    a. Let the augmented cube $C^A_{\mathcal{N}^F,i}$ be the smallest cube centered in $C_{\mathcal{N}^F,i}$ with an edge multiple of ε px, such that the p-value computed through the WMW test between its RIs and all the $\mathcal{N}^F$ values is greater than or equal to $\beta\mu(\bar{p})$, where $\mu(\cdot)$ is the average operator.
    b. To enhance the resolution, the augmented cube $C^A_{\mathcal{N}^F,i}$ is in turn divided into distinct sub-cubes with edges measuring $\varepsilon/2$ px.
    c. For each of these sub-cubes
        i. Its $\varepsilon^3/8$ values are compared with $\varepsilon^3/8$ RIs randomly drawn from the filtered nucleus set $\mathcal{N}^F$.
        ii. If the computed p-value$\geq \alpha T_P$, the examined sub-cube is inserted into the refined nucleus set $\mathcal{N}^R$.
6. All the possible pairs of sub-cubes in the refined nucleus set $\mathcal{N}^R$ are linked through a line segment.
7. A morphological closing is performed to smooth the corners of the resulting 3D polygonal and fill its holes, thus finally obtaining the partial nucleus set $\mathcal{N}_j$, displayed in Figure A.5(i).
8. Steps 1-7 are repeated K times on the same cell, thus obtaining K partial nucleus sets $\mathcal{N}_j$, with $j = 1, 2, \dots, K$, that are slightly different from each other, because in some of the performed WMW tests, the reference set is randomly drawn from a greater one.

9. The sum of all the K partial nucleus sets $\mathcal{N}_j$ provides a tomogram of occurrences, in which each voxel can take integer values $k \in [0, K]$ since each voxel may have been classified nucleus k times. In Figure A.6(a), the central slice of this tomogram of occurrences is reported.

10. An adaptive threshold k^* is set to segment the tomogram of occurrences. Let V_k be the number of voxels that have been classified nucleus at least k times, with $k = 1, 2, \dots, K$. Therefore, V_1 is the number of voxels of logical *or* among all the K partial nucleus sets $\mathcal{N}_j$, while V_K is the number of voxels of logical *and* among all the K partial nucleus sets $\mathcal{N}_j$.

    a. A vector $\bar{V}^P$ of percentage volumes is created, which elements are computed as

(A.8) $$V_k^P = \frac{V_k}{V_1},$$

    with $k = 1,2, \dots, K$, as reported in Figure A.6(b) by blue dots.

The 3D segmented nuclear OCH should be computed as the set of voxels that have occurred at least k^{opt} times. The parameter k^{opt} should maximize simultaneously the accuracy, sensitivity, and specificity of the proposed CSSI method. In Figure A.6(c), these performances are reported for each 3D segmented region composed by voxels that have occurred at least k times, with $k = 1,2, \dots, K$, along with the k^{opt} value, highlighted by the vertical green line. However, in a real experiment these trends are unknown, thus the intersection point cannot be computed. Therefore, a criterion is requested to find the k^* threshold, i.e., a suitable estimate of the k^{opt} threshold.

    b. The k^* threshold (red vertical line in Figure A.6(b)) is found as the k index at which the percentage volume vector $\bar{V}^P$ is nearest to a threshold T_V (orange horizontal line in Figure A.6(b)).

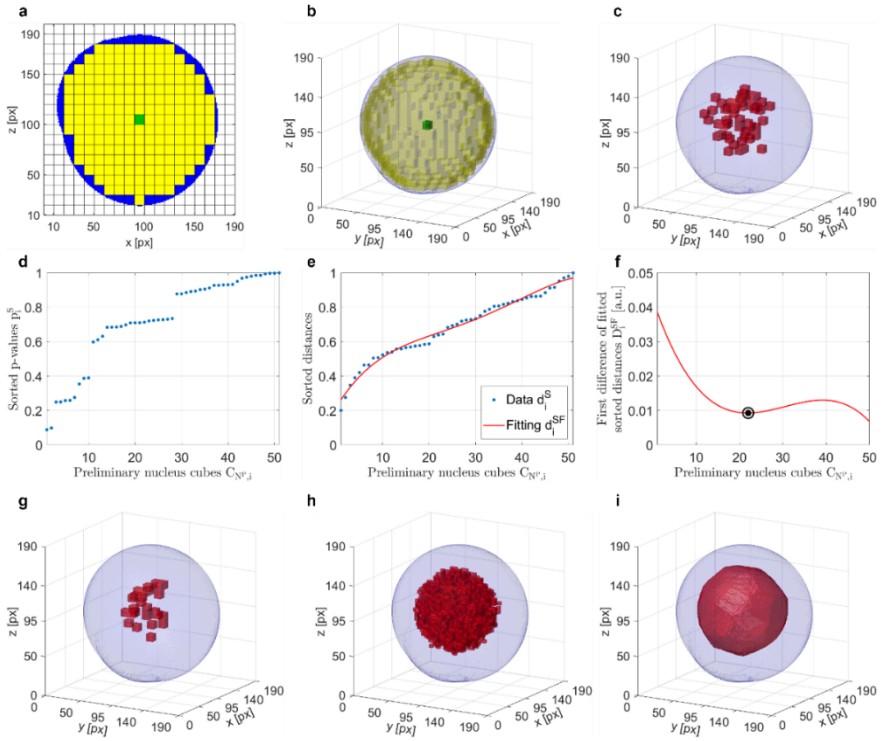

Figure A.5 CSSI of the stain-free nuclear OCH in a 3D numerical cell phantom. **(a)** Central *xz*-slice of the 3D array divided into distinct cubes with edge ε =10 px. The central reference cube C_R is highlighted in green while the investigated cubes C_I are highlighted in yellow within the cell shell in blue. **(b)** 3D array from which the central *xz*-slice in (a) has been selected. **(c)** Preliminary nucleus set $\mathcal{N}^P$ made of ε-cubes classified nucleus after a first rough clustering. **(d)** Vector of sorted p-values $\bar{p}^S$ computed through the WMW test between each cube $C_{\mathcal{N}^P,i}$ in the preliminary nucleus set $\mathcal{N}^P$ and the reduced nucleus set $\mathcal{N}_i^{P-}$, with $i = 1,2,\dots,n$. **(e)** Vector of sorted and normalized Euclidean distances $\bar{d}^S$ (blue dots) between each cube $C_{\mathcal{N}^P,i}$ in the preliminary nucleus set $\mathcal{N}^P$ and the centroid of all cubes in $\mathcal{N}^P$, along with the fourth-degree polynomial fitting $\bar{d}^{SF}$ (red line), with $i = 1,2,\dots,n$. **(f)** First difference $\bar{D}^{SF}$ (red line) of vector of fitted sorted distances $\bar{d}^{SF}$ in (b), with highlighted in black the lowest value with null slope. **(g)** Filtered nucleus set $\mathcal{N}^F$ made of ε-cubes classified nucleus after a spatial and statistical filtering of the preliminary nucleus set $\mathcal{N}^P$ in (c). **(h)** Refined nucleus set $\mathcal{N}^R$ made of $\varepsilon/2$-cubes classified nucleus after increasing resolution in the filtered nucleus set $\mathcal{N}^F$ in (g) through sub-cubes of size $\varepsilon/2$. **(i)** Partial nucleus set $\mathcal{N}_j$ obtained by linking sub-cubes in (h) through segment lines and by using morphological closing. In (b,c,g-i), the blue region is the cell shell and the red region is the segmented nucleus at different steps of the CSSI algorithm.

In Figure A.6(c), where the k^* threshold is highlighted by the red vertical line, it is clear that, despite $k^* \neq k^{opt}$, k^* is located in the same quasi-constant region of k^{opt}, hence this estimated threshold leads to very little differences in terms of clustering performances with respect to the optimal one.

11. The final 3D nuclear OCH $\mathcal{N}$ is made of voxels that have been classified nucleus at least k^* times, as shown in Figure 4.2(d).

In Figure 4.2(d), it is evident that the proposed CSSI algorithm allows segmenting a 3D nuclear OCH very close to the original one, as underlined by accuracy, sensitivity, and specificity reported below the tomograms. Moreover, these values are very close to the optimal ones that could be obtained by using the optimal threshold k^{opt} instead of the estimated one k^*, i.e. $ACC^{opt} = 98.22$ %, $SENS^{opt} = 98.57$ %, and $SPEC^{opt} = 98.10$ %.

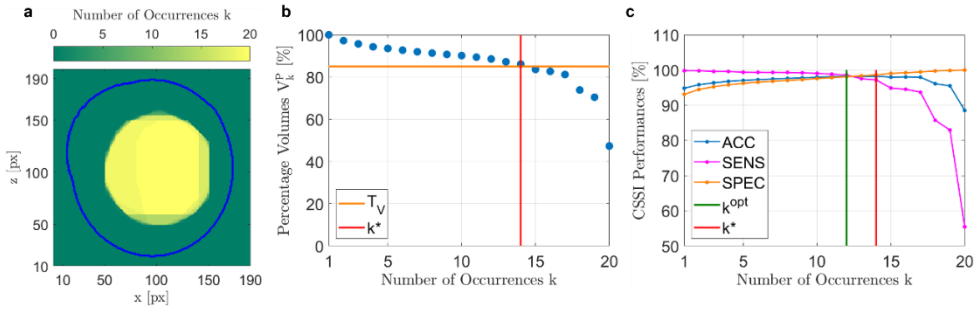

Figure A.6 Setting of the estimated threshold k^*.
(a) Central *xz*-slice of the tomogram of occurrences, in which each voxel can take an integer value k from 0 to $K = 20$, i.e. the number of times it has been classified nucleus after repeating K times steps 1-7 of the CSSI algorithm on the same cell. The blue line is the cell contour. **(b)** Percentage volumes V_k^P (blue dots), i.e. number of voxels V_k classified nucleus at least k times normalized to V_{20}, along with the threshold T_V (horizontal orange line) used to find the estimated threshold k^* (vertical red line) by an intersection analysis. **(c)** CSSI performances associated to each possible threshold k for creating the final 3D nucleus set N, expressed in terms of accuracy (blue), sensitivity (magenta), and specificity (orange), along with the optimum threshold k^{opt} (vertical green line in which performances are simultaneously maximized) and its estimation k^* (vertical red line) computed in (b).

All the parameters involved in the proposed CSSI algorithm are described in Table A.3. It is worth underlining that, in the presented experiments, a resolution factor ε=10 px has been set to analyse arrays made of at least 190 × 190 × 190 voxels, since it was an optimum compromise between the need of having both high resolution in nucleus segmentation and high statistical power in WMW test (see the analysis about the imaging spatial resolution in Section 4.2). The proposed computational processing takes tens of minutes on a conventional desktop computer. However, it can be easily speeded up using GPUs, parallel processing strategies, and faster programming languages (in the proposed implementation, MATLAB® R2020a has been used).

Table A.3 Setting of the parameters involved in the CSSI algorithm to segment the stain-free 3D nuclear OCH from TPM-FC reconstructions (⌊·⌋, ⌈·⌉, and ⌊·⌉ are the floor, ceil, and nearest integer operators, respectively).

$\varepsilon = 10\ px$	$V_{1x} = \frac{L_x - \varepsilon + 2}{2}$	$V_{2x} = \frac{L_x + \varepsilon}{2}$	$V_{1y} = \frac{L_y - \varepsilon + 2}{2}$
$V_{2y} = \frac{L_y + \varepsilon}{2}$	$V_{1z} = \frac{L_z - \varepsilon + 2}{2}$	$V_{2z} = \frac{L_z + \varepsilon}{2}$	$\tau = 0.99$
$M = 10$	$n = \left\lfloor \frac{2}{\varepsilon} \frac{L_x + L_y + L_z}{3} \right\rceil$	$T_5 = \frac{1}{2}[\mu(\bar{p}) + p_{max}]$	$T_4 = \mu(\bar{p})$
$T_3 = \begin{cases} 0.7 & if\ \frac{m+1}{n} < 0.15 \\ 0.95 & if\ \frac{m+1}{n} > 0.85 \\ 0.7 + \frac{5}{14}\left(\frac{m+1}{n} - 0.15\right) & otherwise \end{cases}$			
$T_V = \begin{cases} \frac{\lfloor 5\mu(\bar{V}^P) \rfloor}{5} & if\ \mu(\bar{V}^P) > 50\ \% \\ \frac{\lceil 5\mu(\bar{V}^P) \rceil}{5} & if\ \mu(\bar{V}^P) < 50\ \% \\ \mu(\bar{V}^P) & if\ \mu(\bar{V}^P) = 50\ \% \end{cases}$			
$T_2 = T_3 - 0.1$	$T_1 = T_2 - 0.1$	$\alpha = 0.9$	$\beta = 0.5$	$K = 20$

A.5 CSSI Performances of the Stain-Free Nucleus Identification in Presence of Nucleoli

The nucleolus is the biggest structure inside the nucleus and it is a region particularly dense of genetic material, therefore its malfunctioning has been related to different human diseases [406] [407]. For example, the nuclear-nucleolar volume ratio is expected to change in a cancer cell [408], as well as the number of nucleoli [409]. Moreover, due to its denser genetic composition, on average the nucleolus has a higher RI than the surrounding nucleus [5]. Therefore, the nucleolus has been integrated to the same 1000 numerical 3D cell phantoms described in Section 4.1 and in Appendix A.3 in order to check whether its presence could negatively alter the correct identification of the stain-free nucleus by CSSI [297]. Since in diploid human cells there are up to ten possible nucleoli per cell [409], for each phantom the number of nucleoli are randomly drawn from the uniform distribution $U_3\{a_3, b_3\}$. The overall volume of all the nucleoli in a cell is computed from the nucleus-nucleolus volume ratio randomly drawn from the uniform distribution $U_4\{a_4, b_4\}$ [408], and then it is divided equally among all the nucleoli, each of them being simulated as a sphere. The nucleolus RIs are randomly drawn from the gaussian distribution $N_5(\mu_5, \sigma^2)$, where the mean value μ_5, in turn randomly drawn from the uniform distribution $U_5\{a_5, b_5\}$, depends on the nucleus RIs in order to emulate the biological condition in which the nucleolus average RI is higher than the nucleus one. All the described parameters are reported in Table A.2. Within the 1000 3D numerical cell phantoms, the multiple nucleoli are randomly localized inside the nucleus. In Figure A.7(a,d,g,j), four numerical cell phantoms are displayed with the same 15 mitochondria and the same nucleus, and with 0, 3, 6, and 9 nucleoli, respectively. As reported in the corresponding RI histograms in Figure A.7(b,e,h,k), respectively, the RI values assigned to the nucleoli are greater than the corresponding outer nuclei but still included in their RI distributions in order to consider the worst case condition for segmentation.

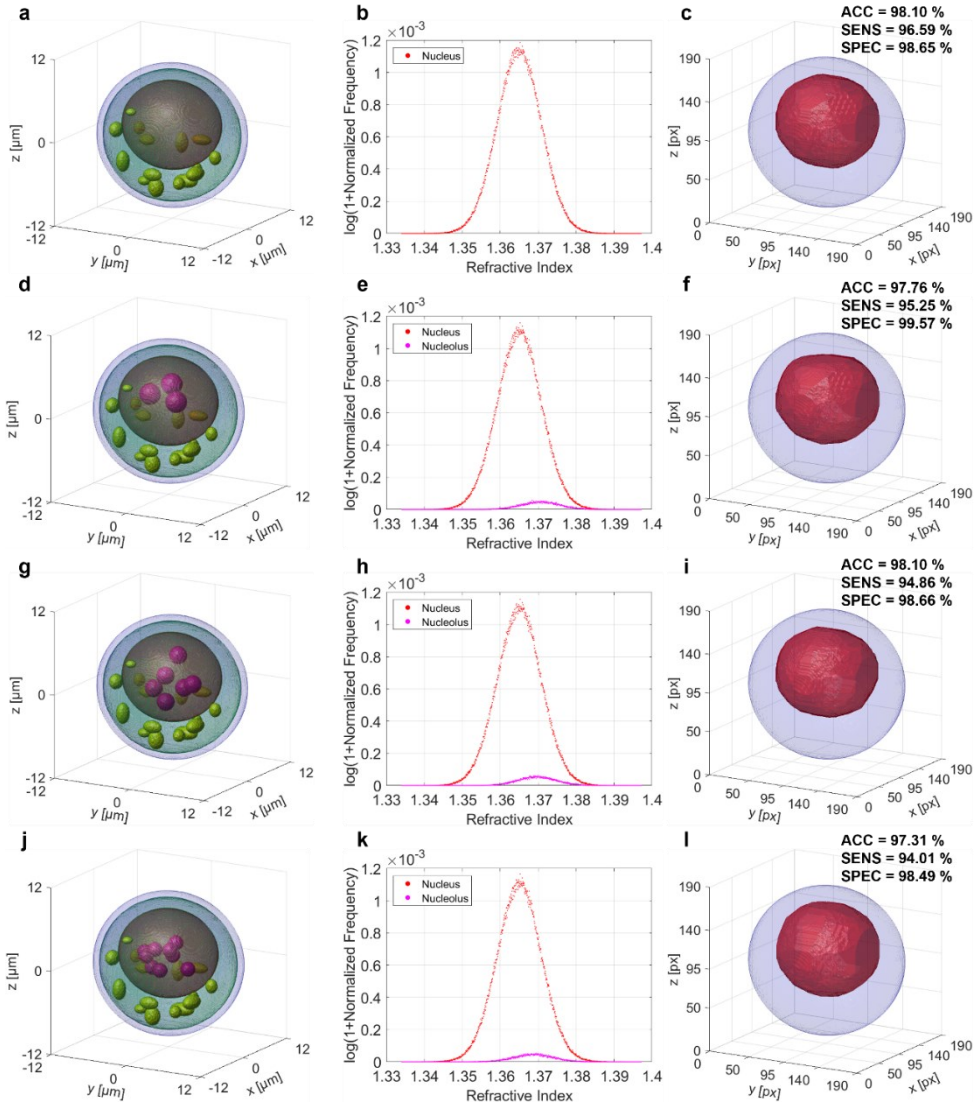

Figure A.7 Numerical assessment of the CSSI algorithm applied to segment the 3D nuclear OCH after the addition of the nucleoli.
(a,d,g,j) Isolevels representation of the 3D cell model, simulated with the same cell membrane, cytoplasm, nucleus, and 15 mitochondria, and with 0, 3, 6, and 9 nucleoli, respectively. **(b,e,h,k)** Histogram of the RI values assigned to the nucleus and the nucleoli in (a,d,g,j), respectively. **(c,f,i,l)** Nuclear OCH segmented by the CSSI algorithm within the cell phantoms in (a,d,g,j), respectively. The corresponding CSSI accuracy, sensitivity, and specificity are reported at top right.

In Figure A.7(c), the nuclear OCH segmented by the CSSI method without considering the presence of nucleoli is mostly overlapped to the nuclear OCHs displayed in Figure A.7(f,i,l) obtained by the CSSI method in presence of 3, 6, and 9 nucleoli, respectively, as also suggested by the values of accuracy, sensitivity, and specificity reported in Figure A.7(c,f,i,l). After applying the CSSI algorithm to the 1000 numerical 3D cell phantoms, the values of 9 metrics have been computed to quantify the CSSI performances in segmenting the stain-free nucleus in the presence of the nucleoli (see the second column of Table 9).

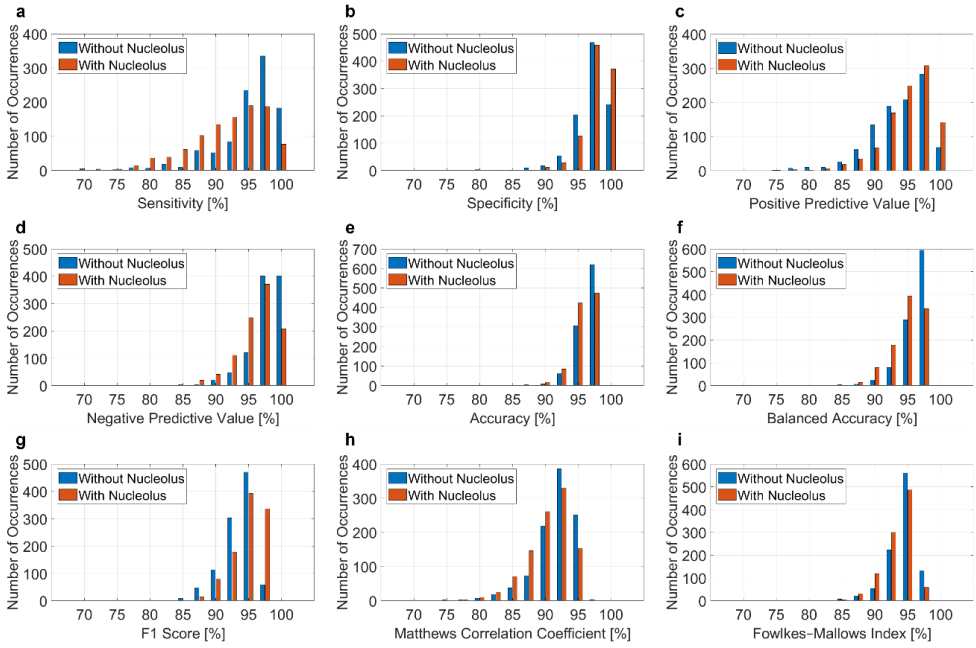

Figure A.8 Histograms of the several metrics in Table 9 used to quantify the performances in computing the nuclear OCH over a dataset of 1000 3D numerical cell phantoms without (blue) and with (orange) the presence of the nucleoli.

(a) Sensitivity (Recall or True Positive Rate). **(b)** Specificity (True Negative Rate). **(c)** Positive Predictive Value (Precision). **(d)** Negative Predictive Value. **(e)** Accuracy. **(f)** Balanced Accuracy. **(g)** F1 Score. **(h)** Matthews Correlation Coefficient (Phi Coefficient). **(i)** Fowlkes–Mallows Index.

The values of the 9 metrics can be directly compared with the corresponding ones in the first column of Table 9 regarding the segmentation of the stain-free nucleus without the simulation of the nucleoli. Moreover, the comparison in Figure A.8 between the histograms of these 9 metrics about the two case studies clearly shows that, despite the presence of the nucleoli, even if performances of the CSSI in identifying the stain-free nucleus have slightly decreased, they still keep very high, over the 90 %. Therefore, the presence of the nucleoli inside the nucleus does not substantially worsen the performances of the CSSI nucleus segmentation algorithm.

A.6 Conventional 2D Imaging of Lipid Droplets

With the aim to demonstrate the advantages of TPM-FC, the results reported in Section 4.3.1 are compared with the currently available gold-standard techniques for LD analysis, namely TEM and FM upon Nile Red staining [291]. Thanks to the high spatial resolution and contrast of TEM images, LDs are visible with a high level of details in A2780 and THP1 cells (see Figure A.9(a,g)), with average LD dimension being 963 nm (SD+/- 242) and 736 nm (SD+/- 150), respectively. The reliable LD counting is not possible when using TEM, due the small FOV and the limited sample section (80 nm) with respect to the cell size (tens of microns). These intrinsic drawbacks of TEM prevent the precise determination of the number of cells harboring LDs, allowing only approximate estimation. On the other hand, the FM analysis permits LD quantification, revealing a higher number of LDs in ovarian cancer model ($p<0.005$, see Figure A.9(b-f) and Figure A.9(h-l)). In particular, LDs have been counted in 11 A2780 and THP1 live cells, obtaining on average 26.55 (SD+/- 4.18) and 10.55 (SD+/- 1.96) organelles per cell, respectively (see Figure A.9(e,k)). In line with TPM data, LDs have been detected in all A2780 cells while they are missing in some THP1 cells.

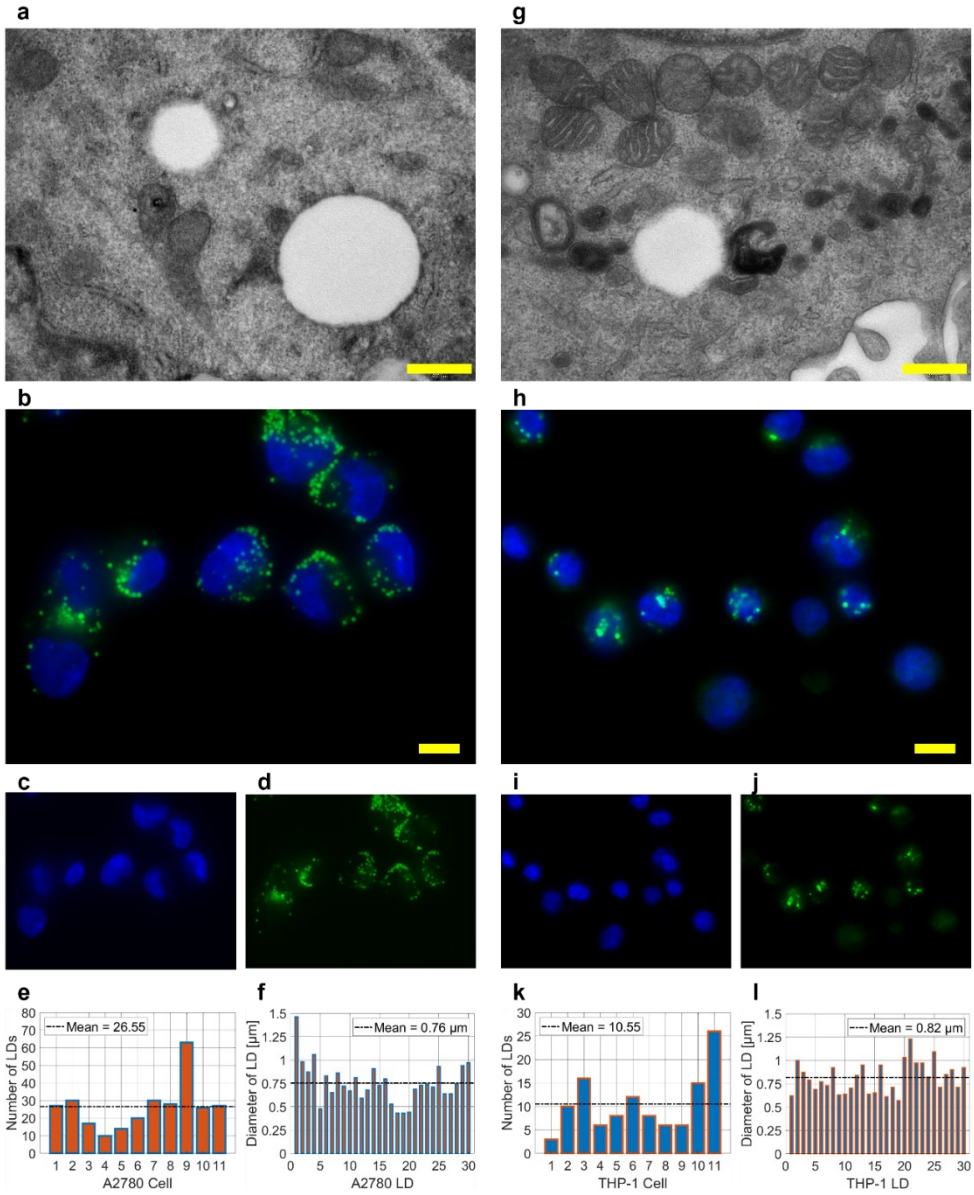

Figure A.9 Conventional 2D imaging of A2780 (a-f) and THP1 (g-l) live cells. **(a,g)** TEM images of LDs. Scale bar is 0.5 µm. **(b,h)** Representative FM images of nuclei (blue) and LDs (green). Scale bar is 10 µm. **(c,i)** FM images of nuclei stained with Hoechst. **(d,j)** FM images of LDs stained with Nile Red. **(e,k)** Number of LDs in 11 live cells imaged by FM. **(f,l)** Diameters of 30 LDs imaged by FM.

No significant difference in LDs size has been observed between the two models. The diameter of 30 LDs per cell type has been measured, revealing the average values of 760 nm (SD+/- 39) in A2780 and 820 nm (SD+/- 29) in THP1 model (see Figure A.9(f,l)). Interestingly, FM images show that LDs within the A2780 cytoplasm are not uniformly distributed, but mainly assembled near the nucleus, confirming the same phenomenon observed in the TPM-FC reconstructions.

A.7 3D Morphological Inspection of nanoGraphene Oxide within Cells

In order to describe the morphometric parameters used to characterize the internalization of nGO after 24 h of cell culture, cells in Figure 4.21(a-c) are considered as example [294]. Let C be the cell centroid and G be the nGO cluster centroid. Let M be the nearest point of the external cell membrane to point G. The line passing for C and G is indicated by c, while the line passing for M and G is indicated by m. Moreover, let g be the line passing for point G and having as slope the 3D nGO cluster orientation.

The graphene-cell normalized distance is defined as

$$\delta(G,C) = \frac{\Delta(G,C)}{\Delta(G,C)+\Delta(G,M)} \tag{A.9}$$

and the graphene-membrane normalized distance is defined as

$$\delta(G,M) = \frac{\Delta(G,M)}{\Delta(G,M)+\Delta(G,C)}, \tag{A.10}$$

where $\Delta(\cdot,\cdot)$ is the Euclidean distance between two points. The normalized distances in Eq. (A.9) and Eq. (A.10) can take values from 0 to 1. In the three cells at 24 h, nGO clusters are about in the same relative position between cell centroid and cell membrane, as shown by the $\delta(G,C)$ vs. $\delta(G,M)$ plot in Figure

4.21(d). Moreover, nGO clusters appear much closer to cell membrane than cell center. This marginal position can be explained by considering that most of cell volume is occupied by nucleus, that in fact does not internalize nGO particles, because they are larger than the functional diameter of the nuclear pores [375]. Moreover, the sphericity Ψ_G is used as a synthetic descriptor parameter of the graphene shape, defined as [410]

$$\Psi_G = \frac{\sqrt[3]{\pi(6V_G)^2}}{A_G}, \tag{A.11}$$

where V_G and A_G are the volume and the surface area of the nGO cluster, respectively. Therefore, Ψ_G measures how similar the shape of the nGO cluster is to that of a perfect sphere, and it takes values in the range [0,1] (1 in the spherical case). In Figure 4.21(e), Ψ_G is reported versus the graphene equivalent radius ρ_G, i.e. the radius of a sphere with the same volume. On the basis of the defined descriptors, it is inferred that the nGO clusters in cell 1 and cell 3 have about the same equivalent radius and sphericity, while the nGO cluster in cell 2 is smaller with a quasi-spherical shape. Moreover, as displayed by the polar plot in Figure 4.21(f), to the higher nGO sphericity Ψ_G corresponds a lower graphene-cell angle θ_{GC}, i.e. the angle between lines g and c in Figure 4.21(a-c), which takes values from 0° to 90°. The lower graphene-cell angle θ_{GC} of cell 2 also corresponds to a lower graphene-cell normalized distance $\delta(G, M)$, as reported by the polar plot in Figure 4.21(g). From Figure 4.21(a-c,f,g), it is clear that nGO clusters arrange within all three 24h-cells with an angle between 75° and 90° with respect to line c.

Instead, for the 3D nuclear decoration observed within the cell in Figure 4.20, a toroid model is used (see inset in Figure 4.22(a)). Its volume can be computed as

$$V_T = 2\pi^2 R_T r_T^2, \tag{A.12}$$

where R_T is the toroid outer radius, i.e. the distance between the centre of the tube c_T and the centre of the toroid C_T, and r_T is the toroid inner radius, i.e. the radius of the generator circle of the tube. The volume V_T is set equal to the

volume of the nGO ring structure in Figure 4.20(e), while R_T is calculated as the mean distance between its centroid and all voxels. Then, r_T can be obtained by inverting Eq. (A.12). By this way, the r_T value measures an estimation of the thickness of the nGO cluster, while R_T provides a rough estimation of the nuclear size, since the 3D nGO structure spreads around nucleus without entering within it [375]. By converting the cartesian coordinates in spherical ones (i.e. azimuthal angle, elevation angle and radial distance), the toroid can be unrolled, thus obtaining a cylinder, as represented in yellow in Figure 4.22(a). The same transformation is done for the nGO ring structure of Figure 4.20(e), as reported in black in Figure 4.22(a). Beyond the clear visual comparison, the unrolling procedure shown in Figure 4.22(a) enables a quantitative evaluation about the surface irregularity of the nGO structure. Indeed, in the case of an ideal toroid, the azimuthal angle takes values in $[-180°, 180°]$, the elevation angle takes values in $[-\tan^{-1}(r_T/R_T), \tan^{-1}(r_T/R_T)]$, and the radial distance takes values in $[R_T - r_T, R_T + r_T]$, as confirmed by their yellow histograms in Figure 4.22(b-d). Same histograms (in black) are obtained for the nGO cluster in Figure 4.22(b-d). To quantify the nGO cluster irregularities with respect to the toroid used as reference, the percentage error between histograms is calculated, resulting in 24.40% for the azimuthal angle, 54.82% for the elevation angle and 30.72% for the radial distance.

A.8 Mathematical Derivation and Computation of 3D Zernike Descriptors

The 3D Zernike functions can be defined in spherical coordinates as

$$Z_{nl}^{m}(r, \vartheta, \varphi) = R_{nl}(r) Y_l^m(\vartheta, \varphi), \tag{A.13}$$

where n, l, m are integer indexes such that $n \geq 0$, $l \leq n$ with $n - l$ even numbers and $m \in [-l, l]$. The radial part $R_{nl}(r)$ of Eq. (A.13) is defined as

$$R_{nl}(r) = r^l \sum_{v=0}^{k} q_{kl}^{v}\, r^{2v}, \tag{A.14}$$

where $k = \frac{n-l}{2}$ and the coefficients q_{kl}^{v} are determined so that the resulting basis functions are orthonormal in the unit ball, i.e.

$$q_{kl}^{v} = \frac{(-1)^k}{2^{2k}} \sqrt{\frac{2l+4k+3}{3}} \binom{2k}{k} (-1)^v \frac{\binom{k}{v}\binom{2(k+l+v)+1}{2k}}{\binom{k+l+v}{k}}. \tag{A.15}$$

The angular part $Y_l^m(\vartheta, \varphi)$ is set as the spherical harmonics, given by

$$Y_l^m(\vartheta, \varphi) = N_l^m P_l^m(cos\, \vartheta)\, e^{im\varphi}, \tag{A.16}$$

where P_l^m denotes the associated Legendre functions and N_l^m is a normalization factor defined as

$$N_l^m = \sqrt{\frac{(2l+1)}{4\pi} \frac{(l-m)!}{(l+m)!}}. \tag{A.17}$$

In order to formulate the 3D Zernike polynomials as homogenous polynomials in the Cartesian coordinates $\mathbf{x} = (x, y, z)^T$, it is needed to rewrite spherical harmonics in harmonic polynomials. By using the conversion between Cartesian and spherical coordinates and the integral formula for associated Legendre functions, one can express the harmonic polynomials as follows

$$h_l^m(\boldsymbol{x}) = r^l Y_l^m(\vartheta, \varphi) = c_l^m \left(\frac{ix-y}{2}\right)^m z^{l-m} \sum_{\mu=0}^{\left\lfloor \frac{l-m}{2} \right\rfloor} \binom{l}{\mu} \binom{l-\mu}{m-\mu} \left(-\frac{x^2+y^2}{4z^2}\right)^{\mu}, \tag{A.18}$$

where c_l^m are normalization factors defined as

$$c_l^m = c_l^{-m} = \frac{\sqrt{(2l+1)(l-m)!(l+m)!}}{l!}. \tag{A.19}$$

The Eq. (A.18) yields homogenous polynomials for $m > 0$. For $m < 0$ the following symmetry relation is used

$$h_l^{-m}(\boldsymbol{x}) = (-1)^m \overline{h_l^m(\boldsymbol{x})}. \tag{A.20}$$

Therefore, the Eq. (A.13) can be rewritten in Cartesian coordinates

$$Z_{nl}^{m}(\boldsymbol{x}) = \sum_{v=0}^{k} q_{kl}^{v} \, |\boldsymbol{x}|^{2v} \, h_{l}^{m}(\boldsymbol{x}). \tag{A.21}$$

To implement the Eq. (A.21), one can derive a more compact formulation by expanding $Z_{nl}^{m}(\mathbf{x})$ through the Eq. (A.18). After some mathematical manipulations (see more details in [386] [387]), the Eq. (A.21) can be rewritten as

$$Z_{nl}^{m}(\boldsymbol{x}) = \sum_{w+s+t\leq n} \chi_{nlm}^{wst} \, x^{w} \, y^{s} \, z^{t}, \tag{A.22}$$

where χ_{nlm}^{wst} is set as

$$\begin{aligned} \chi_{nlm}^{wst} = \; & c_{l}^{m} 2^{-m} \sum_{v=0}^{k} q_{kl}^{v} \sum_{\alpha=0}^{v} \binom{v}{\alpha} \sum_{\beta}^{v-\alpha} \binom{v-\alpha}{\beta} \sum_{u=0}^{m} (-1)^{m-u} \times \\ & \times \binom{m}{u} i^{u} \sum_{\mu=0}^{\left\lfloor \frac{l-m}{2} \right\rfloor} (-1)^{\mu} 2^{-2\mu} \binom{l}{\mu} \binom{l-\mu}{m+\mu} \sum_{\varrho=0}^{\mu} \binom{\mu}{\varrho} \end{aligned}, \tag{A.23}$$

and $w = 2(\varrho + \alpha) + u, s = 2(\mu - \varrho + \beta) + m - u, t = 2(v - \alpha - \beta - \mu) + l - m$. Since the functions in Eq. (A.22) form a complete orthonormal system, it is possible to approximate any 3D object by a finite number of 3DZD. For the presented application, let $T(\mathbf{x})$ be the tomographic reconstruction. Its approximation using the Zernike basis is

$$T(\boldsymbol{x}) \approx \sum_{n,l,m} \Omega_{nl}^{m} Z_{nl}^{m}(\boldsymbol{x}), \tag{A.24}$$

where Ω_{nl}^{m} are the 3DZD. In the proposed implementation, the tomographic reconstruction is enforced to be fitted by Eq. (A.24), hence the 3DZD can be calculated by solving the equivalent linear system after vectorizing the terms in Eq. (A.24). Without lack of generality, the tomogram $T(\mathbf{x})$ is considered calculated within a cube having V voxels per side, such that V^3 is the total number of voxels. Let N be the Zernike fitting order, such that $n\epsilon[0, N]$. It is possibile to evaluate the number of Zernike basis functions to be generated by fixing N as the sum of the first $N + 1$ triangular numbers. Let M be this summation, $M = (N + 1)(N + 2)(N + 3)/6$, hence the Zernike functions can be seen as 4D vector with sizes $V \times V \times V \times M$, i.e. $Z_{nl}^{m}(\mathbf{x}) = [Z\{1\}, Z\{2\}, \dots, Z\{M\}]$ with $Z\{j\}$ having the same dimension of $T(\mathbf{x}) \; \forall \; j\epsilon[1, M]$. Therefore, the Eq. (A.24) can be rewritten and solved as

$$\widehat{\boldsymbol{T}} \approx \overline{\overline{\boldsymbol{Z}}}\widehat{\boldsymbol{\Omega}} \;\Rightarrow\; \widehat{\boldsymbol{\Omega}}_D = pinv\{\overline{\overline{\boldsymbol{Z}}}\}\widehat{\boldsymbol{T}}, \tag{A.25}$$

where $\widehat{\mathbf{T}} = vec(T)$ and $\widehat{\mathbf{\Omega}}_D = vec(\Omega_D)$ with dimensions $V^3 \times 1$ and $M \times 1$, respectively, and $\overline{\overline{\mathbf{Z}}} = [vec(Z\{1\}), vec(Z\{2\}), \dots, vec(Z\{M\})]$, thus having sizes $V^3 \times M$. The operator $pinv$ indicate the pseudo-inverse matrix calculation. Finally, $\widehat{\mathbf{\Omega}}_D$ is the vector containing the 3DZD.

AVGVSTVS FRIDERICVS ROMANORVM IMPERATOR SEMPER

Bibliography

[1] Y. Park, C. Depeursinge and G. Popescu, "Quantitative phase imaging in biomedicine.," *Nat. Photonics,* vol. 12, no. 10, pp. 578-589, 2018.

[2] J. Goodman, Introduction to Fourier Optics, 1996., McGraw-Hill, 1996.

[3] M. K. Kim, "Principles and techniques of digital holographic microscopy.," *SPIE reviews,* vol. 1, no. 1, p. 018005, 2010.

[4] F. Charrière, A. Marian, F. Montfort, J. Kuehn, T. Colomb, E. Cuche, P. Marquet and C. Depeursinge, "Cell refractive index tomography by digital holographic microscopy.," *Opt. Lett.,* vol. 31, no. 2, pp. 178-180, 2006.

[5] P. Y. Liu, L. K. Chin, W. Ser, H. F. Chen, C. M. Hsieh, C. H. Lee, K. B. Sung, T. C. Ayi, P. H. Yap, B. Liedberg, K. Wang, T. Bourouina and Y. Leprince-Wang, "Cell refractive index for cell biology and disease diagnosis: past, present and future.," *Lab Chip,* vol. 16, no. 4, pp. 634-644, 2016.

[6] Z. Wang, V. Bianco, D. Pirone, P. Memmolo, M. M. Villone, P. L. Maffettone and P. Ferraro, "Dehydration of plant cells shoves nuclei rotation allowing for 3D phase-contrast tomography.," *Light: Sci. Appl.,* vol. 10, no. 1, pp. 1-16, 2021.

[7] A. Diaspro, Optical Fluorescence Microscopy., Berlin: Springer, 2011.

[8] D. Gabor, "A new microscope principle," *Nature,* vol. 161, p. 777–778, 1948.

[9] P. Picart and J. Leval, "General theoretical formulation of image formation in digital fresnel holography.," *J. Opt. Soc. Am. A,* vol. 25, no. 7, p. 1744–1761, 2008.

[10] E. Sánchez-Ortiga, A. Doblas, G. Saavedra, M. Martínez-Corral and J. Garcia-Sucerquia, "Off-axis digital holographic microscopy: practical design parameters for operating at diffraction limit.," *Appl. Opt.,* vol. 53, no. 10, pp. 2058-2066, 2014.

[11] E. Cuche, P. Marquet and C. C. Depeursinge, "Aperture apodization using cubic spline interpolation: application in digital holographic microscopy.," *Opt. Commun.,* vol. 182, pp. 59-69, 2000.

[12] E. Cuche, P. Marquet and C. Depeursinge, "Spatial filtering for zero-order and twin-image elimination in digital off-axis holography.," *Appl. Opt.,* vol. 39, pp. 4070-4075, 2000.

[13] P. Memmolo, L. Miccio, M. Paturzo, G. Caprio, G. Coppola, P. Netti and P. Ferraro, "Recent advances in holographic 3d particle tracking," *Adv. Opt. Photonics,* vol. 7, pp. 713-755, 2015.

[14] P. Ferraro, S. De Nicola, A. Finizio, G. Coppola, S. Grilli, C. Magro and G. Pierattini, "Compensation of the inherent wave front curvature in digital holographic coherent microscopy for quantitative phase-contrast imaging.," *App. Opt.,* vol. 42, no. 11, pp. 1938-1946, 2003.

[15] L. Miccio, D. Alfieri, S. Grilli, P. Ferraro, A. Finizio, L. De Petrocellis and S. Nicola, "Direct full compensation of the aberrations in quantitative phase microscopy of thin objects by a single digital hologram.," *Appl. Phys. Lett.,* vol. 90, p. 041104, 2007.

[16] W. Zhou, Y. Yu and A. Asundi, "Study on aberration suppressing methods in digital micro-holography.," *Opt. Lasers Eng.,* vol. 47, no. 2, pp. 264-270, 2009.

[17] J. Bioucas-Dias, V. Katkovnik, J. Astola and K. Egiazarian, "Absolute phase estimation: adaptive local denoising and global unwrapping.," *App. Opt.,* vol. 47, no. 29, pp. 5358-5369, 2008.

[18] J. M. Bioucas-Dias and G. Valadao, "Phase unwrapping via graph cuts.," *IEEE Trans. Image Process.,* vol. 16, no. 3, pp. 698-709, 2007.

[19] J. Kühn, F. Charrière, T. Colomb, E. Cuche, F. Montfort, Y. Emery, P. Marquet and C. Depeursinge, "Axial sub-nanometer accuracy in digital holographic microscopy.," *Meas. Sci. Technol.,* vol. 19, no. 7, p. 074007, 2008.

[20] G. Popescu, Quantitative Phase Imaging of Cells and Tissues, New York: McGraw-Hill, 2011.

[21] L. Miccio, P. Memmolo, F. Merola, P. A. Netti and P. Ferraro, "Red blood cell as an adaptive optofluidic microlens.," *Nat. Commun.,* vol. 6, no. 1, pp. 1-7, 2015.

[22] L. Miccio, P. Memmolo, F. Merola, M. Mugnano and P. Ferraro, "Optobiology: live cells in optics and photonics.," *J. Phys. Photonics,* vol. 3, no. 1, p. 012003, 2020.

[23] P. Jourdain, D. Boss, B. Rappaz, C. Moratal, M. C. Hernandez, C. Depeursinge, P. J. Magistretti and P. Marquet, "Simultaneous optical recording in multiple cells by digital holographic microscopy of chloride current associated to activation of the ligand-gated chloride channel GABAA receptor.," *PLoS One,* vol. 7, no. 12, p. e51041, 2012.

[24] A. Doblas, E. Roche, F. J. Ampudia-Blasco, M. Martìnez-Corral, G. Saavedra and J. Garcia-Sucerquia, "Diabetes screening by telecentric digital holographic microscopy.," *J. Microsc.,* vol. 261, no. 3, pp. 285-290, 2016.

[25] M. Mir, Z. Wang, Z. Shen, M. Bednarz, R. Bashir, I. Golding, S. Presanth and G. Popescu, "Optical measurement of cycle-dependent cell growth.," *Proc. Natl Acad. Sci. USA,* vol. 108, pp. 13124-13129, 2011.

[26] T. Cacace, V. Bianco and P. Ferraro, "Quantitative phase imaging trends in biomedical applications.," *Opt. Lasers Eng.,* vol. 135, p. 106188, 2020.

[27] B. Kemper, D. D. Carl, J. Schnekenburger, I. Bredebusch, M. Schäfer, W. Domschke and G. von Bally, "Investigation of living pancreas tumor cells by digital holographic microscopy.," *J. Biomed. Opt.,* vol. 11, no. 3, p. 034005, 2006.

[28] N. T. Shaked, L. L. Satterwhite, G. A. Truskey, A. P. Wax and M. J. Telen, "Quantitative microscopy and nanoscopy of sickle red blood cells performed

by wide field digital interferometry.," *J. Biomed. Opt.,* vol. 16, no. 3, p. 030506, 2011.

[29] H. V. Pham, B. Bhaduri, K. Tangella, C. Best-Popescu and G. Popescu, " Real time blood testing using quantitative phase imaging.," *PloS One,* vol. 8, no. 2, p. e55676, 2013.

[30] M. Mugnano, P. Memmolo, L. Miccio, F. Merola, V. Bianco, A. Bramanti, A. Gambale, R. Russo, I. Andolfo, A. Iolascon and P. Ferraro, "Label-free optical marker for red-blood-cell phenotyping of inherited anemias.," *Anal. Chem.,* vol. 90, no. 12, pp. 7495-7501, 2018.

[31] K. L. Vom Werth, T. Wörmann, B. Kemper, P. Kümpers, S. Kampmeier and A. Mellmann, "Investigating Morphological Changes of T-lymphocytes after Exposure with Bacterial Determinants for Early Detection of Septic Conditions.," *Microorganisms,* vol. 2, p. 10, 2022.

[32] M. Mugnano, P. Memmolo, L. Miccio, S. Grilli, F. Merola, A. Calabuig, A. Bramanti, E. Mazzon and P. Ferraro, "In vitro cytotoxicity evaluation of cadmium by label-free holographic microscopy.," *J. Biophotonics,* vol. 11, no. 2, p. e201800099, 2018.

[33] K. M. Eder, A. Marzi, Á. Barroso, S. Ketelhut, B. Kemper and J. Schnekenburger, "Label-Free Digital Holographic Microscopy for In Vitro Cytotoxic Effect Quantification of Organic Nanoparticles.," *Cells,* vol. 11, no. 4, p. 644, 2022.

[34] B. Kemper, A. Bauwens, A. Vollmer, S. Ketelhut, P. Langehanenberg, J. Muthing, H. Larch and G. von Bally, "Label-free quantitative cell division monitoring of endothelial cells by digital holographic microscopy.," *J. Biomed. Opt. ,* vol. 15, no. 3, p. 036009 , 2010.

[35] F. Dubois, C. Yourassowsky, O. Monnom, J. C. Legros, O. Debeir IV, P. Van Ham and C. Decaestecker, "Digital holographic microscopy for the three-dimensional dynamic analysis of in vitro cancer cell migration.," *J. Biomed. Opt.,* vol. 11, no. 5, p. 054032, 2006.

[36] N. Pavillon, J. Kühn, C. Moratal, P. Jourdain, C. Depeursinge, P. J. Magistretti and P. Marquet, "Early cell death detection with digital holographic microscopy.," *PloS One,* vol. 7, no. 1, p. e30912, 2012.

[37] B. Rappaz, E. Cano, T. Colomb, J. Kuhn, C. D. Depeursinge, V. Simanis, P. J. Magistretti and P. P. Marquet, "Noninvasive characterization of the fission yeast cell cycle by monitoring dry mass with digital holographic microscopy.," *J. Biomed. Opt.,* vol. 14, no. 3, p. 034049 , 2009.

[38] M. Haifler, P. Girshovitz, G. Band, G. Dardikman, I. Madjar and N. T. Shaked, "Interferometric phase microscopy for label-free morphological evaluation of sperm cells.," *Fertil. Steril.,* vol. 104, no. 1, pp. 43-47, 2015.

[39] B. Kemper, A. Barroso, M. Woerdemann, L. Dewenter, A. Vollmer, R. Schubert, A. Mellmann, G. von Bally and C. Denz, "Towards 3D modelling and imaging of infection scenarios at the single cell level using holographic optical tweezers and digital holographic microscopy.," *J. Biophotonics,* vol. 6, no. 3, pp. 260-266, 2013.

[40] G. Zheng, R. Horstmeyer and C. Yang, "Wide-field, high-resolution Fourier ptychographic microscopy.," *Nat. Photonics,* vol. 7, no. 9, pp. 739-745, 2013.

[41] L. Tian, Z. Liu, L. H. Yeh, M. Chen, J. Zhong and L. Waller, "Computational illumination for high-speed in vitro Fourier ptychographic microscopy.," *Optica,* vol. 2, no. 10, pp. 904-911, 2015.

[42] Z. F. Phillips, M. V. D'Ambrosio, L. Tian, J. J. Rulison, H. S. Patel, N. Sadras, A. V. Gande, N. A. Switz, D. A. Fletcher and L. Waller, "Multi-contrast imaging and digital refocusing on a mobile microscope with a domed LED array.," *PloS One,* vol. 10, no. 5, p. e0124938, 2015.

[43] V. Bianco, B. Mandracchia, J. Běhal, D. Barone, P. Memmolo and P. Ferraro, "Miscalibration-tolerant Fourier ptychography.," *IEEE J. Sel. Topics Quantum Electron.,* vol. 27, no. 4, pp. 1-17, 2020.

[44] V. Bianco, M. D. Priscoli, D. Pirone, G. Zanfardino, P. Memmolo, F. Bardozzo, L. Miccio, G. Ciaparrone, P. Ferraro and R. Tagliaferri, "Deep learning-based, misalignment resilient, real-time Fourier Ptychographic Microscopy

reconstruction of biological tissue slides.," *IEEE J. Sel. Topics Quantum Electron.,* vol. 28, no. 4, pp. 1-10, 2022.

[45] D. Pirone, V. Bianco, M. Valentino, M. Mugnano, V. Pagliarulo, P. Memmolo, L. Miccio and P. Ferraro, "Fourier ptychographic microscope allows multi-scale monitoring of cells layout onto micropatterned substrates.," *Opt. Lasers Eng.,* vol. 156, p. 107103, 2022.

[46] V. Bianco, L. Miccio, D. Pirone, E. Cavalletti, J. Behal, P. Memmolo, A. Sardo and P. Ferraro, "Multi-scale fractal Fourier Ptychographic Microscopy for assessing the dose-dependent impact of copper pollution on living diatoms.," *Under Review.*

[47] D. Jin, R. Zhou, Z. Yaqoob and P. T. So, "Tomographic phase microscopy: principles and applications in bioimaging.," *JOSA B,* vol. 34, no. 5, pp. B64-B77, 2017.

[48] V. Balasubramani, A. Kuś, H. Y. Tu, C. J. Cheng, M. Baczewska, W. Krauze and M. Kujawińska, "Holographic tomography: techniques and biomedical applications.," *App. Opt.,* vol. 60, no. 10, pp. B65-B80, 2021.

[49] W. Choi, C. Fang-Yen, K. Badizadegan, S. Oh, N. Lue, R. R. Dasari and M. S. Feld, "Tomographic phase microscopy.," *Nat. Methods,* vol. 4, no. 9, pp. 717-719, 2007.

[50] K. Kim, K. S. Kim, H. Park, J. C. Ye and Y. Park, "Real-time visualization of 3-D dynamic microscopic objects using optical diffraction tomography.," *Opt. Express,* vol. 21, no. 26, pp. 32269-32278, 2013.

[51] A. Kuś, M. Dudek, B. Kemper, M. Kujawińska and A. Vollmer, "Tomographic phase microscopy of living three-dimensional cell cultures.," *J. Biomed. Opt.,* vol. 19, no. 4, p. 046009, 2014.

[52] M. Habaza, B. Gilboa, Y. Roichman and N. T. Shaked, "Tomographic phase microscopy with 180 rotation of live cells in suspension by holographic optical tweezers.," *Opt. Lett.,* vol. 40, no. 8, pp. 1881-1884, 2015.

[53] J. Kostencka, T. Kozacki, A. Kuś, B. Kemper and M. Kujawińska, "Holographic tomography with scanning of illumination: space-domain reconstruction for

spatially invariant accuracy.," *Biomed. Opt. Express,* vol. 7, no. 10, pp. 4086-4101, 2016.

[54] A. Kuś, W. Krauze and M. Kujawińska, "Active limited-angle tomographic phase microscope.," *J. Biomed. Opt.,* vol. 20, no. 11, p. 111216, 2015.

[55] D. Jin, R. Zhou, Z. Yaqoob and P. T. So, "Dynamic spatial filtering using a digital micromirror device for high-speed optical diffraction tomography.," *Opt. Express,* vol. 26, no. 1, pp. 428-437, 2018.

[56] P. Hosseini, Y. Sung, Y. Choi, N. Lue, Z. Yaqoob and P. So, "Scanning color optical tomography (SCOT).," *Opt. Express,* vol. 23, no. 15, pp. 19752-19762, 2015.

[57] J. Kostencka, T. Kozacki, A. Kuś and M. Kujawińska, "Accurate approach to capillary-supported optical diffraction tomography.," *Opt. Express,* vol. 23, no. 6, pp. 7908-7923, 2015.

[58] M. Kujawińska, W. Krauze, A. Kus, J. Kostencka, T. Kozacki, B. Kemper and M. Dudek, "Problems and solutions in 3-D analysis of phase biological objects by optical diffraction tomography.," *Int. J. Optomechatron.,* vol. 8, no. 4, pp. 357-372, 2014.

[59] Y. C. Lin, H. C. Chen, H. Y. Tu, C. Y. Liu and C. J. Cheng, "Optically driven full-angle sample rotation for tomographic imaging in digital holographic microscopy.," *Opt. Lett.,* vol. 42, no. 7, pp. 1321-1324, 2017.

[60] K. Kim, J. Yoon, S. Shin, S. Lee, S. A. Yang and Y. Park, "Optical diffraction tomography techniques for the study of cell pathophysiology.," *J. Biomed. Photon. Eng.,* vol. 2, no. 2, pp. 020201-1, 2016.

[61] J. Lim, K. Lee, K. H. Jin, S. Shin, S. Lee, Y. Park and J. C. Ye, "Comparative study of iterative reconstruction algorithms for missing cone problems in optical diffraction tomography.," *Opt. Express,* vol. 23, no. 13, pp. 16933-16948, 2015.

[62] E. Wolf, "Three-dimensional structure determination of semi-transparent objects from holographic data.," *Opt. Commun.,* vol. 1, no. 4, pp. 153-156, 1969.

[63] J. Kostencka, T. Kozacki and M. Józwik, "Holographic tomography with object rotation and two-directional off-axis illumination.," *Opt. Express,* vol. 25, no. 20, pp. 23920-23934, 2017.

[64] A. C. Kak and M. Slaney, Principles of computerized tomographic imaging., Philadelphia: Society for Industrial and Applied Mathematics, 2001.

[65] Y. Sung, W. Choi, C. Fang-Yen, K. Badizadegan, R. R. Dasari and M. S. Feld, "Optical diffraction tomography for high resolution live cell imaging.," *Opt. Express,* vol. 17, no. 1, pp. 266-277, 2009.

[66] Y. Sung, W. Choi, N. Lue, R. R. Dasari and Z. Yaqoob, "Stain-free quantification of chromosomes in live cells using regularized tomographic phase microscopy.," *Plos One,* vol. 7, no. 11, p. e49502, 2012.

[67] W. Krauze, P. Makowski, M. Kujawińska and A. Kuś, "Generalized total variation iterative constraint strategy in limited angle optical diffraction tomography.," *Opt. Express,* vol. 24, no. 5, pp. 4924-4936, 2016.

[68] U. S. Kamilov, I. N. Papadopoulos, M. H. Shoreh, A. Goy, C. Vonesch, M. Unser and D. Psaltis, "Optical tomographic image reconstruction based on beam propagation and sparse regularization.," *IEEE Trans. Comput. Imaging,* vol. 2, no. 1, pp. 59-70, 2016.

[69] M. Mir, S. D. Babacan, M. Bednarz, M. N. Do, I. Golding and G. Popescu, "Visualizing Escherichia coli sub-cellular structure using sparse deconvolution spatial light interference tomography.," *PLoS One,* vol. 7, no. 6, p. e39816, 2012.

[70] U. S. Kamilov, I. N. Papadopoulos, M. H. Shoreh, A. Goy, C. Vonesch, M. Unser and D. Psaltis, "Learning approach to optical tomography.," *Optica,* vol. 2, no. 6, pp. 517-522, 2015.

[71] L. Waller and L. Tian, "Machine learning for 3D microscopy.," *Nature,* vol. 523, no. 7561, pp. 416-417, 2015.

[72] A. J. Devaney, "Inverse-scattering theory within the Rytov approximation.," *Opt. Lett.,* vol. 6, no. 8, pp. 374-376, 1981.

[73] J. Lim, A. B. Ayoub, E. E. Antoine and D. Psaltis, "High-fidelity optical diffraction tomography of multiple scattering samples.," *Light Sci. Appl.,* vol. 8, no. 1, pp. 1-12, 2019.

[74] O. Haeberlé, K. Belkebir, H. Giovaninni and A. Sentenac, "Tomographic diffractive microscopy: basics, techniques and perspectives.," *J. Mod. Opt.,* vol. 57, no. 9, pp. 686-699, 2010.

[75] A. Breglia, A. Capozzoli, C. Curcio and A. Liseno, "NUFFT-based interpolation in backprojection algorithms.," *IEEE Geosci. Remote Sens. Lett.,* vol. 18, no. 12, pp. 2117-2121, 2020.

[76] Y. Sung and R. R. Dasari, "Deterministic regularization of three-dimensional optical diffraction tomography.," *J. Opt. Soc. Am. A,* vol. 28, no. 8, pp. 1554-1561, 2011.

[77] A. Beck and M. Teboulle, "Fast gradient-based algorithms for constrained total variation image denoising and deblurring problems.," *IEEE Trans. Image Process.,* vol. 18, no. 11, pp. 2419-2434, 2009.

[78] P. Charbonnier, L. Blanc-Féraud, G. Aubert and M. Barlaud, "Deterministic edge-preserving regularization in computed imaging.," *IEEE Trans. Image Process.,* vol. 6, no. 2, pp. 298-311, 1997.

[79] X. Jin, L. Li, Z. Chen, L. Zhang and Y. Xing, "Anisotropic total variation for limited-angle CT reconstruction.," in *IEEE Nuclear Science Symposuim & Medical Imaging Conference*, Knoxville, TN, USA, 2010.

[80] G. González, V. Kolehmainen and A. Seppänen, "Isotropic and anisotropic total variation regularization in electrical impedance tomography.," *Comput. Math. Appl.,* vol. 74, no. 3, pp. 564-576, 2017.

[81] M. T. McCann, K. H. Jin and M. Unser, "Convolutional neural networks for inverse problems in imaging: A review.," *IEEE Signal Process. Mag.,* vol. 34, no. 6, pp. 85-95, 2017.

[82] T. A. Pham, E. Soubies, A. Ayoub, D. Psaltis and M. Unser, "Adaptive regularization for three-dimensional optical diffraction tomography.," in *IEEE 17th International Symposium on Biomedical Imaging (ISBI)*, 2020.

[83] K. C. Zhou and R. Horstmeyer, "Diffraction tomography with a deep image prior.," *Opt. Express,* vol. 28, no. 9, pp. 12872-12896, 2020.

[84] D. Ryu, D. Ryu, Y. Baek, H. Cho, G. Kim, Y. S. Kim, Y. Lee, Y. Kim, J. C. Ye, H. S. Min and Y. Park, "DeepRegularizer: rapid resolution enhancement of tomographic imaging using deep learning.," *IEEE Trans. Med. Imaging,* vol. 40, no. 5, pp. 1508-1518, 2021.

[85] J. Lim, A. B. Ayoub and D. Psaltis, "Three-dimensional tomography of red blood cells using deep learning.," *Adv. Photonics,* vol. 2, no. 2, p. 026001, 2020.

[86] J. Lim, A. Goy, M. H. Shoreh, M. Unser and D. Psaltis, "Learning tomography assessed using Mie theory.," *Phys. Rev. Appl.,* vol. 9, no. 3, p. 034027, 2018.

[87] H. Park, T. Ahn, K. Kim, S. Lee, S. Y. Kook, D. Lee, I. B. Suh, S. Na and Y. Park, "Three-dimensional refractive index tomograms and deformability of individual human red blood cells from cord blood of newborn infants and maternal blood.," *J. Biomed. Opt.,* vol. 20, p. 111208, 2015.

[88] Y. Park, M. Diez-Silva, G. Popescu, G. Lykotrafitis, W. Choi, M. S. Feld and S. Suresh, "Refractive index maps and membrane dynamics of human red blood cells parasitized by Plasmodium falciparum.," *Proc. Natl. Acad. Sci. USA,* vol. 105, pp. 13730-13735, 2008.

[89] H. Park, S. H. Hong, K. Kim, S. H. Cho, W. J. Lee, Y. Kim, S. E. Lee and Y. Park, "Characterizations of individual mouse red blood cells parasitized by Babesia microti using 3-D holographic microscopy.," *Sci. Rep.,* vol. 5, no. 1, pp. 1-11, 2015.

[90] Y. Kim, H. Shim, K. Kim, H. Park, S. Jang and Y. Park, "Profiling individual human red blood cells using common-path diffraction optical tomography.," *Sci. Rep.,* vol. 4, no. 1, pp. 1-7, 2014.

[91] J. Yoon, K. Kim, H. Park, C. Choi, S. Jang and Y. Park, "Label-free characterization of white blood cells by measuring 3D refractive index maps.," *Biomed. Opt. Express,* vol. 6, no. 10, pp. 3865-3875, 2015.

[92] S. A. Yang, J. Yoon, K. Kim and Y. Park, "Measurements of morphological and biophysical alterations in individual neuron cells associated with early neurotoxic effects in Parkinson's disease.," *Cytometry A,* vol. 91, no. 5, pp. 510-518, 2017.

[93] T. A. Stanly, R. Suman, G. F. Rani, P. J. O'Toole, P. M. Kaye and I. S. Hitchcock, "Quantitative optical diffraction tomography imaging of mouse platelets.," *Front. Physiol.,* vol. 11, p. 568087, 2020.

[94] Y. S. Kim, S. Lee, J. Jung, S. Shin, H. G. Choi, G. H. Cha, W. Park, S. Lee and Y. Park, "Focus: medical technology: combining three-dimensional quantitative phase imaging and fluorescence microscopy for the study of cell pathophysiology.," *Yale J. Biol. Med.,* vol. 91, pp. 267-277, 2018.

[95] T. K. Kim, B. W. Lee, F. Fujii, K. H. Lee, S. Lee, Y. Park, J. K. Kim, S. W. Lee and C. G. Pack, "Mitotic chromosomes in live cells characterized using high-speed and label-free optical diffraction tomography.," *Cells,* vol. 8, no. 11, p. 1368, 2019.

[96] A. Szewczyk, J. Saczko and J. Kulbacka, "Apoptosis as the main type of cell death induced by calcium electroporation in rhabdomyosarcoma cells.," *Bioelectrochemistry,* vol. 136, p. 107592, 2020.

[97] P. Jorgensen and M. Tyers, "How cells coordinate growth and division.," *Curr. Biol.,* vol. 14, no. 23, pp. R1014-R1027, 2004.

[98] Y. Cotte, F. Toy, P. Jourdain, N. Pavillon, D. Boss, P. Magistretti, P. Marquet and C. Depeursinge, "Marker-free phase nanoscopy.," *Nat. Photonics,* vol. 7, no. 2, pp. 113-117, 2013.

[99] Y. Sung, A. Tzur, S. Oh, W. Choi, V. Li, R. R. Dasari, Z. Yaqoob and M. W. Kirschner, "Size homeostasis in adherent cells studied by synthetic phase microscopy.," *Proc. Natl. Acad. Sci. USA,* vol. 110, no. 41, pp. 16687-16692, 2013.

[100] K. L. Cooper, S. Oh, Y. Sung, R. R. Dasari, M. W. Kirschner and C. J. Tabin, "Multiple phases of chondrocyte enlargement underlie differences in skeletal proportions.," *Nature,* vol. 495, no. 7441, pp. 375-378, 2013.

[101] B. Simon, M. Debailleul, A. Beghin, Y. Tourneur and O. Haeberlé, "High-resolution tomographic diffractive microscopy of biological samples.," *J. Biophotonics,* vol. 3, no. 7, pp. 462-467, 2010.

[102] W. C. Hsu, J. W. Su, C. C. Chang and K. B. Sung, "Investigating the backscattering characteristics of individual normal and cancerous cells based on experimentally determined three-dimensional refractive index distributions.," *Proc. SPIE,* vol. 8553, p. 85531O, 2012.

[103] H. Ghaffari, M. S. Saidi and B. Firoozabadi, "Biomechanical analysis of actin cytoskeleton function based on a spring network cell model.," *Proc. Inst. Mech. Eng. C J. Mech. Eng. Sci.,* vol. 231, no. 7, pp. 1308-1323, 2017.

[104] X. Cheng, I. Lang, O. S. Adeniji and L. Griffing, "Plasmolysis-deplasmolysis causes changes in endoplasmic reticulum form, movement, flow, and cytoskeletal association.," *J. Exp. Bot.,* vol. 68, no. 15, pp. 4075-4087, 2017.

[105] A. Adan, G. Alizada, Y. Kiraz, Y. Baran and A. Nalbant, "Flow cytometry: basic principles and applications.," *Crit. Rev. Biotechnol.,* vol. 37, no. 2, pp. 163-176, 2017.

[106] Y. Sung, N. Lue, B. Hamza, J. Martel, D. Irimia, R. R. Dasari, W. Choi, Z. Yaqoob and P. So, "Three-dimensional holographic refractive-index measurement of continuously flowing cells in a microfluidic channel.," *Phys. Rev. Appl.,* vol. 1, no. 1, p. 014002, 2014.

[107] F. Merola, P. Memmolo, L. Miccio, R. Savoia, M. Mugnano, A. Fontana, G. D'Ippolito, A. Sardo, A. Iolascon, A. Gambale and P. Ferraro, "Tomographic flow cytometry by digital holography.," *Light Sci. Appl.,* vol. 6, no. 4, pp. e16241-e16241, 2017.

[108] D. Pirone, P. Memmolo, F. Merola, L. Miccio, M. Mugnano, A. Capozzoli, C. Curcio, A. Liseno and P. Ferraro, "Rolling angle recovery of flowing cells in

holographic tomography exploiting the phase similarity.," *Appl. Opt.,* vol. 60, no. 4, pp. A277-A284, 2021.

[109] D. Pirone, M. M. Villone, P. Memmolo, Z. Wang, V. Tkachenko, W. Xiao, L. Che, L. Xin, X. Li, F. Pan, P. Ferraro and P. L. Maffettone, "On the hydrodynamic mutual interactions among cells for high-throughput microfluidic holographic cyto-tomography," *Opt. Lasers Eng.,* vol. 158 , p. 107190, 2022.

[110] M. J. Wilkerson, "Principles and applications of flow cytometry and cell sorting in companion animal medicine.," *Vet. Clin. North Am. Small Anim. Pract.,* vol. 42, no. 1, pp. 53-71, 2012.

[111] M. G. Macey, "Principles of Flow Cytometry," in *Flow cytometry: principles and applications*, Totowa (NJ), Humana Press, 2010, pp. 1-15.

[112] F. Reggeti and D. Bienzle, "Flow cytometry in veterinary oncology.," *Vet. Pathol.,* vol. 48, no. 1, pp. 223-235, 2011.

[113] D. Betters, "Use of flow cytometry in clinical practice.," *J. Adv. Pract. Oncol. ,* vol. 6, p. 435–440, 2015.

[114] N. S. Barteneva, E. Fasler-Kan and I. A. Vorobjev, "Imaging flow cytometry: coping with heterogeneity in biological systems.," *J. Histochem. Cytochem.,* vol. 60, no. 10, pp. 723-733, 2012.

[115] Y. Han, Y. Gu, A. C. Zhang and Y. H. Lo, "Imaging technologies for flow cytometry.," *Lab Chip,* vol. 16, no. 24, pp. 4639-4647, 2016.

[116] D. A. Basiji, W. E. Ortyn, L. Liang, V. Venkatachalam and P. Morrissey, "Cellular image analysis and imaging by flow cytometry.," *Clin. Lab. Med.,* vol. 27, no. 3, pp. 653-670, 2007.

[117] S. H. Cho, C. H. Chen, F. S. Tsai, J. M. Godin and Y. H. Lo, "Human mammalian cell sorting using a highly integrated micro-fabricated fluorescence-activated cell sorter (μFACS).," *Lab Chip,* vol. 10, no. 12, pp. 1567-1573, 2010.

[118] EMDMillipore, "https://pedsresearch.org/_files/INSPIRE_User_Manual_MkII_082912.pdf," *INSPIRE®,* 2012.

[119] Y. Zheng, J. Nguyen, Y. Wei and Y. Sun, "Recent advances in microfluidic techniques for single-cell biophysical characterization.," *Lab Chip,* vol. 13, no. 3, pp. 2464-2483, 2013.

[120] B. Danis, T. C. George, S. Goriely, B. Dutta, J. Renneson, L. Gatto, P. Fitzgerald-Bocarsly, A. Marchant, M. Goldman, F. Willems and D. De Wit, "Interferon regulatory factor 7-mediated responses are defective in cord blood plasmacytoid dendritic cells.," *Eur. J. Immunol.,* vol. 38, no. 2, pp. 507-517, 2008.

[121] S. Henery, T. George, B. Hall, D. Basiji, W. Ortyn and P. Morrissey, "Quantitative image based apoptotic index measurement using multispectral imaging flow cytometry: a comparison with standard photometric methods.," *Apoptosis,* vol. 13, no. 8, pp. 1054-1063, 2008.

[122] A. Ploppa, T. C. George, K. E. Unertl, B. Nohe and M. E. Durieux, "ImageStream cytometry extends the analysis of phagocytosis and oxidative burst.," *Scand. J. Clin. Lab. Invest.,* vol. 71, no. 5, pp. 362-369, 2011.

[123] A. Filby, E. Perucha, H. Summers, P. Rees, P. Chana, S. Heck, G. M. Lord and D. Davies, "An imaging flow cytometric method for measuring cell division history and molecular symmetry during mitosis.," *Cytometry A,* vol. 79, no. 7, pp. 496-506, 2011.

[124] H. Vallhov, C. Gutzeit, S. M. Johansson, N. Nagy, M. Paul, Q. Li, S. Friend, T. C. George, E. Klein, A. Scheynius and S. Gabrielsson, "Exosomes containing glycoprotein 350 released by EBV-transformed B cells selectively target B cells through CD21 and block EBV infection in vitro.," *J. Immunol.,* vol. 186, pp. 73-82, 2011.

[125] S. Domhan, L. Ma, A. Tai, Z. Anaya, A. Beheshti, M. Zeier, L. Hlatky and A. Abdollahi, "Intercellular communication by exchange of cytoplasmic material via tunneling nano-tube like structures in primary human renal epithelial cells.," *Plos One,* vol. 6, no. 6, p. e21283, 2011.

[126] C. Ouk, C. Jayat-Vignoles, M. Donnard and J. Feuillard, "Both CD62 and CD162 antibodies prevent formation of CD36-dependent platelets, rosettes, and artefactual pseudoexpression of platelet markers on white blood cells: A study with ImageStream®.," *Cytometry A,* vol. 79, p. 477–484, 2011.

[127] E. K. Zuba-Surma, M. Kucia, L. Rui, D. M. Shin, W. Wojakowski, J. Ratajczak and M. Z. Ratajczak, "Fetal liver very small embryonic/epiblast like stem cells follow developmental migratory pathway of hematopoietic stem cells.," *Ann. NY Acad. Sci.,* vol. 1176, p. 205–218, 2009.

[128] H. Mikami, C. Lei, N. Nitta, T. Sugimura, T. Ito, Y. Ozeki and K. Goda, "High-speed imaging meets single-cell analysis.," *Chem,* vol. 4, no. 10, pp. 2278-2300, 2018.

[129] O. Maguire, C. Collins, K. O'Loughlin, J. Miecznikowski and H. Minderman, "Quantifying nuclear p65 as a parameter for NF-κB activation: Correlation between ImageStream cytometry, microscopy, and Western blot.," *Cytometry A,* vol. 79, no. 6, pp. 461-469, 2011.

[130] T. C. George, D. A. Basiji, B. E. Hall, D. H. Lynch, W. E. Ortyn, D. J. Perry, M. J. Seo, C. A. Zimmerman and P. J. Morrissey, "Distinguishing modes of cell death using the ImageStream® multispectral imaging flow cytometer.," *Cytometry A,* vol. 59, pp. 237-245, 2004.

[131] B. T. Bosworth and M. A. Foster, "High-speed ultrawideband photonically enabled compressed sensing of sparse radio frequency signals.," *Opt. Lett.,* vol. 38, no. 22, pp. 4892-4895, 2013.

[132] R. Wollman and N. Stuurman, "High throughput microscopy: from raw images to discoveries.," *J. Cell Sci.,* vol. 120, no. 21, pp. 3715-3722, 2007.

[133] N. Nitta, T. Sugimura, A. Isozaki, H. Mikami, K. Hiraki, S. Sakuma, T. Iino, F. Arai, T. Endo, Y. Fujiwaki, H. Fukuzawa, M. Hase, T. Hayakawa, K. Hiramatsu, Y. Hoshino, M. Inaba, T. Ito, H. Karakawa, Y. Kasai, K. Koizumi and al., "Intelligent image-activated cell sorting.," *Cell,* vol. 175, no. 1, pp. 266-276, 2018.

[134] A. Isozaki, H. Mikami, K. Hiramatsu, S. Sakuma, Y. Kasai, T. Iino, T. Yamano, A. Yasumoto, Y. Oguchi, N. Suzuki, Y. Shirasaki, T. Endo, T. Ito, K. Hiraki, M.

Yamada, S. Matsusaka, T. Hayakawa, H. Fukuzawa, Y. Yatomi, F. Arai and al., "A practical guide to intelligent image-activated cell sorting.," *Nat. Protoc.,* vol. 14, no. 8, pp. 2370-2415, 2018.

[135] A. A. Nawaz, M. Urbanska, M. Herbig, M. Nötzel, M. Kräter, P. Rosendahl, C. Herold, N. Toepfner, N. Kubankova, R. Goswami, S. Abuhattum, F. Reichel, P. Muller, A. Taubenberger, S. Girardo, A. Jacobi and J. Guck, "Intelligent image-based deformation-assisted cell sorting with molecular specificity.," *Nat. Methods,* vol. 17, no. 6, pp. 595-599, 2020.

[136] M. Doan, I. Vorobjev, P. Rees, A. Filby, O. Wolkenhauer, A. E. Goldfeld, J. Lieberman, N. Narteneva, A. E. Carpenter and H. Hennig, "Diagnostic potential of imaging flow cytometry.," *Trends Biotechnol.,* vol. 36, no. 7, pp. 649-652, 2018.

[137] L. F. Grimwade, K. A. Fuller and W. N. Erber, "Applications of imaging flow cytometry in the diagnostic assessment of acute leukaemia.," *Methods,* vol. 112, pp. 39-45, 2017.

[138] A. Y. Chen, C. Yu, B. Gatto and L. F. LIu, "DNA minor groove-binding ligands: a different class of mammalian DNA topoisomerase inhibitors.," *Proc. Natl Acad. Sci. USA,* vol. 90, no. 17, pp. 8131-8135, 1993.

[139] K. Wojcik and J. W. Dobrucki, "Cytometry A," *Interaction of a DNA intercalator DRAQ5, and a minor groove binder SYTO17, with chromatin in live cells—influence on chromatin organization and histone—DNA interactions. ,* vol. 73, pp. 555-562, 2008.

[140] H. G. Miltenburger, G. Sachse and M. Schliermann, "S-phase cell detection with a monoclonal antibody.," *Dev. Biol. Stand,* vol. 66, pp. 91-99, 1987.

[141] K. C. Lee, M. Wang, K. S. Cheah, G. C. Chan, H. K. So, K. K. Wong and K. K. Tsia, "Quantitative phase imaging flow cytometry for ultra-large-scale single-cell biophysical phenotyping.," *Cytometry A,* vol. 95, no. 5, pp. 510-520, 2019.

[142] T. Blasi, H. Hennig, H. D. Summers, F. J. Theis, J. Cerveira, J. O. Patterson, D. Davies, A. Filby, A. E. Carpenter and P. Rees, "Nat. Commun.," *Label-free cell*

cycle analysis for high-throughput imaging flow cytometry., vol. 7, no. 1, pp. 1-9, 2016.

[143] J. Min, B. Yao, V. Trendafilova, S. Ketelhut, L. Kastl, B. Greve and B. Kemper, "Quantitative phase imaging of cells in a flow cytometry arrangement utilizing Michelson interferometer-based off-axis digital holographic microscopy.," *J. Biophotonics,* vol. 12, no. 9, p. e201900085, 2019.

[144] T. A. Zangle and M. A. Teitell, "Live-cell mass profiling: an emerging approach in quantitative biophysics.," *Nat. Methods,* vol. 11, no. 12, pp. 1221-1228, 2014.

[145] E. K. Hoffmann, I. H. Lambert and S. F. Pedersen, "Physiology of cell volume regulation in vertebrates.," *Physiol. Rev.,* vol. 89, no. 1, pp. 193-277, 2009.

[146] P. Girshovitz and N. T. Shaked, "Generalized cell morphological parameters based on interferometric phase microscopy and their application to cell life cycle characterization.," *Biomed. Opt. Express,* vol. 3, no. 8, pp. 1757-1773, 2012.

[147] O. Otto, P. Rosendahl, A. Mietke, S. Golfier, C. Herold, D. Klaue, S. Girardo, S. Pagliara, A. Ekpenyong, A. Jacobi, M. Wobus, N. Töpfner, U. F. Keyser, J. Mansfeld, E. Fischer-Friedrich and J. Guck, "Real-time deformability cytometry: on-the-fly cell mechanical phenotyping.," *Nat. Methods,* vol. 12, no. 3, pp. 199-202, 2015.

[148] M. Masaeli, D. Gupta, S. O'Byrne, H. T. Tse, D. R. Gossett, P. Tseng, A. S. Utada, H. J. Jung, S. Young, A. T. Clark and D. Di Carlo, "Multiparameter mechanical and morphometric screening of cells.," *Sci. Rep.,* vol. 6, no. 1, pp. 1-11, 2016.

[149] M. Xavier, P. Rosendahl, M. Herbig, M. Kräter, D. Spencer, M. Bornhäuser, R. O. C. Oreffo, H. Morgan, J. Guck and O. Otto, "Mechanical phenotyping of primary human skeletal stem cells in heterogeneous populations by real-time deformability cytometry.," *Integr. Biol.,* vol. 8, no. 5, pp. 616-623, 2016.

[150] H. T. Tse, D. R. Gossett, Y. S. Moon, M. Masaeli, M. Sohsman, Y. Ying, K. Mislick, R. P. Adams, J. Rao and D. Di Carlo, "Quantitative diagnosis of malignant

pleural effusions by single-cell mechanophenotyping.," *Sci. Transl. Med.,* vol. 5, no. 212, pp. 212ra163-212ra163, 2013.

[151] D. Damania, H. Subramanian, V. Backman, E. C. Anderson, M. H. Wong, O. J. McCarty and K. G. Phillips, "Network signatures of nuclear and cytoplasmic density alterations in a model of pre and postmetastatic colorectal cancer.," *J. Biomed. Opt.,* vol. 19, p. 016016, 2014.

[152] S. Byun, V. C. Hecht and S. R. Manalis, "Characterizing cellular biophysical responses to stress by relating density, deformability, and size.," *Biophys. J.,* vol. 109, no. 8, pp. 1565-1573, 2015.

[153] J. M. Park, J. Y. Lee, J. G. Lee, H. Jeong, J. M. Oh, Y. J. Kim, H. J. Lee, J. H. Oh, S. S. Lee, W. J. Lee and N. Huh, "Highly efficient assay of circulating tumor cells by selective sedimentation with a density gradient medium and microfiltration from whole blood.," *Anal. Chem.,* vol. 84, no. 17, pp. 7400-4707, 2012.

[154] N. A. Turko and N. T. Shaked, "Erythrocyte volumetric measurements in imaging flow cytometry using simultaneous three-wavelength digital holographic microscopy.," *Biomed. Opt. Express,* vol. 11, no. 11, pp. 6649-6658, 2020.

[155] D. Roitshtain, L. Wolbromsky, E. Bal, H. Greenspan, L. L. Satterwhite and N. T. Shaked, "Quantitative phase microscopy spatial signatures of cancer cells.," *Cytometry A,* vol. 91, no. 5, pp. 482-493, 2017.

[156] D. Dannhauser, D. Rossi, P. Memmolo, A. Finizio, P. Ferraro, P. A. Netti and F. Causa, "Biophysical investigation of living monocytes in flow by collaborative coherent imaging techniques.," *Biomed. Opt. Express,* vol. 9, no. 11, pp. 5194-5204, 2018.

[157] S. S. Gorthi and E. Schonbrun, "Phase imaging flow cytometry using a focus-stack collecting microscope.," *Opt. Lett.,* vol. 37, no. 4, pp. 707-709, 2012.

[158] K. C. Lee, A. K. Lau, A. H. Tang, M. Wang, A. T. Mok, B. M. Chung, W. Yan, H. C. Shum, K. S. E. Cheah, G. C. F. Chan, H. K. H. So, K. K. Y. Wong and K. K. Tsia, "Multi-ATOM: ultrahigh-throughput single-cell quantitative phase imaging

with subcellular resolution.," *J. Biophotonics,* vol. 12, no. 7, p. e201800479, 2019.

[159] F. Merola, P. Memmolo, L. Miccio, V. Bianco, M. Paturzo and P. Ferraro, "Diagnostic tools for lab-on-chip applications based on coherent imaging microscopy.," *Proc. IEEE,* vol. 103, no. 2, pp. 192-204, 2015.

[160] M. I. Lapsley, L. Wang and T. J. Huang, "On-chip flow cytometry: where is it now and where is it going?," *Biomark. Med.,* vol. 71, no. 1, pp. 75-78, 2013.

[161] H. Zhu, S. O. Isikman, O. Mudanyali, A. Greenbaum and A. Ozcan, "Optical imaging techniques for point-of-care diagnostics.," *Lab Chip,* vol. 13, no. 1, pp. 51-67, 2013.

[162] S. O. Isikman, W. Bishara, O. Mudanyali, I. Sencan, T. W. Su, D. K. Tseng, ,. O. Yaglidere, U. Sikora and A. Ozcan, "Lensfree on-chip microscopy and tomography for biomedical applications.," *IEEE J. Sel. Top. Quantum Electron.,* vol. 18, no. 3, pp. 1059-1072, 2011.

[163] Z. Göröcs, M. Tamamitsu, V. Bianco, P. Wolf, S. Roy, K. Shindo, K. Yanny, Y. Wu, H. C. Koydemir, Y. Rivenson and A. Ozcan, "A deep learning-enabled portable imaging flow cytometer for cost-effective, high-throughput, and label-free analysis of natural water samples.," *Light Sci. Appl.,* vol. 7, no. 1, pp. 1-12, 2018.

[164] Y. Fang, N. Yu, Y. Jiang and C. Dang, "High-precision lens-less flow cytometer on a chip.," *Micromachines,* vol. 9, no. 5, p. 227, 2018.

[165] NanoLive, [Online]. Available: http://nanolive.ch.

[166] TomoCube, [Online]. Available: http://www.tomocube.com.

[167] J. Li, A. C. Matlock, Y. Li, Q. Chen, C. Zuo and L. Tian, "High-speed in vitro intensity diffraction tomography.," *Adv. Photonics,* vol. 1, no. 6, p. 066004, 2019.

[168] A. B. Ayoub, A. Roy and D. Psaltis, "Optical Diffraction Tomography Using Nearly In-Line Holography with a Broadband LED Source.," *Appl. Sci.,* vol. 12, no. 3, p. 951, 2022.

[169] N. T. Nguyen, S. T. Wereley and S. A. M. Shaegh, Fundamentals and applications of microfluidics., Norwood, MA, USA: Artech house, 2019.

[170] S. Torino, M. Iodice, I. Rendina, G. Coppola and E. Schonbrun, "A microfluidic approach for inducing cell rotation by means of hydrodynamic forces.," *Sensors,* vol. 16, no. 8, p. 1326, 2016.

[171] C. Trujillo, R. Castañeda, P. Piedrahita-Quintero and J. Garcia-Sucerquia, "Automatic full compensation of quantitative phase imaging in off-axis digital holographic microscopy.," *Appl. Opt.,* vol. 55, no. 36, pp. 10299-10306, 2016.

[172] Q. Kemao, "Windowed Fourier transform for fringe pattern analysis.," *Appl. Opt.,* vol. 43, no. 13, pp. 2695-2702, 2004.

[173] D. Sirico, E. Cavalletti, L. Miccio, V. Bianco, D. Pirone, P. Memmolo, A. Sardo and P. Ferraro, "Holographic tracking and imaging of free-swimming Tetraselmis by off-axis holographic microscopy.," in *International Workshop on Metrology for the Sea (MetroSea) - IEEE*, Reggio Calabria, Italy, 2021.

[174] P. Memmolo, C. Distante, M. Paturzo, A. Finizio, P. Ferraro and B. Javidi, "Automatic focusing in digital holography and its application to stretched holograms.," *Opt. Lett.,* vol. 36, no. 10, pp. 1945-1947, 2011.

[175] M. M. Villone, P. Memmolo, F. Merola, M. Mugnano, L. Miccio, P. L. Maffettone and P. Ferraro, "Full-angle tomographic phase microscopy of flowing quasi-spherical cells.," *Lab Chip,* vol. 18, no. 1, pp. 126-131, 2018.

[176] Z. Wang, A. C. Bovik, H. R. Sheikh and E. P. Simoncelli, "Image quality assessment: from error visibility to structural similarity.," *IEEE Trans. Image Process.,* vol. 13, no. 4, pp. 600-612, 2004.

[177] Z. Wang and A. C. Bovik, "A universal image quality index.," *IEEE Signal Process. Lett.,* vol. 9, no. 3, pp. 81-84, 2002.

[178] W. Xue, L. Zhang, X. Mou and A. C. Bovik, "Gradient magnitude similarity deviation: A highly efficient perceptual image quality index.," *IEEE Trans. Image Process.,* vol. 23, no. 2, pp. 684-695, 2013.

[179] Y. Wen, Z. Chen, J. Lu, E. Ables, J. L. Scemama, L. V. Yang, J. Lu and X. H. Hu, "Quantitative analysis and comparison of 3D morphology between viable and apoptotic MCF-7 breast cancer cells and characterization of nuclear fragmentation.," *PLoS One,* vol. 12, no. 9, p. e0184726, 2017.

[180] K. Haseda, K. Kanematsu, K. Noguchi, H. Saito, N. Umeda and Y. Ohta, "Significant correlation between refractive index and activity of mitochondria: single mitochondrion study.," *Biomed. Opt. Express,* vol. 6, no. 3, pp. 859-869, 2015.

[181] A. Kleiber, D. Kraus, T. Henkel and W. Fritzsche, "Tomographic imaging flow cytometry.," *Lab Chip,* vol. 21, no. 19, pp. 3655-3666, 2021.

[182] T. Ohashi, Y. Ishii, Y. Ishikawa, T. Matsumoto and M. Sato, "Experimental and numerical analyses of local mechanical properties measured by atomic force microscopy for sheared endothelial cells.," *Biomed. Mater. Eng.,* vol. 12, no. 3, pp. 319-327, 2002.

[183] M. M. Villone, M. A. Hulsen, P. D. Anderson and P. L. Maffettone, "Simulations of deformable systems in fluids under shear flow using an arbitrary Lagrangian Eulerian technique.," *Comput. Fluids,* vol. 90, pp. 88-100, 2014.

[184] H. H. Hu, N. A. Patankar and M. Zhu, "Direct numerical simulations of fluid–solid systems using the arbitrary Lagrangian–Eulerian technique.," *J. Comput. Phys.,* vol. 169, no. 2, pp. 427-462, 2001.

[185] N. O. Jaensson, M. A. Hulsen and P. D. Anderson, "Stokes–Cahn–Hilliard formulations and simulations of two-phase flows with suspended rigid particles.," *Comput. Fluids,* vol. 111, pp. 1-17, 2015.

[186] M. M. Villone, "Lateral migration of deformable particles in microfluidic channel flow of Newtonian and viscoelastic media: a computational study.," *Microfluid. Nanofluid.,* vol. 23, no. 3, pp. 1-13, 2019.

[187] D. Di Carlo, "Inertial microfluidics.," *Lab Chip,* vol. 9, no. 21, pp. 3038-3046, 2009.

[188] A. Pratapa, M. Doron and J. C. Caicedo, "Image-based cell phenotyping with deep learning.," *Curr. Opin. Chem. Biol,* vol. 65, pp. 9-17, 2021.

[189] K. C. Lee, J. Guck, K. Goda and K. K. Tsia, "Toward deep biophysical cytometry: prospects and challenges.," *Trends Biotechnol.,* vol. 39, no. 12, pp. 1249-1262, 2021.

[190] S. Luo, Y. Shi, L. K. Chin, P. E. Hutchinson, Y. Zhang, G. Chierchia, H. Talbot, X. Jiang, T. Bourouina and A. Q. Liu, "Machine-Learning-Assisted Intelligent Imaging Flow Cytometry: A Review.," *Adv. Intell. Syst.,* vol. 3, no. 11, p. 2100073, 2021.

[191] M. Doan, C. Barnes, C. McQuin, J. C. Caicedo, A. Goodman, A. E. Carpenter and P. Rees, "Deepometry, a framework for applying supervised and weakly supervised deep learning to imaging cytometry.," *Nat. Protoc.,* vol. 16, no. 7, pp. 3572-3595, 2021.

[192] Y. Jo, H. Cho, S. Y. Lee, G. Choi, G. Kim, H. S. Min and Y. Park, "Quantitative phase imaging and artificial intelligence: a review.," *IEEE J. Sel. Top. Quantum Electron.,* vol. 25, no. 1, pp. 1-14, 2018.

[193] P. Memmolo, G. Aprea, V. Bianco, R. Russo, I. Andolfo, M. Mugnano, F. Merola, L. Miccio, A. Iolascon and P. Ferraro, "Differential diagnosis of hereditary anemias from a fraction of blood drop by digital holography and hierarchical machine learning.," *Biosens. Bioelectron.,* vol. 201, p. 113945, 2022.

[194] G. Kim, Y. Jo, H. Cho, H. S. Min and Y. Park, "Learning-based screening of hematologic disorders using quantitative phase imaging of individual red blood cells.," *Biosens. Bioelectron.,* vol. 123, pp. 69-76, 2019.

[195] Y. H. Lin, K. Y. K. Liao and K. B. Sung, "Automatic detection and characterization of quantitative phase images of thalassemic red blood cells using a mask region-based convolutional neural network.," *J. Biomed. Opt.,* vol. 25, no. 11, p. 116502, 2020.

[196] N. Goswami, Y. R. He, Y. H. Deng, C. Oh, N. Sobh, E. Valera, R. Bashir, N. Ismail, H. Kong, T. H. Nguyen, K. Best-Popescu and G. Popescu, "Label-free SARS-CoV-2 detection and classification using phase imaging with computational specificity.," *Light Sci. Appl. ,* vol. 10, no. 1, pp. 1-12, 2021.

[197] T. O'Connor, J. B. Shen, B. T. Liang and B. Javidi, "Digital holographic deep learning of red blood cells for field-portable, rapid COVID-19 screening.," *Opt. Lett.,* vol. 46, no. 10, pp. 2344-2347, 2021.

[198] Y. R. He, S. He, M. E. Kandel, Y. J. Lee, C. Hu, N. Sobh, M. A. Anastasio and G. Popescu, "Cell cycle stage classification using phase imaging with computational specificity.," *ACS Photonics,* vol. 9, no. 4, pp. 1264-1273, 2022.

[199] A. V. Belashov, A. A. Zhikhoreva, T. N. Belyaeva, A. V. Salova, E. S. Kornilova, I. V. Semenova and O. S. Vasyutinskii, "Machine Learning Assisted Classification of Cell Lines and Cell States on Quantitative Phase Images.," *Cells,* vol. 10, no. 10, p. 2587, 2021.

[200] Y. Li, B. Cornelis, A. Dusa, G. Vanmeerbeeck, D. Vercruysse, E. Sohn, K. Blaszkiewicza, D. Prodanova, P. Schelkensc and L. Lagae, "Accurate label-free 3-part leukocyte recognition with single cell lens-free imaging flow cytometry.," *Comput. Biol. Med.,* vol. 96, pp. 147-156, 2018.

[201] M. Ugele, M. Weniger, M. Stanzel, M. Bassler, S. W. Krause, O. Friedrich, O. Hayden and L. Richter, "Label-free high-throughput leukemia detection by holographic microscopy.," *Adv. Sci.,* vol. 5, no. 12, p. 1800761, 2018.

[202] M. Rubin, O. Stein, N. A. Turko, Y. Nygate, D. Roitshtain, L. Karako, I. Barnea, R. Giryes and N. T. Shaked, "TOP-GAN: Stain-free cancer cell classification using deep learning with a small training set.," *Med. Image Anal.,* vol. 57, pp. 176-185, 2019.

[203] C. X. Chen, H. S. Park, H. Price and A. Wax, "Automated Classification of Breast Cancer Cells Using High-Throughput Holographic Cytometry.," *Front. Phys.,* vol. 9, p. 759142, 2021.

[204] M. Ugele, M. Weniger, M. Leidenberger, Y. Huang, M. Bassler, O. Friedrich, B. Kappes, O. Hayden and L. Richter, "Label-free, high-throughput detection of P.

falciparum infection in sphered erythrocytes with digital holographic microscopy.," *Lab Chip,* vol. 18, no. 2, pp. 1704-1712, 2018.

[205] D. K. Singh, C. C. Ahrens, W. Li and S. A. Vanapalli, "Label-free, high-throughput holographic screening and enumeration of tumor cells in blood.," *Lab Chip,* vol. 17, no. 17, pp. 2920-2932, 2017.

[206] N. Nissim, M. Dudaie, I. Barnea and N. T. Shaked, "Real-Time Stain-Free Classification of Cancer Cells and Blood Cells Using Interferometric Phase Microscopy and Machine Learning.," *Cytometry A,* vol. 99, no. 5, pp. 511-523, 2021.

[207] L. Xin, W. Xiao, L. Che, J. Liu, L. Miccio, V. Bianco, P. Memmolo, P. Ferraro, X. Li and F. Pan, "Label-free assessment of the drug resistance of epithelial ovarian cancer cells in a microfluidic holographic flow cytometer boosted through machine learning.," *ACS Omega,* vol. 6, no. 46, pp. 31046-31057, 2021.

[208] J. Yoon, Y. Jo, M. H. Kim, K. Kim, S. Lee, S. J. Kang and Y. Park, "Identification of non-activated lymphocytes using three-dimensional refractive index tomography and machine learning.," *Sci. Rep.,* vol. 7, no. 1, pp. 1-10, 2017.

[209] D. Ryu, J. Kim, D. Lim, H. S. Min, I. Y. Yoo, D. Cho and Y. Park, "Label-free white blood cell classification using refractive index tomography and deep learning.," *BME Front.,* vol. 2021, p. 9893804, 2021.

[210] Y. Rivenson, Y. Wu and A. Ozcan, "Deep learning in holography and coherent imaging.," *Light Sci. Appl.,* vol. 8, no. 1, pp. 1-8, 2019.

[211] T. Zeng, Y. Zhu and E. Y. Lam, "Deep learning for digital holography: a review.," *Opt. Express,* vol. 29, no. 24, pp. 40572-40593, 2021.

[212] A. Isozaki, J. Harmon, Y. Zhou, S. Li, Y. Nakagawa, M. Hayashi, H. Mikami, C. Lei and K. Goda, "AI on a chip.," *Lab Chip,* vol. 20, no. 17, pp. 3074-3090, 2020.

[213] D. Pirone, D. Sirico, L. Miccio, V. Bianco, M. Mugnano, P. Ferraro and P. Memmolo, "Speeding up reconstruction of 3D tomograms in holographic flow cytometry via deep learning.," *Lab Chip,* vol. 22, no. 4, pp. 793-804, 2022.

[214] M. D. Priscoli, P. Memmolo, G. Ciaparrone, V. Bianco, F. Merola, L. Miccio, F. Bardozzo, D. Pirone, M. Mugnano, F. Cimmino, M. Capasso, A. Iolascon, P. Ferraro and R. Tagliaferri, "Neuroblastoma cells classification through learning approaches by direct analysis of digital holograms.," *IEEE J. Sel. Top. Quantum Electron.,* vol. 27, no. 5, pp. 1-9, 2021.

[215] D. Pirone, A. Montella, D. Sirico, M. Mugnano, D. Del Giudice, I. Kurelac, M. Tirelli, A. Iolascon, V. Bianco, P. Memmolo, M. Capasso, L. Miccio and P. Ferraro, "Phenotyping neuroblastoma cells through intelligent scrutiny of stain free biomarkers in holographic flow-cytometry," *Under Review.*

[216] V. Bianco, D. Pirone, P. Memmolo, F. Merola and P. Ferraro, "Identification of microplastics based on the fractal properties of their holographic fingerprint.," *ACS Photonics,* vol. 8, no. 7, pp. 2148-2157, 2021.

[217] D. Pirone, L. Xin, V. Bianco, L. Miccio, W. Xiao, L. Che, X. Li, P. Memmolo, F. Pan and P. Ferraro, "Identification of drug-resistant cancer cells in flow cytometry combining 3D holographic tomography with machine learning.," *Sens. Actuators B: Chem.,* vol. 375, p. 132963, 2023

[218] G. Barbastathis, A. Ozcan and G. Situ, "On the use of deep learning for computational imaging.," *Optica,* vol. 6, no. 8, pp. 921-943, 2019.

[219] Z. Ren, Z. Xu and E. Y. Lam, "Learning-based nonparametric autofocusing for digital holography.," *Optica,* vol. 5, no. 4, pp. 337-344, 2018.

[220] K. Jaferzadeh, S. H. Hwang, I. Moon and B. Javidi, "No-search focus prediction at the single cell level in digital holographic imaging with deep convolutional neural network.," *Biomed. Opt. Express,* vol. 10, no. 8, pp. 4276-4289., 2019.

[221] T. Pitkäaho, A. Manninen and T. J. Naughton, "Focus prediction in digital holographic microscopy using deep convolutional neural networks.," *Appl. Opt.,* vol. 58, no. 5, pp. A202-A208, 2019.

[222] T. Nguyen, V. Bui, V. Lam, C. B. Raub, L. C. Chang and G. Nehmetallah, "Automatic phase aberration compensation for digital holographic microscopy based on deep learning background detection.," *Opt. Express,* vol. 25, no. 16, pp. 15043-15057, 2017.

[223] W. Xiao, L. Xin, R. Cao, X. Wu, R. Tian, L. Che, L. Sun, P. Ferraro and F. Pan, "Sensing morphogenesis of bone cells under microfluidic shear stress by holographic microscopy and automatic aberration compensation with deep learning.," *Lab Chip,* vol. 21, no. 7, pp. 1385-1394, 2021.

[224] G. Dardikman-Yoffe, D. Roitshtain, S. K. Mirsky, N. A. Turko, M. Habaza and N. T. Shaked, "PhUn-Net: ready-to-use neural network for unwrapping quantitative phase images of biological cells.," *Biomed. Opt. Express,* vol. 11, no. 2, pp. 1107-1121, 2020.

[225] Y. Rivenson, Y. Zhang, H. Günaydın, D. Teng and A. Ozcan, "Phase recovery and holographic image reconstruction using deep learning in neural networks.," *Light Sci. Appl.,* vol. 7, no. 2, pp. 17141-17141, 2018.

[226] H. Wang, M. Lyu and G. Situ, "eHoloNet: a learning-based end-to-end approach for in-line digital holographic reconstruction.," *Opt. Express,* vol. 26, no. 18, pp. 22603-22614, 2018.

[227] Z. Ren, Z. Xu and E. Y. Lam, "End-to-end deep learning framework for digital holographic reconstruction.," *Adv. Photonics,* vol. 1, no. 1, p. 016004, 2019.

[228] K. Wang, J. Dou, Q. Kemao, J. Di and J. Zhao, "Y-Net: a one-to-two deep learning framework for digital holographic reconstruction.," *Opt. Lett.,* vol. 44, no. 19, pp. 4765-4768, 2019.

[229] T. Zeng, H. K. H. So and E. Y. Lam, "RedCap: residual encoder-decoder capsule network for holographic image reconstruction.," *Opt. Express,* vol. 28, no. 4, pp. 4876-4887, 2020.

[230] Q. Chen, J. Xu and V. Koltun, " Fast image processing with fully-convolutional networks.," *In Proceedings of the IEEE International Conference on Computer Vision,* pp. 2497-2506, 2017.

[231] F. Yu and V. Koltun, "Multi-scale context aggregation by dilated convolutions.," *In International Conference on Learning Representations,* 2016.

[232] K. K. Matthay, J. M. Maris, G. Schleiermacher, A. Nakagawara, C. L. Mackall, L. Diller and W. A. Weiss, "Neuroblastoma," *Nat. Rev. Dis. Primers,* vol. 10, no. 2, p. 16078, 2016.

[233] M. Capasso and S. J. Diskin, "Genetics and genomics of neuroblastoma.," *Cancer Genet.,* vol. 155, pp. 65-84, 2010.

[234] D. Formicola, G. Petrosino, V. A. Lasorsa, P. Pignataro, F. Cimmino, S. Vetrella, L. Longo, G. P. Tonini, A. Oberthuer, A. Iolascon, M. Fisher and M. Capasso, "An 18 gene expression-based score classifier predicts the clinical outcome in stage 4 neuroblastoma.," *J. Transl. Med.,* vol. 14, no. 1, pp. 1-9, 2016.

[235] G. P. Tonini and M. Capasso, "Genetic predisposition and chromosome instability in neuroblastoma.," *Cancer Metastasis Rev.,* vol. 39, no. 1, pp. 275-285, 2020.

[236] D. A. Weiser, D. C. West-Szymanski, E. Fraint, S. Weiner, M. A. Rivas, C. W. Zhao, C. He and M. A. Applebaum, "Progress toward liquid biopsies in pediatric solid tumors.," *Cancer Metastasis Rev.,* vol. 38, no. 4, pp. 553-571, 2019.

[237] G. De Rubis, S. R. Krishnan and M. Bebawy, "Liquid biopsies in cancer diagnosis, monitoring, and prognosis.," *Trends Pharmacol. Sci.,* vol. 40, no. 3, pp. 172-186, 2019.

[238] F. Cimmino, V. A. Lasorsa, S. Vetrella, A. Iolascon and M. Capasso, "A targeted gene panel for circulating tumor DNA sequencing in neuroblastoma.," *Front. Oncol.,* vol. 10, p. 596191, 2020.

[239] V. Plaks, C. D. Koopman and Z. Werb, "Circulating tumor cells.," *Science,* vol. 341, no. 6151, pp. 1186-1188, 2013.

[240] K. Pantel and M. R. Speicher, "The biology of circulating tumor cells.," *Oncogene,* vol. 35, no. 10, pp. 1216-1224, 2016.

[241] L. Miccio, F. Cimmino, I. Kurelac, M. M. Villone, V. Bianco, P. Memmolo, F. Merola, M. Mugnano, M. Capasso, A. Iolascon, P. L. Maffettone and P. Ferraro,

"Perspectives on liquid biopsy for label-free detection of “circulating tumor cells” through intelligent lab-on-chips.," *View,* vol. 1, no. 3, p. 20200034, 2020.

[242] X. Liu, Z. Zhang, B. Zhang, Y. Zheng, C. Zheng, B. Liu, S. Zheng, K. Dong and R. Dong, "Circulating tumor cells detection in neuroblastoma patients by EpCAM-independent enrichment and immunostaining-fluorescence in situ hybridization.," *EBioMedicine,* vol. 35, pp. 244-250, 2018.

[243] S. Merugu, L. Chen, E. Gavens, H. Gabra, M. Brougham, G. Makin, A. Ng, D. Murphy, A. S. Gabriel, M. L. Robinson, J. H. Wright, S. A. Burchill, A. Humphreys, N. Bown, D. Jamieson and D. A. Tweddle, "Detection of Circulating and Disseminated Neuroblastoma Cells Using the ImageStream Flow Cytometer for Use as Predictive and Pharmacodynamic Biomarkers," *Clin. Cancer Res.,* vol. 26, no. 1, pp. 122-134, 2020.

[244] H. H. Lam, P. W. M. Tsang and T. C. Poon, "Ensemble convolutional neural network for classifying holograms of deformable objects.," *Opt. Express,* vol. 27, no. 23, pp. 34050-34055, 2019.

[245] B. Schneider, G. Vanmeerbeeck, R. Stahl, L. Lagae and P. Bienstman, "Using neural networks for high-speed blood cell classification in a holographic-microscopy flow-cytometry system.," *Proc. SPIE 9328, Imag., Manipulation, Anal. Biomolecules, Cells, Tissues XIII,* 2015.

[246] S. J. Kim, C. Wang, B. Zhao, H. Im, J. Min, H. J. Choi, J. Tadros, N. R. Choi, C. M. Castro, R. Weissleder, H. Lee and K. Lee, "Deep transfer learning-based hologram classification for molecular diagnostics.," *Sci. Rep.,* vol. 8, no. 1, pp. 1-12, 2018.

[247] T. Y. Lin, M. Maire, S. Belongie, J. Hays, P. Perona, D. Ramanan, P. Dollar and C. L. Zitnick, "Microsoft coco: Common objects in context.," *Proc. Europ. Conf. Comput. Visi.,* pp. 740-755, 2014.

[248] V. K. Lam, T. C. Nguyen, B. M. Chung, G. Nehmetallah and C. B. Raub, "Quantitative assessment of cancer cell morphology and motility using telecentric digital holographic microscopy and machine learning.," *Cytometry A,* vol. 93, no. 3, pp. 334-345, 2018.

[249] K. He, G. Gkioxari, P. Dollár and R. Girshick, "Mask r-cnn.," *In Proceedings of the IEEE international conference on computer vision,* pp. 2961-2969, 2017.

[250] W. Abdulla, "Mask R-Cnn for Object Detection and Instance Segmentation on Keras and Tensorflow," 2017. [Online]. Available: https://github.com/matterport/Mask_RCNN.

[251] Y. LeCun, L. Bottou, Y. Bengio and P. Haffner, "Gradient-based learning applied to document recognition.," *Proc. IEEE,* vol. 86, no. 11, pp. 2278-2324, 1998.

[252] H. Abdi and L. J. Williams, "Principal component analysis.," *Wiley Interdiscip. Rev. Comput. Stat.,* vol. 2, no. 4, pp. 433-459, 2010.

[253] O. Mudanyali, D. Tseng, C. Oh, S. O. Isikman, I. Sencan, W. Bishara, C. Oztoprak, S. Seo, B. Khademhosseini and A. Ozcan, "Compact, light-weight and cost-effective microscope based on lensless incoherent holography for telemedicine applications.," *Lab Chip,* vol. 10, no. 11, pp. 1417-1428, 2010.

[254] P. C. Costa, Z. Guang, P. Ledwig, Z. Zhang, S. Neill, J. J. Olson and F. E. Robles, "Towards in-vivo label-free detection of brain tumor margins with epi-illumination tomographic quantitative phase imaging.," *Biomed. Opt. Express,* vol. 12, no. 3, pp. 1621-1634, 2021.

[255] B. Mandelbrot, The Fractal Geometry of Nature., W. H. Freeman & Co., 1983.

[256] G. Franceschetti and D. Riccio, Scattering, Natural Surfaces, and Fractals, Elsevier, 2007.

[257] G. A. Losa, D. Merlini, T. F. Nonnenmacher and E. R. Weibel, Fractals in Biology and Medicine, Springer, 2005.

[258] D. P. Popescu, C. Flueraru, Y. Mao, S. Chang and M. G. Sowa, "Signal attenuation and box-counting fractal analysis of optical coherence tomography images of arterial tissue.," *Biomed. Opt. Express,* vol. 1, no. 1, pp. 268-277, 2010.

[259] G. Landini, P. I. Murray and G. P. Misson, "Local connected fractal dimensions and lacunarity analyses of 60 degrees fluorescein angiograms.," *Invest. Ophthalmol. Visual Sci.,* vol. 36, no. 13, pp. 2749-2755, 1995.

[260] P. Pandithevan and G. Saravana Kumar, "Personalised bone tissue engineering scaffold with controlled architecture using fractal tool paths in layered manufacturing.," *Virtual Phys. Prototyp.,* vol. 4, no. 3, pp. 165-180, 2009.

[261] F. Yasar and F. Akgunlu, "Fractal dimension and lacunarity analysis of dental radiographs.," *Dentomaxillofacial radiology,* vol. 34, no. 5, pp. 261-267, 2005.

[262] A. Di Ieva, F. J. Esteban, F. Grizzi, W. Klonowski and M. Martín-Landrove, "Fractals in the neurosciences, part II: clinical applications and future perspectives.," *Neuroscientist,* vol. 21, no. 1, pp. 30-43, 2015.

[263] S. Krohn, M. Froeling, A. Leemans, D. Ostwald, P. Villoslada, C. Finke and F. J. Esteban, "Evaluation of the 3D fractal dimension as a marker of structural brain complexity in multiple-acquisition MRI.," *Hum. Brain Mapp.,* vol. 40, no. 11, pp. 3299-3320, 2019.

[264] A. L. Karperien and H. F. Jelinek, "Fractal, multifractal, and lacunarity analysis of microglia in tissue engineering.," *Front. Bioeng. Biotechnol.,* vol. 3, p. 51, 2015.

[265] T. G. Smith Jr, G. D. Lange and W. B. Marks, "Fractal methods and results in cellular morphology-dimensions, lacunarity and multifractals.," *J. Neurosci. Methods,* vol. 69, no. 2, pp. 123-136, 1996.

[266] W. Malina, "On an extended Fisher criterion for feature selection.," *IEEE Trans. Pattern Anal. Mach. Intell.,* vol. 5, pp. 611-614, 1981.

[267] L. Van der Maaten and G. Hinton, "Visualizing data using t-SNE.," *J. Mach. Learn. Res.,* vol. 9, no. 11, pp. 2579-2605, 2008.

[268] F. Bray, J. Ferlay, I. Soerjomataram, R. L. Siegel, L. A. Torre and A. Jemal, "Global cancer statistics 2018: GLOBOCAN estimates of incidence and

mortality worldwide for 36 cancers in 185 countries.," *CA Cancer J. Clin.,* vol. 68, no. 6, pp. 394-424, 2018.

[269] J. Lortet-Tieulent, J. Ferlay, F. Bray and A. Jemal, "International patterns and trends in endometrial cancer incidence, 1978–2013.," *J. Nat. Cancer Inst.,* vol. 110, no. 4, pp. 354-361, 2018.

[270] Y. Xiao, L. Jin, C. Deng, Y. Guan, E. Kalogera, U. Ray, P. Thirusangu, J. Staub, S. S. Bhattacharya, H. Xu, X. Fang and V. Shridhar, "Inhibition of PFKFB3 induces cell death and synergistically enhances chemosensitivity in endometrial cancer.," *Oncogene,* vol. 40, no. 8, pp. 1409-1424, 2021.

[271] T. L. Rižner, "Discovery of biomarkers for endometrial cancer: current status and prospects.," *Expert Rev. Mol. Diagn.,* vol. 16, no. 2, pp. 1315-1336, 2016.

[272] T. Yao, R. Cao, W. Xiao, F. Pan and X. Li, "An optical study of drug resistance detection in endometrial cancer cells by dynamic and quantitative phase imaging.," *J. Biophotonics,* vol. 12, no. 7, p. e201800443, 2019.

[273] P. Gheibi, S. Zeng, K. J. Son, T. Vu, A. H. Ma, M. A. Dall'Era, S. A. Yap, R. White, C. X. Pan and A. Revzin, "Microchamber cultures of bladder cancer: a platform for characterizing drug responsiveness and resistance in PDX and primary cancer cells.," *Sci. Rep.,* vol. 7, no. 1, pp. 1-10, 2017.

[274] Y. Kanintronkul, R. Worayuthakarn, N. Thasana, P. Winayanuwattikun, K. Pattanapanyasat, R. Surarit, S. Ruchirawat and J. Svasti, "Overcoming multidrug resistance in human lung cancer with novel benzo [a] quinolizin-4-ones.," *Anticancer Res.,* vol. 31, no. 3, pp. 921-927, 2011.

[275] A. Pasqualato, A. Palombo, A. Cucina, M. A. Mariggiò, L. Galli, D. Passaro, S. Dinicola, S. Proietti, F. D'Anselmi, P. Coluccia and M. Bizzarri, "Quantitative shape analysis of chemoresistant colon cancer cells: correlation between morphotype and phenotype.," *Exp. Cell Res.,* vol. 318, no. 7, pp. 835-846, 2012.

[276] N. A. Puspita and A. Bedford, "Morphological Changes of Cisplatin-resistant Human Breast Cancer MCF-7 Cell Line.," *Int. J. Integr. Health Sci.,* vol. 5, no. 1, pp. 8-14, 2017.

[277] Z. Zhao, R. Zhang, J. Cox, D. Duling and W. Sarle, "Massively parallel feature selection: an approach based on variance preservation.," *Mach. Learn.,* vol. 92, no. 1, pp. 195-220, 2013.

[278] J. Benesty, J. Chen, Y. Huang and I. Cohen, in *Pearson Correlation Coefficient. In: Noise Reduction in Speech Processing.*, Springer, 2009, pp. 37-40.

[279] I. S. Thaseen and C. A. Kumar, "Intrusion detection model using fusion of chi-square feature selection and multi class SVM.," *J. King Saud Univ. - Comput. Inf. Sci.,* vol. 29, no. 4, pp. 462-472, 2017.

[280] M. Skurichina and R. P. Duin, "Bagging, boosting and the random subspace method for linear classifiers.," *Pattern Anal. App.,* vol. 5, no. 2, pp. 121-135, 2002.

[281] Y. Rivenson, T. Liu, Z. Wei, Y. Zhang, K. de Haan and A. Ozcan, "PhaseStain: the digital staining of label-free quantitative phase microscopy images using deep learning.," *Light: Sci. Appl.,* vol. 8, no. 1, pp. 1-11, 2019.

[282] N. Borhani, A. J. Bower, S. A. Boppart and D. Psaltis, "Digital staining through the application of deep neural networks to multi-modal multi-photon microscopy.," *Biomed. Opt. Express,* vol. 10, no. 3, pp. 1339-1350, 2019.

[283] Y. Rivenson, H. Wang, Z. Wei, K. de Haan, Y. Zhang, Y. Wu, H. Günaydın, J. E. Zuckerman, T. Chong, A. E. Sisk, L. M. Westbrook, W. D. Wallace and A. Ozcan, "Virtual histological staining of unlabelled tissue-autofluorescence images via deep learning.," *Nat. Biomed. Eng.,* vol. 3, no. 6, pp. 466-477, 2019.

[284] M. E. Kandel, Y. R. He, Y. J. Lee, T. H. Y. Chen, K. M. Sullivan, O. Aydin, M. T. A. Saif, H. Kong, N. Sobh and G. Popescu, "Phase imaging with computational specificity (PICS) for measuring dry mass changes in sub-cellular compartments.," *Nat. Commun.,* vol. 11, no. 1, pp. 1-10, 2020.

[285] Y. N. Nygate, M. Levi, S. K. Mirsky, N. A. Turko, M. Rubin, I. Barnea, G. Dardikman-Yoffe, M. Haifler, A. Shalev and N. T. Shaked, "Holographic virtual staining of individual biological cells.," *Proc. Natl. Acad. Sci. USA,* vol. 117, no. 17, pp. 9223-9231, 2020.

[286] J. Lee, H. Kim, H. Cho, Y. Jo, Y. Song, D. Ahn, K. Lee, Y. Park and S. J. Ye, "Deep-learning-based label-free segmentation of cell nuclei in time-lapse refractive index tomograms.," *IEEE Access,* vol. 7, pp. 83449-83460, 2019.

[287] Y. Jo, H. Cho, W. S. Park, G. Kim, D. Ryu, Y. S. Kim, M. Lee, S. Park, M. J. Lee, H. Joo, H. Jo, S. Lee, S. Lee, H.-S. Min, W. D. Heo and Y. Park, "Label-free multiplexed microtomography of endogenous subcellular dynamics using generalizable deep learning.," *Nat. Cell Biol.,* vol. 23, no. 12, pp. 1329-1337, 2021.

[288] E. J. Gualda, H. Pereira, G. G. Martins, R. Gardner and N. Moreno, "Three-dimensional imaging flow cytometry through light-sheet fluorescence microscopy.," *Cytometry A,* vol. 91, no. 2, pp. 144-151, 2017.

[289] Y. Han, R. Tang, Y. Gu, A. C. Zhang, W. Cai, V. Castor, S. H. Cho, W. Alaynick and Y. H. Lo, "Cameraless high-throughput three-dimensional imaging flow cytometry.," *Optica,* vol. 6, no. 10, pp. 1297-1304, 2019.

[290] D. Pirone, J. Lim, F. Merola, L. Miccio, M. Mugnano, V. Bianco, F. Cimmino, F. Visconte, A. Montella, M. Capasso, A. Iolascon, P. Memmolo, D. Psaltis and P. Ferraro, "Stain-free nucleus specificity in tomographic phase microscopy in flow cytometry".

[291] D. Pirone, D. Sirico, L. Miccio, V. Bianco, M. Mugnano, D. del Giudice, G. Pasquinelli, S. Valente, S. Lemma, L. Iommarini, I. Kurelac, P. Memmolo and P. Ferraro, "3D imaging lipidometry in single cell by in-flow holographic tomography.," *Opto-Electron. Adv.,* vol. 6, p. 220048 , 2023.

[292] J. Behal, D. Pirone, D. Sirico, V. Bianco, M. Mugnano, D. del Giudice, B. Cavina, I. Kurelac, P. Memmolo, L. Miccio and P. Ferraro, "On monocytes and lymphocytes biolens clustering by in flow holographic microscopy," *Cytometry A.*

[293] D. Pirone, D. Sirico, M. Mugnano, D. del Giudice, I. Kurelac, B. Cavina, P. Memmolo, L. Miccio and P. Ferraro, "Finding intracellular lipid droplets from the single-cell biolens' signature in holographic flow-cytometry assay".

[294] D. Pirone, M. Mugnano, P. Memmolo, F. Merola, G. C. Lama, R. Castaldo, L. Miccio, V. Bianco, S. Grilli and P. Ferraro, "Three-dimensional quantitative

intracellular visualization of graphene oxide nanoparticles by tomographic flow cytometry.," *Nano Lett.,* vol. 21, no. 14, pp. 5958-5966, 2021.

[295] P. Memmolo, D. Pirone, D. G. Sirico, L. Miccio, V. Bianco, A. B. Ayoub, D. Psaltis and P. Ferraro, "Single-cell phase-contrast tomograms data encoded by 3D Zernike descriptors.," *arXiv preprint,* https://doi.org/10.48550/arXiv.2207.04854, 2022.

[296] D. Kim, S. Lee, M. Lee, J. Oh, S. A. Yang and Y. Park, "Holotomography: refractive index as an intrinsic imaging contrast for 3-D label-free live cell imaging.," in *Advanced Imaging and Bio Techniques for Convergence Science*, Singapore, Springer, 2021, pp. 211-238.

[297] D. Pirone, J. Lim, F. Merola, L. Miccio, M. Mugnano, V. Bianco, F. Cimmino, F. Visconte, A. Montella, M. Capasso, A. Iolascon, P. Memmolo, D. Psaltis and P. Ferraro, "Stain-free identification of cell nuclei using tomographic phase microscopy in flow cytometry.," *Nat. Photonics,* vol. 16, pp. 851-859, 2022.

[298] H. B. Mann and D. R. Whitney, "On a test of whether one of 2 random variables is stochastically larger than the other.," *Annals of Mathematical Statistics,* vol. 18, p. 50-60, 1947.

[299] F. Wilcoxon, "Individual comparisons by ranking methods.," *Biometrics Bulletin,* vol. 1, p. 80-83, 1945.

[300] P. J. McIntire, J. T. Snow, S. S. Elsoukkary, L. Soong, J. Sweeney, B. D. Robinson and M. T. Siddiqui, "Digital image analysis supports a nuclear-to-cytoplasmic ratio cutoff value below 0.7 for positive for high-grade urothelial carcinoma and suspicious for high-grade urothelial carcinoma in urine cytology specimens.," *Cancer Cytopathol.,* vol. 127, no. 2, pp. 120-124, 2019.

[301] J. Liu, Y. Xu, W. Wang, Y. Wen, H. Hong, J. Q. Lu, P. Tian and X. H. Hu, "Machine learning of diffraction image patterns for accurate classification of cells modeled with different nuclear sizes.," *J. Biophotonics,* vol. 13, no. 9, p. e202000036, 2020.

[302] M. J. Moore, J. A. Sebastian and M. C. Kolios, "Determination of cell nucleus-to-cytoplasmic ratio using imaging flow cytometry and a combined ultrasound

and photoacoustic technique: a comparison study.," *J. Biomed. Opt.,* vol. 24, p. 106502 , 2019.

[303] D. Zink, A. H. Fischer and J. A. Nickerson, "Nuclear structure in cancer cells.," *Nat. Rev. Cancer,* vol. 4, pp. 677-687, 2004.

[304] T. Takaki, M. Montagner, M. P. Serres, M. Le Berre, M. Russell, L. Collinson, K. Szuhai, M. Howell, S. J. Boulton, E. Sahai and M. Petronczki, "Actomyosin drives cancer cell nuclear dysmorphia and threatens genome stability.," *Nat. Commun.,* vol. 8, no. 1, pp. 1-13, 2017.

[305] G. Willems, G. Pison, P. J. Rousseeuw and S. Van Aelst, "A robust Hotelling test.," *Metrika ,* vol. 55, no. 1, pp. 125-138, 2002.

[306] H. G. Schwarzacher and F. Wachtler, "The nucleolus.," *Anat. Embryol.,* vol. 188, no. 6, pp. 515-536, 1993.

[307] D. J. Murphy, "The dynamic roles of intracellular lipid droplets: from archaea to mammals.," *Protoplasma ,* vol. 249, p. 541–585, 2012.

[308] J. A. Olzmann and P. Carvalho, "Dynamics and functions of lipid droplets.," *Nat. Rev. Mol. Cell Biol.,* vol. 20, p. 137–155, 2019.

[309] F. Geltinger, L. Schartel, M. Wiederstein, J. Tevini, E. Aigner, T. K. Felder and M. Rinnerthaler, "Friend or Foe: Lipid Droplets as Organelles for Protein and Lipid Storage in Cellular Stress Response, Aging and Disease.," *Molecules ,* vol. 25, p. 5053 , 2020.

[310] Y. Imai, R. S. Cousins, S. Liu, B. M. Phelps and J. A. Promes, "Connecting pancreatic islet lipid metabolism with insulin secretion and the development of type 2 diabetes.," *Ann. N. Y. Acad. Sci.,* vol. 1461, p. 53–72, 2020.

[311] K. J. Williams and I. Tabas, "The Response-to-Retention Hypothesis of Early Atherogenesis.," *Arterioscler. Thromb. Vasc. Biol.,* vol. 15, p. 551–561, 1995.

[312] N. L. Gluchowski, M. Becuwe, T. C. Walther and R. V. Farese, "Lipid droplets and liver disease: from basic biology to clinical implications.," *Nat. Rev. Gastroenterol. Hepatol.,* vol. 14, p. 343–355, 2017.

[313] L. Liu, K. Zhang, H. Sandoval, S. Yamamoto, M. Jaiswal, E. Sanz, Z. Li, J. Hui, B. H. Graham, A. Quintana and H. J. Bellen, "Glial lipid droplets and ROS induced by mitochondrial defects promote neurodegeneration.," *Cell,* vol. 160, pp. 177-190, 2015.

[314] A. L. S. Cruz, E. d. A. Barreto, N. P. B. Fazolini, J. P. B. Viola and P. T. Bozza, "Lipid droplets: platforms with multiple functions in cancer hallmarks.," *Cell Death Dis.,* vol. 11, p. 105, 2020.

[315] L. Tirinato, F. Pagliari, T. Limongi, M. Marini, A. Falqui, J. Seco, P. Candeloro, C. Liberale and E. Di Fabrizio, "An overview of lipid droplets in cancer and cancer stem cells.," *Stem Cells Int.,* vol. 2017, pp. 1-17, 2017.

[316] R. C. N. Melo and P. F. Weller, "Lipid droplets in leukocytes: Organelles linked to inflammatory responses.," *Exp. Cell Res.,* vol. 340, p. 193–197, 2016.

[317] E. A. Monson, A. M. Trenerry, J. L. Laws, J. M. Mackenzie and K. J. Helbig, "Lipid droplets and lipid mediators in viral infection and immunity.," *FEMS Microbiol. Rev.,* vol. 45, no. 4, p. fuaa066, 2021.

[318] R. Nardacci, F. Colavita, C. Castilletti, D. Lapa, G. Matusali, S. Meschi, F. Del Nonno, D. Colombo, M. R. Capobianchi, A. Zumla, G. Ippolito, M. Piacentini and L. Falasca, "Evidences for lipid involvement in SARS-CoV-2 cytopathogenesis.," *Cell Death Dis.,* vol. 12, no. 3, pp. 1-12, 2021.

[319] A. S. Martins, I. C. Martins and N. C. Santos, "Methods for Lipid Droplet Biophysical Characterization in Flaviviridae Infections.," *Front. Microbiol.,* vol. 9, p. 1951, 2018.

[320] T. Fam, A. Klymchenko and M. Collot, "Recent Advances in Fluorescent Probes for Lipid Droplets.," *Materials ,* vol. 11, p. 1768, 2018.

[321] T. Fujimoto, Y. Ohsaki, M. Suzuki and J. Cheng, "Imaging lipid droplets by electron microscopy.," in *Methods in cell biology*, Academic Press, 2013, pp. 227-251.

[322] M. H. Wilson, S. C. Ekker and S. A. Farber, "Imaging cytoplasmic lipid droplets in vivo with fluorescent perilipin 2 and perilipin 3 knock-in zebrafish.," *eLife ,* vol. 10, p. e66393, 2021.

[323] P. Ferraro, D. Alferi, S. De Nicola, L. De Petrocellis, A. Finizio and G. Pierattini, "Quantitative phase-contrast microscopy by a lateral shear approach to digital holographic image reconstruction.," *Opt. Lett.,* vol. 31, no. 10, pp. 1405-1407, 2006.

[324] P. A. Sandoz, C. Tremblay, F. G. van der Goot and M. Frechin, "Image-based analysis of living mammalian cells using label-free 3D refractive index maps reveals new organelle dynamics and dry mass flux.," *PLoS Biol.,* vol. 17, p. e3000553 , 2019.

[325] C. M. Hsieh, P. Y. Liu, L. K. Chin, J. B. Zhang, K. Wang, K. B. Sung, W. Ser, T. Bourouina, Y. Leprince-Wang and A. Q. Liu, "Regulation of lipid droplets in live preadipocytes using optical diffraction tomography and Raman spectroscopy.," *Opt. Express,* vol. 27, no. 16, pp. 22994-23008, 2019.

[326] Y. Huang, W. Xia, Z. Lu, Y. Liu, H. Chen, J. Zhou, L. Fang and Y. Zhang, "Noise-powered disentangled representation for unsupervised speckle reduction of optical coherence tomography images.," *IEEE Trans. Med. Imaging,* vol. 40, no. 10, pp. 2600-2614, 2020.

[327] J. Jung, S. J. Hong, H. B. Kim, G. Kim, M. Lee, S. Shin, S. Lee, D.-J. Kim, C.-G. Lee and Y. Park, "Label-free non-invasive quantitative measurement of lipid contents in individual microalgal cells using refractive index tomography.," *Sci. Rep.,* vol. 8, no. 1, pp. 1-10, 2018.

[328] K. Kim, S. Lee, J. Yoon, J. Heo, C. Choi and Y. Park, "Three-dimensional label-free imaging and quantification of lipid droplets in live hepatocytes.," *Sci. Rep.,* vol. 6, no. 1, pp. 1-8, 2016.

[329] S. Park, J. W. Ahn, Y. Jo, H. Y. Kang, H. J. Kim, Y. Cheon, J. W. Kim, Y. Park, S. Lee and K. Park, "Label-free tomographic imaging of lipid droplets in foam cells for machine-learning-assisted therapeutic evaluation of targeted nanodrugs.," *ACS Nano,* vol. 14, no. 2, pp. 1856-1865, 2020.

[330] I. Y. Yanina, E. N. Lazareva and V. V. Tuchin, "Refractive index of adipose tissue and lipid droplet measured in wide spectral and temperature ranges.," *Appl. Opt.,* vol. 57, no. 17, pp. 4839-4848, 2018.

[331] L. Sheneman, G. Stephanopoulos and A. E. Vasdekis, "Deep learning classification of lipid droplets in quantitative phase images.," *Plos One,* vol. 16, no. 4, p. e0249196, 2021.

[332] T. C. Walther and R. V. Farese Jr, "Lipid droplets and cellular lipid metabolism.," *Annu. Rev. Biochem.,* vol. 81, p. 687, 2012.

[333] R. V. Farese Jr and T. C. Walther, "Lipid droplets go nuclear.," *J. Cell Biol.,* vol. 212, no. 1, p. 7, 2016.

[334] Y. Ohsaki, K. Sołtysik and T. Fujimoto, "The Lipid Droplet and the Endoplasmic Reticulum.," in *Organelle Contact Sites. Advances in Experimental Medicine and Biology*, Singapore, Springer, 2017, pp. 111-120.

[335] K. Bersuker, C. W. Peterson, M. To, S. J. Sahl, V. Savikhin, E. A. Grossman, D. K. Nomura and J. A. Olzmann, "A proximity labeling strategy provides insights into the composition and dynamics of lipid droplet proteomes.," *Dev. Cell,* vol. 44, no. 1, pp. 97-112, 2018.

[336] T. Pan, D. Lu, H. Xin and B. Li, "Biophotonic probes for bio-detection and imaging.," *Light: Sci. Appl.,* vol. 10, no. 1, pp. 1-22, 2021.

[337] X. Liu, Y. Li, X. Xu, Y. Zhang and B. Li, "Red-blood-cell-based microlens: application to single-cell membrane imaging and stretching.," *ACS Appl. Bio Mater.,* vol. 2, no. 7, pp. 2889-2895, 2019.

[338] Y. Li, X. Liu and B. Li, "Single-cell biomagnifier for optical nanoscopes and nanotweezers.," *Light: Sci. Appl.,* vol. 8, no. 1, pp. 1-12, 2019.

[339] S. Lee, H. Park, K. Kim, Y. Sohn, S. Jang and Y. Park, "Refractive index tomograms and dynamic membrane fluctuations of red blood cells from patients with diabetes mellitus.," *Sci. Rep.,* vol. 7, no. 1, pp. 1-11, 2017.

[340] T. Go, J. H. Kim, H. Byeon and S. J. Lee, "Machine learning-based in-line holographic sensing of unstained malaria-infected red blood cells.," *J. Biophotonics,* vol. 11, no. 9, p. e201800101, 2018.

[341] T. Go, H. Byeon and S. J. Lee, "Label-free sensor for automatic identification of erythrocytes using digital in-line holographic microscopy and machine learning.," *Biosens. Bioelectron.,* vol. 103, pp. 12-18, 2018.

[342] F. Merola, Á. Barroso, L. Miccio, P. Memmolo, M. Mugnano, P. Ferraro and C. Denz, "Biolens behavior of RBCs under optically-induced mechanical stress.," *Cytometry A,* vol. 91, no. 5, pp. 527-533, 2017.

[343] J. Behal, D. Pirone, D. Sirico, V. Bianco, M. Mugnano, D. del Giudice, B. Cavina, I. Kurelac, P. Memmolo, L. Miccio and P. Ferraro, "On monocytes and lymphocytes biolens clustering by in flow holographic microscopy," *Cytometry A,* 2022.

[344] X. Chen, T. Wu, Z. Gong, J. Guo, X. Liu, Y. Zhang, Y. Li, P. Ferraro and B. Li, "Lipid droplets as endogenous intracellular microlenses.," *Light: Sci. Appl.,* vol. 10, no. 1, pp. 1-11, 2021.

[345] D. Pirone, D. Sirico, M. Mugnano, D. del Giudice, I. Kurelac, B. Cavina, P. Memmolo, L. Miccio and P. Ferraro, "Finding intracellular lipid droplets from the single-cell biolens' signature in holographic flow-cytometry assay," *Biomed. Opt. Express,* vol. 13, no. 11, pp. 5585-5598, 2022.

[346] C. R. Santos and A. Schulze, "Lipid metabolism in cancer.," *FEBS J.,* vol. 279, no. 15, pp. 2610-2623, 2012.

[347] D. Howie, A. Ten Bokum, A. S. Necula, S. P. Cobbold and H. Waldmann, "The role of lipid metabolism in T lymphocyte differentiation and survival.," *Front. Immunol.,* vol. 8, p. 1949, 2018.

[348] S. Chowdhury, M. Chen, R. Eckert, D. Ren, F. Wu, N. Repina and L. Waller, "High-resolution 3D refractive index microscopy of multiple-scattering samples from intensity images.," *Optica,* vol. 6, no. 9, pp. 1211-1219, 2019.

[349] A. J. Izenman, Modern multivariate statistical techniques, New York: Springer, 2008.

[350] F. Bonaccorso, Z. Sun, H. T. A. and A. C. Ferrari, "Graphene photonics and optoelectronics.," *Nat. Photonics,* vol. 4, no. 9, p. 611, 2010.

[351] R. Castaldo, G. C. Lama, P. Aprea, G. Gentile, V. Ambrogi, M. Lavorgna and P. Cerruti, "Humiditydriven mechanical and electrical response of graphene/cloisite hybrid films.," *Adv. Funct. Mat.,* vol. 29, no. 14, p. 1807744, 2019.

[352] V. Palmieri and M. Papi, "Can graphene take part in the fight against COVID-19?," *Nano Today,* vol. 33, p. 100883, 2020.

[353] R. M. Torrente-Rodríguez, H. Lukas, J. Tu, J. Min, Y. Yang, C. Xu, H. B. Rossiter and W. Gao, "SARS-CoV-2 RapidPlex: A Graphene-Based Multiplexed Telemedicine Platform for Rapid and Low-Cost COVID-19 Diagnosis and Monitoring.," *Matter,* vol. 3, no. 6, pp. 1981-1998, 2020.

[354] Z. Liu, J. T. Robinson, X. Sun and H. Dai, "PEGylated nanographene oxide for delivery of water-insoluble cancer drugs.," *J. Am. Chem. Soc.,* vol. 130, no. 33, pp. 10876-10877, 2008.

[355] F. Liu, J. Y. Choi and T. S. Seo, "Graphene oxide arrays for detecting specific DNA hybridization by fluorescence resonance energy transfer.," *Biosens. Bioelectron.,* vol. 25, no. 10, pp. 2361-2365, 2010.

[356] H. Chang, L. Tang, Y. Wang, J. Jiang and J. Li, "Graphene fluorescence resonance energy transfer aptasensor for the thrombin detection.," *Anal. Chem.,* vol. 82, no. 6, pp. 2341-2346, 2010.

[357] J. H. Jung, D. S. Cheon, F. Liu, K. B. Lee and T. S. Seo, "A graphene oxide based immuno-biosensor for pathogen detection.," *Angew. Chem.,* vol. 122, no. 33, pp. 5844-5847, 2010.

[358] Y. Wen, F. Xing, S. He, S. Song, L. Wang, Y. Long, D. Li and C. Fan, "A graphene-based fluorescent nanoprobe for silver (I) ions detection by using graphene

oxide and a silver-specific oligonucleotide.," *Chem. Commun.,* vol. 46, no. 15, pp. 2596-2598, 2010.

[359] Y. Song, K. Qu, C. Zhao, J. Ren and X. Qu, "Graphene oxide: intrinsic peroxidase catalytic activity and its application to glucose detection.," *Adv. Mater.,* vol. 22, no. 19, pp. 2206-2210, 2010.

[360] W. Cao, L. He, W. Cao, X. Huang, K. Jia and J. Dai, "Recent Progress of Graphene Oxide as a Potential Vaccine Carrier and Adjuvant.," *Acta Biomaterialia,* vol. 112, pp. 14-28, 2020.

[361] M. Orecchioni, C. Ménard-Moyon, L. G. Delogu and A. Bianco, "Graphene and the immune system: Challenges and potentiality.," *Adv. Drug Deliv. Rev.,* vol. 105, pp. 163-175, 2016.

[362] L. Belyanskaya, P. Manser, P. Spohn, A. Bruinink and P. Wick, "The reliability and limits of the MTT reduction assay for carbon nanotubes–cell interaction.," *Carbon,* vol. 45, no. 13, pp. 2643-2648, 2007.

[363] V. Gies and S. Zou, "Systematic toxicity investigation of graphene oxide: evaluation of assay selection, cell type, exposure period and flake size.," *Toxicol. Res.,* vol. 7, no. 1, pp. 93-101, 2018.

[364] H. Dong, W. Gao, F. Yan, H. Ji and H. Ju, "Fluorescence resonance energy transfer between quantum dots and graphene oxide for sensing biomolecules.," *Anal. Chem.,* vol. 82, no. 13, pp. 5511-5517, 2010.

[365] J. Farkas and A. M. Booth, "Are fluorescence-based chlorophyll quantification methods suitable for algae toxicity assessment of carbon nanomaterials?," *Nanotoxicology ,* vol. 11, pp. 569-577, 2017.

[366] M. Zhang, Z. Fu, C. Li, A. Liu, D. Peng, F. Xue, W. He, S. Gao, F. Xu and D. Xu, "Fast super-resolution imaging technique and immediate early nanostructure capturing by a photoconvertible fluorescent protein.," *Nano Lett.,* vol. 20, no. 4, pp. 2197-2208, 2020.

[367] W. Liu, B. Naydenov, S. Chakrabortty, B. Wuensch, K. Hgbner, S. Ritz, H. Cçlfen, H. Barth, K. Koynov, H. Qi, R. Leiter, R. Reuter, J. Wrachtrup, F. Boldt, J. Scheuer, U. Kaiser, M. Sison, T. Lasser, P. Tinnefeld, F. Jelezko and al.,

"Fluorescent Nanodiamond–Gold Hybrid Particles for Multimodal Optical and Electron Microscopy Cellular Imaging.," *Nano Lett.,* vol. 16, pp. 6236-6244, 2016.

[368] H.-J. van Manen and C. Otto, "Hybrid Confocal Raman Fluorescence Microscopy on Single Cells Using Semiconductor Quantum Dots.," *Nano Lett.,* vol. 7, pp. 1631-1636, 2007.

[369] X. Wang, H. Yi, I. Gdor, M. Hereld and N. F. Scherer, "Nanoscale Resolution 3D Snapshot Particle Tracking by Multifocal Microscopy.," *Nano Lett.,* vol. 19, no. 10, pp. 6781-6787, 2019.

[370] M. Eliášová Sohová, M. Bodík, P. Siffalovic, N. Bugárová, M. Labudová, M. Zatovičová, T. Hianik, M. Omastová, E. Majková, M. Jergel and S. Pastoreková, "Label-Free Tracking of Nanosized Graphene Oxide Cellular Uptake by Confocal Raman Microscopy.," *Analyst,* vol. 143, pp. 3686-3692, 2018.

[371] H. Shin, M. Kwak, T. G. Lee and J. Y. Lee, "Quantifying the level of nanoparticle uptake in mammalian cells using flow cytometry.," *Nanoscale ,* vol. 12, no. 29, pp. 15743-15751, 2020.

[372] A. Jochums, E. Friehs, F. Sambale, A. Lavrentieva, D. Bahnemann and T. Scheper, "Revelation of different nanoparticle-uptake behavior in two standard cell lines NIH/3T3 and A549 by flow cytometry and time-lapse imaging.," *Toxics ,* vol. 5, no. 3, p. 15, 2017.

[373] S. Mues, J. Antunovic, R. Ossig, B. Kemper and J. Schnekenburger, "Optical analysis of nanomaterial-cell interactions: Flow cytometry and digital holographic microscopy.," *Proc. SPIE,* vol. 9529, p. 95290E, 2015.

[374] C. Zheng, D. Jin, Y. He, H. Lin, J. Hu, Z. Yaqoob, P. T. C. So and R. Zhou, "High spatial and temporal resolution synthetic aperture phase microscopy.," *Adv. Photonics,* vol. 2, no. 6, p. 065002, 2020.

[375] M. Mugnano, G. C. Lama, R. Castaldo, V. Marchesano, F. Merola, D. del Giudice, A. Calabuig, G. Gentile, V. Ambrogi, P. Cerruti and P. Memmolo, "Cellular Uptake of Mildly Oxidized Nanographene for Drug-Delivery Applications.," *ACS Appl. Nano Mater.,* vol. 3, no. 1, pp. 428-439, 2019.

[376] A. Laurentini, "The visual hull concept for silhouette-based image understanding.," *IEEE Trans. Pattern Anal. Mach. Intell.,* vol. 16, no. 2, p. 150–162, 1994.

[377] F. Merola, L. Miccio, P. Memmolo, G. Di Caprio, A. Galli, R. Puglisi, D. Balduzzi, G. Coppola, P. Netti and P. Ferraro, "Digital holography as a method for 3D imaging and estimating the biovolume of motile cells.," *Lab Chip,* vol. 13, no. 23, pp. 4512-4516, 2013.

[378] T. Lammel, P. Boisseaux, M. L. Fernandez-Cruz and J. M. Navas, "Internalization and cytotoxicity of graphene oxide and carboxyl graphene nanoplatelets in the human hepatocellular carcinoma cell line Hep G2.," *Part. Fibre Toxicol.,* vol. 10, p. 27, 2013.

[379] B. Ge, Y. He, M. Deng, M. H. Rahman, Y. Wang, Z. Wu, C. H. N. Wong, M. K. Chan, J.-P. Ho, L. Duan, Z. Yaqoob, P. T. C. So, G. Barbastathis and R. Zhou, "Single-frame label-free cell tomography at speed of more than 10,000 volumes per second," *arXiv preprint,* vol. https://doi.org/10.48550/arXiv.2202.03627, 2022.

[380] W. B. Pennebaker and J. L. Mitchell, JPEG: Still image data compression standard., Springer Science & Business Media, 1992.

[381] J. R. Ohm, G. J. Sullivan, H. Schwarz, T. K. Tan and T. Wiegand, "Comparison of the coding efficiency of video coding standards—including high efficiency video coding (HEVC).," *IEEE Trans. Circuits Syst. Video Technol.,* vol. 22, no. 12, pp. 1669-1684, 2012.

[382] L. F. Lucas, N. M. Rodrigues, L. A. da Silva Cruz and S. M. de Faria, "Lossless compression of medical images using 3-D predictors.," *IEEE Trans. Med. Imaging,* vol. 36, no. 11, pp. 2250-2260, 2017.

[383] D. Rossinelli, G. Fourestey, F. Schmidt, B. Busse and V. Kurtcuoglu, "High-throughput lossy-to-lossless 3D image compression.," *IEEE Trans. Med. Imaging,* vol. 40, no. 2, pp. 607-620, 2020.

[384] D. Xue, H. Ma, L. Li, D. Liu and Z. Xiong, "aiWave: Volumetric Image Compression with 3-D Trained Affine Wavelet-like Transform.," p. arXiv preprint arXiv:2203.05822, 2022.

[385] T. Bruylants, P. Schelkens and A. Tzannes, "JP3D–Extensions for Three-Dimensional Data (Part 10).," in *The JPEG 2000 Suite*, Wiley-Blackwell, 2009, pp. 199-227.

[386] N. Canterakis, "3D Zernike moments and zernike affine invariants for 3D image analysis and recognition.," in *11th Scandinavian Conference on Image Analysis*, 1999.

[387] M. Novotni and R. Klein, "Shape retrieval using 3D Zernike descriptors.," *Comput. Aided Des.,* vol. 36, no. 11, pp. 1047-1062, 2004.

[388] L. Di Rienzo, L. De Flaviis, G. Ruocco, V. Folli and E. Milanetti, "Binding site identification of G protein-coupled receptors through a 3D Zernike polynomials-based method: application to C. elegans olfactory receptors.," *J. Comput. Aided Mol. Des. ,* vol. 36, pp. 11-24, 2022.

[389] A. B. Ayoub, T. A. Pham, J. Lim, M. Unser and D. Psaltis, "A method for assessing the fidelity of optical diffraction tomography reconstruction methods using structured illumination.," *Opt. Commun.,* vol. 454, p. 124486, 2020.

[390] D. G. Sirico, L. Miccio, Z. Wang, P. Memmolo, W. Xiao, L. Che, L. Xin, F. Pan and P. Ferraro, "Compensation of aberrations in holographic microscopes: main strategies and applications.," *Appl. Phys. B,* vol. 128, no. 4, pp. 1-19, 2022.

[391] T. A. Pham, E. Soubies, A. Ayoub, J. Lim, D. Psaltis and M. Unser, "Three-dimensional optical diffraction tomography with Lippmann-Schwinger model.," *IEEE Trans. Comput. Imaging,* vol. 6, pp. 727-738, 2020.

[392] P. Memmolo, D. Pirone, L. Miccio, F. Cimmino, I. Kurelac, M. M. Villone, V. Bianco, F. Merola, M. Mugnano, M. Capasso, A. Iolascon, P. L. Maffettone and P. Ferraro, "Tomographic flow cytometry as the key-enabling technology for label-free liquid biopsy.," in *29th Mediterranean Conference on Control and Automation (MED) - IEEE*, Puglia, Italy, 2021.

[393] C. Alix-Panabières and K. Pantel, "Challenges in circulating tumour cell research.," *Nat. Rev. Cancer,* vol. 14, no. 9, pp. 623-631, 2014.

[394] A. Fabisiewicz, M. Szostakowska-Rodzos, A. J. Zaczek and E. A. Grzybowska, "Circulating tumor cells in early and advanced breast cancer; biology and prognostic value.," *Int. J. Mol. Sci.,* vol. 21, no. 5, p. 1671, 2020.

[395] P. P. Wang, S. H. Liu, C. T. Chen, L. Lv, D. Li, Q. Y. Liu, G. L. Liu and Y. Wu, "Circulating tumor cells as a new predictive and prognostic factor in patients with small cell lung cancer.," *J. Cancer,* vol. 11, no. 8, p. 2113, 2020.

[396] C. Yang, B. R. Xia, W. L. Jin and G. Lou, "Circulating tumor cells in precision oncology: Clinical applications in liquid biopsy and 3D organoid model.," *Cancer Cell Int.,* vol. 19, no. 1, pp. 1-13, 2019.

[397] S. Riethdorf, L. O'Flaherty, C. Hille and K. Pantel, "Clinical applications of the CellSearch platform in cancer patients.," *Adv. Drug Deliv. Rev.,* vol. 125, pp. 102-121, 2018.

[398] E. Moen, D. Bannon, T. Kudo, W. Graf, M. Covert and D. Van Valen, "Deep learning for cellular image analysis.," *Nat. Methods,* vol. 16, no. 2, pp. 1233-1246, 2019.

[399] A. Kleiber, A. Ramoji, G. Mayer, U. Neugebauer, J. Popp and T. Henkel, "3-Step flow focusing enables multidirectional imaging of bioparticles for imaging flow cytometry.," *Lab Chip,* vol. 20, no. 9, pp. 1676-1686, 2020.

[400] D. K. Singh, C. C. Ahrens, W. Li and S. A. Vanapalli, "Label-free fingerprinting of tumor cells in bulk flow using inline digital holographic microscopy.," *Biomed. Opt. Express,* vol. 8, no. 2, pp. 536-554, 2017.

[401] F. Moisy, "Boxcount.," MATLAB Central File Exchange, [Online]. Available: https://www.mathworks.com/matlabcentral/fileexchange/13063-boxcount. [Accessed 17 02 2021].

[402] G. Bouligand, "Sur la notion d'ordre de mesure d'un ensemble plan.," *Bull. Sci. Math.,* vol. 2, pp. 185-192, 1929.

[403] R. E. Plotnick, R. H. Gardner and R. V. O'Neill, "Lacunarity indices as measures of landscape texture.," *Landsc. Ecol.,* vol. 8, pp. 201-211, 1993.

[404] M. Schürmann, J. Scholze, P. Müller, J. Guck and C. J. Chan, "Cell nuclei have lower refractive index and mass density than cytoplasm.," *J. Biophotonics,* vol. 9, no. 10, pp. 1068-1076, 2016.

[405] M. A. Yurkin, "How a phase image of a cell with nucleus refractive index smaller than that of the cytoplasm should look like?," *J. Biophotonics,* vol. 11, p. e201800033, 2018.

[406] R. Y. Tsai and T. Pederson, "Connecting the nucleolus to the cell cycle and human disease.," *FASEB J.,* vol. 28, no. 8, pp. 3290-3296, 2014.

[407] L. Núñez Villacís, M. S. Wong, L. L. Ferguson, N. Hein, A. J. George and K. M. Hannan, "New roles for the nucleolus in health and disease.," *Bioessays,* vol. 40, no. 5, p. 1700233, 2018.

[408] P. H. Guttman and S. Halpern, "Nuclear-nucleolar volume ratio in cancer.," *Am. J. Cancer,* vol. 25, no. 4, pp. 802-806, 1935.

[409] K. I. Farley, Y. Surovtseva, J. Merkel and S. J. Baserga, "Determinants of mammalian nucleolar architecture.," *Chromosoma ,* vol. 124, no. 3, pp. 323-331, 2015.

[410] H. Wadell, "Volume, Shape and Roundness of Quartz Particles.," *The Journal of Geology,* vol. 43, no. 3, pp. 250-280, 1935.

Author's Publications

Peer-Reviewed Journals

- **D. Pirone**, J. Lim, F. Merola, L. Miccio, M. Mugnano, V. Bianco, F. Cimmino, F. Visconte, A. Montella, M. Capasso, A. Iolascon, P. Memmolo, D. Psaltis and P. Ferraro, "Stain-free identification of cell nuclei using tomographic phase microscopy in flow cytometry.," *Nat. Photonics,* vol. 16, pp. 851-859, 2022.
- **D. Pirone**, D. Sirico, L. Miccio, V. Bianco, M. Mugnano, D. del Giudice, G. Pasquinelli, S. Valente, S. Lemma, L. Iommarini, I. Kurelac, P. Memmolo and P. Ferraro, "3D imaging lipidometry in single cell by in-flow holographic tomography.," *Opto-Electron. Adv.,* vol. 6, p. 220048 , 2023.
- **D. Pirone**, L. Xin, V. Bianco, L. Miccio, W. Xiao, L. Che, X. Li, P. Memmolo, F. Pan and P. Ferraro, "Identification of drug-resistant cancer cells in flow cytometry combining 3D holographic tomography with machine learning.," *Sens. Actuators B: Chem.,* vol. 375, p. 132963, 2023.
- **D. Pirone**, D. Sirico, L. Miccio, V. Bianco, M. Mugnano, P. Ferraro and P. Memmolo, "Speeding up reconstruction of 3D tomograms in holographic flow cytometry via deep learning.," *Lab Chip,* vol. 22, no. 4, pp. 793-804, 2022.
- **D. Pirone**, M. M. Villone, P. Memmolo, Z. Wang, V. Tkachenko, W. Xiao, L. Che, L. Xin, X. Li, F. Pan, P. Ferraro and P. L. Maffettone, "On the hydrodynamic mutual interactions among cells for high-throughput microfluidic holographic cyto-tomography.," *Opt. Lasers Eng.,* vol. 158, p. 107190, 2022.

- **D. Pirone**, D. Sirico, M. Mugnano, D. del Giudice, I. Kurelac, B. Cavina, P. Memmolo, L. Miccio and P. Ferraro, "Finding intracellular lipid droplets from the single-cell biolens' signature in holographic flow-cytometry assay.," *Biomed. Opt. Express*, vol. 13, no. 11, pp. 5585-5598, 2022.
- **D. Pirone**, V. Bianco, M. Valentino, M. Mugnano, V. Pagliarulo, P. Memmolo, L. Miccio and P. Ferraro, "Fourier ptychographic microscope allows multi-scale monitoring of cells layout onto micropatterned substrates.," *Opt. Lasers Eng.,* vol. 156, p. 107103, 2022.
- J. Behal, **D. Pirone**, D. Sirico, V. Bianco, M. Mugnano, D. del Giudice, B. Cavina, I. Kurelac, P. Memmolo, L. Miccio and P. Ferraro, "On monocytes and lymphocytes biolens clustering by in flow holographic microscopy.," *Cytometry A*, 2022.
- Bianco, M. D. Priscoli, **D. Pirone**, G. Zanfardino, P. Memmolo, F. Bardozzo, L. Miccio, G. Ciaparrone, P. Ferraro and R. Tagliaferri, "Deep learning-based, misalignment resilient, real-time Fourier Ptychographic Microscopy reconstruction of biological tissue slides.," *IEEE J. Sel. Topics Quantum Electron.,* vol. 28, no. 4, pp. 1-10, 2022.
- P. Memmolo, **D. Pirone**, D. G. Sirico, L. Miccio, V. Bianco, A. B. Ayoub, D. Psaltis and P. Ferraro, "Single-cell phase-contrast tomograms data encoded by 3D Zernike descriptors.," *arXiv preprint,* https://doi.org/10.48550/arXiv.2207.04854, 2022.
- **D. Pirone**, M. Mugnano, P. Memmolo, F. Merola, G. C. Lama, R. Castaldo, L. Miccio, V. Bianco, S. Grilli and P. Ferraro, "Three-dimensional quantitative intracellular visualization of graphene oxide nanoparticles by tomographic flow cytometry.," *Nano Lett.,* vol. 21, no. 14, pp. 5958-5966, 2021.
- V. Bianco, **D. Pirone**, P. Memmolo, F. Merola and P. Ferraro, "Identification of microplastics based on the fractal properties of their holographic fingerprint.," *ACS Photonics,* vol. 8, no. 7, pp. 2148-2157, 2021.

- **D. Pirone**, P. Memmolo, F. Merola, L. Miccio, M. Mugnano, A. Capozzoli, C. Curcio, A. Liseno and P. Ferraro, "Rolling angle recovery of flowing cells in holographic tomography exploiting the phase similarity.," *Appl. Opt.,* vol. 60, no. 4, pp. A277-A284, 2021.
- Z. Wang, V. Bianco, **D. Pirone**, P. Memmolo, M. M. Villone, P. L. Maffettone and P. Ferraro, "Dehydration of plant cells shoves nuclei rotation allowing for 3D phase-contrast tomography.," *Light: Sci. Appl.,* vol. 10, no. 1, pp. 1-16, 2021.
- M. D. Priscoli, P. Memmolo, G. Ciaparrone, V. Bianco, F. Merola, L. Miccio, F. Bardozzo, **D. Pirone**, M. Mugnano, F. Cimmino, M. Capasso, A. Iolascon, P. Ferraro and R. Tagliaferri, "Neuroblastoma cells classification through learning approaches by direct analysis of digital holograms.," *IEEE J. Sel. Top. Quantum Electron.,* vol. 27, no. 5, pp. 1-9, 2021.
- **D. Pirone**, A. Montella, D. Sirico, M. Mugnano, D. Del Giudice, I. Kurelac, M. Tirelli, A. Iolascon, V. Bianco, P. Memmolo, M. Capasso, L. Miccio and P. Ferraro, "Phenotyping neuroblastoma cells through intelligent scrutiny of stain free biomarkers in holographic flow-cytometry.," *Under Review*.
- V. Bianco, L. Miccio, **D. Pirone**, E. Cavalletti, J. Behal, P. Memmolo, A. Sardo and P. Ferraro, "Multi-scale fractal Fourier Ptychographic Microscopy for assessing the dose-dependent impact of copper pollution on living diatoms.," *Under Review*.

Conference Proceedings

- **D. Pirone**, D. G. Sirico, L. Miccio, L. Bianco, A. Capozzoli, C. Curcio, A. Liseno, P. Memmolo and P. Ferraro, "On the 3D Pose Dynamics of Flowing Cells in Holo-Tomographic Flow Cytometry," in *Digital Holography and Three-Dimensional Imaging - Optica Publishing Group*, Cambridge, UK, 2022.
- **D. Pirone**, D. Sirico, L. Miccio, V. Bianco, M. Mugnano, P. Ferraro and P. Memmolo, "End-to-end holographic reconstruction by deep learning for

tomographic flow cytometry," in *Digital Holography and Three-Dimensional Imaging - Optica Publishing Group*, Cambridge, UK, 2022.

- L. Miccio, **D. Pirone**, D. Sirico, F. Merola, P. Memmolo, V. Bianco, Z. Wang, J. Behal, D. del Giudice, M. Mugnano and P. Ferraro, "Tomographic phase microscopy at single cell scale without a-priori knowledge of cell orientations: smart strategies for rotation angles recovery.," in *SPIE Photonics Europe - Unconventional Optical Imaging III*, Strasbourg, France, 2022.
- V. Bianco, P. Memmolo, J. Běhal, **D. Pirone**, M. Valentino, M. Mugnano, V. Pagliarulo, L. Miccio and P. Ferraro, "On the use of multilook Fourier ptychographic microscopy for observing cells and tissues.," in *SPIE Photonics Europe - Unconventional Optical Imaging III*, Strasbourg, France, 2022.
- V. Bianco, M. Valentino, J. Běhal, **D. Pirone**, S. Itri, R. Mossotti, G. Dalla Fontana, E. Stella, L. Miccio, P. Memmolo and P. Ferraro, "Digital holography in microplastic identification.," in *SPIE Photonics Europe - Unconventional Optical Imaging III*, Strasbourg, France, 2022.
- V. Bianco, M. D. Priscoli, M, Valentino, **D. Pirone**, J. Behal, G. Zanfardino, P. Memmolo, F. Bardozzo, L. Miccio, G. Ciaparrone, R. Tagliaferri and P. Ferraro, "Real-time FPM reconstruction and misalignment correction by numerical Multi-Look and GAN.," in *Computational Optical Sensing and Imaging - Optica Publishing Group*, Vancouver, Canada, 2022.
- **D. Pirone**, P. Memmolo, F. Merola, L. Miccio, M. Mugnano, A. Capozzoli, C. Curcio, A. Liseno and P. Ferraro, "Tracking-based rolling angles recovery method for holographic tomography of flowing cells.," in *SPIE Optical Metrology - Optical Methods for Inspection, Characterization, and Imaging of Biomaterials V*, Online Only, Germany, 2021.
- **D. Pirone**, V. Bianco, P. Memmolo, F. Merola and P. Ferraro, "A fractal analysis of the holographic diffraction patterns for detecting microplastics

among diatoms.," in *International Workshop on Metrology for the Sea (MetroSea) - IEEE*, Reggio Calabria, Italy, 2021.

- P. Memmolo, **D. Pirone**, L. Miccio, F. Cimmino, I. Kurelac, M. M. Villone, V. Bianco, F. Merola, M. Mugnano, M. Capasso, A. Iolascon, P. L. Maffettone and P. Ferraro, "Tomographic flow cytometry as the key-enabling technology for label-free liquid biopsy.," in *29th Mediterranean Conference on Control and Automation (MED) - IEEE*, Puglia, Italy, 2021.
- D. Sirico, E. Cavalletti, L. Miccio, V. Bianco, **D. Pirone**, P. Memmolo, A. Sardo and P. Ferraro, "Holographic tracking and imaging of free-swimming Tetraselmis by off-axis holographic microscopy.," in *International Workshop on Metrology for the Sea (MetroSea) - IEEE*, Reggio Calabria, Italy, 2021.
- E. Cavalletti, A. Sardo, V. Bianco, L. Miccio, **D. Pirone**, D. Sirico, M. Valentino, M. Spinelli and P. Ferraro, "Microalgae as potential bioindicators for heavy metal pollution.," in *International Workshop on Metrology for the Sea (MetroSea) - IEEE*, Reggio Calabria, Italy, 2021.
- M. D. Priscoli, P. Memmolo, G. Ciaparrone, V. Bianco, F. Merola, L. Miccio, F. Bardozzo, **D. Pirone**, M. Mugnano, F. Cimmino, M. Capasso, A. Iolascon, P. Ferraro and R. Tagliaferri, "Raw holograms based machine learning for cancer cells classification in microfluidics.," in *Digital Holography and Three-Dimensional Imaging - Optica Publishing Group*, Washington, DC United States, 2021.
- V. Bianco, P. Memmolo, **D. Pirone**, P. Carcagnì, F. Merola, L. Miccio, M. Paturzo, C. Distante and P. Ferraro, "Holographic fingerprint as a morphological marker to identify micro-plastics.," in *SPIE Optical Metrology - Optical Measurement Systems for Industrial Inspection XII*, Online Only, Germany, 2021.
- Z. Wang, V. Bianco, **D. Pirone**, P. Memmolo, M. M. Villone, P. L. Maffettone and P. Ferraro, "Investigation of plant cells intracellular dynamics by digital

holography.," in *SPIE Optical Metrology - Optical Methods for Inspection, Characterization, and Imaging of Biomaterials V*, Online Only, Germany, 2021.

- Z. Wang, **D. Pirone**, V. Bianco, P. Memmolo, M. M. Villone, P. L. Maffettone and P. Ferraro, "Induced dehydration as a method to enhance phase-contrast observation of plant cells intracellular dynamics.," in *Digital Holography and Three-Dimensional Imaging - Optical Society of America*, Washington, DC United States, 2021.
- M. Mugnano, G. C. Lama, R. Castaldo, F. Merola, D. del Giudice, S. Grilli, G. Gentile, V. Ambrogi, P. Cerruti, P. Memmolo, V. Pagliarulo, **D. Pirone** and P. Ferraro, "Cytocompatibility and 3D biodistribution with oxidized nanographene assessed by digital holographic microscopy.," in *SPIE Optical Metrology - Optical Methods for Inspection, Characterization, and Imaging of Biomaterials V*, Online Only, Germany, 2021.
- L. Miccio, F. Cimmino, I. Kurelac, M. M. Villone, V. Bianco, M. Mugnano, F. Merola, P. Memmolo, **D. Pirone**, M. Capasso, A. Iolascon, P. L. Maffettone and P. Ferraro, "Label-free microfluidic platform for blood analysis based on phase-contrast imaging.," in *8th International Workshop on Metrology for AeroSpace - IEEE*, Naples, Italy, 2021.
- Z. Wang, V. Bianco, **D. Pirone**, P. Memmolo, M. Paturzo and P. Ferraro, "Holographic phase imaging to observe intracellular dynamics of plant cells during dehydration.," in *Frontiers in Optics - Optica Publishing Group*, Washington, DC United States, 2020.